Title
Physical conditions in Damped Lyman alpha Systems

Author
Jorgenson, Regina A.

Publication Date
2008

UNIVERSITY OF CALIFORNIA, SAN DIEGO

Physical Conditions in Damped Lyman alpha Systems

A dissertation submitted in partial satisfaction of the
requirements for the degree Doctor of Philosophy
in
Physics

by

Regina A. Jorgenson

Committee in charge:

Arthur M. Wolfe, Chair
Kim Greist
Michael L. Norman
Kevin B. Quest
Mark H. Thiemens

2008

The dissertation of Regina A. Jorgenson is approved, and it is acceptable in quality and form for publication on microfilm:

Chair

University of California, San Diego

2008

To my parents

Maja and Wil

For their unconditional love and boundless support,

and for inspiring never-ending wonder with the world.

TABLE OF CONTENTS

LIST OF FIGURES

LIST OF TABLES

ACKNOWLEDGEMENTS

This is perhaps the most difficult part of this thesis to write. To actually put into mere words how thankful I am to so many people who have been so important to me and so vital to my getting to this place, is a daunting task to say the least. So I begin by thanking my advisor, Art, without whom this thesis would not exist. Thank you for taking a chance on me years ago and for always being an exemplary model of what a scientist and a person should be. Thank you also to all the folks at CASS. I will miss you all. To my other womyn in the house, Christel – thank you for your friendship, especially during this last year. I don't know what I would have done without you. Your ability to combine rockin' physics with rockin' fashion is an inspiration to me. Did I tell you that I love that headscarf? To David and Maggie, for being such awesome, funny, interesting people and of course, for looking after Gil. I will miss you guys. To Tommy, for being a good friend and generally cool guy – I can't wait for you to save the world. To Anna and Novi, three words: grad school POW – we share a special bond having been through our first year together – thanks for being such great friends. A special thank you goes to Marc, for being my grad student group buddy and of course, Mac guru. Thanks for being so kind and generous with your support and knowledge. To Paul and Pete, computer-support team extraordinaire, thank you for always fielding my dumb questions and printer problems.

Outside of CASS, there are so many friends and family, near and far, who have been key to my success. First, I thank my parents. Words cannot capture the gratitude that I feel towards you for your eternal strength and support. And of course, for always inspiring my questioning and need to know more. You taught me to believe in myself always and that there was nothing I couldn't do if I worked hard. Obviously, this thesis would not have happened without you. To my brother Erik and his family who always help me to forget my all-consuming 'problems' and to see the larger meaning of life. To Steve, for listening to me bitch, helping me to understand the 'men's world' of physics, valiantly trying to boost my self-confidence, and for generally being an important part of my life. You will always hold a special place in my heart. To Shannon, my most kindred of spirits, who embarked on this grad school journey with me and was a source of constant support and an ardent cheerleader. I never could have done this without you. To my housemates, Amy and Caroline, while it's sad we are all so far apart, our reunions are cherished events for me – hanging out with you guys always makes me feel like myself again. To Rachael and Latha, you will always be a part of my life and no part of my life goes by without your influence. Thanks for being such great friends over the (many!) years. To my Maria Mitchell peeps – Ben, Amy, Angela, Sarah...I will meet you at Cambridge Street –the beer is on me. Finally, I thank Gilbert, the one person who truly kept me sane by forcing me to come home at night, and he is a cat. I could have done without the whole lilly-eating incident however...

To my mentors far away – Vladimir at the Maria Mitchell Observatory, thank you for your support and always wise council over the years. I chose the hard road and as you predicted it paid off. Perhaps now it is time for me to become a champion in the hammer-throw... To Alan at UPS, what I wouldn't give to be back in one of your physics classes (or out on Blue Water). Thank you for laying the foundation from which I grew. I am blessed and honored to have had you all in my life and I thank you all from the bottom of my heart.

Official Stuff:

Chapter 2, in full (with minor exceptions to conform to this thesis), is a reprint of "The UCSD Radio-Selected Quasar Survey for Damped Lyman-α Systems", Jorgenson, R. A., Wolfe, A. M., Prochaska, J. X., Lu, L., Howk,

J. C., Cooke, J., Gawiser, E., & Gelino, D. M. 2006, The Astrophysical Journal, Vol. 646, p. 730. The dissertation author was the primary investigator and first author of the paper. Chapter 4, in full (with minor exceptions to conform to this thesis), is a reprint of "Bimodality in Damped Lyman-α Systems", Wolfe, A. M., Prochaska, J. X., Jorgenson, R. A., & Rafelski, M. 2008, The Astrophysical Journal, Vol. 681, p. 881. Chapter 5, in full (with minor exceptions to conform to this thesis), is a reprint of "An 84 μG Magnetic Field in a Galaxy at Redshift $z = 0.692$", Wolfe, A. M., Jorgenson, R. A., Robishaw, T., Heiles, C., & Prochaska, J. X., 2008, Nature, Accepted August 2008.

VITA

EDUCATION

2008	Ph.D. Physics, University of California, San Diego
2007	C.Phil., Physics, University of California, San Diego
2005	M.S., Physics, University of California, San Diego
1998	B.S., *Coolidge Otis Chapman Honors Scholar*, Physics, University of Puget Sound

AWARDS AND HONORS

2002 - 2005	GAANN Graduate Fellowship
2002 - 2005	San Diego Graduate Fellowship
1998 - 1999	Thomas J. Watson Foundation Fellowship
1998	Phi Beta Kappa
1998	Sigma Pi Sigma

PUBLICATIONS

Understanding Physical Conditions in High Redshift Galaxies through Neutral Carbon Fine Structure Lines
Jorgenson, R. A., Wolfe, A.M., & Prochaska, J. X., in preperation

An 84 μG Magnetic Field in a Galaxy at Redshift $z = 0.692$
Wolfe, A.M., **Jorgenson, R. A.**, Robishaw, T., Heiles, C, & Prochaska, J. X., Accepted by *Nature*, August 2008.

Bimodality in Damped Lyman α Systems
Wolfe, A.M., Prochaska, J. X., **Jorgenson, R. A.**, & Rafelski, M., 2008, ApJ, 681, 881

The UCSD Radio-Selected Quasar Survey for Damped Lyman α Systems
Jorgenson, R. A., Wolfe, A.M., Prochaska, J. X., Lu, L., Howk, J.C., Cooke, J., Gawiser, E., & Gelino, D.M., 2006, ApJ, 646, 730

3 Year Monitoring of Millimeter-Wave Radio Recombination Lines from MWC 349
Gordon, M. A., Holder, B. P., Jisonna, L. J., Jr., **Jorgenson, R. A.**, Strelnitski, V. S., 2001, ApJ, 559, 402

Complex Variability of the Peculiar Emission-Line Star MWC349
Jorgenson, R. A. , 2001, JAAVSO, 29, 154

Red Light Curve of MWC349 in the Years 1967 - 1981: Possible Periodicity
Jorgenson, R. A., Kogan, L.R., Strelnitski, V., 2000, AJ, 119, 3060

Two-year Monitoring of MWC349 in Optical and Radio Domains
Hornstein, S., Jisonna, L., **Jorgenson, R. A.**, Lu, E., Gordon, M., Strelnitski, V., 1999, AAS, 195, 505

PROCEEDINGS, PROPOSALS, ETC.

"A Fast MagE Survey for Molecular Hydrogen in Damped Lyman α Systems" Jorgenson, R. A., & Murphy, M., 2008, *Magellan Telescope, MagE* Winter Semester Proposal.

"On Women in Physics" Jorgenson, R. A., & Smith C. J., Invited presentation, June 2008, UC Santa Barbara

"Supernova 2008ax in NGC 4490" Li, W., van Dyk, S. D., Cuillandre, J.-C., Filippenko, A. V., Foley, R. J., Chornock, R., Smith, N., Wang, X., Wolfe, A. M., Jorgenson, R., Rafelski, M., *Central Bureau Electronic Telegrams*, 2008, 1290, 1

"Understanding Physical Conditions in High Redshift Galaxies through CI Fine Structure Lines Jorgenson, R. A., 2008, *Aspen Center for Physics*, Winter Meeting

"Probing Physical Conditions in the Highly Magnetized Gas in a Galaxy at z$\sim$1" Wolfe, A.M., Jorgenson, R.A., Heiles, C., Robishaw, T., & Prochaska, J. X., 2008, *Hubble Space Telescope*, Cycle 17 Proposal

"OSIRIS Search for Emission from High z Damped Lyman alpha Systems" Wolfe, A. M., Jorgenson, R. A., Prochaska, J. X., 2008, 2007 & 2006, *Keck Telescope OSIRIS* Proposals

"ESI-HIRES Survey for CII* Absorption in Damped Lyman alpha Systems" Wolfe, A. M., Jorgenson, R. A. & Prochaska, J. X., 2008, 2007 & 2006 *Keck Telescope ESI and HIRES* Proposals

“Understanding Physical Conditions in High Redshift Galaxies through CI Fine Structure Lines” Jorgenson, R. A., 2008, *American Astronomical Society Meeting*, 211, 73.02

“Detection of B Fields in Damped Lyman alpha Systems” Wolfe, A. M., Jorgenson, R. A., Heiles, C., Robishaw, T. 2007, *Green Bank Telescope* Proposal

“Probing Conditions in High Redshift Galaxies through CI fine structure Lines Jorgenson, R. A., 2007, *Keck Science Meeting*

“Understanding Galaxy Formation and Evolution Through Quasar Absorption Lines Jorgenson, R. A., 2007, Invitied Talk, *Maria Mitchell Observatory*, Nantucket, MA

“Investigation of Bright Flat-Spectrum Radio Sources without Optical Counterparts for Evidence of Obscuration by Foreground Damped Lyman alpha Systems” Wolfe, A. M., Jorgenson, R. A., di Polletta, M., Stern, D., Werner, M., Brookes, M., Prochaska, J. X., 2007, *Spitzer* Cycle 14 Proposal

“The UCSD Radio-Selected Quasar Survey for Damped Lyman-alpha Systems Jorgenson, R. A., 2007, Invited Talk, *Green Bank Telescope*, Green Bank, West Virginia

“A Search for 21 cm Absorption Toward Ratio Loud Sources with Extremely Faint Optical Counterparts” Wolfe, A. M., Jorgenson, R. A., Darling, J., 2005, *Green Bank Telescope* Proposal

“The UCSD Radio-Selected Quasar Survey for Damped Lyman-alpha Systems Jorgenson, R. A., 2005, *CAM: Canadian-American-Mexican Physics Graduate Student Conference*, San Diego, CA

“Plate-related work at the Maria Mitchell Observatory” Strelnitski, V., Samus, N, Jorgenson, R., Springob, C., 1999, *International workshop: Treasure-hunting in astronomical plate archives*, p. 84

“CCD Photometry of MWC349A Separated from Its Companion” Billings, K. & Jorgenson, R. A. 1998, *American Astronomical Society Meeting*, 193, 102.09

“Periodic Light Variations in MWC349?” Jorgenson, R. A. & Strelnitski, V. 1997, *American Astronomical Society Meeting*, 191, 43.11

FIELDS OF STUDY

Major Field: Physics and Astrophysics

Studies in Mathematical Physics:
Professor Donald R. Fredkin

Studies in Theoretical Mechanics:
Professor Patrick H. Diamond

Studies in Quantum Mechanics:
Professor Lu Sham

Studies in Advanced Classical Electrodynamics:
Professor Thomas M. O'Neil

Studies in Equilibrium and Statistical Mechanics:
Professor Terrence Hwa

Studies in Stellar Structure and Evolution:
Professor George M. Fuller

Studies in Cosmology:
Professor Michael Norman

Studies in Physics of the Interstellar Medium:
Professor Arthur M. Wolfe

Studies in Galaxies and Galactic Dynamics:
Professor Arthur M. Wolfe

Studies in Physics of Turbulence:
Professor Paolo Padoan

Studies in Instruments for Physics and Astrophysics:
Professor David Tytler

ABSTRACT OF THE DISSERTATION

Physical Conditions in Damped Lyman alpha Systems

by

Regina A. Jorgenson
Doctor of Philosophy in Physics
University of California, San Diego, 2008
Arthur M. Wolfe, Chair

The primary goal of this thesis is to determine physical conditions in high redshift galaxies known as Damped Lymna α Systems. To this end, we present several key results. First, we discuss a radio-selected quasar survey that demonstrates that dust bias is likely *not* an issue affecting surveys for DLAs. In other words, we are seeing the true and complete population of DLAs and not missing some very high column density, dusty DLAs. Second, we use neutral carbon (C I) fine structure states to show the presence of gas with densities and pressures $1-2$ orders of magnitude larger than those expected in the global DLA, i.e. the presence of knots of dense cold gas existing in the larger diffuse DLA. To solve the imbalance of pressure between these two phases, we speculate that these regions are created by shocks that provide relatively high densities that in turn allow for the existence of C I. Alternatively, these could be photodissociation regions on the edges of even more dense molecular clouds that could even be hosting star formation. This model would explain the presence of a radiation field generally above the background. We also present unambiguous evidence of the presence of cold gas in DLAs – the discovery of narrow sub-resolution, sub-1km s^{-1} C I components with thermal temperatures $< \sim$100 K. In the third section we summarize 10+ years of high resolution observations of DLAs that reveal a bimodality in their implied cooling rate, ℓ_c. This cooling rate is linked to the star formation rate via the assumption of thermal equilibrium.

The bimodality shows that the two populations, the ”high-cool” and the ”low-cool” DLAs may be representative of two types of DLAs – the high-cool DLAs are heated by a centrally located core of star formation, i.e. a bright, star-forming Lyman Break Galaxy (LBG), while the low-cool DLAs are not hosting a central LBG. Finally, we discuss our discovery of a strong (84 μG) magnetic field at a redshift of z $\sim$ 0.7. This is unexpected given the current theories of dynamo formation of magnetic fields (for time scale arguments) and also because the general magnetic field permeating the Milky Way is more than order of magnitude smaller at $\sim$ 6 μG. While this single detection could be a unique event caused by some unique geometry, it certainly inspires further observations of other objects to test whether large magnetic fields could possibly be a general feature of high redshift galaxies. In either case, it spawns the idea that magnetic fields likely play a larger role in galaxy formation and cosmology than has been previously appreciated.

1

Introduction

1.1 Galaxy Formation and Evolution

The current paradigm of galaxy formation favors the hierarchical buildup of galaxies, also known as the “bottom-up” model, over the Monolithic Collapse Model, or “top-down” model. For some time, the Monolithic Collapse Model, proposed by Eggen et al. (1962) in 1962 and used to describe the collapse of a gas cloud into a rotating disk, or spiral galaxy, was widely accepted. Recent observations and computational work however, have shown that the opposite process, in which large galaxies form as a result of mergers of smaller galaxies, is more likely to be true.

The current model of galaxy formation and evolution is based on what is called the Λ Cold Dark Matter, or ΛCDM model. Λ represents the cosmological constant, originally proposed by Albert Einstein in order to allow his equations of General Relativity to mesh with the paradigm of the day, the static Universe. He later removed the constant after Hubble’s discovery of the expanding Universe, famously calling it his “biggest blunder”. However, in 1998−99, two groups (Riess et al. 1998) and (Perlmutter et al. 1999), used the Hubble diagram of distant type Ia supernovae to show that the expansion of the Universe is actually accelerating, a fact that reintroduces the need for the cosmological constant, now also known as dark energy. The WMAP mission (Spergel et al. 2007), which mapped the temperature fluctuations of the Cosmic Microwave Background radiation (CMB), together with the supernovae studies and other observations, have successfully solved for the cosmological parameters, finding that Ω_Λ, the fraction of the total energy density of the Universe contained in the cosmological constant, is $\Omega_\Lambda \sim 0.74$, or 74%.

The second part of the model describes the second largest contributor to the energy density, the Cold Dark Matter. Cold dark matter is defined as being non-baryonic, dissipationless, collisionless matter having non-relativistic velocities. Dark matter is necessary to explain the rotation curves of galaxies – essentially, the circular velocity as a function of radius – that should fall off in a Keplerian way, but rather remain flat out to large radii. This widely observed property is explained by the presence of a much larger dark matter halo enveloping the central, visible galaxy. Cold dark matter makes up ∼22% of the energy density of the Universe. An additional ∼4% of the energy density resides in baryonic matter in stars, galaxies, and the media between them.

ΛCDM predicts that galaxies gain mass through clustering and merging, also known as the hierarchical model. The model predicts that early on, primordial density fluctuations grew as the Universe cooled, causing dark matter halos to condense out of the expanding background. These proto-galaxies were composed primarily of dark matter and gas. These dark matter halos interact through gravity. Clustering of the dark matter halos eventually leads to mergers and the formation of larger dark matter halos. As these proto-galaxies gain mass, the gas within them contracts, rotating faster and collapsing to form a disk and condensing to make stars. These ideas were first presented by Press & Schechter (1974), who developed formalism to calculate the mass function of halos at a given epoch, and White & Rees (1978) who proposed that the small scale dark halos merge and the gas can cool and self-gravitate to form galaxies.

There exists much observational and computational evidence for the hierarchical model of galaxy formation. Large surveys of visible galaxies, such as the Sloan Digital Sky Survey (SDSS) and the 2dF Galaxy Redshift Survey have allowed for mapping of the large-scale structure of the Universe and the measurement of the matter power spectrum, while large N-body simulations reproduce many aspects of the observations. However, there are problems with the hierarchical model. For example, the mechanism that stops the contraction is not fully understood, and theoretical models are not able to reproduce the rotation speed and size of disk galaxies. Additionally, the timescales of the collapse and formation are not well constrained.

Recent observations of high redshift galaxies could prove a potential challenge for the ΛCDM model. For example, in 2006, Genzel et al. (2006) discovered what may be a large, massive rotating disk at a time when the Universe was only ∼20% of its current age. They used an Integral Field Unit (IFU) and Adaptive Optics to obtain high angular resolution observations of large massive proto-disks at $z \sim 2-3$. While they generally are unable to distinguish between mergers or disk rotation scenarios, in one case they claim their data shows no evidence for a major merger. They estimate star formation rates and ages that are suggestive of very rapid formation. If this really is a large rotating disk galaxy at high redshift, assuming it is not some outlying rare event, this could challenge the hierarchical model in which large well-formed, rotating disk galaxies should be scarce in the early Universe.

However, the evidence is not conclusive and the question of how galaxies form remains open. Moreover, these bright star forming galaxies are *not* normal galaxies – those that contain the bulk of the gas – and they are unlikely to evolve into the typical spiral galaxies we see today. They have merely been selected because their extreme luminosity allows them to be observed at high redshifts. If we are interested in the population of objects that dominate the gas mass and likely form the majority of modern galaxies, we must understand the Damped Lyman α Systems (DLAs) – the focus of this thesis. The primary difference between DLAs and the purported rotating disks observed by Genzel et. al. is that DLAs dominate the neutral gas content of the Universe. DLAs likely have a large role in galaxy formation and are possibly the only way to study the formation of normal galaxies at high redshifts.

In the spirit of this quest we embark on a more detailed description of a key player in this game, the Interstellar Medium (ISM). The lifeblood of a galaxy, the ISM condenses via shocks or gravitational collapse to form molecular clouds, out of which stars are born. Those stars feed back metals to enrich the ISM through winds and supernovae explosions in a continual cycle of formation and enrichment. Hence, it is difficult to understand galaxies without a solid understanding of the ISM. We first describe the local ISM, followed by a description of how we analyze the ISM of high redshift DLAs.

1.2 Physical Conditions in the Milky Way and local Universe

The ISM is a multi-phase, turbulent medium with a distribution of temperatures and densities. While the majority of the gas mass is contained in neutral H I clouds and in dense, cold molecular clouds, most of the volume is occupied by diffuse hot gas that pressure confines the cooler clouds. The elemental make up of the ISM is roughly 90% hydrogen and 10% helium by number density, with trace amounts of heavier elements, referred to as 'metals' in astrophysics.

The ISM of the Milky Way consists of the following components, presented here in order of decreasing density (see Figure 1.1 for a pictorial representation):

- *Molecular Clouds* : At <1% of the fractional volume, molecular clouds exist out to scale heights of 70 pc with typical temperatures of 10−20 K and densities of n = 10^2−10^6 cm^{-3}. As the name suggests they consist primarily of molecular (hydrogen) gas and are considered to be the birth place of stars.
- *Cold Neutral Medium* (*CNM*) : The CNM contributes 1−5% of the fractional volume, is found at scale heights of 100−300 pc and temperatures of 50−100 K, with densities of n = 20−50 cm^{-3}. The CNM is made of neutral atomic gas and detected by HI 21 cm line absorption.
- *Warm Neutral Medium* (*WNM*) : The WNM contributes 10−20% of the fractional volume, is found up to scale heights of 300−400 pc and temperatures of 6,000−10,000 K, with densities of n = 0.2−0.5 cm^{-3}. The WNM is made of neutral atomic gas and detected by HI 21 cm line emission.
- *Warm Ionized Medium* (*WIM*) : The WIM fills 20−50% of the fractional volume, has a scale height of 1,000 pc, temperature of 8,000 K and density n = 0.2−0.5cm^{-3}. It is ionized gas and detected by H-α emission and pulsar dispersion measures.
- *HII regions* : A very small fractional component at <1% consists of ionized H II regions. They have typical temperatures T = 8,000 K and densities n = 10^2−10^4 cm^{-3}. They are seen via their H−α emission.
- *Hot Ionized Medium* (*HIM*) : The largest fractional volume is taken up by the HIM at 30−70%. Typical scale height is 1,000−3,000 pc and temperatures T = 10^6−10^7 cm^{-3} and densities n = 10^{-4}−10^{-2}cm^{-3}. The HIM is detected by X-ray emission and highly ionized UV absorption lines such as O VI.

1.2.1 Molecular Hydrogen

Molecular hydrogen (H_2) is an important coolant of the ISM for gas temperatures above ∼300 K. It is also the first neutral molecule to form and

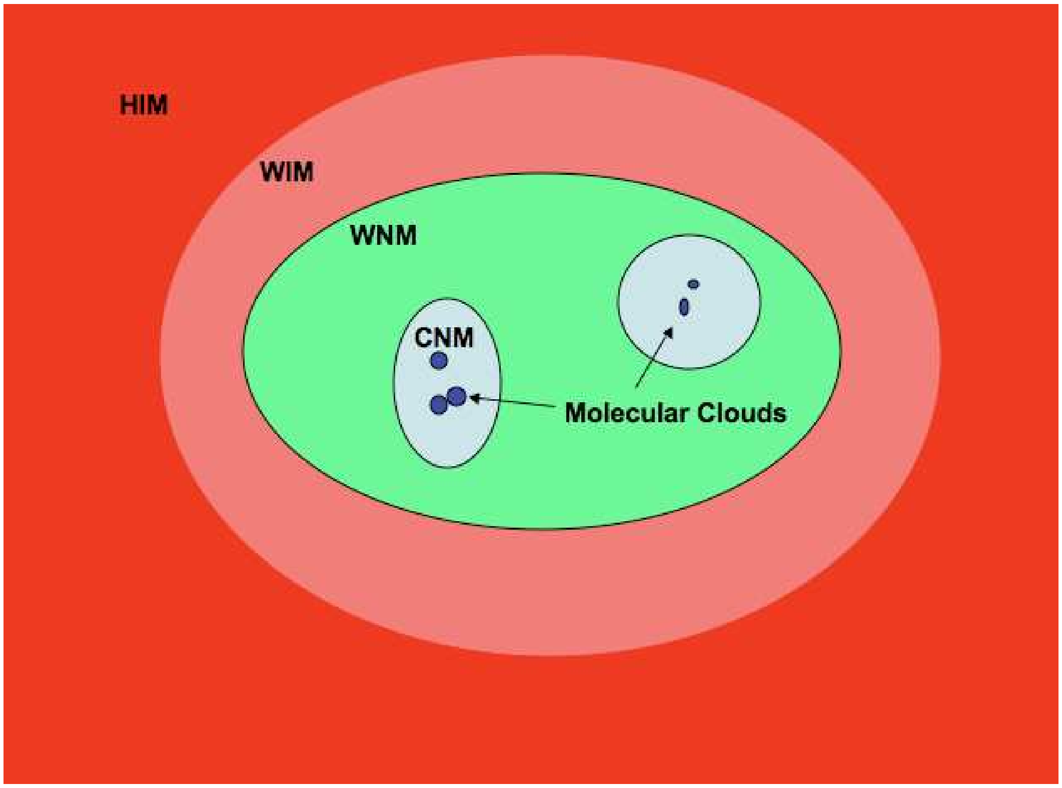

Figure 1.1: Cartoon representation of the different parts of the ISM.

therefore has obvious importance for understanding star formation. The most common formation mechanism of molecular hydrogen is on the surfaces of dust grains. It is destroyed, or dissociated, by UV Lyman-Werner band photons with energies of $\sim$10 eV. Because it has no dipole moment molecular hydrogen can only radiate via the electric quadrupole interaction, and the lifetimes of the excited states are long. Therefore, the level population in the excited J states can be used to determine the kinetic temperature of the gas via the Boltzmann equation. We discuss this process in more detail in Chapter 3.

1.2.2 Magnetic Fields

An important yet often ignored component of the ISM is the magnetic field. Because magnetic fields are difficult to measure and even more difficult to interpret – as line of sight effects can obscure the true nature of the field – they are often ignored in models of galaxy formation. However, even at their relatively weak global strengths, i.e. the mean field of the Galaxy has been measured to be $\sim 6\mu$G, they likely play a large role in the regulation of star formation and transportation of energy throughout the Galaxy.

Numerous techniques for measuring magnetic fields exist: synchrotron radiation intensity and polarization, polarization of starlight, polarization of infrared emission from dust, Faraday rotation and Zeeman splitting (Zweibel & Heiles 1997). However, the only *direct* technique, that does not require assumptions about electron density or equipartition of energy, is Zeeman splitting. Zeeman splitting is the breaking of the degeneracy of a electronic state caused by the application of a magnetic field. The detection of Zeeman splitting however, requires the presence of a strong line and therefore, the technique is limited by a lack of suitable sources.

There are two leading theories on the origin of large scale fields, 1) dynamo theory, in which a field grows over time and 2) primordial theory, in which the field is present at the time of galaxy formation. While neither theory is fully understood or supported, in Chapter 5 we discuss our discovery of a strong magnetic field in a galaxy at an intermediate redshift that may challenge the dynamo theory and stresses the importance including magnetic fields in theories of galaxy formation.

1.3 Quasar Absorption Line Systems

Quasars are the most distant (z up to ∼6.5), most energetic objects observed in the Universe. While their exact nature is still not fully understood, it is believed that their massive energy output is powered by accretion onto a super-massive black hole. For the purposes of this work however, the exact nature of the quasar is of little importance. We will merely take advantage of two features of many quasars: 1) they exist at high redshifts, meaning that the radiation emitted by the quasar had to travel through a large part of the Universe to reach our telescopes here on earth, and 2) the continuum radiation emitted by the quasar can be easily modeled. During its travels to us, the quasar radiation can be absorbed by gas contained in the intervening Interstellar and Intergalactic Medium (ISM and IGM respectively). It is this absorption that reveals a wealth of information about the "stuff" between the quasar and earth. The majority of the results presented in this work are are possible through detailed analysis of quasar absorption line systems. In the following section, we provide background on the primary analysis techniques.

1.3.1 Formation and Detection of Quasar Absorption Line Systems

The study of quasar absorption line systems requires a bright, distant quasar, that acts as a point source of light, the absorption of which, probes the intervening material. As the light from the distant quasar enters an intervening neutral hydrogen cloud, the photons with energy $E = h\nu = 10.2$ eV, or $\lambda =$

1216$\mathring{A}$, are absorbed in the process of exciting the neutral hydrogen atoms from the 1s to 2p state. (2p represents n=2, l = 1 where n is the principal quantum number and l is the orbital quantum number. l = 0 is designated by s). In addition to this process called 'line' absorption, continuum radiation from the quasar is also absorbed by the gas. This continuous absorption is cause by the ionization of the hydrogen atom, which happens for photons of energy E $\geq$ 13.6 eV, or $\lambda \leq 912\mathring{A}$.

In the case of line absorption, the absence of photons creates an absorption line in the continuum spectrum of the quasar. The features of the absorption line can be summarized by three key parameters, that essentially measure the strength/size, shape and location of the line: N, the column density, b, the Doppler parameter, and z, the redshift. The redshift relates the observed wavelength of the line centroid to the rest wavelength of that line measured in the laboratory frame. Specifically,

$$z = \frac{\lambda_{observed}}{\lambda_{rest}} - 1 \quad . \tag{1.1}$$

The Doppler parameter, b, describes the width of the line in velocity space. This width is attributed to three main effects, thermal and turbulent motions of the particles doing the absorbing, collectively named the Doppler term, and quantum mechanical broadening of the specific line, termed natural broadening. The first two characterize the situation in the cloud itself, i.e. the thermal motions relating to the temperature of the gas, and turbulent motions describing all other motions of particles within the cloud [1]. Together, these are described by a Gaussian profile. The quantum mechanical broadening, also known as natural broadening, is an effect of the Uncertainty Principle, ΔE Δt = $\hbar$, which implies that the energy of a given transition can only be known to a certain accuracy that is proportional to the inverse lifetime of the state. The resulting profile

---

[1] $b^2 = b^2_{thermal} + b^2_{turbulent}$ and in the absence of turbulence, $b = \sqrt{2kT/m}$

is described by a Lorentzian profile, also termed a Damping profile. The final observed absorption line is a convolution of the Gaussian and Lorentzian profiles and is termed a Voigt profile. While the Doppler profile dominates in the core of a line, the Damping profile dominates in the wings.

Finally, the column density N(X) is a measure of the number of particles cm^{-2} and can be thought of as the number density of particles of ion X in the cloud, n, multiplied by the pathlength, s, through the cloud such that,

$$N(X) = \int nds \quad . \tag{1.2}$$

However, for a given absorption line, while neither n or s are directly observable, the column density N(X) is measured directly from the absorption line of ion X as outlined in the following section.

Equivalent width

The column density N is determined by measuring the equivalent width, defined as an intensity-weighted width normalized to the continuum of the background source. The equivalent width in wavelength units, W_λ, is defined as follows,

$$W_\lambda = \int [1 - \frac{I}{I_0}]d\lambda \ = \frac{\lambda^2}{c} \int [1 - e^{-\tau_\nu}]d\nu \tag{1.3}$$

where I_0 is the inherent intensity of the continuum source and I is the measured intensity, affected by the absorption line. The measured equivalent width is independent of the instrument resolution and is related to the column density through the optical depth, τ. N is related to the optical depth to radiation, τ, by

$$\tau_\lambda = N\sigma_\lambda \tag{1.4}$$

where σ_λ is the cross section. In the case of small τ, or weak absorption lines, also know as the optically thin regime, the equivalent width takes the following form:

$$\frac{W_\lambda}{\lambda} = \frac{\pi e^2}{m_e c^2} N\lambda \, f_{jk} \tag{1.5}$$

where f_{jk} is the oscillator strength of the transition. Because W_λ is proportional to N and insensitive to b, this is called the linear regime of the curve of growth and N can be determined directly. As τ becomes large, the Doppler core saturates and the curve of growth flattens, allowing for a large increase in N to have little effect on the measured equivalent width. In the limit of large τ,

$$\frac{W_\lambda}{\lambda} \simeq \frac{2b\sqrt{ln\tau}}{c} \tag{1.6}$$

Finally, as τ increases even more the equivalent width becomes dominated by the damping wings of the feature and W_λ is proportional to the square root of N. This "Damping" portion of the curve of growth, also known as the "square-root" portion, is characterized as

$$\frac{W_\lambda}{\lambda} = \frac{2}{c}(\lambda^2 N \frac{\pi e^2}{m_e c} f_{jk}\delta_k)^{1/2} \tag{1.7}$$

where $\delta_k = \frac{1}{4\pi} \sum A_{km}$ where A are the Einstein probability coefficients for downward spontaneous transitions.

1.3.2 Classes of Absorption Line Systems

While there are several classes of absorption line systems, we focus here on three types of systems that are differentiated by column density. In Figure 1.2 we present a typical quasar spectrum that contains examples of the three types of absorption systems. The spectrum shows the characteristic Lyman-α emission peak located at $1216\mathring{A}$ in the rest frame (in this case located at

$\sim$4900$\mathring{A}$ observed) produced by the quasar, as well as the weaker N V, Si IV and C IV emission features. It is seen that blueward (towards shorter wavelengths) of the Lyman-α emission peak there exist many small absorption lines, almost reminiscent of noise in the spectrum. These are the Lyman-α forest absorbers, which are defined as having a column density N(H I) $< 1 \times 10^{17}$ cm^{-2}. The absorption is caused by filaments of hydrogen gas along the line of sight to the quasar, that are optically thin at the Lyman limit (13.6 eV which corresponds to $\lambda = 912\mathring{A}$) and therefore, ionized by background radiation. The prevalence of these absorbers in the UV of high redshift quasar spectra motivated the use of the term 'forest' to describe them. And while there are many of them, in fact, they are so ionized that in total they comprise only 10^{-5} of the total neutral hydrogen.

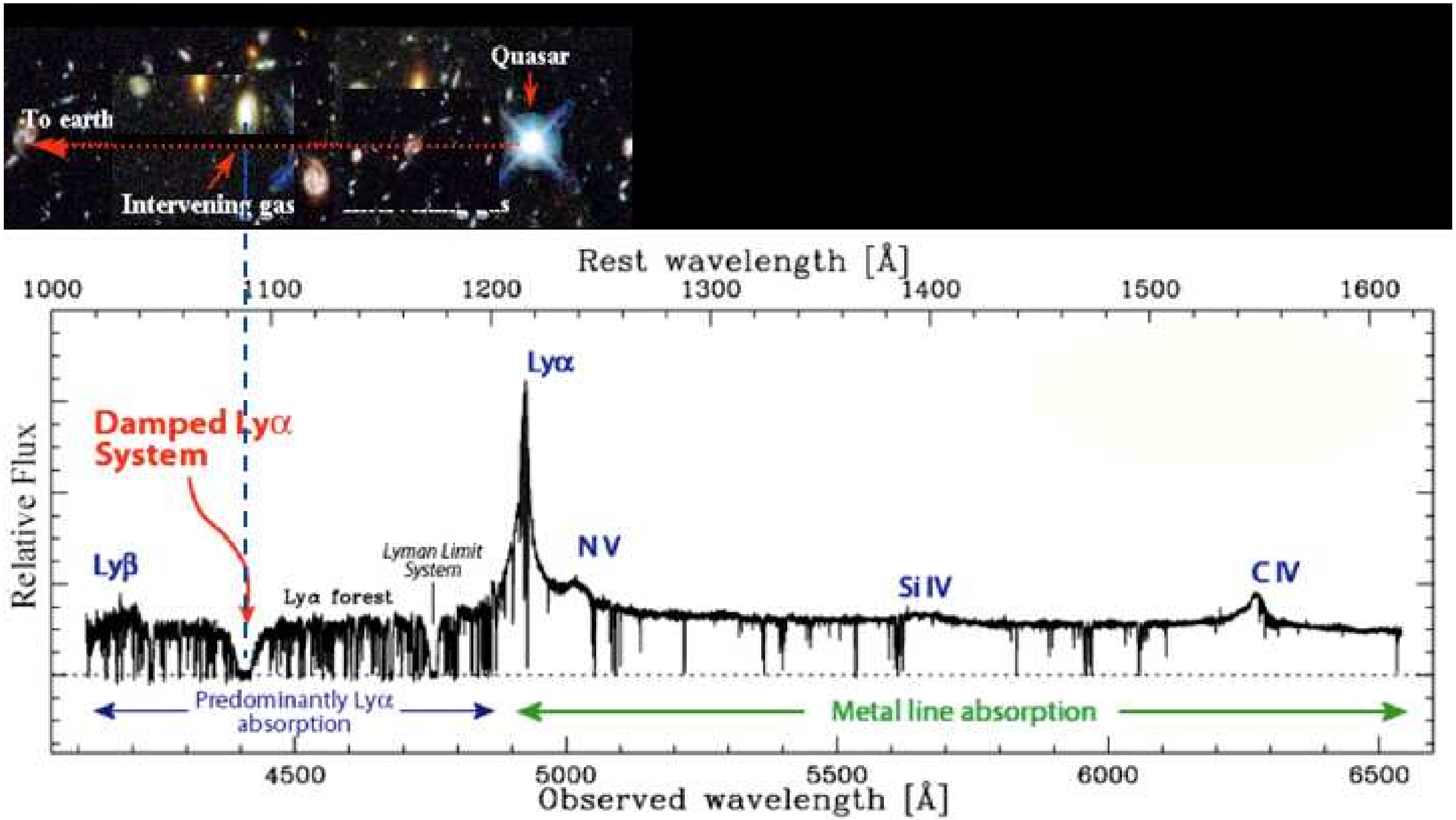

Figure 1.2: Typical Quasar Spectrum. The redshift of the quasar can be determined from the location of the most prominent feature, the Lyman α emission line at $1216\mathring{A}$ rest wavelength. In this case, the observed wavelength of the Lyman α emission line is $\sim 4940\mathring{A}$, corresponding to an emission redshift of $z_{em} \sim 3.06$.

As the H I column density of an absorption line system increases, it becomes a Lyman Limit System (LLS), defined as having 1×10^{17} cm^{-2} $<$ N(H I) $>$ 2×10^{20} cm^{-2}. In Figure 1.2 there is a LLS at observed $\lambda \sim 4750\mathring{A}$. LLSs are optically thick at the Lyman limit, but are still primarily ionized. Figure 1.3 shows some examples of absorbers with column densities log N(H I) = 17.2 cm^{-2} $-$ 21.5 cm^{-2}. It is clear how the profile grows. Also note the disappearance of flux blueward of $912\mathring{A}$, caused by the ionization of Hydrogen by photons with E $\geq$ 13.6 eV. As the column density increases (i.e. logN(H I) = 21.5 cm^{-2} in the figure) the damping wings of the profile appear. This is an example of a Damped Lyman-α System (DLAs), defined as having N(H I) $>$ 2×10^{20} cm^{-2}. DLAs are optically thick at the Lyman Limit and are a subset of LLSs, however, they consist of primarily neutral gas. This key feature sets them apart from the other absorbers and defines their importance in this entire study. We devote the next section to a more detailed description of their properties.

1.4 Damped Lyman α Systems

The class of quasar absorption systems known as Damped Lyman α Systems, or DLAs, is defined as having a neutral hydrogen column density of N(H I) $\geq$ 2×10^{20} cm^{-2}. While this threshold was originally conceived because of observational constraints, it also happens to represent the column density at which the majority of the hydrogen gas is neutral. This neutrality is one of the key features of DLAs. Neutrality implies that we do not make ionization corrections when calculating the metallicities, that we can calculate the star formation rate per hydrogen atom in a relatively direct way (explained later in the text), and perhaps most important, it supports, along with other evidence, the belief that DLAs are the neutral gas reservoirs out of which modern galaxies have formed. Neutral, cold gas that can host molecular clouds is a necessary component for star formation, as it is believed that stars are unlikely to form

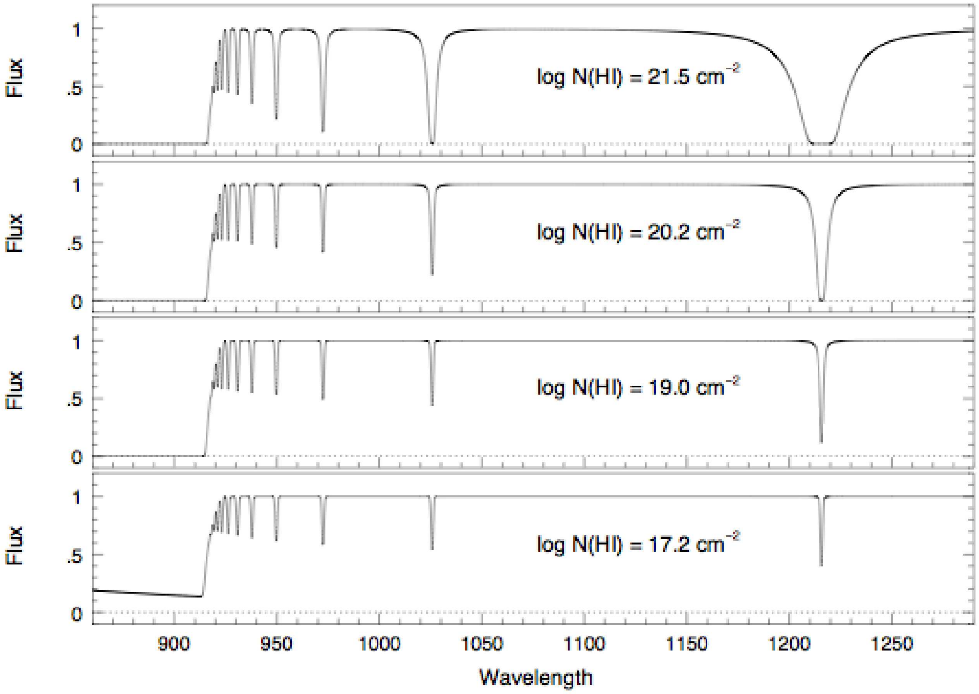

Figure 1.3: Examples of four different H I column density absorbers. All four cases are considered Lyman Limit Systems, while only the top panel shows an example of a DLA. Note prominence of the damping wings of the profile. The smaller absorption features blueward of Lyman α are the Lyman series, Lyman β, Lyman γ, etc. The Lyman break is seen at $912\mathring{A}$.

out of warm, ionized gas.

Additional observational support for the picture of DLAs as progenitor galaxies comes from the fact that the measurements of their neutral gas content show that they dominate the neutral gas content of the Universe between a redshift z = [0, 5]. Additionally, the gas content of DLAs between z = [3, 4] is roughly equal to the amount of matter in stars today, which supports the idea that these DLA turn into modern galaxies (Storrie-Lombardi & Wolfe 2000).

1.4.1 Surveys for DLAs

In the 1970s, motivated by the lack of observational evidence of galaxies at high redshift, Dr. Wolfe along with several investigators began searching for neutral hydrogen in galaxies at high redshift. They were hoping to discover the progenitors of modern spiral galaxies like the Milky Way. Initial efforts were focused on obtaining the redshifted 21-cm absorption feature that would be the signature of this gas. 21-cm absorption is caused by the by the spin-flip transition of the hyperfine levels of the ground state of H I, and is observed with radio telescopes. Most of the work was done at Aricebo and the Green Band Telescope (GBT). However, the difficulty of detecting 21-cm – i.e. the small redshift path available because of the receivers, terrestrial interference, and covering factor issues, limited the search to finding only a few very strong examples. However, this work motivated the search for Damped Lyman-α absorbers in the optical regime. The optical spectra to search for Lyman-α absorption naturally cover a much larger redshift path, making the search quicker and without the hinderance of terrestrial interference. Hence began the first optical surveys for DLAs.

The first optical survey for DLAs was completed by Wolfe et al. (1986) in 1986. They surveyed 68 high redshift quasars and found 15 DLAs. Other surveys followed (i.e. Sargent et al. 1989: 53 quasars, Lanzetta et al. 1991, 1995: 57 and 260 quasars, etc.), but it was not until the vast power of the Sloan

Digitized Sky Survey that surveys for DLAs entered the realm of statistically significant.

The Sloan Digitized Sky Survey (SDSS), is a massive undertaking of photometric and spectral coverage of a large area of the northern hemisphere sky. The SDSS increased the numbers of quasars with optical spectra many-fold and enabled the SDSSDR1, 3 and now 5, to be released by the group lead by Prochaska, et. al. For the first time, significant statistics of DLAs were measured. The SDSS enabled not only a description of the $N_{\rm HI}$ column density distribution function, but also dN/dX, the number of absorbers per unit absorption distance along the line of sight, as well as Ω_g, the contribution of DLAs to the overall cosmic baryon budget. In addition, it provided a rich sample of interesting targets for high resolution follow-up spectroscopy.

Large samples of high resolution studies of DLAs were first presented in a series of papers reporting on the UCSD HIRES/Keck I DLA Abundance Database, see for example, Prochaska et al. (2001) and Prochaska & Wolfe (2002) where data is presented on 39 DLAs. Prochaska et al. (2003a) presented the ESI Keck II DLA database that presented data on 37 DLAs at z >2.5. High resolution studies of DLAs continue today and are the basis of much of the work presented in this thesis.

The one caveat to all of the afore mentioned surveys is that they were all completed using optically-selected quasars. This type of magnitude-limited survey means that they may be subject to biasing by dust. High dust content in a foreground DLA, or anywhere along the line of sight, may obscure background quasars, thus excluding them from sample selection. A part of this work (Chapter 2) is devoted to this issue, which can be overcome by using a radio-selected quasar survey, since radio wavelengths are not affected by dust. In Chapter 2 we show that the statistics of a radio-selected sample are similar to those of the optically-selected sample and therefore conclude that dust-bias is likely not an issue affecting quasar surveys for DLAs.

1.4.2 Physical Conditions in DLAs

Observations of DLAs have been extremely effective in measuring the gas kinematics (Prochaska & Wolfe 1997) and chemical abundances of the DLAs. The metallicities of DLAs are typically $<\sim 1/10$ of the solar metallicity with a measurable dependence on redshift. Prochaska et al. (2003) showed that in a large sample of high resolution DLAs, the metallicity is seen to increase with decreasing redshift, as expected if gas is being enriched by more and later generations of star formation. While there is certainly a small amount of ionized gas in DLAs, as evidenced by the highly ionized metal absorption lines seen in many DLAs, it is the large H I column densities, $\log(N_{\rm HI}) \geq 20.2$ cm^{-2} that ensure the majority of the gas is neutral. It is generally accepted that DLAs consist of a two-phase medium with cold (CNM) and warm neutral (WNM) gas in pressure equilibrium.

Other work has attempted to estimate the mass and the nature of the gas contained in DLAs. Recent work on cross-correltion of DLAs with high redshift, bright star forming galaxies (Lyman-Break Galaxies or LBGs) provides an estimation of the underlying dark matter halo mass of DLAs (Cooke 2006). They showed that the estimated masses were similar to those of the LBGs. In fact, one model of DLAs places a subset of them in the outskirts of centrally located LBGs. This idea came from the work of Wolfe & Chen (2006) who put a limit on the in-situ star formation rates of DLAs using the Hubble Ultra-Deep Field. This limit implies that the DLAs are heated instead by a nearby LBG. Their study was inspired by the work of Wolfe, Prochaska & Gawiser (2003) who developed a method for directly measuring the star formation rate per unit area of DLAs using the C II* fine structure transition. They show that the star formation rate per unit area in DLAs is similar to that measured in the Milky

Way.

While the exact location of the star formation – either in situ, in localized clumps, or in a centrally located LBG, is not yet fully understood, several DLAs show what may be a product or a precursor of star formation – measurable amounts of H_2. However, because the detection of H_2 requires difficult to obtain observations of the blue part of the spectrum close to the atmospheric cutoff, it has generally not been observed in routine DLA observations and therefore, the true covering factor of H_2 in DLAs is yet unknown. While H_2 molecules are found in DLAs, nothing the equivalent of a molecular cloud has ever been seen. This is expected however, given the density ($n \sim 1{,}000$ cm^{-3}) and dust content of a typical molecular cloud, that would effectively block out the background quasar, thus evading detection in the first place.

It is clear that the while much is known about DLAs, a comprehensive model of a DLA and its place in the larger picture of galaxy evolution does not yet exist. Given that observations of most DLAs consist of only a pencil-beam line of sight through the gas, it is difficult to infer the true size, mass and morphology of the DLAs. While the sight line allows for a determination of the column density of gas within the beam, it gives no information on volume densities or temperatures of the gas. These last two traits must be inferred by taking advantage of metal lines that are sensitive to the densities and temperatures of the gas, such as neutral carbon (C I) fine structure – a major focus of this work (see Chapter 3) – silicon fine structure, higher ionized states of low-ion metals and molecular hydrogen rotational J states. A determination of volume densities and pressures will help to constrain the sizes and physical environment of DLAs, which is a major focus of this work.

2

Radio-Selected Quasar Survey for Damped Lyman α Systems

This chapter is a reprint of “The UCSD Radio-Selected Quasar Survey for Damped Lyman-α Systems”, by Regina A. Jorgenson, Arthur M. Wolfe, Jason X. Prochaska, Limin Lu, Christopher J. Howk, Jeff Cooke, Eric Gawiser, and Dawn Gelino, published in the The Astrophysical Journal, 2006, Vol. 646, p. 730.

2.1 Abstract

As large optical quasar surveys for DLAs become a reality and the study of star forming gas in the early Universe achieves statistical robustness, it is now vital to identify and quantify the sources of systematic error. Because the nature of optically-selected quasar surveys makes them vulnerable to dust obscuration, we have undertaken a radio-selected quasar survey for DLAs to address this bias. We present the definition and results of this survey. We then combine our sample with the CORALS dataset to investigate the H I column density distribution function $f_{\rm HI}(N, X)$ of DLAs toward radio-selected quasars. We find that $f_{\rm HI}(N, X)$ is well fit by a power-law $f_{\rm HI}(N, X) = k_1 N^{\alpha_1}$, with $\log k_1$

= 22.90 and $\alpha_1 = -2.18^{+0.20}_{-0.26}$. This power-law is in excellent agreement with that of optically-selected samples at low $N_{\rm HI}$, an important yet expected result given that obscuration should have negligible effect at these gas columns. However, because of the relatively small size of the radio-selected sample, 26 DLAs in 119 quasars, $f_{\rm HI}(N, X)$ is not well constrained at large $N_{\rm HI}$ and the first moment of the H I distribution function, Ω_g, is, strictly speaking, a lower limit. The power-law is steep enough, however, that extrapolating it to higher column densities implies only a modest, logarithmic increase in Ω_g. The radio-selected value of $\Omega_g = 1.15^{+0.37}_{-0.38} \times 10^{-3}$, agrees well with the results of optically-selected surveys. While our results indicate that dust obscuration is likely not a major issue for surveys of DLAs we estimate that a radio-selected sample of $\approx$ 100 DLAs will be required to obtain the precision necessary to absolutely confirm an absence of dust bias.

2.2 Introduction

The introduction of large data sets from surveys such as the Sloan Digital Sky Survey (SDSS) has made possible statistically significant studies of Damped Lyα systems (DLAs) (Prochaska et al. 2005, hereafter PHW05), quasar absorption systems defined as having an H I column density $N_{\rm HI} \geq 2 \times 10^{20}\,{\rm cm}^{-2}$ and which contain most of the neutral gas in the redshift interval z=[0, 5] (Wolfe, Gawiser, & Prochaska 2005). These large surveys for DLAs shed light on the history of the neutral gas content of the Universe and show how it is affected by star formation and gas replenishment. However, one major problem consistently affects magnitude-limited optical surveys: the issue of intervening dust and the possibility of obscuration bias. Because the metalicities of DLAs can be as high as 1/3 solar and are always above 1/1000 solar (Prochaska 2003), the presence of dust in these objects is not surprising. Specifically, evidence from element abundance patterns suggests the presence of depletion (Pettini et al. 1999), while evidence for differential reddening suggests that dust obscuration is possible (Pei & Fall 1995). Dust obscuration in optically-selected surveys could be introducing a selection bias against DLAs whose high dust optical depth would hide the background quasar. This effect could seriously impact the results of statistics and derived values like Ω_g, the cosmological density of neutral gas (see Pei & Fall (1995)), particularly since high column density systems that dominate Ω_g, would be theoretically most likely to have strong dust obscuration. Here and throughout the paper we will use Ω_g to mean $\Omega_g^{\rm DLA}$, the neutral gas contained in systems defined as being DLAs, i.e. with an H I surface density $N_{\rm HI} \geq 2 \times 10^{20}\,{\rm cm}^{-2}$. For a detailed discussion of the rationale behind this choice, see PHW05.

Because radio observations are insensitive to the presence of dust, a radio-selected sample of quasars does not suffer from this dust obscuration selection effect. Therefore, a radio-selected survey is a check on the possible introduction of biases in the magnitude-limited, optical surveys. One previous survey, the Complete Optical and Radio Absorption Line System (CORALS) survey by Ellison et al. (2001), attempted to answer the question of the importance of dust obscuration by selecting quasars from the Parkes quarter-Jansky Flat-spectrum Radio Survey (Jackson et al. 2002), and then following up with optical observations of the selected quasars, regardless of magnitude, to search for the presence of DLAs. Ellison et al. found a slightly higher incidence of DLAs than that found by optical surveys. From their measurement of Ω_g, Ellison et al. concluded that the effects of dust could be suppressing the magnitude-limited value of Ω_g by no more than a factor of two.

The radio-selected surveys were motivated by several studies which indicated that dust obscuration would significantly bias the results of Ω_g and other quantities derived from optical surveys. Fall & Pei (1993) constructed models to predict the possibility of dust obscuration of quasars and found that between 10 and 70% of quasars at $z = 3$ could be obscured, resulting in an underestimate of Ω_g by the optical surveys. Recently, Wild & Hewett (2005) report on a survey of SDSS quasars for Ca II absorption-line systems with $0.84 < z_{abs} < 1.3$. Using Ca II along with Fe and Mg lines, they claim that most of their sample likely contains DLAs and a significant amount of reddening. By modeling the reddening of these systems they make an estimate that they are missing $\approx 40\%$ of Ca II systems from the SDSS due to dust obscuration, which they compare favorably to the upper limit of the CORALS survey.

On the other hand, the SDSS-DR3 survey which found 525 DLAs (PHW05), indicates that a dust bias, if present, is not an important effect. Prochaska et al. examine their results as a function of quasar magnitude, separating out the brightest 33% and the faintest 33% of the sample in each of four redshift bins. While there is not a statistically significant difference in the line density, they measure 40% higher Ω_g values towards brighter quasars at the 95% c.l. Since this is the opposite effect of what the dust bias would naively imply (a dust bias may imply that $\Omega_g^{bright} < \Omega_g^{faint}$, since the brightest observed quasars should have less foreground dust obscuration which implies a smaller $N_{\rm HI}$ value and hence smaller Ω_g), the SDSS-DR3 results with a statistically significant higher value of Ω_g towards brighter quasars point to the conclusion that dust obscuration is not an important effect. When Murphy & Liske (2004) examined the results of the SDSS-DR2, a sample including 70 DLAs they found no evidence for reddening. After examining the much larger SDSS-DR3 Murphy et al. (2005) find evidence for reddening, but at a very low level – the implied dust to gas ratio is less than 0.02, where dust to gas ratio is defined relative to that of the Milky Way (see equation 7 of Wolfe, Prochaska & Gawiser (2003)). However, with all of these studies it is important to remember that optical samples cannot measure dust bias in objects so heavily extincted that they are missing from the samples. As larger optical surveys for DLAs become feasible, due to surveys like the SDSS, and the statistical uncertainties become $< 5\%$, potential causes of systematic uncertainties, such as dust obscuration, must be fully understood.

In this paper we will present the results of a radio-selected quasar survey that was undertaken by our group. This UCSD sample is approximately the same size as the CORALS sample and presents a comparable assessment of dust obscuration. We will analyze the combined results, attempt to assess the H I column density distribution function, $f_{\rm HI}(N, X)$, and show that our results for Ω_g do not differ in a statistically significant way from the results of optically-selected surveys, therefore suggesting that dust obscuration is most likely not a major problem affecting optically-selected quasar samples for DLAs.

The organization of this paper is as follows: In § 2.3 we describe the UCSD quasar sample, DLA identification method and analysis processes. In § 2.4 we review the standard DLA statistical analysis methods. We discuss the results of the UCSD, CORALS and combined samples in § 3.4, as well our process for dealing with the Empty Fields. And finally, in § 2.6 we will compare our results with the most recent optical surveys.

Throughout the paper we will use cosmological parameters consistent with the latest WMAP results (Bennett et al. 2003): $\Omega_\Lambda = 0.7, \Omega_m = 0.3, H_0 = 70{\rm km\ s^{-1}\ Mpc^{-1}}$.

2.3 The UCSD Sample

The UCSD sample consists of 68 objects selected from the 411 sources that comprise the complete Caltech-Jodrell Bank radio catalogs, including the Pearson-Readhead sample (PR), the Caltech-Jodrell Bank VLBI Surveys 1 and 2 (CJ1 and CJ2), and the Caltech-Jodrell Bank Flat-spectrum sample completion. While each sample was selected by a progressively lower flux density threshold, the sources for each sample were all selected to have declination (B1950) $\delta \geq 35°$ and Galactic latitude $\mid b \mid \geq 10°$. The PR sample includes 65 objects with flux density at 6 cm (4859 MHz), $S_{6cm} \geq 1.3$ Jy (Pearson & Readhead 1988). The CJ1 sample includes 135 sources with flux density at 6 cm, 1.3Jy$\geq S_{6cm} \geq$0.7Jy (Polatidis et al. 1995, Thakkar et al. 1995, Xu et al. 1995), and the CJ2 sample consists of 193 mostly flat-spectrum objects with a flux density $S_{6cm} \geq$350 mJy (Taylor et al. 1994, Henstock et al. 1995). The CJF (CJF; Taylor et al. 1996) is a compilation of the flat-spectrum radio sources (spectral index flatter than $\alpha^{4850MHz}_{1400MHz} \geq -0.5$) from the previous three surveys, plus and additional 18 sources for completion.

An optical campaign to determine the type of source, magnitude, and redshift of the radio catalog objects followed, the results of which were compiled in the CJ catalogs. The object optical identification and determination of the R magnitude was done by automated scanning of the POSS plates or by eye. Redshifts were primarily taken from Veron-Cetty, M.-P. & Veron, P. (1993) and from Henstock et al. (1997).

From this large radio sample, our selection criterion included all objects identified as quasars with $z_{em} > 2.0$ regardless of optical magnitude. The $z_{em} > 2.0$ cutoff was chosen to ensure sufficient spectral coverage to search for DLAs at wavelengths redward of the atmospheric cutoff at $\approx$ 3200Å. We also included in our sample of 68 objects all 14 sources designated as optical empty fields in order to be sure that we were not artificially selecting objects brighter than an arbitrary optical magnitude. And finally, we included the 5 sources for which there was a tenative optical identification, but no redshift information.

2.3.1 Observations and Analysis

Observations of most quasar candidate objects were first carried out at Palomar, with follow-up done at Keck for faint or “Empty Field” (EF) objects (see Table 3.1). The majority of our spectra have better than 6 Å FWHM. Five of the 68 objects in our sample were previously observed at moderate spectral

Table 2.1. DETAILS OF OBSERVATIONS

Telescope	Date (No. nights)	Resolution (at 4000 Å)	No. of quasars observed
Palomar	Nov 1995 (2)	4-6 Å	17
Palomar	Apr 1996 (1)	4-6 Å	8
Palomar	May 1996 (2)	4-6 Å	9
Palomar	Dec 1996 (2)	4-6 Å	16
Palomar	June 1997 (1)	4-6 Å	7
Keck LRIS	Nov 2001 (1)	4-6 Å	3
Keck ESI	Apr 2002 (1)	0.5 Å	14
Keck ESI	Aug 2002 (1)	0.5 Å	7
Keck LRIS	Dec 2002 (1)	11 Å	1
Keck LRIS	May 2003 (1)	3-5 Å	14

resolution and the data or results for these objects were taken from the literature. These included quasars Q0014+813, Q0201+365, Q0636+680, Q0642+449 which were observed by Sargent et al. (1989), and quasar Q1124+571 which was taken from Lanzetta et al. (1991). The $N_{\rm HI}$ measurement for the DLA towards Q0201+365 was taken from Lu et al. (1993).

Initial observations of most other targets were made with the 200-inch Hale telescope of the Palomar Observatory. Observations were made with the Double Spectrograph and utilized gratings that were 300 lines mm^{-1} in the blue and the 315 lines mm^{-1} in the red, resulting in 4-6 Å resolution using the 1″slit, and ≈10 Å resolution using the 2″slit when conditions were poor. All data was reduced using standard IRAF reduction packages.

Follow up observations of empty fields and faint quasars were done at Keck with the Echellette Spectrograph and Imager (ESI, Sheinis et al. 2002) and the Low Resolution Imaging Spectrometer (LRIS, Oke et al. 1995). With LRIS, the slit size was generally 0.7″. The ESI observations utilized the 1.0″slit in LowD mode and the 0.5″slit in echellette mode.

Fifteen of the original 68 objects were excluded from the final statistical data set for the following reasons: Seven were determined to be galaxies, stars, or low redshift quasars, and the remaining eight were deemed empty fields (EFs). Table 2.2 contains the details of the final 53 quasars used in the UCSD statistics, while Table 2.3 and Table 2.4 contain a summary of the empty fields and the discarded objects respectively.

Table 2.2. UCSD SURVEY SAMPLE

Quasar	z_{em}	R mag	$N_{\rm HI} \times 10^{20}\,{\rm cm}^{-2}$	z_{abs}	z_{min}	z_{max}	6cm Flux [Jy]	Survey[d]
Q0014+813	3.384	15.9	...	...	1.591	3.340	0.551	CJ2
Q0153+744	2.338	16.0	...	...	1.568	2.305	1.794	PR
Q0201+365	2.912	17.5	2.4[a]	2.461	1.632	2.873	0.349	CJ2
Q0212+735	2.367	19.0	...	...	1.742	2.333	2.444	PR
Q0604+728	3.53	20.3	...	...	2.651	3.485	0.654	CJ2
Q0609+607	2.710	19.0	...	...	1.650	2.673	1.059	CJ2
Q0620+389	3.470	20.0	...	...	1.842	3.425	0.87	CJ1
Q0627+532	2.200	18.5	...	...	1.619	2.168	0.485	CJ2
Q0636+680	3.174	16.2	...	...	1.591	3.132	0.499	CJ2
Q0642+449	3.406	18.5	...	...	1.591	3.362	0.78	CJ1
Q0727+409	2.501	17.0	...	...	1.578	2.466	0.468	CJ2
Q0738+491	2.318	21.0	...	...	1.928	2.285	0.352	CJ2
Q0749+426	3.590	18.1	...	...	2.118	3.544	0.461	CJ2
Q0800+618	3.04	19.6	3.16 ± 0.15	2.9603 ± 0.0017	2.234	3.000	0.981	CJ2
Q0803+452	2.102	19.6	...	...	1.594	2.071	0.414	CJ2
Q0824+355	2.249	19.7	2.0[b]	2.2433	1.655	2.217	0.746	CJ2
Q0833+585	2.101	18.0	...	...	1.546	2.070	1.11	CJ1
Q0836+710	2.180	16.5	...	...	1.507	2.148	2.423	PR
Q0902+490	2.690	17.2	...	...	1.550	2.653	0.547	CJ2
Q0917+449	2.180	19.0	...	...	1.578	2.148	0.80	CJ1
Q0930+493	2.590	18.4	...	...	1.666	2.554	0.574	CJ2
Q1014+615	2.800	18.1	2.5[b]	2.7670	2.263	2.757	0.631	CJ2
Q1053+704	2.492	18.5	...	...	1.801	2.457	0.71	CJ1
Q1124+571	2.890	18.0	...	...	1.796	2.851	0.597	CJ2

Table 2.2—Continued

Quasar	z_{em}	R mag	$N_{\mathrm{HI}} \times 10^{20}\,\mathrm{cm}^{-2}$	z_{abs}	z_{min}	z_{max}	6cm Flux [Jy]	Survey[d]
Q1144+542	2.201	20.5	...	...	1.632	2.169	0.88	CJ1
Q1155+486	2.028	19.9	...	...	1.632	1.998	0.445	CJ2
Q1214+588	2.547	19.5	...	...	1.632	2.512	0.307	CJ2
Q1239+376	3.818	19.5	2.0 ± 0.15	3.4082[c]	2.344	3.770	0.446	CJ2
Q1325+436	2.073	18.5	...	...	1.549	2.042	0.533	CJ2
Q1333+459	2.449	18.5	...	...	1.612	2.414	0.76	CJ1
Q1337+637	2.558	18.5	...	...	1.550	2.522	0.431	CJ2
Q1413+373	2.360	17.3	...	...	1.607	2.326	0.383	CJ2
Q1421+482	2.220	18.9	...	...	1.549	2.188	0.536	CJ2
Q1427+543	2.980	20.7	...	...	2.331	2.940	0.718	CJ2
Q1435+638	2.068	15.0	...	...	1.591	2.037	1.24	CJ1
Q1526+670	3.020	17.1	...	...	1.977	2.980	0.417	CJ2
Q1547+507	2.169	18.5	...	...	1.582	2.137	0.74	CJ1
Q1602+576	2.858	16.8	...	...	1.630	2.819	0.351	CJ2
Q1624+416	2.550	22.0	...	...	1.732	2.515	1.632	PR
Q1645+635	2.380	19.4	3.55 ± 0.15	2.1253 ± 0.0003	1.536	2.346	0.444	CJ2
Q1745+624	3.886	18.3	...	...	3.085	3.837	0.580	CJ2
Q1755+578	2.110	18.6	25.1 ± 0.15	1.9698 ± 0.0009	1.630	2.079	0.455	CJ2
Q1758+388	2.092	17.8	...	...	1.512	2.061	0.92	CJ1
Q1834+612	2.274	17.6	...	...	1.599	2.241	0.590	CJ2
Q1839+389	3.094	19.5	5.0 ± 0.15	2.7746 ± 0.0009	1.911	3.053	0.476	CJ2
Q1850+402	2.120	17.9	20.0 ± 0.25	1.9888 ± 0.0058	1.669	2.089	0.535	CJ2
Q2015+657	2.845	19.1	...	...	2.734	2.807	0.500	CJ2
Q2017+745	2.187	17.9	...	...	1.602	2.155	0.500	CJ2

Table 2.2—Continued

Quasar	z_{em}	R mag	$N_{\rm HI} \times 10^{20}\,{\rm cm}^{-2}$	z_{abs}	z_{min}	z_{max}	6cm Flux [Jy]	Survey[d]
Q2136+824	2.350	18.9	...	...	2.002	2.317	0.509	CJ2
Q2255+416	2.150	20.9	...	...	2.119	2.119	0.99	CJ1
Q2259+371	2.228	20.4	...	...	1.632	2.196	0.406	CJ2
Q2310+385	2.181	17.5	...	...	1.630	2.149	0.484	CJ2
Q2356+385	2.704	18.6	...	...	1.771	2.666	0.449	CJ2

[a] $N_{\rm HI}$ value taken from Lu et al. (1993).

[b] Associated systems: z_{abs} within $\approx$ 3,000 km s^{-1} of z_{em}.

[c] Weak metals, therefore best fit determined by eye.

[d] CJ1, CJ2 = Caltech Jodrell Bank, PR = Pearson-Readhead

Table 2.3. EMPTY OR EXTENDED FIELDS

Object	RA(J2000)	Dec(J2000)	Exp. time (s)	Morphology	6cm Flux (Jy)	Survey
0102+480	01 05 49.9	+48 19 03	294	no detection[a] to R $\approx$ 23	1.080	CJ1
0633+596	06 38 02.87	+59 33 22.21	500	no detection[a] to R $\approx$?	0.482	CJ2
0718+793	07 26 11.74	+79 11 31.0	500	extended, $7'' \times 3''$, R $\approx$ 23.9	0.467@1.4GHz	CJ2
1107+607	11 10 13.1	+60 28 43	600	extended, $4'' \times 2.5''$, R $\approx$ 24.6	0.400	CJ2
1205+544	12 08 27.50	+54 13 19.53	600	possibly extended	0.397	CJ2
1312+533	13 14 43.83	+53 06 27.73	600	extended, $3'' \times 3''$, R $\approx$ 24.5	0.433	CJ2
1828+399	18 29 56.52	+39 57 34.69	900	no detection[a] to R $\approx$ 25	0.353	CJ2
2054+611[b]	20 55 38.84	+61 22 00.64	900	possibly extended	0.414	CJ2

[a] 1σ above sky background

[b] Uncertain identification, either $z = 1.588$, 3.0, 3.3

Table 2.4. DISCARDED OBJECTS

Object	Reason for Discard	Survey
0843+575	galaxy	CJ2
1125+596	quasar at $z_{em} = 1.78$	CJ2
1308+471	galaxy	CJ2
1436+763	star	CJ2
1809+568	No significant emission feature	CJ2
2238+410	Spectrum dubious	CJ2
2319+444	quasar at $z_{em} = 1.24$	CJ2

2.3.2 Damped Lyα systems

The Palomar data was reduced using standard IRAF packages, while the Keck data was reduced using IDL reduction software[1]. The reduced quasar spectra were continuum fitted and normalized and then analyzed to find regions in which the restframe equivalent width of an absorption feature was ≥ 5 Å and located in a region of good signal to noise. The equivalent width of the spectrum was calculated and an equivalent width array was then analyzed for regions that were greater than the 5 Å restframe cutoff, as explained by Wolfe et al. (1995). We searched all regions of the spectrum blueward of Lyα emission, beginning with the lowest wavelength at which the error was below the restframe equivalent width threshold of ≥ 5 Å at the 5σ level. All candidate detections were then inspected by eye to determine if they were indeed DLAs. False detections were usually quite obvious to exclude as blended lines, Lyβ, etc.

Nine DLAs were found, two of which, towards quasars Q0824+355 and Q1014+615, were within 3,000 km s^{-1} of the Lyα emission peak, and therefore considered "associated". Following the standard practice, we exclude these "associated" DLAs from the sample in order to insure that we are not detecting objects that are physically associated with the quasar. Discarding these two

---

[1] http://www.ucolick.org/~xavier/IDL

leaves a final seven DLAs to be included in the UCSD sample.

Lyα Fits

The DLA systems were fitted with Voigt profiles using the IDL tool[2] *x_fitdla* which allows the user to interactively modify the Voigt profile and continuum placement. In all but one case, that of Q1239+376, the DLA redshift was constrained by the corresponding metal lines with errors as given in Table 2.2. In the case of Q1239+376, the metal lines were too weak for use in constraining the DLA redshift and we instead determined the best fit interactively by eye using *x_fitdla*. This method results in larger uncertainties for z_{abs} and $N_{\rm HI}$.

For most of our sample DLAs a conservative estimate of the uncertainty in $N_{\rm HI}$ is 0.15 dex. However in one case, that of Q1850+402, where the Voigt profile proved difficult to fit, we report an uncertainty of 0.25 dex in $N_{\rm HI}$. Figure 2.1 shows Voigt profile fits for each DLA, except for the $z_{abs} = 2.461$ DLA towards Q0201+365, which is in the existing literature (Sargent et al. 1989). Now we will give brief details on each DLA system.

Q0201+365: $N_{\rm HI}$ fit taken from Lu et al. (1993) and discussion therein.

Q0800+618: The difficulty in estimating the continuum placement in such close proximity to the Lyα emission peak made this DLA system somewhat difficult to fit. There is also a possibility of some blended absorption.

Q1239+376: High signal to noise and good placement. The only problem with this fit was some blending on the red side.

Q1645+635: High signal to noise and lack of blending resulted in a good Voigt profile fit to this DLA profile.

Q1755+578: Close proximity to Lyα emission peak and blending on the blueward side made the fit difficult.

Q1839+389: Straightforward fit and good continuum.

---

[2] http://www.ucolick.org/∼xavier/IDL

Q1850+402: Close proximity to Lyα emission peak, lower signal to noise and blending made this a more difficult fit, yielding an increased error margin on the Voigt profile of 0.25 dex.

2.4 DLA statistics

Our goal of determining the impact of dust obscuration in surveys of DLAs requires that we be able to compare our radio-selected survey to the results of optically-selected surveys. We will now introduce some of the standard statistical quantities used to describe and quantify surveys of DLAs.

2.4.1 Δz, $g(z)$, and $n(z)$

The redshift path, Δz, is defined as the total redshift interval along which a damped Lyα feature with rest frame equivalent width exceeding 5Å would be detected at more than 5σ significance. It is defined as follows,

$$\Delta z = \sum_{i=1}^{n} (z_i^{max} - z_i^{min}) \tag{2.1}$$

where the summation is over the n quasars in the survey, z_{min} is determined to be the lowest spectral wavelength with good signal-to-noise, and z_{max} is the redshift corresponding to the maximum spectral wavelength included in the search. We define z_{max} by,

$$z_{max} \equiv z_{qso} - (1 + z_{qso})/100 \quad . \tag{2.2}$$

This corresponds to 3000 km s^{-1} blueward of the Lyα emission feature. This cutoff ensures that a damped Lyα system is not physically associated with the quasar.

The redshift path density, $g(z)$, gives an idea of the statistical significance as a function of redshift of a survey for DLAs. It is defined as the number

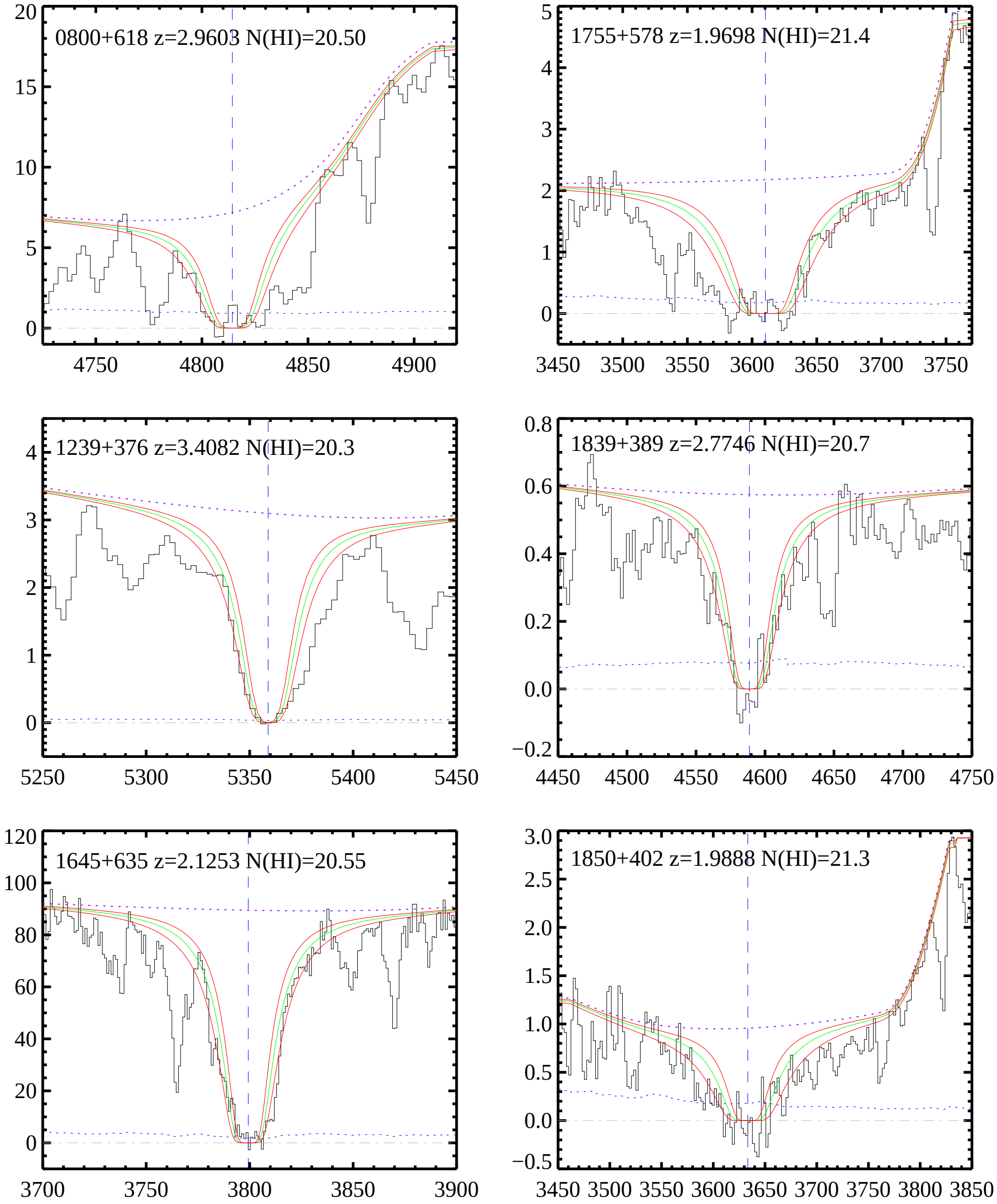

Figure 2.1: Voigt profile DLA fits for the six new DLA systems in the UCSD sample. The best Voigt profile is indicated by the green curve, surrounded by profiles with $N_{\rm HI}$ displacements $\pm$ 0.15 dex (or $\pm$ 0.25 dex) in red. The continuum placement can be seen as the purple dotted line, while the error array is represented by the blue dotted line.

of quasars with sightlines containing a particular redshift interval (Lanzetta et al. 1991). Specifically,

$$g(z) = \sum_{i=1}^{n} H(z_i^{max} - z)H(z - z_i^{min}) \quad , \tag{2.3}$$

where H is the Heaviside step function, the sum is over n quasars (Lanzetta et al. 1991) and,

$$\Delta z = \int g(z)dz \quad , \tag{2.4}$$

where the integral is over all z paths in the survey. The DLA number density, $n(z)$, is simply the number of DLAs per unit redshift,

$$n(z) = \frac{m}{\Delta z} \quad , \tag{2.5}$$

where m is the number of DLAs.

2.4.2 $f_{\rm HI}(N, X)$: The H I Frequency Distribution Function

Following the direction of previous works such as Lanzetta et al. (1991) and PHW05, we can define a neutral hydrogen frequency distribution function that describes the number of DLAs in a range of column densities, $(N, N + dN)$, and a range of absorption distances, $(X, X + dX)$,

$$f_{\rm HI}(N, X)dNdX \quad , \tag{2.6}$$

where the absorption distance, ΔX, is defined as follows:

$$\Delta X = \int dX \equiv \int \frac{H_0}{H(z)}(1 + z)^2 dz \tag{2.7}$$

where H_0 is Hubble's constant.

2.4.3 $\ell_{\rm DLA}(X)$: The Damped Lyα Line Density

The zeroth moment of the H I frequency distribution function is known as the line-density of DLAs $\ell_{\rm DLA}(X)$. The line-density represents the number of systems per unit absorption distance and is defined as:

$$\ell_{\rm DLA}(X) = \int_{N_t}^{\infty} f_{\rm HI}(N, X) dN \quad . \tag{2.8}$$

As described in PHW05, the line-density is related to the covering fraction of DLAs on the sky. This relationship is apparent if we describe the frequency distribution function in terms of an average cross-section $A(X)$, and the comoving number density of DLAs $n_{DLA}(X)$:

$$f_{\rm HI}(N, X) \equiv (c/H_0) n_{DLA}(X) A(X) \quad . \tag{2.9}$$

(see Wolfe, Gawiser, & Prochaska 2005, for details).

2.4.4 Ω_g: The Cosmological Neutral Gas Mass Density

An important parameter in describing any quasar survey for DLAs is the first moment of the H I frequency distribution function, the neutral gas mass density, Ω_g. It is believed that Ω_g is closely related to the amount of neutral hydrogen available for star formation and hence, places an important tracer of the history of star formation in the Universe. Acquiring this parameter through surveys for DLAs is an important constraint on the neutral gas reservoir available for star formation in the early ($z > 2$) Universe. Ω_g is defined as follows:

$$\Omega_g(X) \equiv \frac{\mu m_H H_0}{c \rho_c} \int_{N_{min}}^{N_{max}} N f_{\rm HI}(N, X) dN \tag{2.10}$$

where μ is the mean molecular mass of the gas (taken to be 1.3), m$_H$ is the mass of the hydrogen atom, ρ_c is the critical mass density, $f_{\rm HI}(N, X)$ is the frequency distribution function of neutral gas found in DLAs and the integration is from $N_{min} = 2 \times 10^{20}\,\mathrm{cm}^{-2}$ to $N_{max} = \infty$. We follow previous works, i.e. Lanzetta et al. (1991), and replace this frequency distribution function by its evaluation in the discrete limit as follows,

$$\Omega_g = \frac{\mu m_H H_0}{c\rho_c} \frac{\Sigma N(\mathrm{HI})}{\Delta X} \quad , \tag{2.11}$$

where the sum is performed over the N_{HI} measurements of the DLA systems in a given redshift interval with total pathlength ΔX. As emphasized by PHW05 and discussed below, equation 2.11 only provides an accurate evaluation of equation 2.10 if the survey is sufficiently large that the observed $f_{\mathrm{HI}}(N, X)$ distribution becomes steeper than N^{-2} at large N_{HI}. If this is not the case, equation 2.11 provides only a lower limit to Ω_g.

2.5 Results

We will now describe the results of the UCSD radio-selected survey, the CORALS radio-selected survey, and the combination of these two surveys, which we will refer to as the combined sample. Details of the results of each survey are listed in Table 2.5.

2.5.1 UCSD Survey Results

The UCSD sample consists of 7 DLAs in 53 quasars of $z_{em} \geq 2.0$ with a total redshift path of $\Delta z = 41.15$. This resulted in a number of DLAs per unit redshift, $n(z) = 0.17^{+0.08}_{-0.07}$, where the error bars are the standard 1σ Poissonian errors using Gehrels' tables for small number statistics (Gehrels 1986). Figure 2.2 presents $g(z)$ versus z for the UCSD sample in green. The line density of DLAs over the cosmological redshift path of $\Delta X = 130.43$ resulted in $\ell_{\mathrm{DLA}}(X) = 0.05^{+0.03}_{-0.02}$, while the mass density of neutral gas is $\Omega_g = 0.84^{+0.43}_{-0.45} \times 10^{-3}$. While

Table 2.5. RESULTS

feature	UCSD	CORALS	COMBINED
No. quasars	53	66	119
No. DLAs	7	19	26
Δz	41.15	57.16	98.31
n(z)	$0.17^{+0.08}_{-0.07}$	$0.33^{+0.10}_{-0.07}$	$0.26^{+0.06}_{-0.05}$
$\ell_{\rm DLA}(X)$	$0.05^{+0.03}_{-0.02}$	$0.10^{+0.03}_{-0.02}$	$0.08^{+0.02}_{-0.02}$
$\langle N_{\rm HI} \rangle$ cm^{-2}	8.744×10^{20}	7.532×10^{20}	7.858×10^{20}
$\langle\ z\ \rangle$	2.53	2.50	2.51
$\langle\ z\ \rangle_{weighted}$	2.17	2.33	2.28
$\Sigma N_{\rm HI}\ cm^{-2}$	0.61×10^{22}	1.43×10^{22}	2.04×10^{22}
ΔX	130.43	186.68	317.11
$\Omega_g(\times 10^{-3})$	$0.84^{+0.43}_{-0.45}$	$1.37^{+0.53}_{-0.55}$	$1.15^{+0.37}_{-0.38}$
Error	± 54%	± 41%	± 33%

we report Ω_g as a detection, it is strictly speaking, a lower limit because we do not measure $f_{\rm HI}(N,X)$ to fall off faster than N^{-2} (see § 2.5.3).

2.5.2 CORALS Survey Results

The Complete Optical and Radio Absorption Line Survey (CORALS) (Ellison et al. 2001) was the first attempt to utilize a radio-selected quasar survey as a basis for a search for DLAs. They selected quasars from the complete Parkes quarter-Jansky flat spectrum sample (Jackson et al. 2002), comprised of 878 radio sources with spectral index $\alpha^{5GHz}_{2.7GHz} > -0.4$ and declinations between $+2.5^\circ$ and -80°. Ellison et al. (2001) limited their data set to 66 $z_{em} \geq 2.2$ quasars in which they found 22 DLAs. Three of these DLAs were classified as "associated" and dropped from the final sample. Two more DLAs were excluded because they fell outside of the range $1.8 \leq z_{abs} \leq 3.5$, that Ellison et al. (2001) set for their statistical sample, citing that there appears to be little evolution of Ω_g in this range. Since the UCSD sample did not have this z^{max}_{abs} cutoff, we

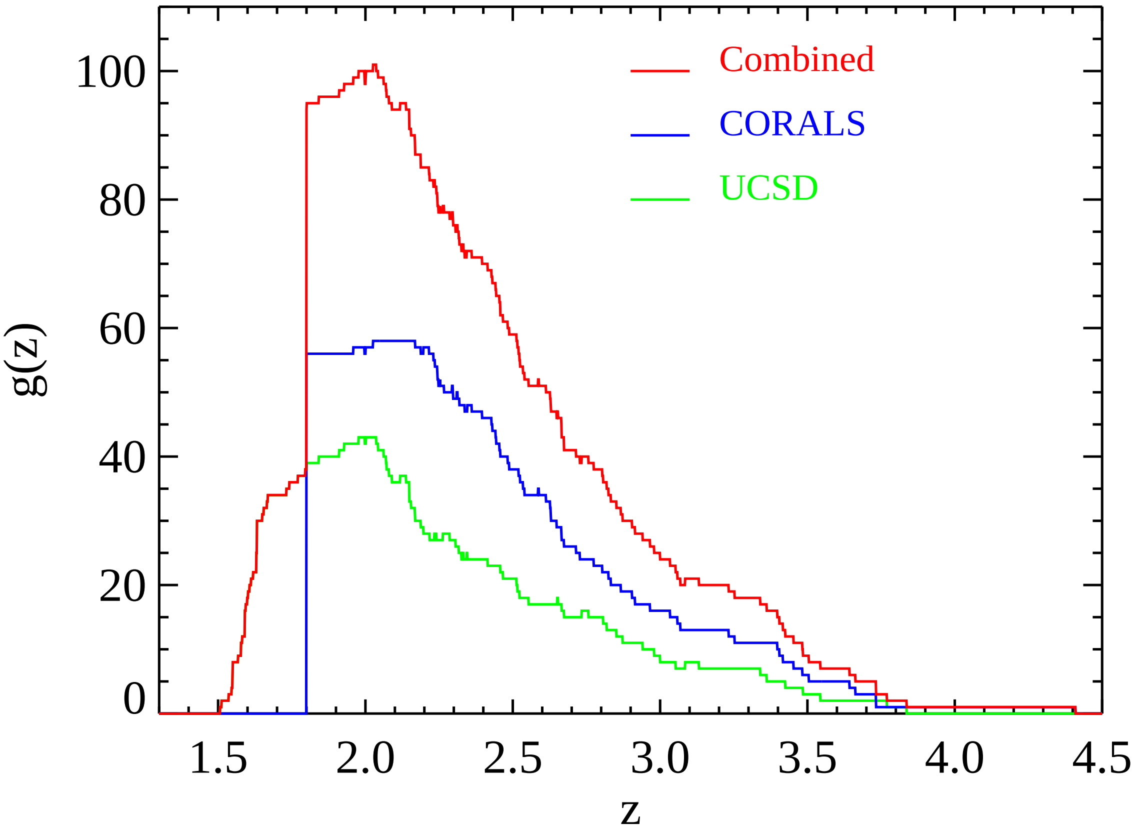

Figure 2.2: Redshift sensitivity function $g(z)$ as a function of redshift for the UCSD survey, the CORALS survey, and the combined sample.

included all 19 CORALS DLAs in the statistics for the combined sample.

Detailed results of the CORALS survey, including the two DLAs in sightlines to quasars with $z_{abs} > 3.5$, are listed in Table 2.5. Statistics for the number density and neutral gas mass density in the CORALS survey resulted in their conclusion that previous, magnitude limited surveys could have underestimated these values by as much as a factor of two. The plot of $g(z)$ versus z for the CORALS survey is shown in blue in Figure 2.2. Over a total redshift interval, $\Delta z = 57.16$, the number of DLAs per unit redshift, $n(z) = 0.33^{+0.10}_{-0.07}$. Over a cosmological redshift path of $\Delta X = 186.68$, the line density of DLAs in the CORALS survey, $\ell_{\mathrm{DLA}}(X) = 0.102^{+0.03}_{-0.02}$, which is double that of the UCSD survey. CORALS compared their neutral gas mass density in DLAs $\Omega_g = 1.37^{+0.53}_{-0.55} \times 10^{-3}$ with the compilation of Péroux et al. (2001) and Rao & Turnshek (2000), and concluded that Ω_g derived from optically-selected surveys could be underestimated by up to a factor of two.

However, Ellison et al. do concede the uncertainty of their conclusion primarily because the small survey fails to fully sample the column density distribution and secondly because their high value of Ω_g is dominated by two relatively high column density systems (both incidentally in front of "moderately bright" quasars, $B = 19.5, 20$, which qualitatively matches the result of PHW05 that there is an anti-correlation between quasar magnitude and N_{HI}).

2.5.3 Combined Results

For simplicity, we present detailed analyses for just the combined sample, which has the greatest statistical significance. Figure 2.2 presents $g(z)$ versus z for the combined sample in red. The CORALS sample begins abruptly at $z = 1.8$, the z_{min} cutoff of their sample. The UCSD sample continues down to a $z_{min} \approx 1.51$ for some quasars. For $z \approx 2$ the combined sample is nearly double that of CORALS. For higher redshift intervals (i.e. $z = 3$), the CORALS survey contributes roughly 2/3 of the pathlength. Of course, the combined sample gives the best constrained estimate of the number density of n(z)= $0.26^{+0.06}_{-0.05}$.

The combined sample is large enough to attempt an analysis of the H I distribution function, $f_{\rm HI}(N, X)$. This sample spans the redshift interval $z = [1.51, 4.4]$ with an integrated absorption pathlength $\Delta X = 317.11$ and a column density weighted mean redshift of 2.28. In practice, we can evaluate $f_{\rm HI}(N, X)$ in the discrete limit and plot the resulting $f_{\rm HI}(N, X)$ in $N_{\rm HI}$ bins of some ΔN. In Figure 2.3, we plot in red $f_{\rm HI}(N, X)$ for the combined sample, in $N_{\rm HI}$ bins of $\Delta N = 0.4\,$dex, calculated in the following way:

$$f_{\rm HI}(N, X) = \frac{m_{DLA}(N, N + \Delta N)}{\Delta X} \quad , \tag{2.12}$$

where m_{DLA} is the number of damped Lyα systems within $(N, N + \Delta N)$ in the ΔX interval and the error bars are determined by Poisson uncertainty at the 68% c.l. according to the value of m_{DLA}. Also plotted, in black, are the results of the optically-selected SDSS-DR3 (PHW05) survey for comparison. Following PHW05, we have overplotted the best-fit solutions of two possible functional forms of $f_{\rm HI}(N, X)$. Because of the small sample size of this survey we will attempt to fit only a single power-law and a Γ-function. The single power-law form is as follows:

$$f_{\rm HI}(N, X) = k_1 N^{\alpha_1} \quad , \tag{2.13}$$

and the Γ-function is (e.g. Fall & Pei 1993):

$$f_{\rm HI}(N, X) = k_2 \left(\frac{N}{N_\gamma} \right)^{\alpha_2} \exp \left(\frac{-N}{N_\gamma} \right) \quad . \tag{2.14}$$

We have performed a maximum likelihood analysis to constrain the parameters and set the constants k_1 and k_2. A summary of the fit parameters, along with those of the optically-selected SDSS-DR3 survey for comparison, is given in Table 2.6. The best fit slope of the single power-law is $\alpha_1 = -2.18^{+0.20}_{-0.26}$. This

Table 2.6. FITS TO $f_{\rm HI}(N,X)$

Form	Parameters	SDSS-DR3 Optical Sample[a,b]	Combined Radio Sample[c]
Single	$\log k_1$	23.36	22.90
	α_1	$-2.19^{+0.05}_{-0.05}$	$-2.18^{+0.20}_{-0.26}$
Gamma	$\log k_2$	$-23.52^{+0.02}_{-0.02}$	$-25.97^{+0.09}_{-0.08}$
	$\log N_\gamma$	$21.48^{+0.07}_{-0.10}$	$22.49^{+0.29}_{-0.36}$
	α_2	$-1.80^{+0.06}_{-0.06}$	$-2.12^{+0.22}_{-0.27}$

[a] Prochaska et al. (2005)

[b] Mean absorption redshift = 3.06

[c] Mean absorption redshift = 2.28

single power-law slope can be compared favorably with the optical SDSS-DR3 survey single power-law slope of $\alpha_1 = -2.19^{+0.05}_{-0.05}$ over their entire redshift range, $z = [2.2, 5.5]$. This correspondence is expected because the radio-selected survey is dominated by the low column density end which matches that of the optical, and can be seen as a confirmation of the two techniques.

While the single-power law gives a good fit to the radio-selected data, we also attempt to fit the Γ-function for the following two reasons: First, the single-power law is unphysical, i.e. the fit must turn over in order for Ω_g to converge, and second, unlike the single-power law, the Γ-function provided a satisfactory fit to the optically-selected data. However, unlike the optically-selected sample, the radio-selected sample gives nearly the same fit for the Γ-function as for the single power-law, $\alpha_2 = -2.12^{+0.22}_{-0.27}$. While we derive a formal value of the break column density $N_\gamma = 22.49^{+0.29}_{-0.36}$, we interpret this as an unrealistic extrapolation of the data. Rather, the small size of the radio-selected sample cannot reliably determine a break column density, and therefore we cannot demonstrate that our Ω_g converges.

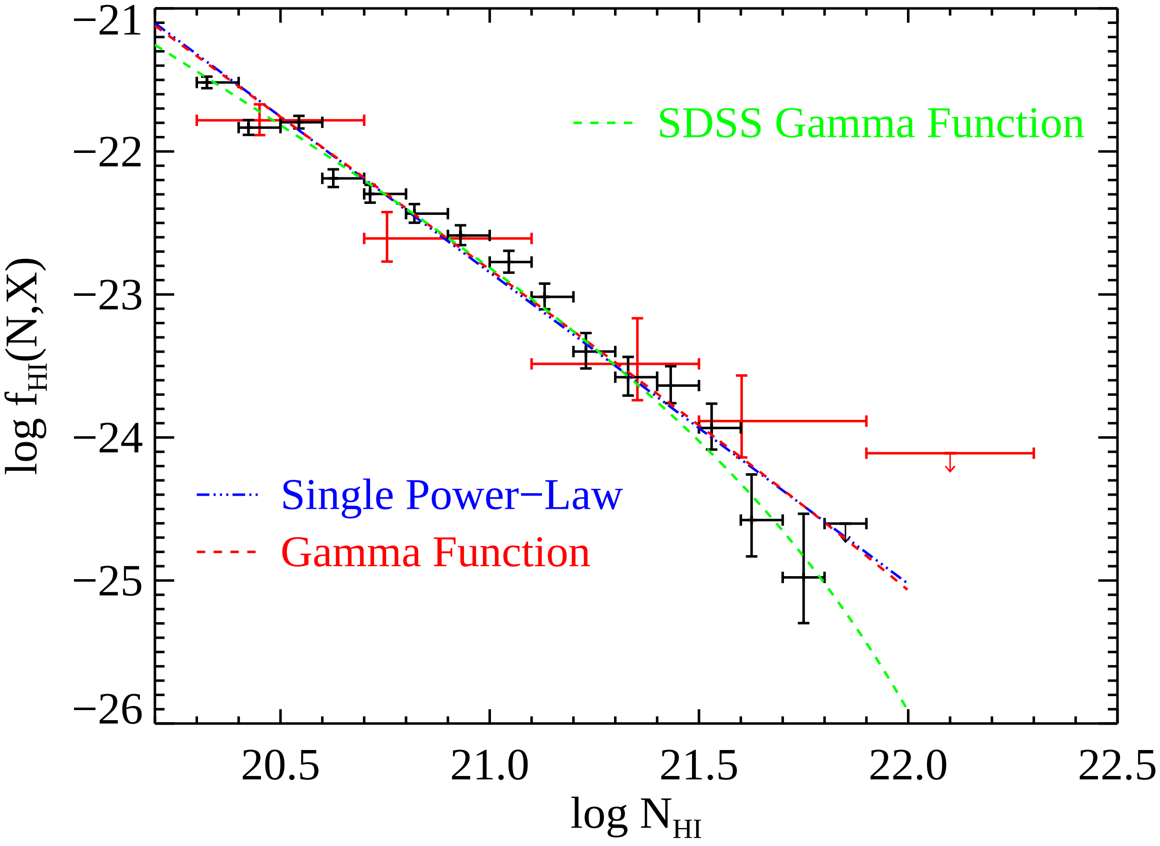

Figure 2.3: The H I frequency distribution $f_{\rm HI}(N, X)$ for the 26 DLAs of the combined sample is plotted in red. Overplotted are the fits of a single power-law, the dot-dashed line in blue, and a Γ-function, the dashed line in red. The last bin contains the 2σ upper limit. Plotted in black is the $f_{\rm HI}(N, X)$ for the optical data from the SDSS-DR3, with the Γ-function fit in green.

To determine if the radio-selected data rules out the optically-selected Γ-function fit, we performed a chi-squared test on the radio-selected data and optically-selected Γ-function fit. The results of the chi-squared test, $\mathrm{Prob}_1(\chi^2 > 5.96) = 1.5\%$ show that we can reject the fit at the 5% level, but not at the 1% level of confidence. While this may be evidence for modest disagreement between the two samples, we interpret this disagreement to be primarily due to the fact that we cannot constrain the radio-selected fit at large N_{HI} , i.e. the radio-selected sample does not contain enough DLAs to fully sample the H I distribution function. We note that a more conservative two-sided KS test shows agreement between the radio-selected data and the optically-selected Γ-function fit at the 77% level.

The line density of DLAs in the combined sample, taken over the entire redshift interval, $z = [1.5,\ 4.4]$, is $\ell_{\mathrm{DLA}}(X) = 0.08^{+0.02}_{-0.02}$ at a median $z = 2.35$, where the errors represent the 1σ Poisson uncertainty in m_{DLA}. In Figure 2.4 we plot $\ell_{\mathrm{DLA}}(X)$ for the combined sample in red, evaluated in the discrete limit,

$$\ell_{\mathrm{DLA}}(X) = \frac{m_{DLA}}{\Delta X} \quad . \tag{2.15}$$

We have grouped the data into four redshift bins, $z = [1.5,\ 2.2]$, $[2.2,\ 2.5]$, $[2.5,\ 3.0]$, and $[3.0,\ 4.4]$ to allow for comparison with the results of PHW05. We have overplotted the results of the SDSS-DR3 optical survey in black. These points are grouped into redshift bins $z = [2.2,\ 2.5]$, $[2.5,\ 3.0]$, $[3.0,\ 3.5]$, $[3.5,\ 4.0]$, $[4.0,\ 5.3]$. The black point marked by a star in redshift bin $z = [1.5,\ 2.2]$ is a compilation of optical surveys for DLAs produced by Peroux et al. (2003). Although the central values of the line densities of the radio and optically-selected surveys are different, the difference is not statistically significant. Note the radio sample gives a somewhat higher line density at all redshifts, and it is interesting to note that beginning at $z = 2.2$, the trend of increasing line density with increasing redshift, $z > 2.2$, is present in both samples. In fact, the central values of the radio sample

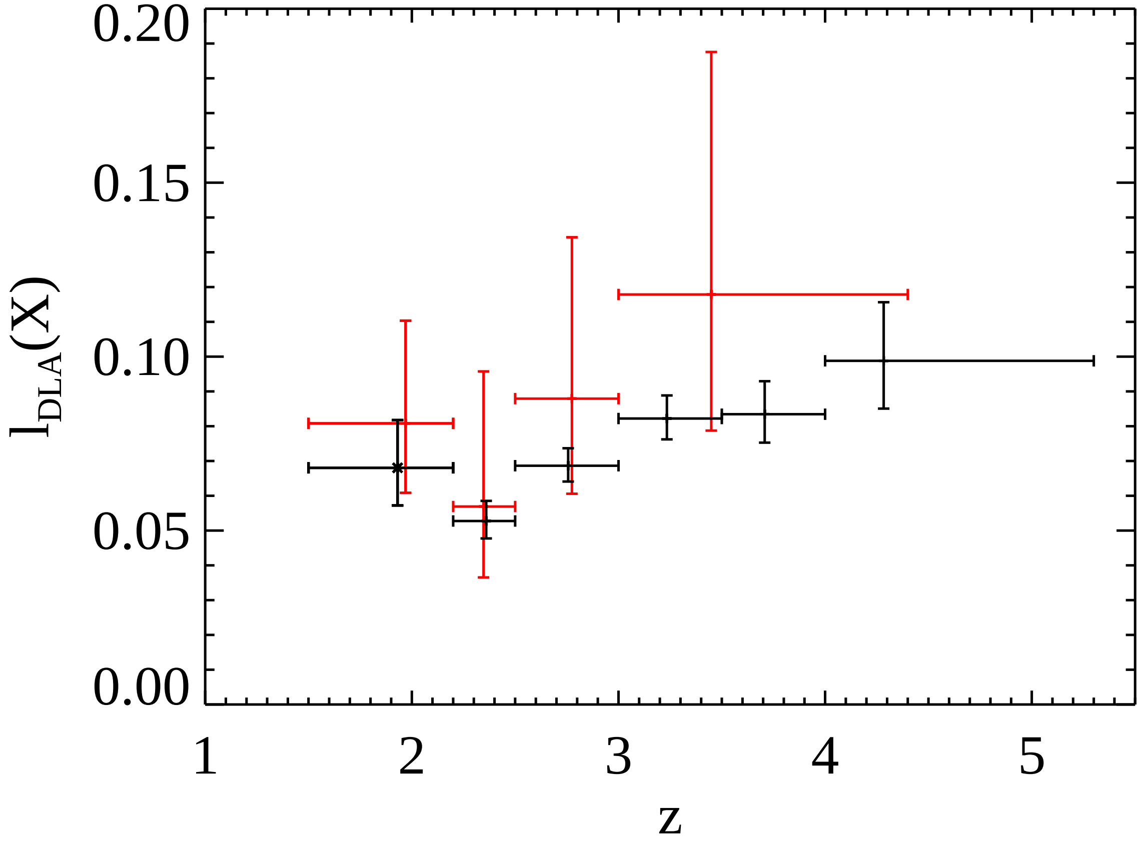

Figure 2.4: Plot of the line density of DLA systems $\ell_{\rm DLA}(X)$ versus redshift for the combined sample (in red). Plotted in black is the $\ell_{\rm DLA}(X)$ for the optical data from the SDSS-DR3 survey and the Péroux compilation.

follow the same qualitative shape, even the unusual 'dip' at $z \approx 2.3$. While it would make sense that the SDSS-DR3 survey, with its statistically significant numbers of quasars and DLAs is actually detecting a physically meaningful trend – PHW05 claim the decline in $\ell_{\rm DLA}(X)$ is due to a decrease in DLA cross-section with time – the correspondence with the combined radio sample, of relatively so few objects, is likely a coincidence. However, although the error bars are large, we can interpret this similarity in line density evolution with the statistically significant results of the SDSS-DR3 as support of our results.

While we report a detection of the neutral gas mass density, $\Omega_g = 1.15^{+0.37}_{-0.38} \times 10^{-3}$, our result is actually a lower limit due to the insufficient size of the combined sample. In Figure 2.5 we plot Ω_g for each of the UCSD, CORALS and combined samples. Errors are calculated using a modified bootstrap method as described by PHW05, and the values are plotted at the $N_{\rm HI}$ weighted mean redshift. Also plotted, in black, are the Ω_g values determined by the optically-selected SDSS-DR3 survey (PHW05), which covers a redshift range $z \geq 2.2$. Because the SDSS-DR3 sample consists of over 500 DLAs the values of Ω_g are plotted in five redshift bins: $z = [2.2, 2.5]$, [2.5, 3.0], [3.0, 3.5], [3.5, 4.0], and [4.0, 5.5]. And finally, plotted in the bin range $z = [1.7, 2.2]$, is the compilation by Peroux et al. (2003). It is seen that the lower limits of all of the radio-selected samples agree well with the optically-selected data.

2.5.4 Empty Fields

The eight fields for which no optical identification of a quasar was obtained are called the "Empty Fields" (EFs). Table 2.3 contains the details of each EF while Figure 2.6 contains Keck images of the EFs. These eight fields were determined to contain either nothing of significance, or merely a faint extended smudge when imaged with Keck in the R band for ≈ 600 seconds. In either case, it was not possible to obtain spectra. While all of the previous analyses in this paper were conducted as if these fields did not exist, we actually must determine a method of including them in the sample in order for our survey to be considered complete. Assuming that the fields were truly empty, i.e. the optical source was fainter than our magnitude limit on Keck, and that pointing errors or some other experimental errors did not result in radio-source misidentification, we can make two extreme, simplifying assumptions. On the one hand, we can assume that no DLAs are present toward these optically faint quasars and calculate a lower limit on Ω_g by including some average redshift path length for each object, where the average pathlength is determined from the known quasars in our survey. On the other extreme we can assume that each EF is actually empty because of the

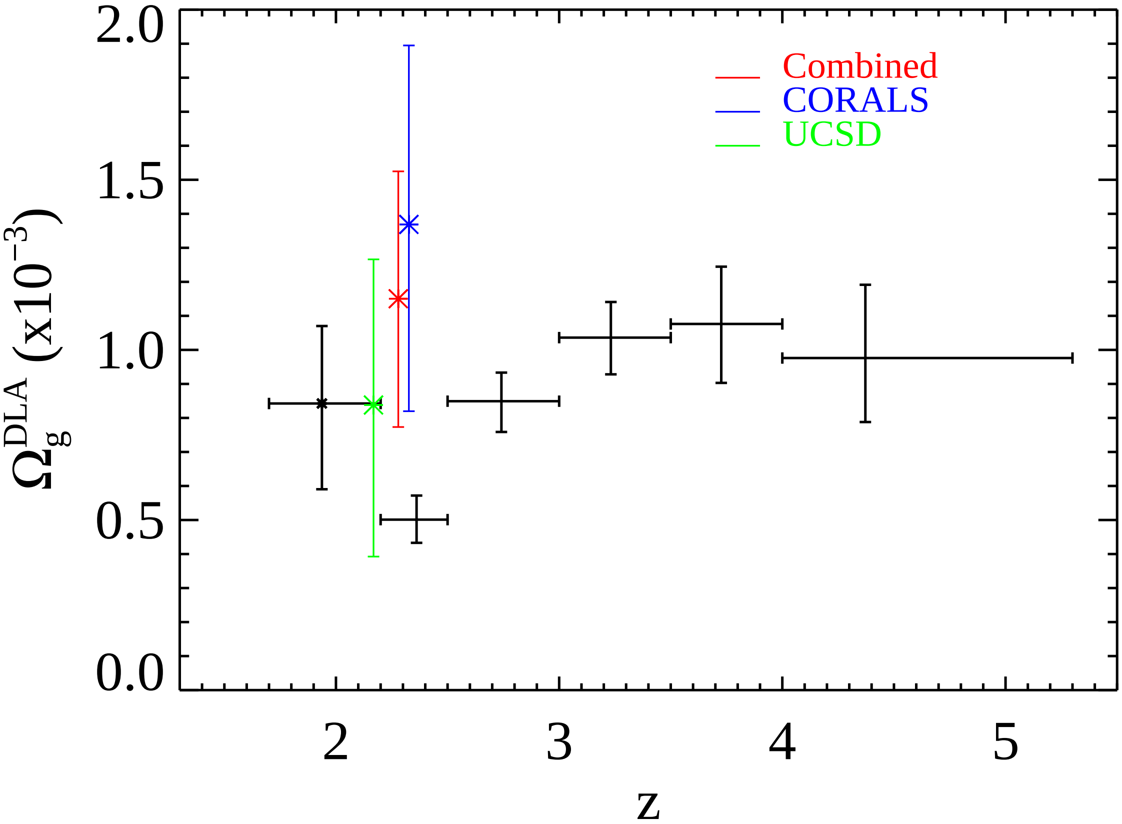

Figure 2.5: The neutral gas mass density, Ω_g, of the UCSD, CORALS and combined samples are plotted in green, blue and red respectively. Also plotted are the values of Ω_g as a function of redshift for the optical SDSS-DR3 survey (black points). The Péroux compilation data point at $z < 2.2$ (marked with a cross) does not include measurements from the SDSS survey. All error bars are 1 σ. The redshift bins of the radio samples (not plotted) are $z_{combined}$ = [1.51, 4.41], z_{ucsd} = [1.51, 3.84], and z_{corals} = [1.80, 4.41] and the points are plotted at the $N_{\rm HI}$ weighted mean redshift.

presence of a high column density, dusty DLA. We can assume that each EF contains an average to high column-density DLA and estimate an upper limit on Ω_g.

Using the results of the combined sample, we determine the average redshift path per quasar to be $< \Delta X >= 2.66$. Assuming that each of the eight EFs would contribute this amount of redshift path gives a new total redshift path searched of $\Delta X = 338.43$. The lower limit on Ω_g, assuming that none of the EFs contained a DLA, is $\Omega_g^{lower} = 1.08 \times 10^{-3}$. The upper limit, assuming that each of the EFs contains a DLA of average column density in our survey, $N_{\rm HI} = 7.86 \times 10^{20}\,{\rm cm}^{-2}$, results in an upper limit of $\Omega_g^{upper} = 1.41 \times 10^{-3}$. While both the lower and upper limit on Ω_g, derived by including the EFs, are clearly within the error of the combined value of $\Omega_g = 1.15^{+0.37}_{-0.38} \times 10^{-3}$, it is notable that the upper limit is only $\approx 22\%$ larger than Ω_g, i.e. even if each EF contains a dusty DLA of our average $N_{\rm HI}$, the effect on Ω_g would be relatively small.

We can take the analysis one step further and allow the average value of $N_{\rm HI}$ to exceed $7.86 \times 10^{20}\,{\rm cm}^{-2}$. To determine the minimum average column density DLA that would affect our results we assume that each EF contains a quasar at our average redshift and a DLA of fixed column density which we vary from the lower limit, $N_{\rm HI} = 2 \times 10^{20}\,{\rm cm}^{-2}$, to the generally observed highest column densities of $N_{\rm HI} \approx 1 \times 10^{22}\,{\rm cm}^{-2}$. We plot the results in Figure 2.7.

As previously stated, if we assume that each EF contains a DLA of average column density in our survey, $N_{\rm HI} = 7.86 \times 10^{20}\,{\rm cm}^{-2}$, we derive an $\Omega_g = 1.41 \times 10^{-3}$, indicated in Figure 2.7 by the blue asterisk. Compare this with the red point and error bar, our radio-selected survey value of Ω_g, derived by ignoring the EFs. For reference, the optically selected SDSS-DR3 survey, at $\Omega_g = 0.82^{+0.05}_{-0.05} \times 10^{-3}$, is plotted in green. From Figure 2.7 it is seen that if each EF contained a DLA of $N_{\rm HI} \approx 10^{21.2}\,{\rm cm}^{-2}$ or larger, a relatively large value occurring in only $\approx 15\%$ of our sample, the impact of the EFs would be large

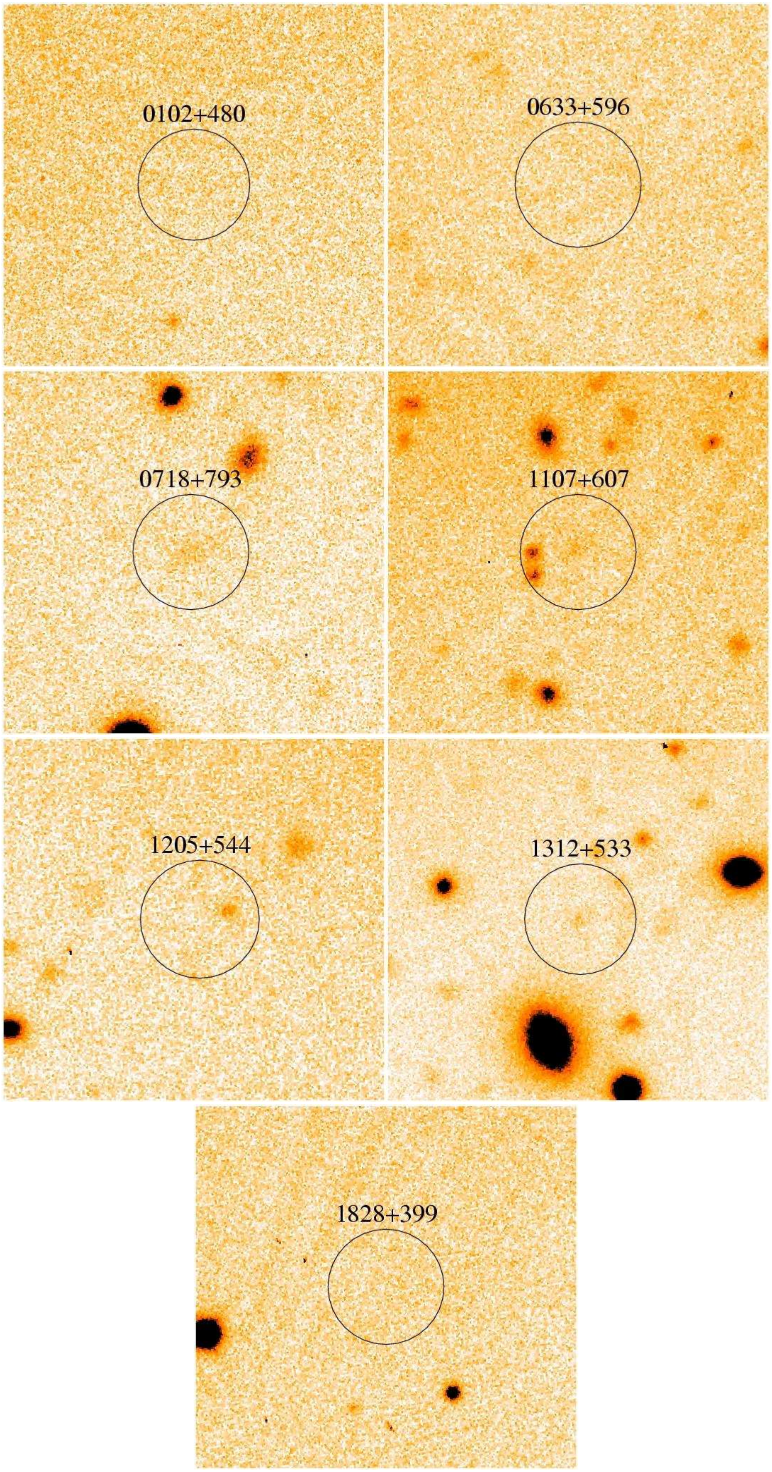

Figure 2.6: R band images of the empty or extended fields. Exposures times are given in Table 2.3. The circle radius is ≈ 5 arcsec. All image orientations are the standard North (up), East (left).

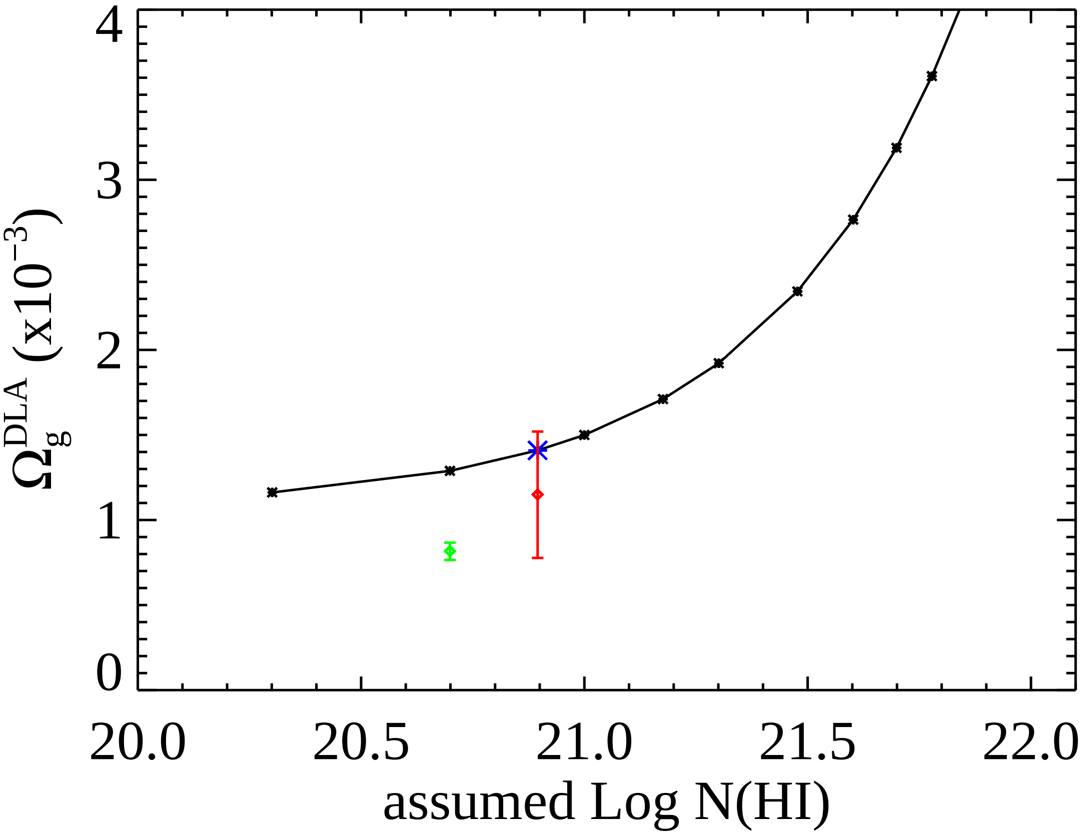

Figure 2.7: This figure demonstrates the potential impact that the empty fields could have on Ω_g, the neutral gas mass density. We calculate the resultant value of Ω_g assuming that each of the eight empty fields contains a DLA of the stated $N_{\rm HI}$. The red point with 1σ error bars is the value of Ω_g found from the combined radio sample, calculated by ignoring the empty fields. The blue asterisk represents the value of Ω_g if each of the empty fields contained a DLA of our average $N_{\rm HI} = 7.86 \times 10^{20}\,{\rm cm}^{-2}$. For reference, the optically selected SDSS survey value is given in green.

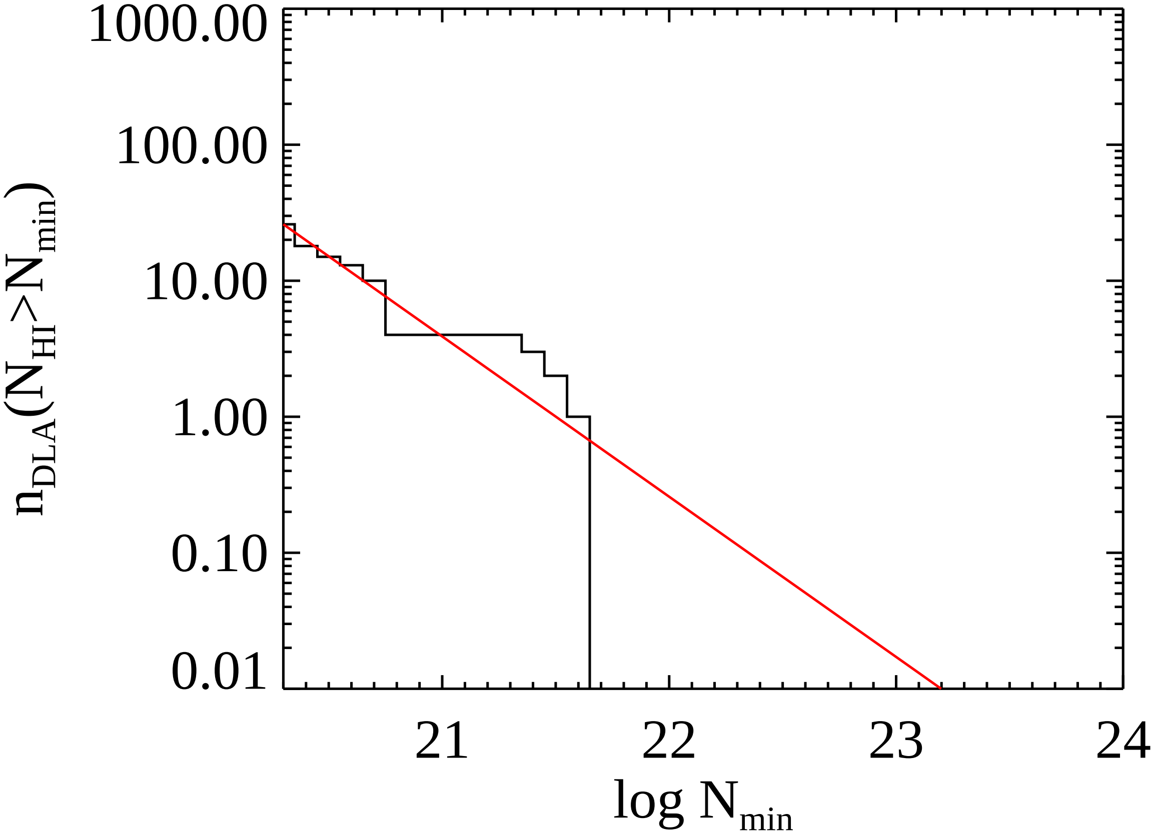

Figure 2.8: The cumulative distribution of the number of DLAs with a specific minimum $N_{\rm HI}$. Overplotted in red is the single power-law fit to the distribution function. It is seen that only 0.3 DLAs are expected with $N_{\rm HI} > 10^{22}\,{\rm cm}^{-2}$.

enough to increase the resultant value of Ω_g by $\approx 50\%$.

There are, however, several arguments for why these EFs are most likely *not* $z_{em} > 2$ quasars extinguished by very dusty, high column density DLAs. If we extrapolate the H I frequency distribution function, $f_{\rm HI}(N, X)$ resulting from the radio-selected sample, as seen in Figure 2.3, we would expect not more than 1 DLA with $N_{\rm HI} > 10^{22}\,{\rm cm}^{-2}$. If two or more high column density systems existed, the resulting $f_{\rm HI}(N, X)$ would be unphysical assuming galaxies have declining surface density profiles. In this case, we would require a bimodal population consisting of high column density, high dust-to-gas ratio systems, such as molecular clouds, that would be missed in optical surveys.

While we cannot rule out the existence of a bimodal population, we can determine exactly how many high column density systems the current radio-selected distribution function would predict. We plot the cumulative number of DLAs above a certain minimum H I column density and extrapolate using our single power-law fit. From this plot, in Figure 2.8, it is apparent that we would expect only 0.3 DLAs with $N_{\rm HI} > 10^{22}\,{\rm cm}^{-2}$. Additionally, in the case of the five fields containing faint extended emission, we can use scaling arguments to show that if we assume this emission is actually the resolved quasar host galaxy, then the quasar would have to be a low redshift object and would not have been included in our $z_{em} > 2.0$ survey. Adopting the typical high-z quasar host galaxy scale length of ≈ 12 kpc (Kuhlbrodt et al. 2005), we can estimate the angular size at $z = 2.0$ to be ≈ 1.4 arcsec. Careful inspection of the extended fields reveals extended blobs on the order of 3 arcsec or larger, making these low z quasars that would not have been included in our survey.

In an effort to determine the nature of the EFs, we are currently conducting an observing program on the Green Bank Telescope (GBT) to search for 21 cm absorption along the sightlines to these EFs. We will carry out a redshift path search from $z = [0.5, 3.9]$ using the frequencies of ≈ 300 MHz - 900 MHz. If a high column density, dusty system does exist along the line of sight and is blocking out the quasar light, it is likely that we will detect it in absorption.

2.6 Analysis & Discussion

The best way of determining the significance of dust obscuration of quasars is to compare the results of magnitude limited and radio-selected quasar surveys for DLAs. The primary problem with this method has so far been the limited survey size of the radio-selected surveys and the resultant large error bars that preclude conclusive results. While the UCSD survey itself was slightly smaller than the previously published CORALS survey, combining the two sur-

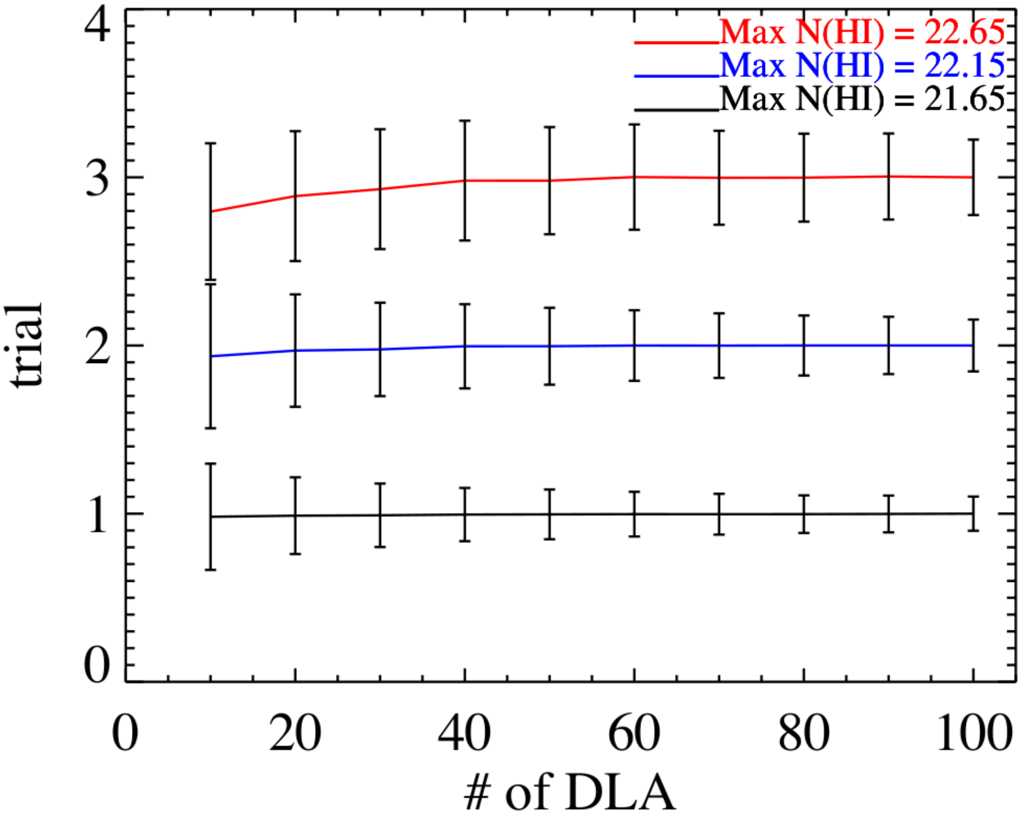

Figure 2.9: The results of bootstrapping error on samples of the given number of DLAs with maximum column densities of $N_{\mathrm{HI}} = 10^{21.65}\,\mathrm{cm}^{-2}$ (to match the combined sample), the black line, $N_{\mathrm{HI}} = 10^{22.15}\,\mathrm{cm}^{-2}$, the blue line, and $N_{\mathrm{HI}} = 10^{22.65}\,\mathrm{cm}^{-2}$, the red line. It is seen that a sample with maximum $N_{\mathrm{HI}} = 10^{21.65}\,\mathrm{cm}^{-2}$, will give an error in the desired range of ±10% at ≈ 100 DLAs.

veys in effect doubles the size. However, the uncertainties of the combined sample, which is still more than an order of magnitude smaller than the current optical samples, are so large that definitive statements remain elusive.

To make a simple estimate of the number of radio selected DLAs necessary to conclusively answer the question of dust bias, we performed the following analysis. If we desire a result with errors of no larger than $\approx 10\%$, we can perform a bootstrap error evaluation on a random sample of DLAs each time increasing the number of DLAs to determine how many DLAs are necessary to give the desired precision. In Figure 2.9 we plot the results of our bootstrap error estimation, normalized to one and offset for each different sample type. The estimation was performed on random $N_{\rm HI}$ samples with minimum $N_{\rm HI} = 10^{20.3}\,{\rm cm}^{-2}$, and three different maximum column densities, $N_{\rm HI} = 10^{21.65}\,{\rm cm}^{-2}$, to match the upper limit of the combined radio sample, $N_{\rm HI} = 10^{22.15}\,{\rm cm}^{-2}$, and $N_{\rm HI} = 10^{22.65}\,{\rm cm}^{-2}$. It can be seen that in a sample with a maximum column density similar to the combined sample, the desired $\approx 10\%$ error is acheived with a sample of ≈ 100 DLAs. As the maximum column density is increased, the error bars increase as well. Note that the bootstrap errors of our actual sample (number of DLAs = 26, error $\approx 30\%$) are slightly bigger than those of the randomly generated samples due to the fact that our sample contains only a few high column density systems.

To definitively answer the question of dust bias we would ideally hope to at least approach the total redshift path searched by optical surveys in order to make valid comparisons. In the combined radio-selected sample, the total cosmological redshift path searched was $\Delta X = 317.11$. Compared with the total redshift path surveyed by the latest large optical survey, SDSS-DR3 with $\Delta X = 7333.2$, we are still more than an order of magnitude smaller.

The combined radio-selected central value of Ω_g is slightly higher than all of the optically-selected values, as plotted in Figure 2.5. However, when considering the 1σ lower limits of the radio-selected values of Ω_g, no difference between the magnitude-limited sample and the radio-selected samples can be ascertained. If we ignore the possibility of evolution in Ω_g we can compare the entire SDSS-DR3 optically-selected survey over the complete redshift range with the radio-selected value. Excluding the Péroux point, the SDSS-DR3 value taken over one redshift bin, $z = [2.2, 5.5]$, gives $\Omega_g = 0.82^{+0.05}_{-0.05} \times 10^{-3}$. Comparing this value with the 1σ lower limit of the combined radio-selected value of $\Omega_g^{low} = 0.77 \times 10^{-3}$ over the range $z = [1.51, 4.4]$, we see excellent agreement. This agreement in Ω_g between the radio and optically-selected surveys for DLAs is the best evidence for our conclusion that dust bias does not have a major effect on the results of optically-selected surveys.

2.7 Copyright

This chapter, in full (with minor exceptions to conform to this thesis), is a reprint of "The UCSD Radio-Selected Quasar Survey for Damped Lyman-α Systems", Jorgenson, R. A., Wolfe, A. M., Prochaska, J. X., Lu, L., Howk, J. C., Cooke, J., Gawiser, E., & Gelino, D. M. 2006, The Astrophysical Journal, Vol. 646, p. 730. The dissertation author was the primary investigator and first author of the paper.

3

Understanding Physical Conditions in Damped Lyman α Systems Through Neutral Carbon Fine Structure Lines

3.1 Introduction

Damped Lyman alpha Systems (DLAs) are high redshift reservoirs of neutral gas that are thought to be the progenitors of modern day galaxies. While much is known about these systems, which are defined as having a column density of neutral hydrogen, $N_{\rm HI} \geq 2 \times 10^{20}\,{\rm cm}^{-2}$, the nature of their detection as absorption line systems limits our ability to fully understand these key links to normal galaxy evolution. For example, while the column density distribution function, the line density, and the contribution to the neutral gas mass density of the Universe of DLAs are all quantified on a statistically significant level, physical properties such as the volume densities, temperatures, physical sizes, and masses are not well constrained.

DLAs are important because they are at present the only means of studying the gaseous progenitors of modern normal galaxies – those that contribute the bulk of the stellar content in the Universe. While the study of DLAs has now entered the realm of the statistically significant, many key aspects of their nature remain unclear. One major question concerns the nature of the gas comprising DLAs. While a reasonable working hypothesis is that DLAs are comprised of a two-phase medium in pressure equilibrium, as in the Milky Way, it is unclear whether most of the gas is in the Cold Neutral Medium (CNM) phase or in the Warm Neutral Medium (WNM) phase. The answer has far reaching implications – specifically, for determining densities, temperatures, and sizes of DLAs and generally, for understanding the big picture of galaxy evolution.

One diagnostic tool for determining temperatures is the detection of 21 cm absorption in known DLAs in the sight line towards radio loud quasars. Because the 21 cm optical depth is inversely proportional to the spin temperature, which is generally equal to the kinetic temperature of dense gas, 21 cm absorption is a tracer of cold gas. Kanekar & Chengalur (2003) performed a relatively deep survey for 21 cm absorption towards 10 DLAs and detected none. They place lower limits on the H I spin temperatures of the neutral gas of generally T_s >1000 K, and in one case, T_s >9000 K. This led them to argue that most of the gas in DLAs is in a WNM. However, the use of 21 cm absorption, or lack thereof, as a diagnostic for temperature, is complicated by the fact that the difference between the beam sizes and source sizes of radio and optical observations introduces confusion in determining the true area covering factor, the amount to which the absorbing gas covers the generally extended radio source. Moreover, the H I column density detected optically may differ from that detected toward the radio source. In fact, Curran & Webb (2006) use related arguments to explain why 21 cm absorption had not, at the time of their paper, been seen at $z_{abs} > 2.3$. They argue that it is a geometric effect based on the fact that the angular diameter distance measure flattens at $z \geq \sim 1$, which means that the high redshift DLAs are less effective at covering the background quasar than absorbers at low redshift.

In the few cases in which DLAs have been detected in 21 cm absorption, Kanekar et al. (2007) argue that the average cold gas fraction must be low. Specifically, in the case of recently discovered 21 cm absorption towards PKS 0201+113 at $z_{abs} \approx 3.39$ they claim that the average cold gas fraction is <17%. However, this lack of low spin temperature detections could be more a reflection of the difficulty of the measurement than of the presence of warm gas. For example, York et al. (2007) recently reported the detection of the first low spin temperature absorber at high redshift. They report the detection of a $T_s = 138 \pm 36$ K in a DLA at $z_{abs} = 2.289$.

On the other hand, Wolfe, Prochaska & Gawiser (2003), hereafter WPG03, Wolfe, Gawiser, & Prochaska (2003), hereafter WGP03, and Wolfe et al. (2004) find that the majority of DLAs containing strong $\mathrm{C\,II}^*$ absorption must be primarily CNM. If they were WNM the inferred [C II] 158μm cooling rate would be a small fraction of the total cooling rate. As a result the luminosity implied by the large heating rate, required to balance cooling, would result in radiation integrated over the DLA population that exceeds the observed bolometric background radiation at z = 0. WPG03 find $\mathrm{C\,II}^*$ absorption in approximately half of the DLAs contained in their sample. This results in an area covering fraction of CNM, or $f_A^{CNM} \approx 0.5$ or 50%. The evidence for bimodality in cooling rates (Wolfe et al. 2008) is drawn from an unbiased sample of DLAs, which is not merely comprised of special lines of sight containing large H I or $\mathrm{C\,II}^*$ column densities. The evidence for this is first, that the H I column density distribution function, $f_{\mathrm{HI}}(N, X)$, of the sample of 75 DLAs closely resembles the statistically significant SDSS sample of over 1000 DLAs (Prochaska et al. 2005). Second, the distributions of the two sub-samples, the "high-cool" and the "low-cool" DLAs, are statistically different in all aspects, such as metallicity, dust to gas ratio, velocity width, and Si II equivalent width, but with the important exception of their H I column densities. In terms of their H I column density distributions, the two samples are indistinguishable. This evidence strongly supports the belief that this is an unbiased sample and hence, the area covering fraction of CNM is truly close to 50%. A second piece of evidence directly supporting the presence of CNM is the individual case of a z_{abs}=4.224 DLA towards quasar PSS 1443+27 (Howk et al. 2005). The detection of strong C II* absorption in this DLA along with high signal to noise ratio enabled the authors to put meaningful limits on the non-detection of Si II* λ1264. This in turn led to a strict 2σ upper limit on the temperature of the gas containing C II* of $T < 954$K.

In this paper, we present observations of DLA gas exhibiting neutral carbon (C I) absorption that strengthen the model in which DLAs (containing C II*) consist of a significant fraction of CNM gas. Our primary diagnostic tool is the ground electronic state of neutral carbon (C I), $2s^2\ 2p^2\ {}^3P_J$ which is split into three fine structure levels denoted as ${}^3P_0$, ${}^3P_1$ and ${}^3P_2$. Following convention, we will refer to these fine structure states as C I, C I*, and C I** . The excited fine structure states are only 23.6 K and 62.4 K above the ground state, which makes them sensitive probes of conditions in cold gas. The advantage of using the fine structure states of C I is that rather than determining only a line of sight column density, the relative excitation of the C I fine structure states allows for a determination of local conditions such as volume density and temperature. And this is the major objective of this paper.

The utility of C I fine structure transitions in probing cold gas has long been understood and applied to the high redshift Universe. The C I fine structure levels are populated by collisional excitation and de-excitation, radiative decay, UV pumping and direct excitation by the Cosmic Microwave Background (CMB) radiation. Because of this sensitivity to the CMB, CI fine structure lines in DLAs were first used to determine the temperature of the CMB at high redshifts as a test of Big Bang Cosmology (i.e. Songalia et al. (1994)). However, because singly ionized carbon, C II, is the dominant state of carbon in the ISM, C I is not commonly found in DLAs. Additionally, because the C I fine structure transitions are generally weak and suffer significant blending, it is only recently with modern high-resolution Echelle spectrographs that detailed measurements of the lines have been possible.

Inspired by the work of Jenkins & Shaya (1979) and Jenkins & Tripp (2001) who used C I fine structure absorption to probe pressures in the local Milky Way ISM, we implement their technique on high redshift DLAs. Most recently, Jenkins & Tripp (2007) find that most of the C I in the Milky Way is in gas at pressures between $3 <$ log (P/k) <4 cm^{-3} K, with the distribution centered at P/k = 2700 cm^{-3} K. We will show that, interestingly, our results for the high redshift DLAs are similar to those of Jenkins & Tripp (2007) for the Milky Way ISM. In addition, by invoking the sensible assumption of ionization equilibrium, we can use the population of the C I fine structure levels to constrain the total radiation field in some cases. This in turn acts as a check on the radiation field as determined by the C II* technique (WPG03; WGP03).

We report the discovery of C I in 4 high redshift DLAs, and analyze an additional 2 DLAs with previously published C I data. We derive limits on density, temperature, and pressure as well as the radiation field contained in the C I - bearing gas of each DLA. The paper is organized as follows: We discuss our data and data analysis techniques in section 3.2. We present our procedure for analyzing the C I data through the specific example of DLA 1331+17 at z_{abs}=1.776 in section 3.3. We then summarize the results for each of the C I -bearing DLAs in section 3.4. Section 3.5 contains discussion of the DLAs presented here as well as C I -bearing DLAs in general. We conclude in section 3.6. Throughout this paper we make the standard assumption that the ratio of column density of element X is equal to the ratio of volume density, $\frac{N(X^a)}{N(X^b)} = \frac{n(X^a)}{n(X^b)}$, i.e. we are analyzing average conditions along the line of sight.

3.2 Data and Methodology

Data for this paper was taken primarily with the HIRES spectrograph (Vogt et al. 1994) on the Keck I telescope, with a typical decker that resulted in an instrumental resolution FWHM = 6.25 km s^{-1} . Details of specific observations are given in Table 3.1. Data were reduced and continuum fitted using the standard XIDL [1] packages. Because of the complex blending of many close fine structure transitions that typically exhibit several velocity components, we were not able to successfully apply the apparent optical depth technique (Savage & Sembach 1991) for a measurement of the column densities. We also did not have the high signal to noise ratio and resolution of the Jenkins & Tripp (2001) study of interstellar C I, in which they developed a modified AODM technique (Jenkins & Tripp 2001). Instead we used the VPFIT package, version 9.5 [2] to measure the C I fine structure column densities, N(C I), N(C I^*), and N(C I^{**}), redshifts, and b parameters, where b=$\sqrt{2}\sigma$, and σ is the velocity dispersion in km s^{-1} . With one exception, we used the most recent f-values as determined by Jenkins (private communication) and list them in Table 3.2. Specifically, for the f-value of the resonance C I λ1560.3092Å transition, we found significant differences between our data and the solutions from fitting several multiplets simultaneously, using either the latest Jenkins f-value or the traditionally used Morton 2003 value (Morton 2003). Instead, we used our high signal to noise (SNR=30) data on 5 DLAs to determine the C I λ1560.3092 f-value empirically and we report the details in Appendix 1.

---

[1] http://www.ucolick.org/ xavier/IDL/

[2] http://www.ast.cam.ac.uk/ rfc/vpfit.html

Table 3.1. DETAILS OF OBSERVATIONS

Quasar	Telescope/Instrument	Date	Resolution FWHM [km s^{-1}]	Total Exp. Time [s]
FJ0812+32	Keck/HIRES	Mar. 16/17, 2005	6.25	14400
Q1331+17	Keck/HIRES	Jan. 10, 1994	6.25	3600
Q1331+17	VLT/UVES	Dec. 18, 2001	7.0	4500
J2100−06	Keck/HIRES	Sept. 18, 2007	6.25	10800
Q2231−00	Keck/HIRES	Jan. 11, 1995	8.33	5400
J2340−00	Keck/HIRES	Aug. 18/19, 2006	6.25	15000

Table 3.2. C I ATOMIC DATA[a]

λ	Transition	f
1260.735	C I	0.058784
1260.926	C I*	0.026094
1260.996	C I*	0.022055
1261.122	C I*	0.027327
1261.426	C I**	0.020689
1261.552	C I**	0.044189
1270.143	C I	0.002164
1270.408	C I*	0.000408
1276.482	C I	0.011802
1276.750	C I*	0.008245
1277.190	C I**	0.000745
1277.245	C I	0.131344
1277.283	C I*	0.081363
1277.513	C I*	0.039522
1277.550	C I**	0.086265
1277.723	C I**	0.027641
1277.954	C I**	0.003066
1279.056	C I*	0.006099
1279.229	C I**	0.009004
1279.498	C I**	0.003622
1279.891	C I*	0.028180
1280.135	C I	0.048010
1280.333	C I**	0.027556
1280.404	C I*	0.013210
1280.597	C I*	0.017751
1280.847	C I**	0.013297
1328.833	C I	0.089802
1329.085	C I*	0.035986
1329.100	C I*	0.043483
1329.123	C I*	0.030843
1329.578	C I**	0.057891
1329.600	C I**	0.030656

Table 3.2—Continued

λ	Transition	f
1560.309	C I	0.091014[b]
1560.682	C I*	0.098658
1560.709	C I*	0.032895
1561.340	C I**	0.019722
1561.367	C I**	0.001312
1561.438	C I**	0.110389
1656.267	C I*	0.062068
1656.928	C I	0.148832
1657.008	C I**	0.111346
1657.379	C I*	0.037032
1657.907	C I*	0.049481
1658.121	C I**	0.037101

[a] Atomic data is from Jenkins 2006 unless otherwise noted

[b] f value as determined in Appendix 1

In general, we simultaneously fitted as many C I multiplets as possible. In all cases, we included all multiplets that fell redward of the Lyα forest, which generally included the strongest multiplets at 1656Å and 1560Å , and usually the multiplet at 1328Å. In cases where a multiplet fell within the Lyman α forest, yet did not contain any obvious blending with a forest line, we included that multiplet in our analysis. We rejected sections of spectra that contained obvious blending.

All other information about each DLA, including metallicity, dust to gas ratio, and $\log\frac{CII}{CI}$ was determined using the Apparent Optical Depth Method, AODM (Savage & Sembach 1991), unless otherwise stated (i.e. in the cases where we performed a full component by component analysis). To measure the $\log\frac{CII}{CI}$ we must employ the conventional method of measuring N(C II) by proxy using N(Si II), because C II λ1334 is saturated in every DLA. As in Wolfe et al. (2004) we let [C/H] [3] = [Si/H] + $[\mathrm{Fe/Si}]_{int}$ where $[\mathrm{Fe/Si}]_{int} = -0.2$ for a minimal depletion model or $[\mathrm{Fe/Si}]_{int} = 0.0$ for a maximal depletion model. While Wolfe et al. (2004) estimate the error in the measurement of $\frac{C\,II}{C\,I}$ to be 0.1 dex, we use the more conservative estimate of 0.2 dex.

Details of the observations are given in Table 3.1, while the details of the C I measurements are summarized in Table 3.3. In the following we provide a brief summary of the data analysis of each DLA in our sample:

---

[3] The abundance ratio with respect to solar is defined as [X/Y] = log(X/Y) - $\log(X/Y)_{\odot}$

Table 3.3: C I DATA

Quasar	comp.	z_{abs}	FWHM$_{inst}$[a] [km s^{-1}]	b [km s^{-1}]	logN(CI) [cm^{-2}]	logN(CI*) [cm^{-2}]	logN(CI**)] [cm^{-2}]	(f1, f2)[b]
FJ0812+32	1	2.066773(1)	6.25	1.32±0.32	12.919± 0.042	12.915±0.048	12.321±0.113	(0.44, 0.11)
FJ0812+32	1	2.625808(1)	6.25	3.25±1.01	12.133±0.050	11.678±0.160	11.351±0.280	(0.23, 0.11)
FJ0812+32	2	2.626325(1)	...	2.71±0.28	12.697±0.014	12.328±0.035	<11.5(1σ)	(0.29, <0.03
FJ0812+32	3	2.626494(1)	...	0.38±0.04	13.092±0.093	12.993±0.037	12.300±0.054	(0.41,0.08)
Q1331+17	1	1.776369(1)	6.25	4.82±0.26	13.00± 0.01	12.53 ± 0.05	11.80±0.15	(0.242, 0.045)
Q1331+17	2	1.776524(1)	...	0.60± 0.22	12.96 ± 0.24	12.06± 0.16	–	–
Q1331+17	3	1.77655(3)	...	30.87±6.5	12.67±0.06	–	–	–
Q2100−06	1	3.089775(8)	6.25	0.38±1.5	12.04± 0.23	11.82± 0.17	–	–
Q2100−06	2	3.091461(4)	...	2.2± 0.79	12.42± 0.03	12.07± 0.15	–	–
Q2100−06	3	3.09237(2)	...	9.3± 1.8	12.39± 0.07	11.73±0.30	–	–
Q2231−00	1	2.06534(3)	8.33	18.48±4.02	12.54± 0.08	–	–	–
Q2231−00	2	2.066123(5)	...	5.41± 0.85	12.63± 0.03	12.42 ± 0.07	11.57± 0.35	(0.36, 0.05)
J2340−00	1	2.054156(4)	6.25	1.14± 1.34	12.167 ± 0.047	11.745 ± 0.165	<11.36	(0.25, <0.10)
J2340−00	2	2.054284(4)	...	0.25 ± 0.29	12.288 ± 0.191	12.106 ± 0.101	<11.70	(0.34, <0.13)
J2340−00	3	2.054527(2)	...	2.90± 0.20	13.226 ± 0.026	12.931 ± 0.022	<11.64	(0.33, <0.02)
J2340−00	4	2.054611(3)	...	3.01 ± 0.68	12.987 ± 0.037	12.519 ± 0.065	12.003 ± 0.079	(0.24, 0.07)
J2340−00	5	2.054716(1)	...	2.86 ± 0.22	13.200 ± 0.010	12.917 ± 0.014	12.017 ± 0.069	(0.33, 0.04)
J2340−00	6	2.05500(2)	...	9.90 ± 2.13	12.496 ± 0.077	<11.85	11.797 ± 0.178	(<0.16, 0.14)
J2340−00	7	2.055128(4)	...	1.91 ± 1.34	12.298 ± 0.088	11.896 ± 0.104	11.329 ± 0.333	(0.26, 0.07)

[a] Instrumental FWHM

[b] f1 and f2 as defined in the text

•**DLA1331 + 17** : To maximize the UV coverage for DLA 1331+17, we used a Keck HIRES spectrum with instrumental resolution FWHM = 6.25 km s^{-1} in combination with a bluer UVES spectrum of resolution FWHM = 7.0 km s^{-1} kindly provided by R. F. Carswell. This provided coverage of the maximum number of C I multiplets, down to the restframe C I λ1277 multiplet at observed wavelength $\lambda_{obs} \approx 3546$ Å. We included in the fit the following multiplets: C I λ1656, C I λ1560, C I λ1328, C I λ1280, C I λ1277.

Figure 3.1 contains the spectral data of DLA 1331+17, in black, overlaid with our fit, in red, and the C I fine structure lines marked. It is apparent from this figure that 1) in some cases the C I fine structure transitions fall so close to each other that they are blended, and 2) the multi-component velocity structure found in most DLAs further complicates the analysis. As shown in Figure 3.1, DLA 1331+17 requires three C I velocity components. Details of each component, i.e. the redshift, b value and C I column densities are given in Table 3.3. In this paper, we will focus on component 1, at z_{abs}=1.77637 or v = 0 km s^{-1} in Figure 3.1. We do this because this is the component in which we detect all three fine structure levels, C I, C I^*, and C I^{**} in absorption. Component 1 is the strongest component in terms of column density (see Table 3.3) with b $\approx$ 4.8±0.3 km s^{-1} . Component 2, at v ~17km s^{-1} , has a narrow velocity structure (b $\approx$ 0.6±0.22 km s^{-1}), making it interesting in its own right, and it will be discussed in detail in a separate paper (Carswell et. al., 2008). One broad component, at v ~20 km s^{-1} , with b $\approx$ 30.9 ±6.4 km s^{-1} , called component 3, does not exhibit measurable C I^* or C I^{**} absorption.

We can compare our results to another recent measurement of C I absorption in this system. Dessauges-Zavadsky et al. (2004) used VLT and Keck data to measure C I in two components, log N(C I) = 13.12±0.02 at z_{abs} = 1.776365 and log N(C I) = 12.72±0.02 at z_{abs} = 1.776523. While in the latter case, what we call component 2, their measurements agree with ours to within

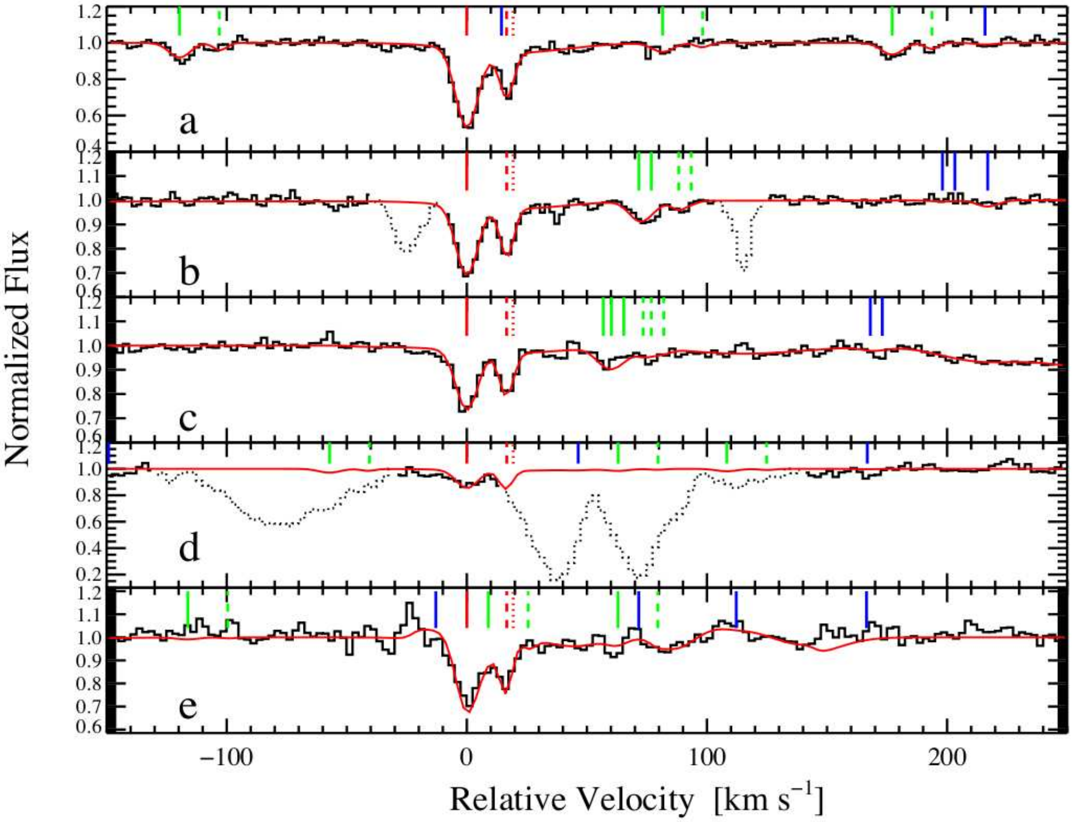

Figure 3.1: Spectral regions covering the five C I multiplets used in the analysis of DLA 1331+17: The multiplets are: **a)** 1656Å, **b)** 1560Å, **c)** 1328Å, **d)** 1280Å, and **e)** 1277Å. Black is the data, red is our fit. The different fine structure transitions are color coded: C I = red, C I* = green, C I** = blue, while the three velocity components are denoted by different linestyles: component 1 at v = 0km s^{-1} , or z$_{abs}$ = 1.77637 is solid, component 2 at v ∼17km s^{-1} , or z$_{abs}$ = 1.77652 is dashed, while component 3 at v ∼20 km s^{-1} , or z$_{abs}$ = 1.77659 is dotted. Interloper lines are denoted by dotted black lines.

1σ errors, the component 1 is in disagreement, with small errors, by 0.12 dex. However this difference is reasonable considering that they did not include fitting of the C I fine structure states which involve considerable blending with the resonance line.

We used AODM to measure log N(Si II) = 15.284 ± 0.004. From this we derive, in the minimal depletion model, the measured $\log(\frac{CII}{CI}) = 2.65\pm0.2$.

While the velocity structure of C I in DLA 1331+17 is well constrained by the fitting of many multiplets, it is also confirmed by the similar velocity structure seen in neutral chlorine, Cl I $\lambda1347$. Because of their similar ionization potentials, both below a Rydberg, C I and Cl I $\lambda1347$ are often observed to have the same velocity structure. This is shown in Figure 3.2 along with several other sub-Rydberg and low-ion transitions that trace the velocity structure of C I, namely, P II $\lambda1152$, S II $\lambda1250$, Mn II $\lambda2576$, and Mg I $\lambda2852$.

•**DLA 0812 + 32, $\mathbf{z_{abs} = 2.62633}$** : In this work we simultaneously fit data from two Keck HIRES runs with details given in Table 3.1. Both nights utilized the C1 decker giving an instrumental resolution of FWHM = 6.25 km s^{-1} . Eight multiplets were used to fit the C I fine structure lines; $\lambda1656$, $\lambda1560$, $\lambda1328$, $\lambda1280$, $\lambda1279$, $\lambda1277$, $\lambda1276$, and $\lambda1270$. The $\lambda1276 - \lambda1280$ multiplets were blended with a C IV doublet at $z_{abs} = 1.992$. Three C I velocity components are required to fit this DLA, see Figure 3.3. Component 1 at z_{abs}=2.625808 with b = 3.25km s^{-1} , or $v \sim -43$ km s^{-1} in Figure 3.3, is the weakest component and contains the largest errors. Component 2 at z_{abs}=2.626325 with b = 2.71km s^{-1} , is located at $v = 0$ km s^{-1} , and we measure an upper limit on N(C I**). Component 3 at $v \sim +14$ km s^{-1} has z_{abs}=2.626494 with b=0.38 km s^{-1} . The C I velocity profile of components 2 and 3 is traced by many more low ions, including Ge II $\lambda1237$, Cl I $\lambda1347$, and Zn II $\lambda2062$, see Figure 3.4, and even though it is blended with the stronger component 2, component 3 is necessary to obtain a good fit.

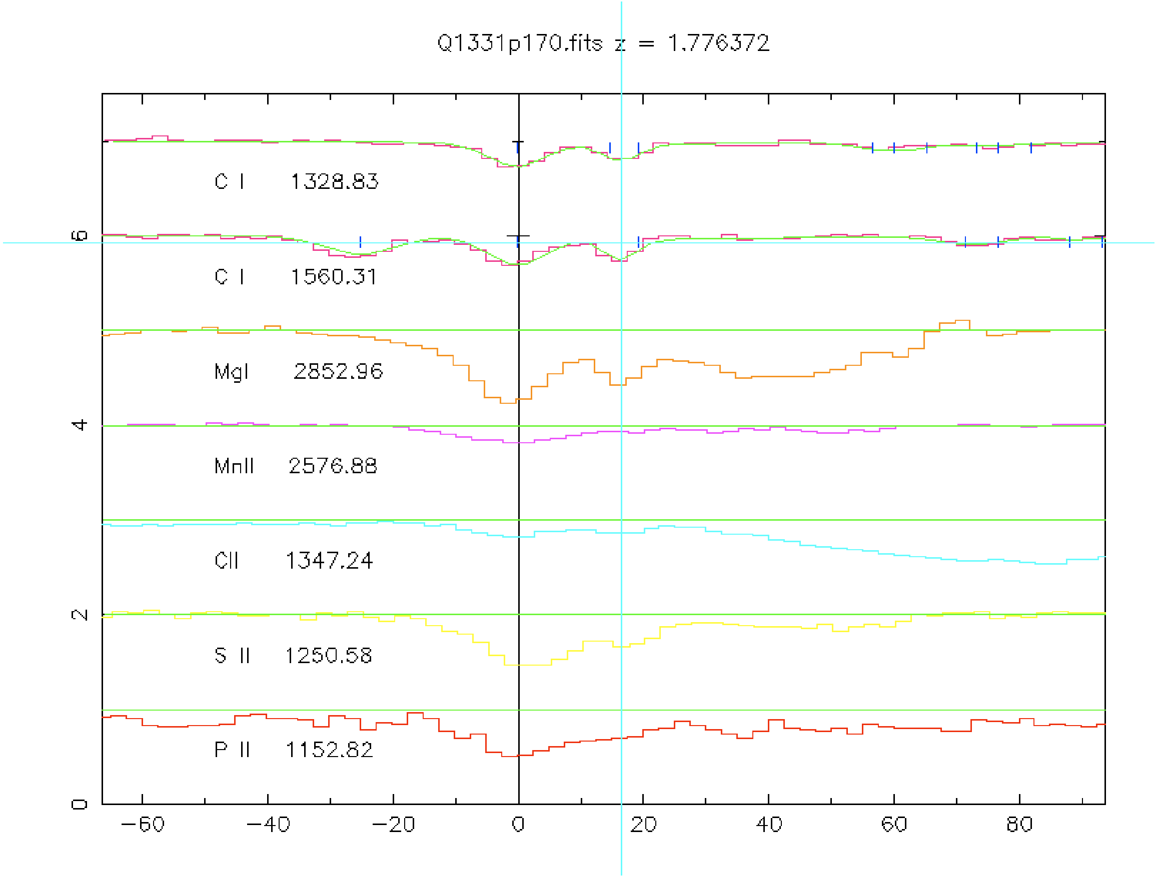

Figure 3.2: Other ions that trace the C I velocity structure of DLA 1331+17. The light blue vertical line marks the location of the narrow C I component. It is apparent that this component is seen in other low ions.

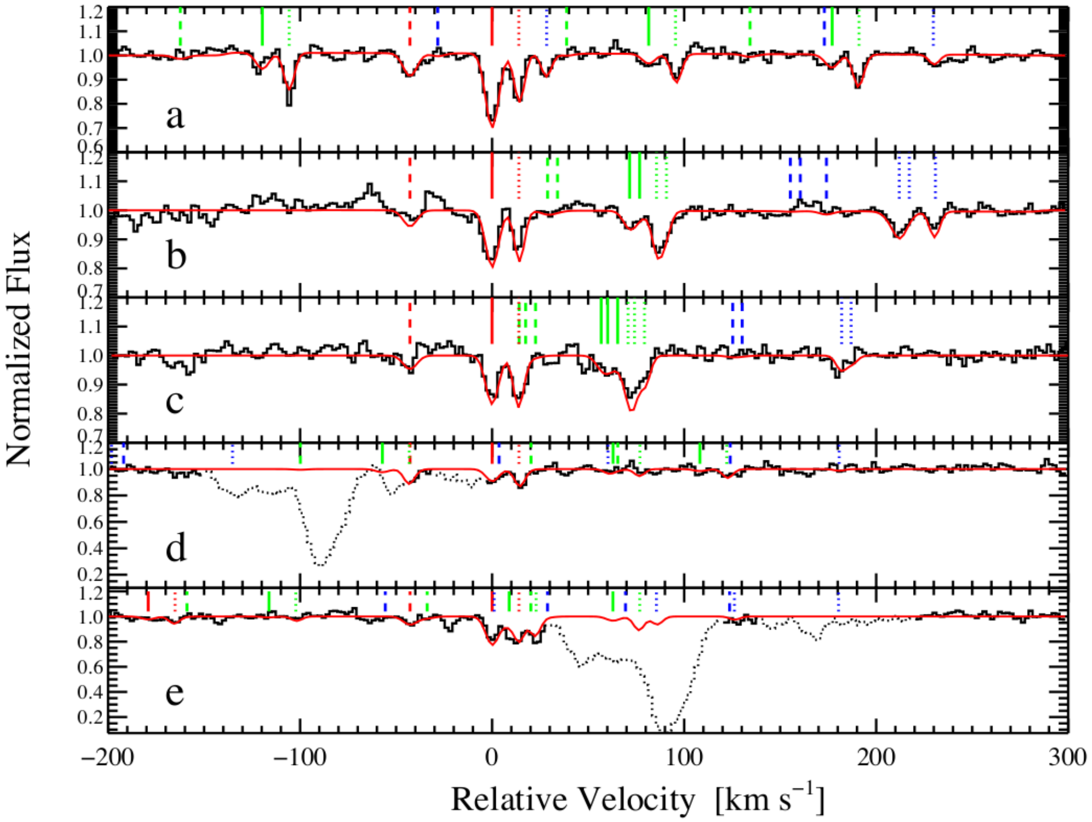

Figure 3.3: DLA 0812+32 C I velocity structure. Notation is explained in Figure 1. The multiplets shown are **a)** 1656Å, **b)** 1560Å, **c)** 1328Å, **d)** 1280Å, and **e)** 1277Å. Component 1 at $v \sim -43$ km s^{-1} , or z$_{abs}$=2.625808 has b = 3.25km s^{-1} . Component 2 is located at $v = 0$ km s^{-1} , or z$_{abs}$=2.626325 with b = 2.71km s^{-1} , while component 3, at $v \sim +14$ km s^{-1} , or z$_{abs}$=2.626494 is a narrow component with b=0.38 km s^{-1} .

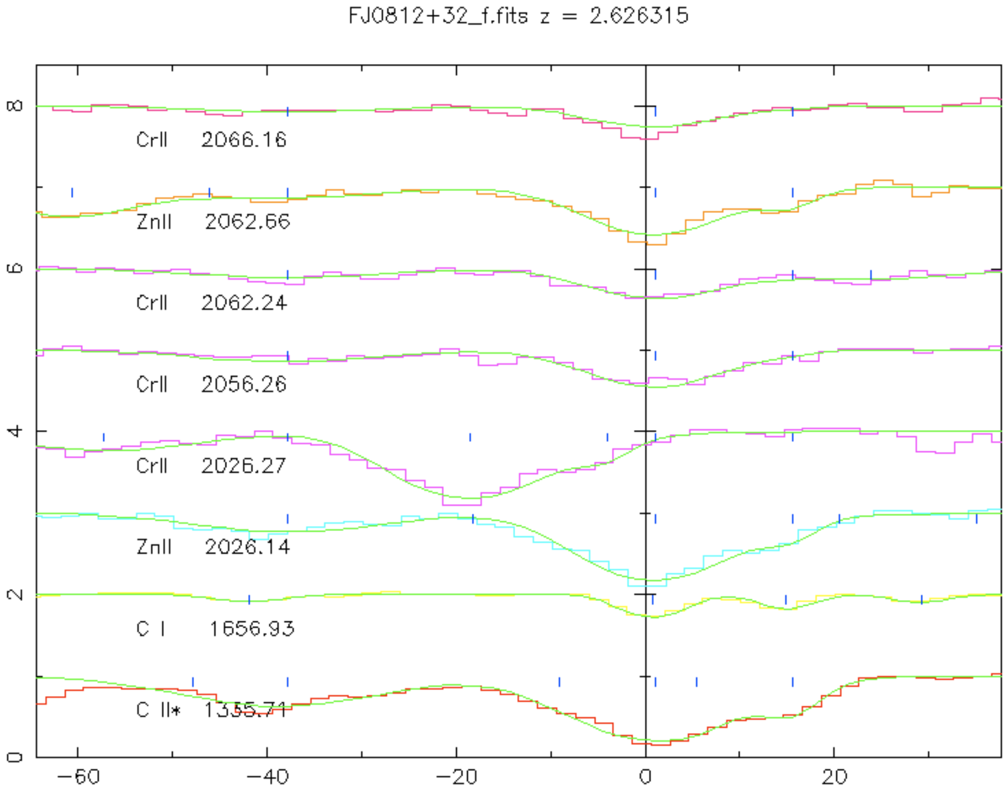

Figure 3.4: Low ions that trace the C I velocity structure of DLA 0812+32. Note that component 3 at ≈= + 15km s^{-1} is strong in Zn II but not in Cr II.

Component 3 is particularly interesting because its narrow velocity width allows for a strict (and cold) upper limit on the temperature of the gas. We discuss the curve of growth analysis of the following section (3.2.1). As in the case of the narrow component in DLA 1331+17 we can estimate the thermal temperature of the gas in this component using $T^{thermal} = 60$ A b^2 where A is the atomic weight. For Carbon, A = 12 and $T^{thermal} \leq\sim 104$ K (1σ).

We used AODM to measure Cr II, Zn II and C II* over the entire profile and report the results in Table 3.4. We note that this DLA also exhibits Cl I absorption that clearly traces the C I velocity profile, as expected (Jura 1974), lending confidence to our fit.

3.2.1 Curve of Growth Analysis of Component 3 of DLA 0812+32

Evidence of the reality of the narrow, unresolved component, component 3 in DLA 0812+32, can be seen in Figure 3.5, which shows the empirically derived curve of growth determined by an independent measurement of the equivalent widths of the C I transitions at $\lambda1656$, $\lambda1560$, $\lambda1328$, $\lambda1280$, and $\lambda1276$. The $\lambda1328$ line is blended with a C I* transition from another component and therefore is an upper limit. It is seen that a b value an order of magnitude larger (b = 3.8 km s^{-1}) will not fit the observed equivalent width ratios, and that even b = 0.88 km s^{-1} is not a good fit. We therefore take the best-fit value derived by VPFIT, b = 0.38 km s^{-1} , to be the true b value. We note that this small b value alone allows us to estimate the thermal temperature of the gas in component 3. Using $b = (\frac{2kT}{m})^{1/2} = 1.290 \times 10^4\ (\frac{T}{A})^{1/2}$ cm s^{-1} (Spitzer (1978), equation 3$-$21), or T = 60 A b^2 where A is the atomic weight. For Carbon, A = 12 and therefore, assuming the turbulent contribution is negligible, $T^{thermal}$ $\leq\sim$ 104 K.

In Figure 3.6 we show the results of a $\Delta\chi^2$ analysis of the C I equivalent widths of $\lambda1656$, $\lambda1560$, $\lambda1280$, and $\lambda1276$. We have excluded λ 1328 because

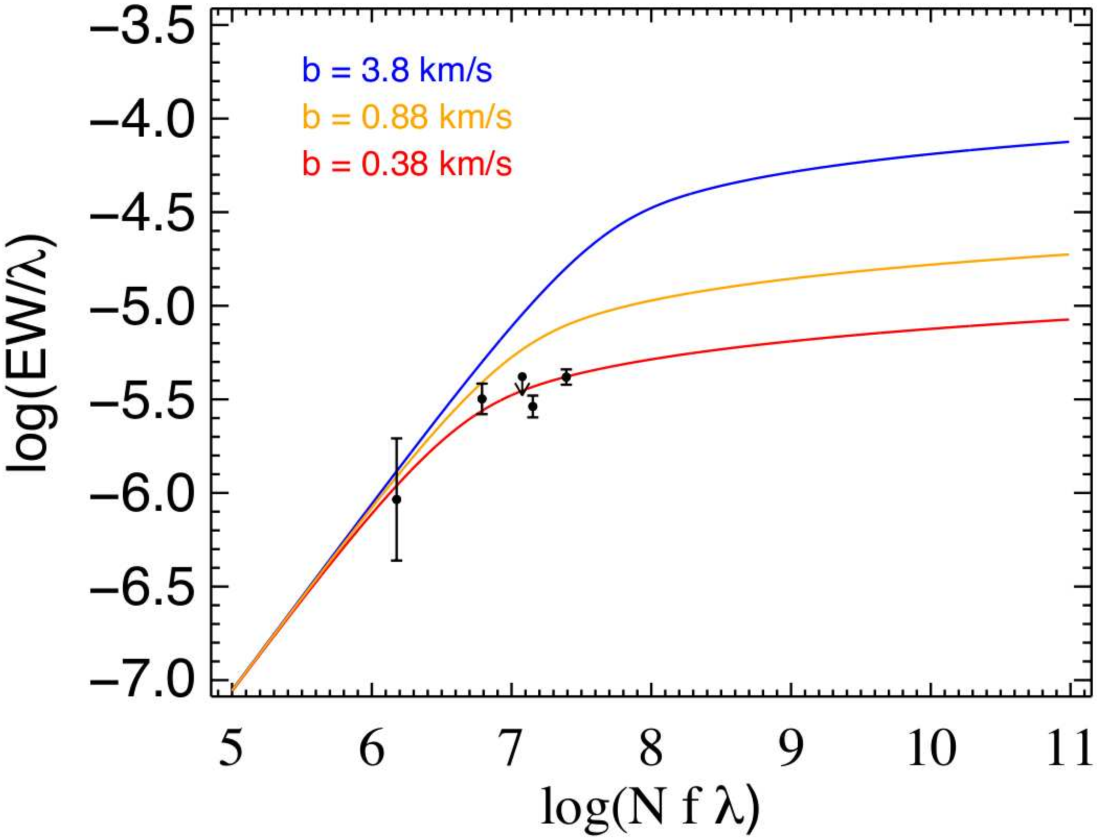

Figure 3.5: The empirically derived curve of growth. Equivalent widths were measured independent of VPFIT. The measurement of λ1328 is an upper limit because of blending with a C I* transition from another component. The measured b = 0.38 km s^{-1} is shown in red, while a curve representing b = 3.8 km s^{-1} , shown in blue, and b = 0.88 km s^{-1} shown in yellow, does not fit the data.

of blending. The 1σ, 2σ and 3σ contours are given in red, blue and purple respectively. It is clear from the figure that values of b $\sim$ 1km s^{-1} are excluded at the 3σ level, and even b $\sim$ 0.5km s^{-1} is not a good fit. The $\Delta\chi^2$ analysis results in a best fit of b = 0.34 km s^{-1} and logN(C I) = 13.01 cm^{-2}, denoted by the red asterisk.

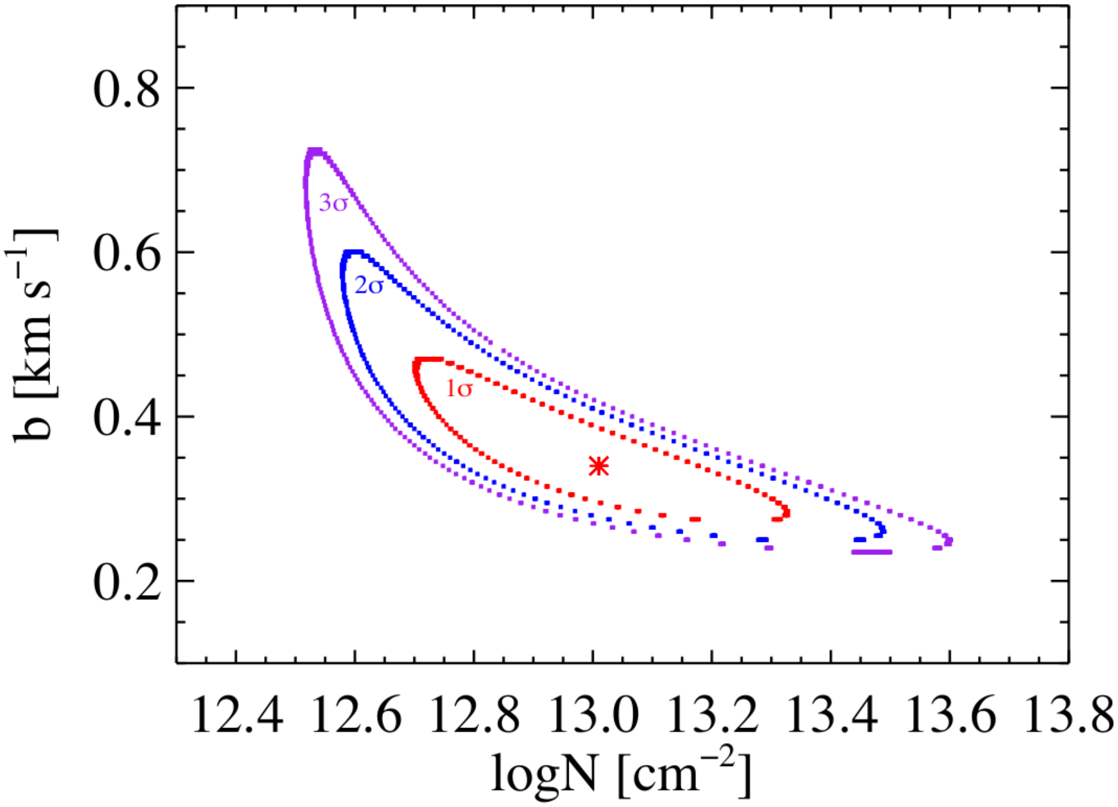

Figure 3.6: The $\Delta\chi^2$ test of the fitting of the equivalent widths of the narrow C I component (component 3) of DLA 0812+32 z_{abs}=2.626. 1σ (red), 2σ(blue) and 3σ(purple) contours are marked. It is seen clearly that b $<$ 1 km s^{-1} , and even b $<$ 0.5 km s^{-1} at the 1σ level. The best fit, denoted by the red asterisk, is given by b = 0.34 km s^{-1} and logN(C I) = 13.01 cm^{-2}.

Table 3.4: DLA PROPERTIES

Quasar	z_{abs}	logN(H I) [cm^{-2}]	logN(C II*) [cm^{-2}]	l_c [ergs s^{-1}H^{-1}]	[M/H]^a	[Fe/H]	logN(CI^{tot})	log $(\frac{C\,II}{C\,I})^b$ [cm^{-2}]	Δv [km s^{-1}]
FJ0812+32	2.06677	21.00 ± 0.10	13.12^c	-27.4^c	-1.380 ± 0.009	-1.611 ± 0.022	13.2293	2.7401 ± 0.20	26
...	...	...	13.92^d	-26.6^d	...	...	...	...	...
FJ0812+32^e	2.62633	21.35 ± 0.10	14.032 ± 0.006	-26.84 ± 0.10	$-0.814^e \pm 0.023$	$-1.617^f \pm 0.028$	13.5273	3.1987 ± 0.20	70
Q1331+17	1.77636	21.14 ± 0.08	<13.54^g	<-27.16	-1.416 ± 0.004	-2.022 ± 0.001	13.4642	2.6498 ± 0.20	72
Q2100−06	3.09237	21.05 ± 0.15	14.089 ± 0.006	-26.48 ± 0.15	-0.734 ± 0.15	-1.198 ± 0.02	–	–	187
Q2231−00	2.06615	20.56 ± 0.10	13.708 ± 0.035	-26.38 ± 0.11	-0.875 ± 0.020	-1.397 ± 0.066	13.0299	3.0451 ± 0.20	122
J2340−00	2.05452	20.35 ± 0.15	13.723 ± 0.012	-26.15 ± 0.15	-0.642 ± 0.151	-0.827 ± 0.035	13.8913	2.2067 ± 0.20	104

[a] M determined by Si II, S II, or Zn II

[b] N(CII) calculated assuming the "minimal depletion model" from Wolfe et al. (2004) where [C/H] = [Si/H] - 0.2. See text for details.

[c] Assume low cool DLA with average low cool ℓ_c. (The measured upper limit on log N(C II*) = 14.06, which includes blending)

[d] Assume high cool DLA with average high cool ℓ_c

[e] Global metallicity and ℓ_c based on Zn II and Cr II measurement.

[f] Based on Cr II instead of Fe II

[g] N(C II*) as determined by fitting constrained by SI II components. Blending means that this is still technically an upper limit.

•**DLA 0812 + 32, $\mathbf{z_{abs}}$ = 2.06677** : Data for this DLA is the same data used in the previous subsection, for DLA 0812+32, z_{abs} =2.62633. There is one C I velocity component in this DLA. To fit C I, we used only the λ1656 and λ1560 multiplets because of heavy blending with the Lyman α forest of the lower multiplets, see Figure 3.7. Using the AODM method we measure N(Si II) = 15.180±0.009 and $\log(\frac{CII}{CI})$ = 2.7401±0.2.

As is the case with many C I objects, DLA 0812+32 at z_{abs} =2.06677 also contains Cl I, with a single velocity component that closely matches that of C I. This increases our confidence in the C I results and the presence of cool gas in this DLA. It is interesting to note however that the centroid of the Cl I profile is displaced by ≈+5km s^{-1} with respect to $v = 0$ km s^{-1} at the C I centroid of z_{abs}= 2.066773. While this is unexpected, it appears that the centroids of the other sub-Rydberg and low-ions are also located at +5km s^{-1} with respect to C I (see Figure 3.8).

•**DLA 1755 + 578** : DLA 1755+578 contains 8 C I components, making it one of the most complex C I systems. It is interesting in its own right because we have discovered the presence of Si II* absorption in this DLA. While Si II* has been observed in GRB-DLAs (Prochaska et al. 2006), this is the first known case of Si II* observations in a high redshift QSO-DLA (Note that Lehner et al. (2008) present evidence for a WNM in a DLA at $z_{abs} \sim 2.4$). Because Si II* is generally thought to arise in warm gas – its excitation energy is 413K – this system is not only unique but also extremely interesting since it appears that several velocity components contain *both* C I and Si II* absorption, indicating that this is one of the rare DLAs exhibiting WNM gas at high z. We discuss this object in more detail in a future paper.

•**DLA 2100 − 06** : While this DLA exhibits measurable C I, our data are not of sufficiently high quality to measure the C I fine structure states. This is in part because the C I lines are not strong, and in part because the strongest

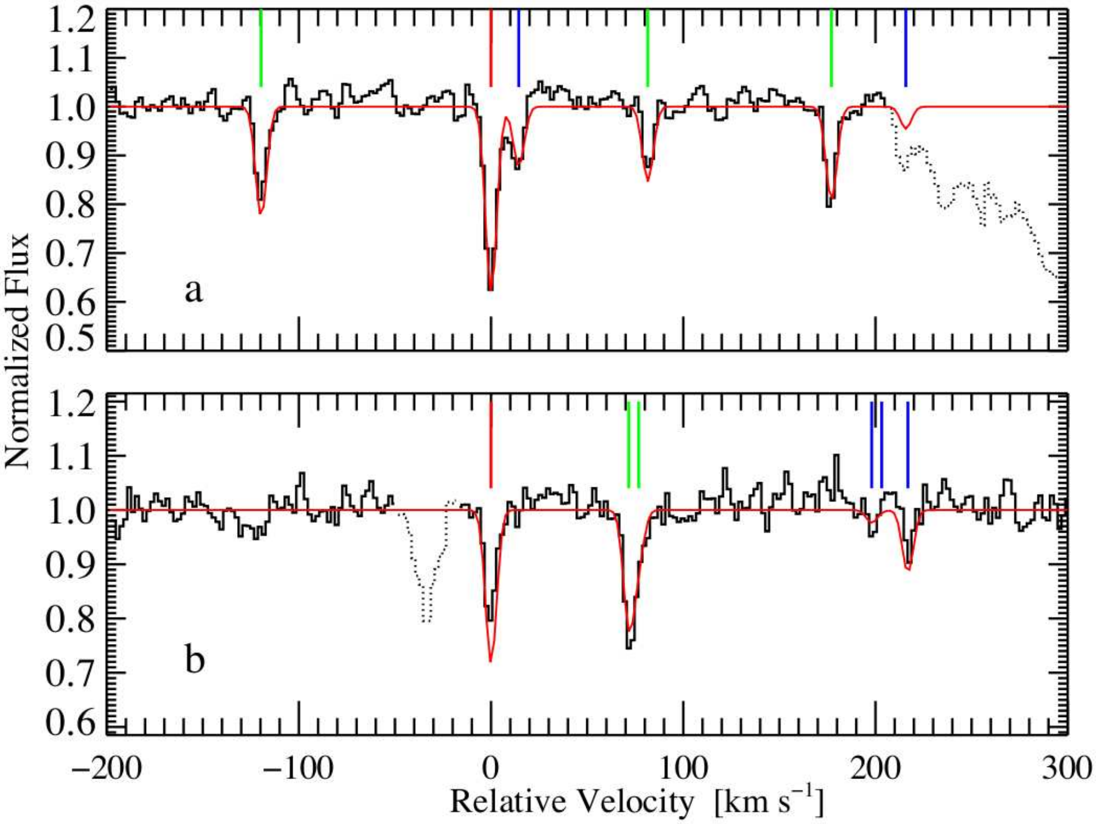

Figure 3.7: DLA 0812+32 z$_{abs}$=2.06 C I velocity structure. Only the 1656$\AA$ **(a)** and 1560$\AA$ **(b)** multiplets were used in the fit because of the serious blending with the Lyman α forest in lower wavelength multiplets. The single C I component is located at $v = 0$ km s^{-1} , with z$_{abs}$= 2.066773.

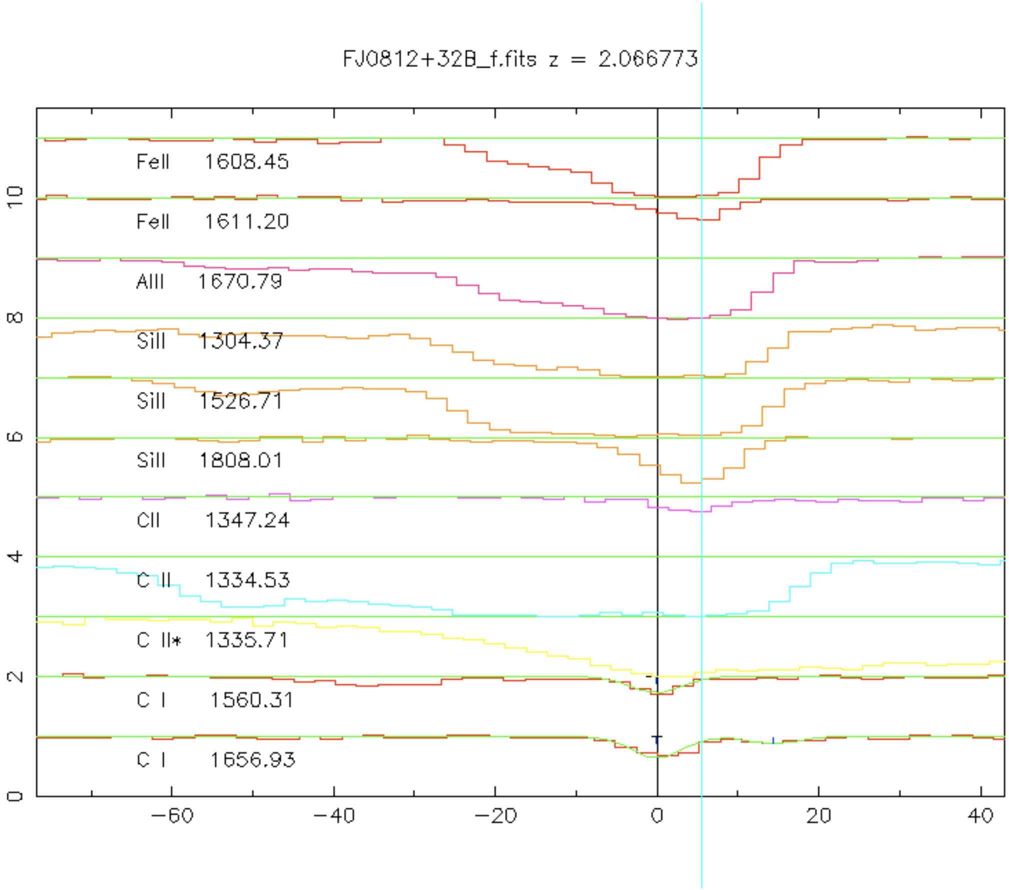

Figure 3.8: Detail of spectrum of DLA 0812+32 z_{abs}=2.06 C I velocity structure along with other low ions, to emphasize the velocity centroid discrepancy between C I, shown here at $v = 0$ km s^{-1} , and the other low ions, which are located ≈+5km s^{-1} with respect to the C I centroid. The difference is particularly pronounced in transitions Fe II λ1611, Si II λ1808, and Cl I λ1347.

multiplet, $\lambda 1656$, falls close to an order gap and as a result is contained in a lower signal to noise region. Therefore, we present only our measurements of N(C I) and N(C I*) in Table 3.3.

•DLA 2231 − 00 : Because the quasar emission redshift is z_{em}=3.02 and the absorption redshift is $z_{abs} = 2.066$, both the $\lambda 1328$ and $\lambda 1560$ C I multiplets fall in the Lyman-alpha forest. While most of the $\lambda 1560$ multiplet is unblended, the $\lambda 1328$ multiplet contains a blend with a large Lyman-alpha forest line. In our analysis we included only the $\lambda 1656$ and $\lambda 1560$ multiplets, see Figure 3.9. The best fit required two C I velocity components: component 1 at $v{\sim}{-77}$ km s^{-1} , or $z_{abs} = 2.06534$, with no measurable fine structure lines, and component 2 at $v{\sim}0$ km s^{-1} , or $z_{abs} = 2.0661223$, with detected C I fine structure lines. These two C I components trace the two strongest components of the other low ions, as seen in Figure 3.9 where component 1 is located at $v = 0$ km s^{-1} and component 2 is located at $v \sim +77$ km s^{-1} . We note that while the large error of N(C I**) measurement of component 2 indicates that it should probably be considered an upper limit, for the purposes of the present analysis we will treat the value as a detection. Using AODM we measure N(Si II) = 15.245±0.02, and log $(\frac{CII}{CI}) = 3.0451 \pm 0.2$.

•DLA 2340 − 00 : The complex multi-component nature of the C I in this $z_{abs} = 2.054924$ DLA made it difficult to fit despite the fact that seven C I multiplets ($\lambda 1270$, $\lambda 1276$, $\lambda 1277$, $\lambda 1279$, $\lambda 1328$, $\lambda 1560$ and $\lambda 1656$) have been included in the fit. The $\lambda 1279$ multiplet was only partially used due to blending with interlopers. Seven C I components were required in the fit, see figure 3.10. The components are labeled components $1 - 7$ from lowest to highest relative redshift and located at the following velocities: $v \sim -36$ km s^{-1} , -23 km s^{-1} , 0 km s^{-1} , 9 km s^{-1} , 19 km s^{-1} , 47 km s^{-1} , 59 km s^{-1} . To determine upper limits for non-detected fine structure states, generally for N(C I**), we used VPFIT, which allows for an estimation of the 1σ upper limit by inserting a "reasonable

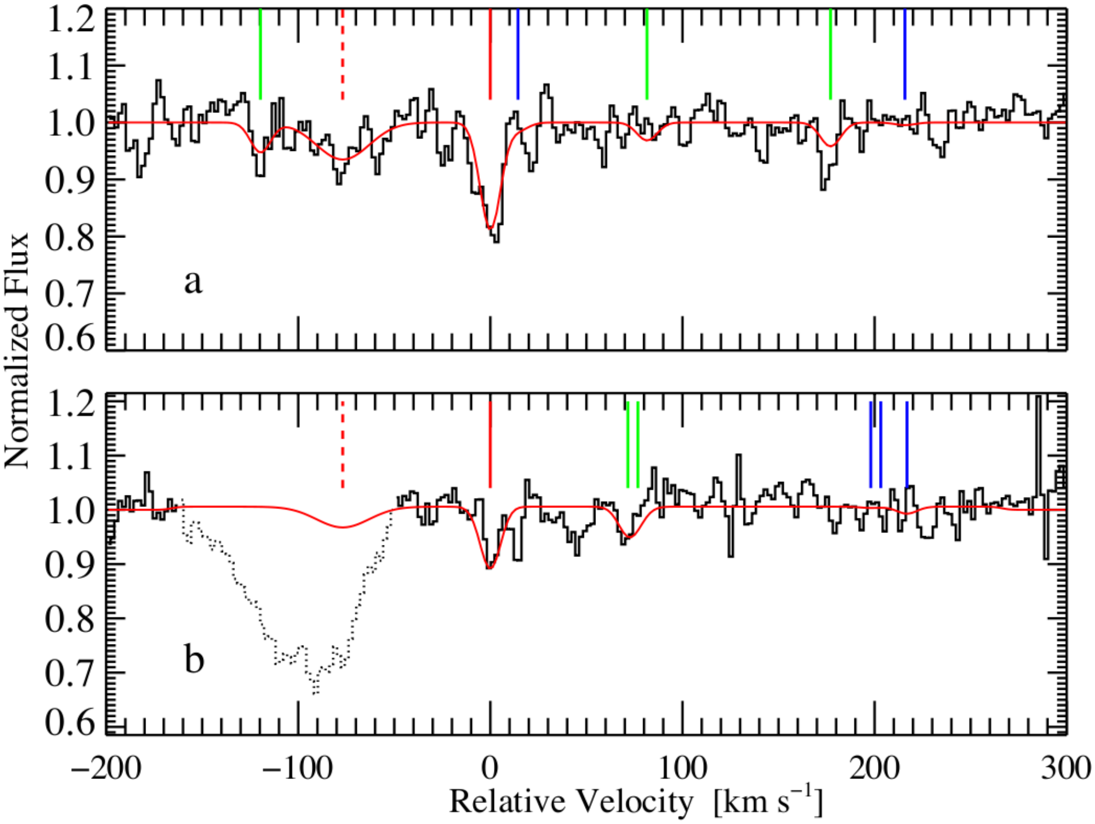

Figure 3.9: Spectra of DLA 2231−00 covering the 1656$\mathring{A}$ **(a)** and 1560$\mathring{A}$ **(b)** multiplets. The best fit required two C I velocity components: component 1 at $v\sim-77$ km s^{-1}, or z_{abs} = 2.06534, with no measurable fine structure lines, and component 2 at $v\sim0$ km s^{-1}, or z_{abs} = 2.0661223, with detected C I fine structure lines.

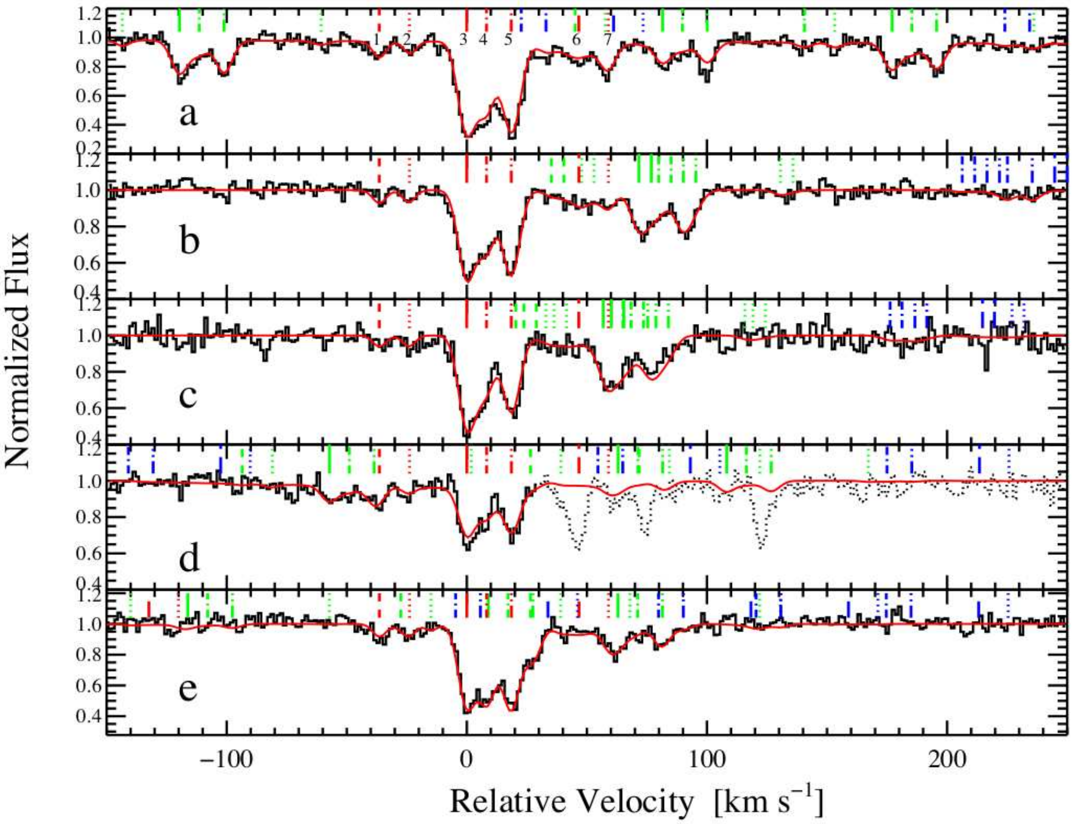

Figure 3.10: J2340 C I velocity profiles over five multiplets: **a)** 1656Å, **b)** 1560Å, **c)** 1328Å, **d)** 1280Å, and **e)** 1277Å. The components are labeled in **(a)**, from 1 − 7 from lowest to highest relative redshift and located at the following velocities: $v \sim -36$ km s^{-1} , -23 km s^{-1} , 0 km s^{-1} , +9 km s^{-1} , +19 km s^{-1} , +47 km s^{-1} , +59 km s^{-1} .

guess" of the column density and re-running the fit to give linear errors. The error is then taken as the 1σ upper limit. For a conservative reasonable guess we used the measured column density of the line with the smallest measured column density, usually N(C I*), since it is almost always the case that N(C I**) < N(C I*). This results in a conservative upper limit of the N(C I**).

DLA 2340−00 has a relatively high total column density of molecular hydrogen, logN(H_2) = 18.20 , giving an H_2 fraction f = 0.014, making it one of the few relatively H_2- rich DLAs. This DLA also contains Cl I that traces the components, lending confidence to the fit. This DLA also contains Phosphorus $\lambda 1152\AA$.

3.3 Applying the C I fine structure technique

3.3.1 The Steady State Equation

We developed an in-house code based on POPRATIO (Silva & Viegas 2001) to calculate the theoretical C I fine structure level populations by making the physically reasonable assumption of steady state. Following Silva & Viegas (2001) we considered spontaneous radiative decay, direct excitation by the CMB, UV pumping, and collisional excitation and de-excitation. As in POPRATIO, the rate equations leading to steady state populations of state i is given by

$$\sum_j n_j(A_{ji}+B_{ji}u_{ji}+\Gamma_{ji}+\sum_k n^k q^k_{ji}) = n_i \sum_j (A_{ij}+B_{ij}u_{ij}+\Gamma_{ij}+\sum_k n^k q^k_{ij}) \quad (3.1)$$

where A_{ij} are the spontaneous decay transition probabilities, B_{ij} are the Einstein coefficients, u_{ij} is the spectral energy density of the radiation field, Γ_{ij} is the indirect excitation rate due to fluorescence and is defined by Silva & Viegas (2001). The quantity n^k is the volume density of the collision partner k, where k = (H^o, n_e, n_p) and $q^k_{ij} = < \sigma v >$, is the collision rate coefficient. The reverse rates are calculated using the assumption of detailed balance. All coefficients were taken to be the same as those used in POPRATIO, with the exception of collisions with neutral hydrogen, for which we used the more recent rate coefficients calculated using the analytical formula by Abrahamsson et al. (2007) extended to the temperature range of T=10,000K. For the sake of simplicity, we did not consider excitation by collisions with either molecular hydrogen (H_2) or helium (He I). In the case of the former, the paucity of H_2 found in DLAs, at typical fractions of less than $\approx 10^{-5}$ renders the effect of collisions with H_2 so small as to be negligible. However, even in DLAs in which the H_2 fraction is relatively large (for DLA 1331+17, the molecular fraction was determined by Cui et al. (2005) to be f = 0.056 or 5.6%±0.7%), H_2 does not have a large effect on the collisional excitation of C I. [4] In the latter case of He I, collision rates are significantly lower than those of other partners. Additionally, the density of He I compared with that of H I is typically n(He I) = 0.0975 n(H I) (Anders & Grevesse 1989), making collisions with He I relatively unimportant.

Direct excitation by the CMB is calculated assuming the standard cosmology and a CMB temperature of $T = T_0(1 + z)$ where $T_0 = 2.725K$ (Mather et al. 1999). At high redshift, the CMB radiation generally has the strongest effect on the C I fine structure level populations because of the small temperature difference between the ground and first fine structure states. However, depending on the physical circumstances, other mechanisms such as UV pumping or collisions can dominate.

We included UV pumping due to a radiation field consisting of two components that we will call ${J_\nu}^{Bkd}$, and ${J_\nu}^{local}$, and let ${J_\nu}^{total} = {J_\nu}^{local} + {J_\nu}^{Bkd}$. ${J_\nu}^{Bkd}$ is the background radiation due to the integrated contribution from high z galaxies and quasars, known as the Haardt-Madau background (Haardt & Madau (1996): and more recently using CUBA[5]). In all cases, the minimum value of the total radiation field is determined by ${J_\nu}^{Bkd}$. In each case the value of ${J_\nu}^{Bkd}$ is calculated based on the redshift of the DLA, and evaluated at $1500\mathring{A}$. These values are summarized in Table 3.5. For an explanation of these values, see Wolfe et al. (2004) Figure 1. Because each C I -bearing DLA also contains strong C II*

---

[4] I.e. the rate of excitation due to collisions with neutral hydrogen at T=100K is $n^{H\,I}\ q_{01}^{H\,I} = 2.976 \times 10^{-10}$ n(H I) s^{-1}, where we use the conventional notation of representing C I, C I*, C I** by the indices 0, 1, 2 respectively. If we take the fraction of H_2 to be 5.6% of H I, the rate for collisions with H_2 is $n^{H2}\ q_{01}^{H2} = 6.7 \times 10^{-11}$ (0.056) n(H I) = 3.75×10^{-12} n(H I) s^{-1}, which is roughly two orders of magnitude smaller than $q_{01}^{H\,I}$.

[5] CUBA (F. Haardt & P. Madau 2003) is available at: http://pitto.mib.infn.it/ haardt/cosmology.html

λ1335.7 absorption, we used the C II* technique (see WPG03 and Wolfe et al. (2004)) to estimate the local radiation field due to star formation, ${J_\nu}^{local,C\,II^*}$, and included this contribution in the UV pumping. In general however, as shown in Figure 3.11, the radiation field must be relatively strong, i.e. $J_\nu > 10^{-18.5}$ergs cm^{-2} s^{-1} Hz^{-1} sr^{-1} , before it affects the C I fine structure level populations, and therefore, while we included the effects of the field for self-consistency, they were generally not significant, unless the star formation rate was high.

To quantitatively determine the effects of the radiation field on the C I fine structure level populations, we plot the $\frac{n(C\,I^*)}{n(C\,I)}$ and $\frac{n(C\,I^{**})}{n(C\,I)}$ versus neutral hydrogen density for excitation by a wide range of radiation fields in Figure 3.11.In this example we have considered collisions with neutral hydrogen at T=100 K, spontaneous radiative decay, and the excitation by the CMB at z=2, in addition to a radiation field of varying strengths as denoted in Figure 3.11. At low density, excitation by the CMB is dominant, unless the input UV radiation field is strong, in which case, the UV dominates. At higher densities, i.e. n(H I) > 10 cm^{-3}, collisional excitation becomes important and finally at n(H I) >∼1000 cm^{-3} the levels thermalize. In other words, at low densities the CMB sets the floor of $\frac{n(C\,I^*)}{n(C\,I)}$. Only when the radiation field exceeds a total strength of approximately ${J_\nu}^{total} \geq 10^{-18.5}$ ergs cm^{-2} s^{-1} Hz^{-1} sr^{-1}, does $\frac{n(C\,I^*)}{n(C\,I)}$ begin to significantly exceed that caused by the CMB alone. As a result, the Haardt-Madau background alone at a redshift of $z_{abs}\sim2$, has essentially no effect on the C I fine structure excitation. However, we include the backgrounds because they contribute significantly to the heating rate required to balance the ℓ_c cooling rates.

3.3.2 Steady State Solution

The steady state densities in each of the C I fine structure states are found by solving three homogeneous equations with three unknowns. To solve

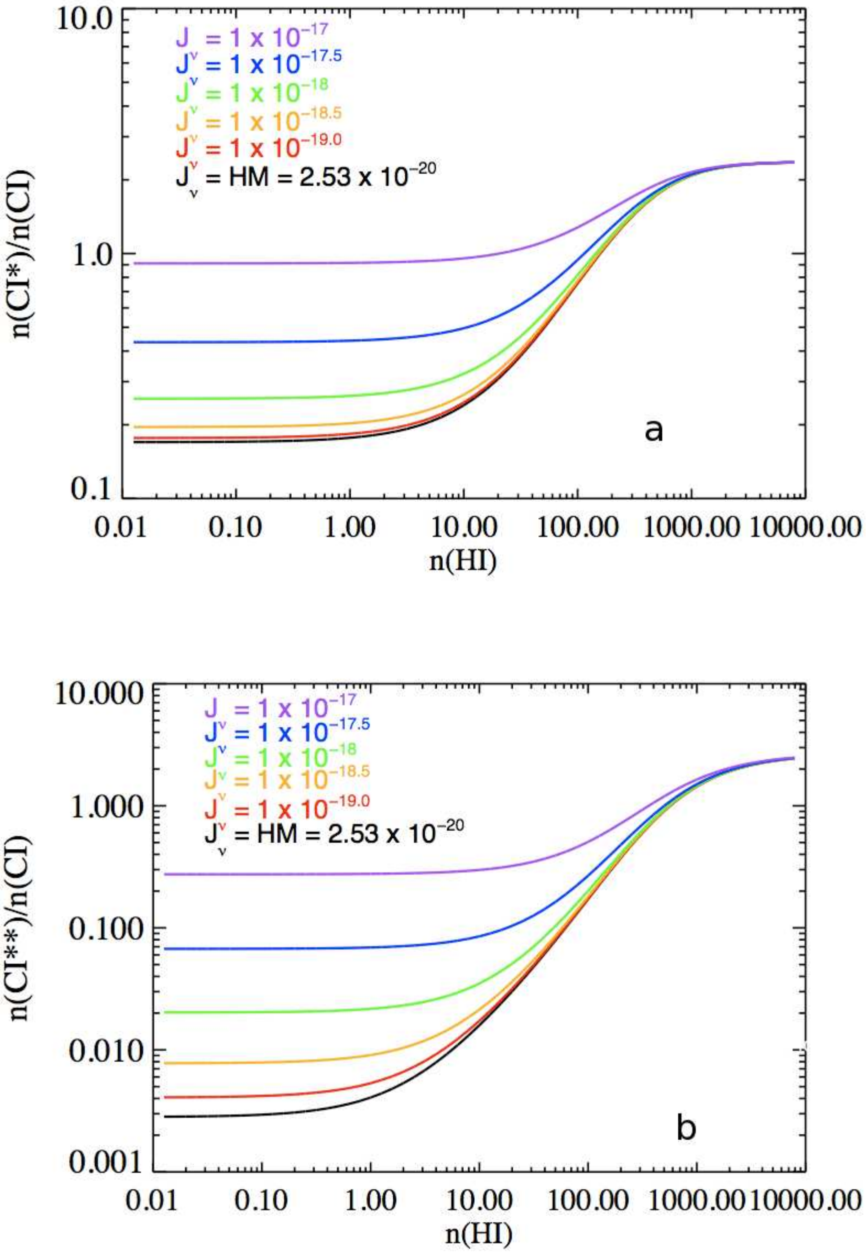

Figure 3.11: Excitation of the fine structure level C I* (plot a) and C I** (plot b) caused by increasing the strength of the radiation field. We plot the ratio $\frac{n(CI*)}{n(CI)}$ and $\frac{n(CI**)}{n(CI)}$ and have included spontaneous radiative decay, excitation by the CMB at z_{abs}=2, and collisions with neutral hydrogen at a temperature of T=100K.

Table 3.5. CII* TECHNIQUE SOLUTIONS

Quasar	z_{abs}	${J_\nu}^{local\ a}$ $/1\times10^{-19}$	${J_\nu}^{Bkdd}$ $/1\times10^{-20}$
FJ0812+32	2.06677	0.43^b	2.564
FJ0812+32	2.06677	3.46^c	2.564
FJ0812+32	2.06677	36.38^d	2.564
FJ0812+32^{global}	2.62633	7.17	2.454
FJ0812+32$^{comp1}_{div}$	2.62633	32.6	2.454
FJ0812+32$^{comp2}_{div}$	2.62633	14.8	2.454
FJ0812+32$^{comp3}_{div}$	2.62633	235.5	2.454
Q1331+17	1.77636	3.09	2.53
J2100−06	3.0924	17	2.329
Q2231−00	2.0661	24.7	2.564
J2340−00	2.05452	52.4^e,10.8^f	2.564

[a] Evaluated at 1500Å

[b] C II* in forest. Assumed low l_c=−27.4 and [Fe/Si]=0.0, the maximal depletion model

[c] C II* in forest. Assumed low l_c=−27.4 and [Fe/Si]=−0.2, the minimal depletion model

[d] C II* in forest. Assumed high l_c=−26.6 and [Fe/Si]=−0.2

[e] ${J_\nu}^{local}$ determined for components 3, 4, 5

[f] ${J_\nu}^{local}$ determined for components 6 & 7

the three homogeneous equations, we solve for the ratio of each excited state relative to the ground state. We denote all terms involving CMB excitation, UV pumping and collisions by the shorthand, $\mathrm{R}_{ij} = \mathrm{B}_{ij}\ \mathrm{u}_{ij} + \Gamma_{ij} + \sum_k n^k q^k_{ij}$ which is summed over the different collision partners, where all terms were defined in the previous subsection. Reverse reaction rates are calculated through the principle of detailed balance. As in equations 10 and 11 of Jenkins & Tripp (2001), solving the system of equations gives:

$$\frac{n(C\,I^{*})}{n(C\,I)} = \frac{(R_{0,1})(A_{2,1} + A_{2,0} + R_{2,1} + R_{2,0}) + (R_{0,2})(A_{2,1} + R_{2,1})}{(R_{1,2})(A_{2,0} + R_{2,0}) + (A_{1,0} + R_{1,0})(A_{2,1} + A_{2,0} + R_{2,1} + R_{2,0})} \tag{3.2}$$

and

$$\frac{n(C\,I^{**})}{n(C\,I)} = \frac{(R_{0,2})(A_{2,0} + R_{1,0} + R_{1,2}) + (R_{0,1})(R_{1,2})}{(R_{1,2})(A_{2,0} + R_{2,0}) + (A_{1,0} + R_{1,0})(A_{2,1} + A_{2,0} + R_{2,1} + R_{2,0})} \tag{3.3}$$

where the states C I, C I*, C I** are denoted by the indices 0, 1, 2 respectively. The resulting theoretical solutions are functions of the density of neutral hydrogen, n(H I), and the temperature. Following Jenkins & Shaya (1979) we define,

$$f1 = \frac{n(C\,I^{*})}{n(C\,I)_{tot}} = \frac{\frac{n(C\,I^{*})}{n(C\,I)}}{1.0 + \frac{n(C\,I^{*})}{n(C\,I)} + \frac{n(C\,I^{**})}{n(C\,I)}} \tag{3.4}$$

and

$$f2 = \frac{n(C\,I^{**})}{n(C\,I)_{tot}} = \frac{\frac{n(C\,I^{**})}{n(C\,I)}}{1.0 + \frac{n(C\,I^{*})}{n(C\,I)} + \frac{n(C\,I^{**})}{n(C\,I)}} \tag{3.5}$$

where $n(C\,I)_{tot} = n(C\,I) + n(C\,I^{*}) + n(C\,I^{**})$. We list the values of (f1, f2) for each DLA in Table 3.3.

In Figure 3.12 we plot the theoretical solutions in the (f1, f2) plane for the example case of DLA 1331+17. In this case, ${J_\nu}^{total,C\,II^{*}}$ as derived from the

C II* technique, is ${J_\nu}^{total,C\,II^*} = 3.3 \times 10^{-19}$ ergs cm^{-2} s^{-1} Hz^{-1} sr^{-1}. The solutions follow tracks, one for each temperature from T=10K − 10,000K increasing in steps of 0.1 dex. Along each track, n(H I) increases from $10^{-3.5}$ cm^{-3} to $10^{4.1}$ cm^{-3} in steps of 0.02 dex, each density being represented by an individual point. We chose the ranges of temperatures and densities to ensure that we had broad coverage of the entire plane of possible solutions. The data point at (f1, f2) ≈ (0.242, 0.045) is determined by our VPFIT fits to the data for component 1 (see Table 3.3). 1σ (2σ) errors are determined by calculating the values of f1 and f2 using the upper and lower allowed values as determined by the 1σ (2σ) error bars for each column density measurement. The resulting polygon defines a region of space in the f1 versus f2 plane that contains the acceptable 1σ(2σ) solutions. We show this in Figure 3.12 which contains both the 1σ, inner (red) polygon, and 2σ, outer (blue) polygon. In Figure 3.13 we plot the predicted theoretical solutions that fall within the 1σ (in red) and 2σ (in blue) error polygons of the data, on a graph of density versus temperature. These are the allowed density and temperature combinations derived from the C I data.

3.3.3 Ionization Equilibrium

To further constrain the C I solutions we introduce the assumption of ionization equilibrium and utilize the measured $\frac{C\,II}{C\,I}$ ratio, which we assume is equal to $\frac{n(C\,II)}{n(C\,I)} = \frac{N(C\,II)}{N(C\,I)}$. Ionization equilibrium is a reasonable assumption because the densities in these clouds are generally relatively high, thereby ensuring that the recombination times are shorter than the typical dynamical timescales. In basic form, ionization equilibrium can be written: n_e n(X$^+$) α = n(X) Γ, where α is the case A recombination coefficient of ion X$^+$ to X and Γ represents the ionization rate. From this equation we get, $\frac{n(C\,II)}{n(C\,I)} = \frac{\Gamma}{n_e \alpha}$, i.e. the ratio $\frac{C\,II}{C\,I}$ is a function of Γ, which is proportional to the radiation intensity, n_e, the electron density, and α, which is a function of temperature. Therefore, for a

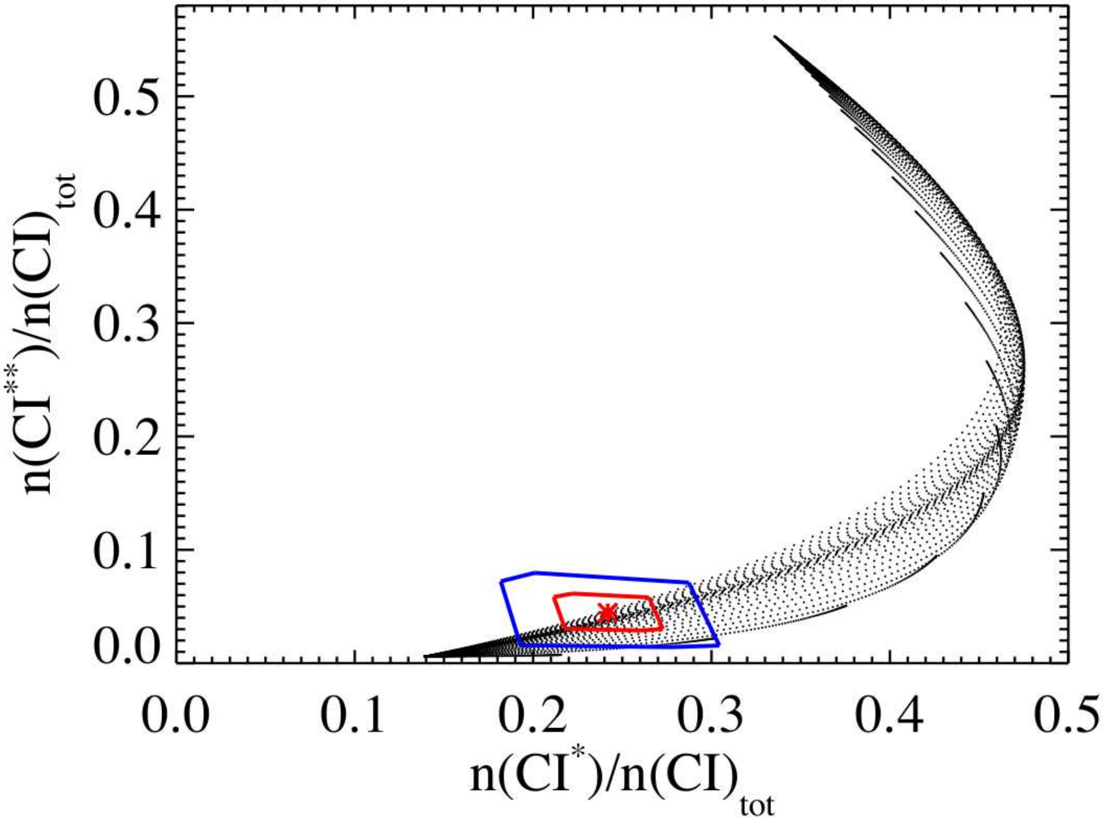

Figure 3.12: f1 verus f2 (denoted here as n(C I*)/n(C I)$_{tot}$ versus n(C I**)/n(C I)$_{tot}$) for component 1 of DLA 1331+17. The data point is marked by a red asterisk and the 1σ error polygon is marked in red, while the 2 σ error polygon is blue. Theoretical tracks are indicated by black points and run from T = 10 − 10,000 K and n(H I) = $10^{-3.5} - 10^{4.1}$ cm^{-3}.

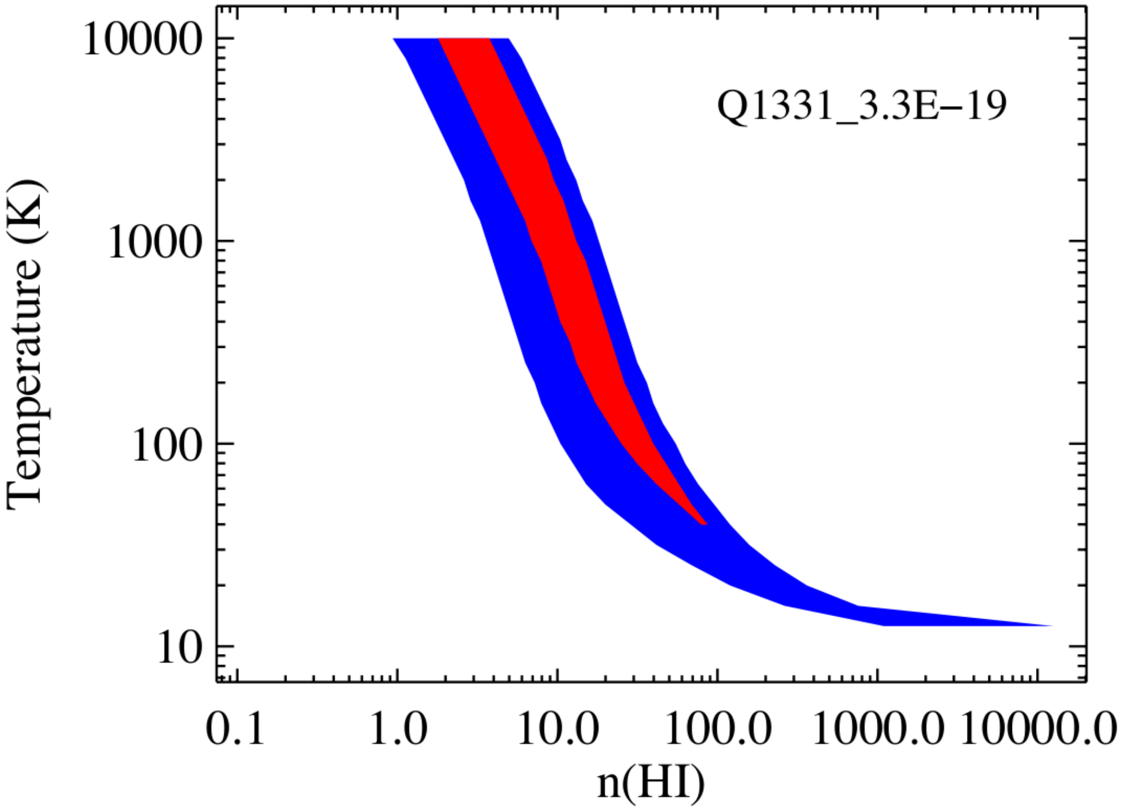

Figure 3.13: n(H I) versus temperature for the allowed solutions of DLA 1331+17 component 1. 1σ results are in red while 2σ is in blue.

given radiation field and temperature, we determine $\frac{C\,II}{C\,I}$ for a range of possible electron densities, n_e (Details of the ionization equilibrium are given in WPG03). We then use the measured $\frac{C\,II}{C\,I}$ of each DLA to constrain our allowed solutions. While we measure N(C I) directly, we must employ the conventional method of measuring N(C II) by proxy using N(Si II), because C II λ1334 is saturated in every DLA. We generally measure the Si II or S II and Fe II using the standard apparent optical depth method (AODM), which is well suited for cases such as these in which we have more than one transition of an ion. As in Wolfe et al. (2004) we let [C/H] [6] = [Si/H] + $[\mathrm{Fe/Si}]_{int}$ where the intrinsic (nucleosynthetic) ratio $[\mathrm{Fe/Si}]_{int} = -0.2$ for a minimal depletion model or $[\mathrm{Fe/Si}]_{int} = 0.0$ for a maximal depletion model. The minimal depletion model assumption is derived from the measurements of [Fe/Si] in 56 DLAs, which show that as metallicity decreases, the [Fe/Si] ratio asymptotically approaches [Fe/Si] = −0.3, (see Figure 8 of Wolfe, Gawiser, & Prochaska (2005)). This implies that the intrinsic ratio is [Fe/Si] = −0.3, rather than 0, which would indicate a solar ratio. The adoption of $[\mathrm{Fe/Si}]_{int} = -0.2$ is a conservative upper limit on this value. We follow Murphy & Liske (2004) and adopt the minimal depletion model in this work, and analyze the implications of the minimal versus maximal depletion model in section 3.5.1. While Wolfe et al. (2004) estimate the error in the measurement of $\frac{C\,II}{C\,I}$ to be 0.1 dex, we use the more conservative estimate of 0.2 dex.

To demonstrate the constraints imposed by ionization equilibrium, in Figure 3.14 we plot the C I solutions in terms of n(H I) versus $\log(\frac{C\,II}{C\,I})$. The measured $\log(\frac{C\,II}{C\,I})$, which in the example case of DLA 1331+17 is $\log(\frac{C\,II}{C\,I})=$ 2.65, is indicated by the red dashed line with a range of ±0.2 dex indicated by green dashed lines. It is obvious that the region of allowed C I fine structure solutions is further constrained by invoking ionization equilibrium. In this particular case, it is seen that there are no acceptable 1σ (red) solutions. For clarification,

---

[6] The abundance ratio with respect to solar is defined as [X/Y] = log(X/Y) - $\log(X/Y)_\odot$

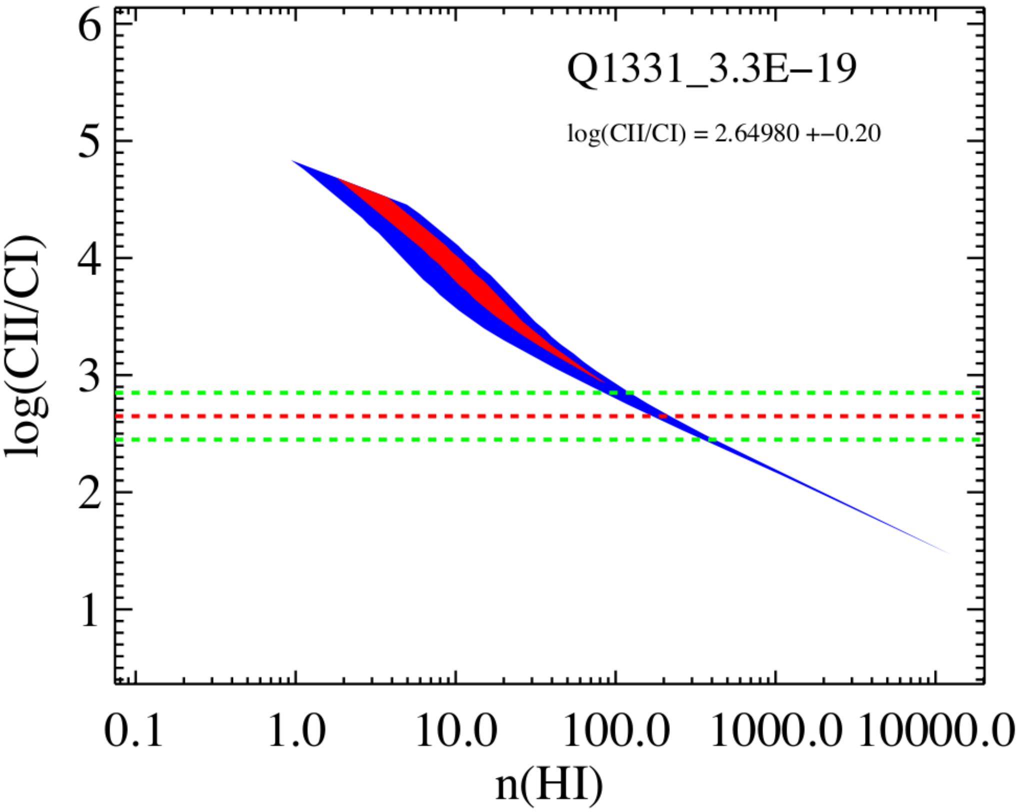

Figure 3.14: n(H I) versus $\log(\frac{C\,II}{C\,I})$ for the allowed solutions of DLA 1331+17 component 1. The measured $\log(\frac{C\,II)}{C\,I})$ is indicated by the red line with dashed lines indicating the errors of ±0.2 dex.

in Figure 3.15 we re-plot the density versus temperature diagram, however now we denote the final solutions, those constrained by the $\frac{C\,II}{C\,I}$ ratio, in yellow. As a result, invoking ionization equilibrium results in even tighter constraints on the densities and temperatures of the C I -bearing cloud.

Using Ionization Equilibrium to Constrain the Radiation Field

Until now we have assumed the UV radiation field due to star formation, $J_\nu{}^{local}$, is determined by the C II* technique. We will now relax this constraint and allow the input local radiation field to vary, repeat the above analysis for

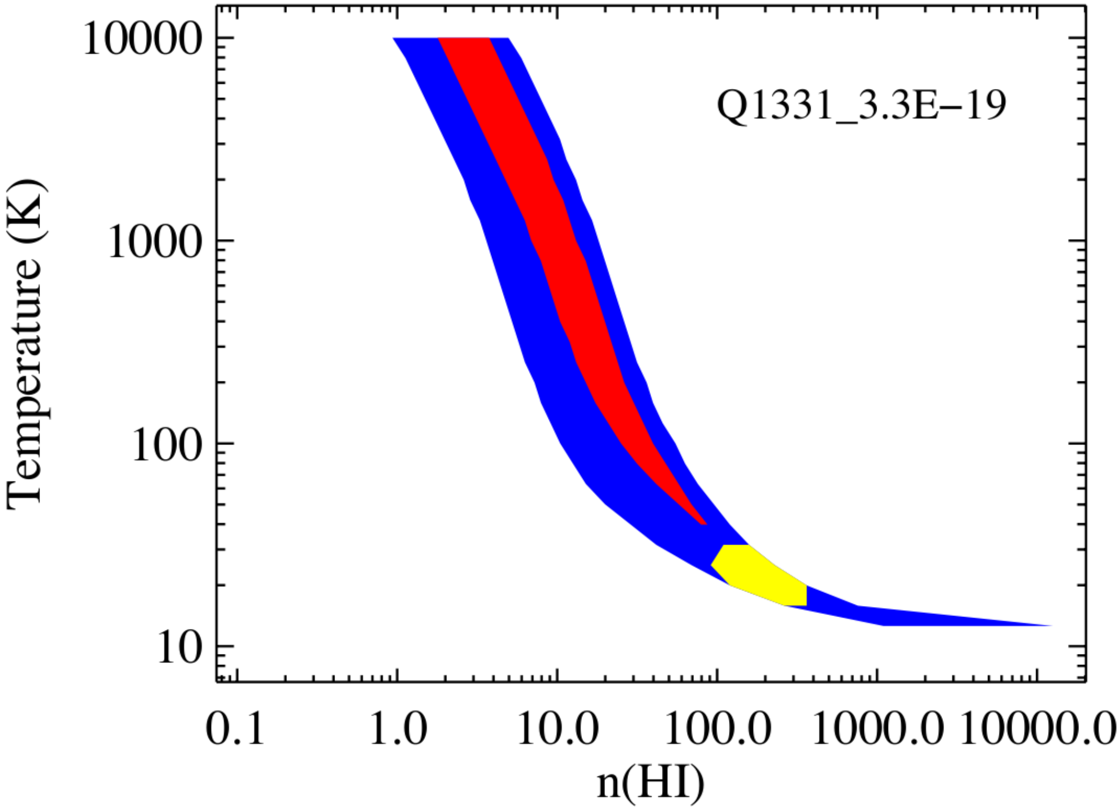

Figure 3.15: n(H I) versus temperature for the allowed solutions of DLA 1331+17 component 1. The final solutions, as constrained by $\frac{C\,II}{C\,I}$, are shown in yellow (2σ). There are no 1σ solutions.

each case, and examine the results as a function of radiation field. We show that for some C I -bearing clouds we can place upper and lower limits on the allowed radiation field utilizing only the C I fine structure data and the assumption of ionization equilibrium. We use a grid of ${J_\nu}^{local}$ values from ${J_\nu}^{local} \approx 10^{-21} - 10^{-16}$ ergs cm^{-2} s^{-1} Hz^{-1} sr^{-1}. To differentiate these radiation fields from those predicted by the C II* technique, we will call them ${J_\nu}^{local,C\,I}$. For each ${J_\nu}^{local,C\,I}$ we first add the ${J_\nu}^{Bkd}$ to obtain a ${J_\nu}^{total,C\,I}$, and then rerun the above analysis, calculating the f1 versus f2 tracks for each ${J_\nu}^{total,C\,I}$. We calculate the ionization equilibrium for each ${J_\nu}^{total,C\,I}$.

In Figure 3.16 we plot the 1σ C I results for our example case of DLA 1331+17 on a graph of $\frac{C\,II}{C\,I}$ versus n(H I) where for clarity we show only a sub-sample of the entire ${J_\nu}^{total,C\,I}$ grid results. Solutions corresponding to each ${J_\nu}^{total,C\,I}$ are represented by different colors. Again, we use the $\frac{C\,II}{C\,I}$ data to constrain the allowed solutions, and it is apparent that for ${J_\nu}^{total,C\,I} \geq\sim 3 \times 10^{-19}$ergs cm^{-2} s^{-1} Hz^{-1} sr^{-1}, there are no acceptable solutions. In Figure 3.17 (a) we plot $\log(\frac{C\,II}{C\,I})$ versus density for the entire ionization grid and in (b) we plot the allowed ${J_\nu}^{total,C\,I}$ values versus density (the 2σ solutions are given in (c) and (d)). We see clearly the limit ${J_\nu}^{total,C\,I} \leq \sim 3 \times 10^{-19}$ ergs cm^{-2} s^{-1} Hz^{-1} sr^{-1}. This limit on ${J_\nu}^{total,C\,I}$ is actually quite strict considering that the Haardt-Madau background is only ∼1 order of magnitude lower than this value. Our technique places an upper limit on the local radiation field, and hence the star formation rate, using only C I fine structure absorption and the assumption of ionization equilibrium, without invoking any assumptions about star formation from the C II* technique. Note that the strength of the radiation field as determined by the C II* technique, which for DLA 1331+17 is ${J_\nu}^{total,C\,II^*} = 3.3 \times 10^{-19}$ ergs cm^{-2} s^{-1} Hz^{-1} sr^{-1}, is just slightly higher than the 1σ limit derived independently from the C I data.

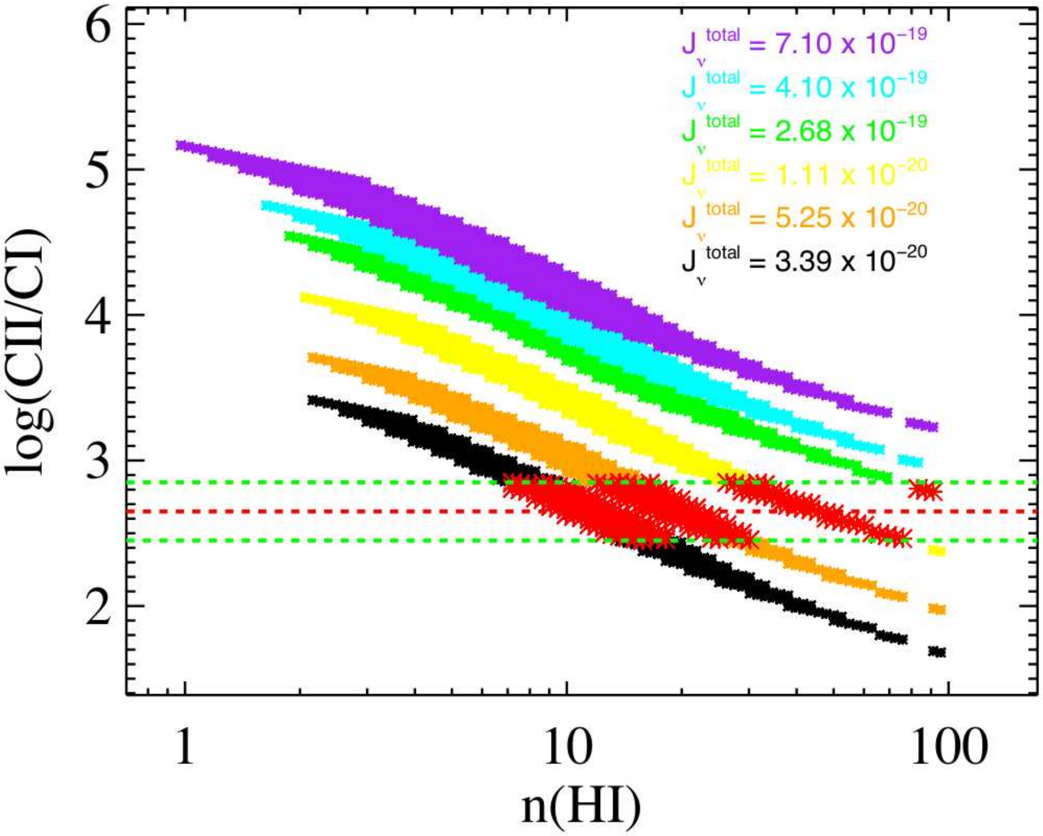

Figure 3.16: Plotting log($\frac{CII}{CI}$) versus n(H I) for a selection of J_ν values. Solutions falling within the allowed range of log($\frac{CII}{CI}$) are marked in red. It is seen that for ${J_\nu}^{total} >\sim 3\times10^{-19}$ ergs cm^{-2} s^{-1} Hz^{-1} sr^{-1}, there are no acceptable solutions. Note: This is for the 1σ C I solutions. It is also apparent that the range of allowed densities is constrained to be $5 \leq$ n ≥ 100 cm^{-3}.

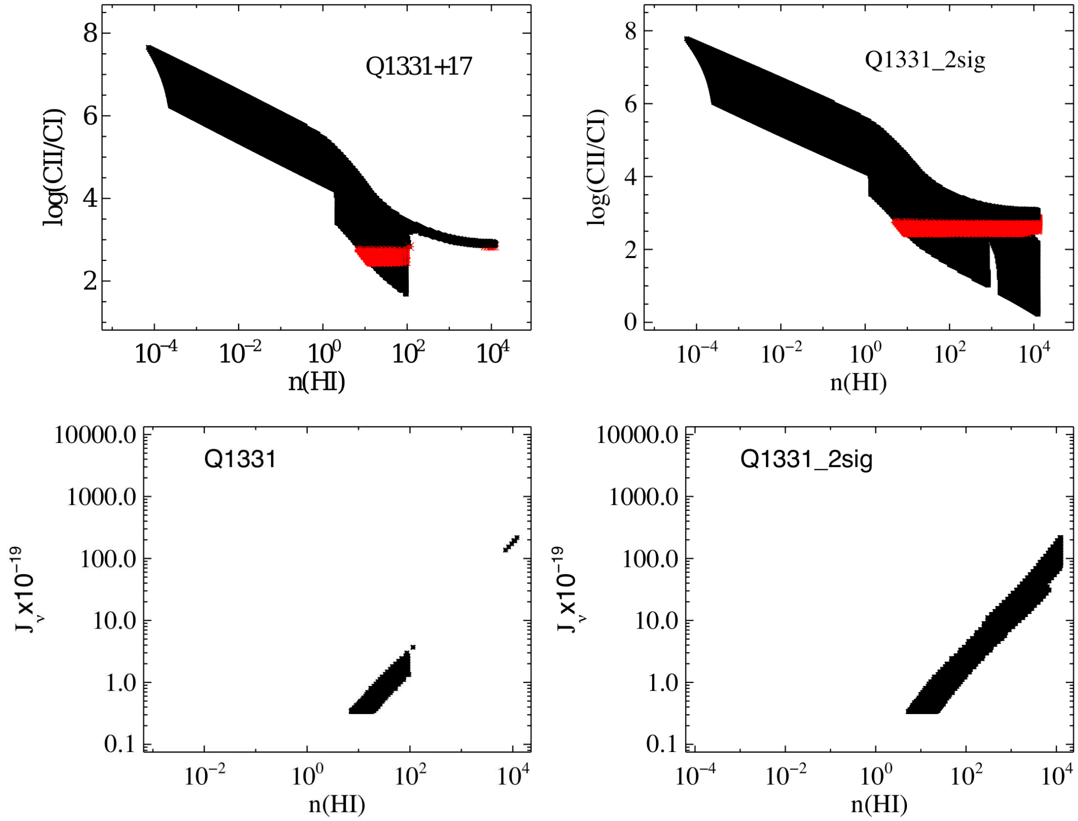

Figure 3.17: The top row shows $\log(\frac{C\,II}{C\,I})$ versus n(H I) for the entire range of J_ν values for DLA 1331+17. The 1σ C I results are on the left and $2\ \sigma$ C I results on the right. Solutions falling within the allowed range of $\log(\frac{C\,II}{C\,I})$ are marked in red. The bottom row shows the range of J$_\nu$s, versus density. It is seen that densities below about n $\sim$ 5 cm^{-3} are not allowed. Additionally, in the 1σ case the upper limit on ${J_\nu}^{total} \leq \sim 4\times10^{-19}$ergs cm^{-2} s^{-1} Hz^{-1} sr^{-1}, is a rather strict limit at only $\sim$1 order of magnitude above ${J_\nu}^{Bkd}$.

3.4 Results

We now briefly describe the results of each C I -bearing DLA. A summary of the details of each DLA are presented in the following tables: Table 3.3: a summary of the physical parameters inferred from C I fine structure measurements, Table 3.4: a summary of general DLA information, Table 3.5: the resultant radiation fields derived from the C II* technique, and in Table 3.6: the final C I fine structure solutions giving allowed ranges of densities, temperatures and pressures. Finally, in Table 3.7, we list the results of applying the grid of radiation fields and the constraints that the C I data provide on the total allowed radiation field.

Table 3.6: C I TECHNIQUE SOLUTIONS

DLA	**comp**	$J_\nu{}^{total}$ $/10^{-19}$	**log($\frac{C\,II}{C\,I}$)**	**1σ C I constraints**			**2σ C I constraints**			**best χ^2 fit**		
				n(H I) [cm^{-3}]	**T [K]**	**log(P/K) [cm^{-3}K]**	**n(H I) [cm^{-3}]**	**T [K]**	**log(P/K) [cm^{-3}K]**	**n(H I) [cm^{-3}]**	**T [K]**	**log(P/K) [cm^{-3}K]**
0812+32[a]	1	0.43[b]	2.9401±0.2	29−72	398− 2512	4.32−4.94	21−87	316−3162	4.06−5.16	63	501	4.50
0812+32[a]	1	3.46[c]	2.7401±0.2	158− 661	32−79	3.98− 4.42	138−758	25−126	3.76− 4.58	501	40	4.30
0812+32[a]	1	36.38[d]	2.7401±0.2	1738−10471	20−25	4.54−5.42	1445−10964	16−32	4.36− 5.44	2089	25	4.72
$0812+32_{global}$[e]	1	7.4	3.1987±0.2	46−158	25− 63	3.36−3.6	14−316	10− 200	2.16− 4.44	46	50	3.36
$0812+32_{global}$[e]	2[f]	7.4	3.1987±0.2	24−138	16− 40	2.68−3.48	14−138	10− 40	2.16−3.48	50	32	3.20
$0812+32_{global}$[e]	3	7.4	3.1987±0.2	66−251	40−126	3.72−4.10	55− 288	32−158	3.54−4.26	174	50	3.94
$0812+32_{div}$[e]	1	32.8	3.8243±0.2	6−44	10− 25	1.76−2.4	6−158	10−398	1.76−4.52	32	10	2.50
$0812+32_{div}$[e]	2	15	3.9268±0.2	2 −23	10− 63	1.36−2.86	2−23	10−63	1.36− 2.86	10	50	2.68
$0812+32_{div}$[e]	3	236	4.0763±0.2	none	–	–	–	–	–	–	–	–
1331+17	1	3.3	2.6498±0.2	–	–	–	91− 363	16− 32	3.36−3.86	110	32	3.54
2231−00	2	25	3.0451±0.2	138 −912	16− 40	3.34−4.36	87−1096	10−50	2.94−4.54	436	20	3.94
2340−00	1	0.39[g]	2.2067±0.2	1−66	10−794	1.16 − 4.46	1−69	10−794	1.16 −4.48	17	316	3.74
2340−00	2	”	2.2067±0.2	–	–	–	1−83	10−1000	1.16− 4.70	32	794	4.40
2340−00	3	”	2.2067±0.2	none	–	–	–	–	–	–	–	–
2340−00	4	”	2.2067±0.2	–	–	–	19−50	100−501	3.60 − 4.16	22	398	3.94
2340−00	5	”	2.2067±0.2	–	–	–	23−48	126−501	3.74 − 4.06	48	126	3.78
2340−00	6[h]	”	2.2067±0.2	none	–	–	–	–	–	–	–	–
2340−00	7	”	2.2067±0.2	10−63	50−794	3.10 − 4.44	1−158	10−2511	1.16− 5.32	20	398	3.90
2340−00	1	none[i]	–	–	–	–	–	–	–	–	–	–
2340−00	2	none[i]	–	–	–	–	–	–	–	–	–	–
2340−00	3	52.7	1.94046±0.2	none	–	–	–	–	–	–	–	–
2340−00	4	52.7	1.94046±0.2	none	–	–	–	–	–	–	–	–
2340−00	5	52.7	1.94046±0.2	none	–	–	–	–	–	–	–	–
2340−00	6[h]	11	2.46959±0.2	none	–	–	–	–	–	–	–	–

Continued on Next Page…

Table 3.6 – Continued

DLA	**comp**	$J_{\nu}{}^{total}$ $/10^{-19}$	**log**$(\frac{C\,II}{C\,I})$	**1σ C I constraints**			**2σ C I constraints**			**best χ^2 fit**		
				n(H I) **[cm^{-3}]**	**T** **[K]**	**log(P/K)** **[cm^{-3}K]**	**n(H I)** **[cm^{-3}]**	**T** **[K]**	**log(P/K)** **[cm^{-3}K]**	**n(H I)** **[cm^{-3}]**	**T** **[K]**	**log(P/K)** **[cm^{-3}K]**
2340−00	7	11	2.46959±0.2	7−120	10−158	1.82−3.98	7− 288	10− 631	1.82−5.0	29	79	3.36

---

[a] z_{abs}=2.06

[b] Maximal depletion model, assuming the low cool l_c; [Fe/Si] = −0.0

[c] The most likely model, Minimal depletion model , low l_c object with [Fe/Si] = −0.2

[d] Minimal depletion model, assuming high cool l_c object with [Fe/Si] = −0.2

[e] z_{abs}=2.62

[f] Using the 1σ upper limit on logN(C I**) < 11.39

[g] Minimum background assumption ∼Haardt-Madau for this object

[h] Upper limit on N(CI*)

[i] Solar (or super-solar) Fe/H precludes calculation.

3.4.1 DLA 1331+17

Background information on DLA 1331+17

Wolfe & Davis (1979) discovered 21 cm absorption towards QSO1331+17 at z_{abs}=1.77642, a similar redshift at which a DLA had previously been discovered at optical wavelengths (Carswell et al. 1975). They deduced a spin temperature of $T_s \approx 770 - 980$ K by combining the 21 cm line equivalent width with the N(H I) obtained from Lyman α absorption.

One of the first attempts to measure the CMB temperature at high redshift using C I was made by Meyer et al. (1986) using DLA 1331+17. They measured C I and put an upper limit on the ratio n(C I*)/n(C I) that allowed them put an upper limit on the temperature of the CMB, T_{CMB} <16 K at $z_{abs} = 1.776$. Later, Songalia et al. (1994) used the Keck telescope to make more precise measurements. They succeeded in measuring the C I* transition and derived a CMB temperature of T = 7.4 K that agreed well with the theoretical prediction. More recently, Cui et al. (2005) discovered an unusually high level of molecular hydrogen (H_2) in DLA 1331+17 using Hubble Space Telescope. They derive an excitation temperature of the H_2- bearing component of $T_{ex} = 152$ K. Additional evidence of cold gas in this DLA is Carswell et al.'s (2008) recent discovery of a narrow velocity component of C I that must be attributed to gas with T < 350 K (private communication, see upcoming paper).

DLA 1331+17, this work

As stated earlier, the results from fitting the C I fine structure lines are listed in Table 3.3. In the following we will discuss only component 1, at z_{abs} = 1.77636, the only component for which we measure all three fine structure states. The Haardt-Madau background at the redshift of this DLA is given by ${J_\nu}^{Bkd} = 2.53\times10^{-20}$ ergs cm^{-2} s^{-1} Hz^{-1} sr^{-1}. To estimate the contribution from

Table 3.7: 1 σ C I TECHNIQUE SOLUTIONS: FULL $J_{\nu}{}^{total}$ GRID

DLA	comp.	$\log(\frac{C\,II}{C\,I})$	n(H I) [cm^{-3}]	T [K]	log(P/k) [cm^{-3}K]	$J_{\nu}{}^{total}$ /1×10^{-19} [a]
0812+32[b]	1	2.7401±0.2	25− 12589	20− 3162	4.0−5.4	0.41− 190
0812+32[c]$_{global}$	1	3.1987±0.2	5−11479	10− 5012	2.72−5.06	0.33− 772
0812+32[c]$_{global}$	2	3.1987±0.2	3−549	10−3162	2.28−4.24	0.33− 39
0812+32[c]$_{global}$	3	3.1987±0.2	8−12586	10− 7943	3.10− 5.20	0.33− 772
0812+32[c]$_{div}$	1	3.8243±0.2	2−44	10 − 10000	1.4 − 4.7	0.66 − 37
0812+32[c]$_{div}$	2	3.9268±0.2	1− 42	10− 10000	0.9− 4.3	0.41− 24
0812+32[c]$_{div}$	3	4.0763±0.2	6− 275	10− 10000	2.4− 4.9	0.72−94
1331+17[d]	1	2.6498 ± 0.2	7− 12021	10− 1995	3.5− 5.1	0.34−220
1331+17[e]	1	2.6498 ± 0.2	7−114	32−1995	3.46−4.34	0.34−3.7
2231−00	2	3.0451±0.2	5−12587	10− 10000	3.2− 5.3	0.34−750
2340−00	1	2.42585±0.2	1−12588	10− 1995	0.72− 5.20	0.39−148.9
2340−00	2	2.42585±0.2	7−12588	10− 2512	3.00 − 5.40	0.39−148.9
2340−00	3	1.94046±0.2	132− 12588	13 − 32	3.62 −5.20	0.55−29.9
2340−00	4	1.94046±0.2	–	–	–	–
2340−00	5	1.94046±0.2	100−1585	16− 50	3.70− 4.40	0.4−5.5
2340−00	7	2.46959±0.2	6−12588	10−1995	3.06− 5.20	0.39−167

[a] [ergs cm^{-2} s^{-1} Hz^{-1} sr^{-1}]

[b] z_{abs}=2.06

[c] z_{abs}=2.62

[d] entire $J_{\nu}{}^{total}$ grid including unrealistically high density solutions.

[e] $J_{\nu}{}^{total}$ grid excluding the unrealistically high density solutions.

local starlight to the UV field we utilized the C II* technique. While WPG03 report logN(C II*) = 14.05±0.05 cm^{-2} for this object, the C II* transition is likely blended with a lyman alpha forest line because its velocity profile is very different from that of the low ions, see Figure 3.18. Generally, the C II* velocity profile traces that of low ions such as SiII λ1808. Therefore, we cannot exclude the possibility that the C II* transition is blended with a forest line, and we take the WPG03 value of logN(C II*) = 14.05±0.05 cm^{-2} as an upper limit. To obtain an estimate of the actual N(C II*), we (Carswell 2007; private communication) fixed the shape of the velocity profile to that of SiII λ1808 and normalized the C II* contribution by fitting the profile simultaneously with the Lyα line. Summing over the C II* components results in an estimate of the true N(C II*) of log N(C II*) < 13.54 cm^{-2}. Combining this estimate with the C II* technique we find a radiation field of ${J_\nu}^{local,CII^*} \approx 3.1\times 10^{-19}$ ergs cm^{-2} s^{-1} Hz^{-1} sr^{-1}. We shall assume the total input radiation field, that is, ${J_\nu}^{Bkd} + {J_\nu}^{local,CII^*}$, to be ${J_\nu}^{total,CII^*} \approx 3.3\times 10^{-19}$ ergs cm^{-2} s^{-1} Hz^{-1} sr^{-1}. The excitation rates due to the local star formation are $\Gamma_{01} = 1.37\times10^{-9}$s^{-1}, $\Gamma_{02} = 1.04 \times10^{-9}$s^{-1}, and $\Gamma_{12} = 4.56 \times10^{-10}$s^{-1}. These can be compared with those of the Haardt-Madau background at the redshift of this DLA that produces excitation rates $\Gamma_{01} = 1.12 \times10^{-10}$s^{-1}, $\Gamma_{02} = 8.48\times10^{-11}$s^{-1}, $\Gamma_{12} = 3.73\times10^{-11}$s^{-1}. Finally, the C I fine structure data constrained by ionization equilibrium, gives 2σ results of 16 K $\leq$ T $\leq$ 32 K, 91 cm^{-3} $\leq$ n(H I) $\leq$ 363 cm^{-3}, and 3.36 $\leq$ log(P/k) $\leq$ 3.86 cm^{-3} K .

We can compare our results to those of Cui et al. (2005), who used CLOUDY to derive a best fit model to their H_2 data that resulted in a hydrogen number density n(H I) $\approx$ 0.2 cm^{-3} and T $\approx$ 140 K for the H_2 bearing cloud at z_{abs} = 1.776553. This cloud is clearly not in pressure equilibrium with the C I cloud of our analysis, i.e. while the temperature is somewhat higher, the density is more than two orders of magnitude lower, resulting in pressures of P/k $\approx$ 28 cm^{-3}K for the H_2 -bearing cloud. The C I -bearing cloud more closely resembles

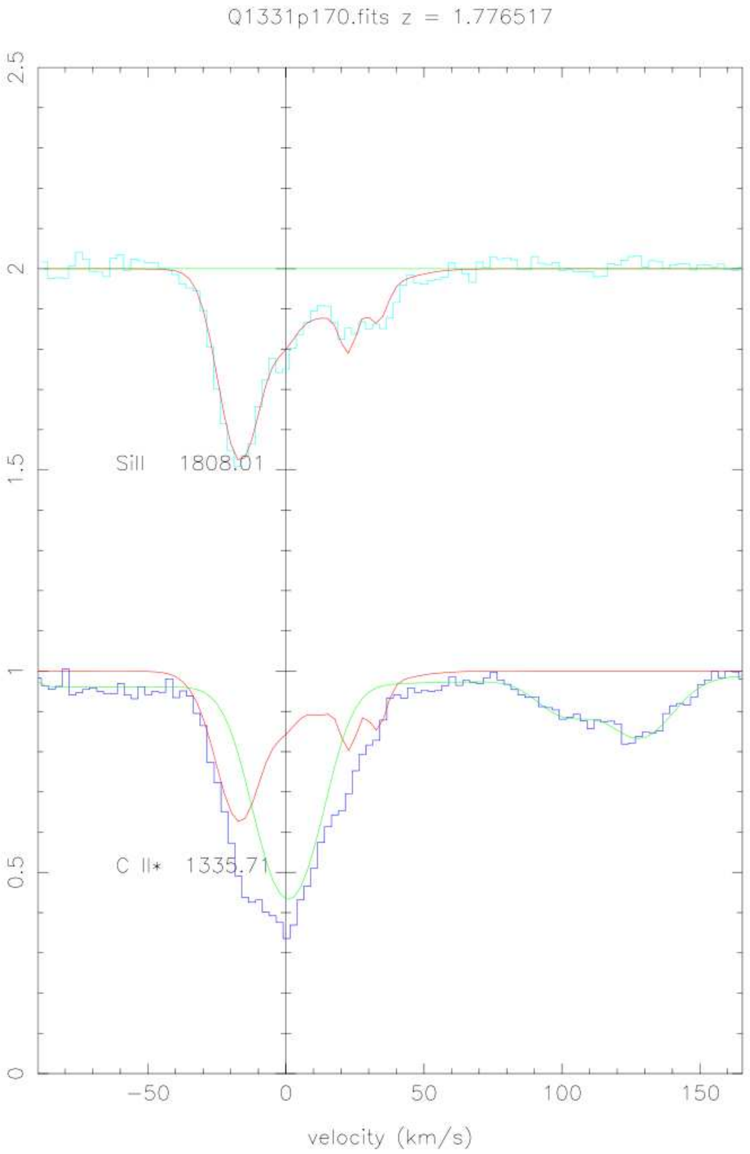

Figure 3.18: Velocity profiles of the low ions and C II* for DLA1331+17. Note, that the C II* profile is different from that of Si II 1808, indicative of blending with a Lyman-α forest line. We fit the line with C II* fixed in z and b to Si II to obtain a realistic value of the actual N(C II*), here shown in red, along with a Lyman α line in green. However, strictly speaking, because of the uncertainty caused by the likely blending, the C II* measurement is an upper limit (Figure courtesy of Bob Carswell).

the C I -bearing clouds in the local ISM as found by Jenkins & Tripp (2007) and Jenkins & Tripp (2001) with pressures of $10^3 < \mathrm{P/k} < 10^4$ cm^{-3}K with the distribution centered at P/k ≈ 2700 cm^{-3}K. We discuss these similarities further in section 3.5.3.

We can use the constraints on the volume density to estimate the physical size of the cloud. Using the neutral hydrogen column density logN(H I) = 21.14 cm^{-2} and for example, the average volume density n(H I)≈ 227 cm^{-3}, we can estimate the size of the C I -bearing cloud to be ℓ = N(H I)/n(H I) ≈ 6.1 $\times 10^{18}$ cm, or ≈ 2 pc (or ≈5 pc using our 2σ lower limit n(H I) = 91 cm^{-3}).

As previously mentioned, Cui et al. (2005) discovered an unusually high fraction of molecular hydrogen (H_2) in DLA 1331+17 using the Hubble Space Telescope. They detect a molecular fraction of 5.6%±0.7% in the component at z_{abs}=1.7766, which we note is a different component than the C I component discussed in this paper, component 1 at z_{abs}=1.77637 [7]. They determine a photoabsorption rate based on the population of H_2 in the J=0 and J=4 states, the latter of which is optically thin and therefore measures the intensity of radiation outside the cloud. Solving for this radiation field they get $J_\nu(\lambda = 1000\AA) \approx 6.7\times10^{-23}$ ergs cm^{-2} s^{-1} Hz^{-1} sr^{-1}, which is ≈ 400 times lower than the background. They do recognize that the radiation field as determined by the H_2 states is ∼3 orders of magnitude weaker than that determined by the C II* technique and comment that this is a discrepancy. More importantly however, this radiation field is ∼3 orders of magnitude below the Haardt-Madau background, which must be a lower limit to the radiation field. It is difficult to understand why the molecular hydrogen excitation is not consistent with this minimum radiation field. A solution exists however, if the bulk of the H_2 gas

---

[7] However, given the ambiguous nature of absorption line velocity profiles, we cannot say for certain that these components are physically distinct. Also, the precision of the redshift of the Cui et al. (2005) H_2 component is questionable, because if those lines are saturated, which they appear to be from their Figure 3, the redshift likely has a large error. They report z_{abs}=1.776553 ±0.000003 (1σ error), which we believe is an underestimate of the error.

resides in the narrow C I velocity component, i.e. component 2, and hence, has been missed because of the effects of hidden saturation. Carswell et al. (2008) have completed an analysis of this narrow component and include a detailed explanation of the H_2 data.

As discussed in section 3.3.3, we can relax the constraint of the radiation field as determined by the C II* technique and allow the field to vary. As we already showed for this DLA in section 3.3.3, at the 1σ level we can constrain the radiation field to ${J_\nu}^{total,C\,I}$ $<\sim 3 \times 10^{-19}$ ergs cm^{-2} s^{-1} Hz^{-1} sr^{-1}. Note that there exists a small set of solutions with T = 10 K, n(H I) = 7243$-$12021 cm^{-3}, and ${J_\nu}^{total,C\,I}$ $\approx$ 137$-$217 $\times 10^{-19}$ ergs cm^{-2} s^{-1} Hz^{-1} sr^{-1}, see Figure 3.17 (a). We exclude these solutions as unphysical because densities this high would imply an unrealistically small cloud size of $\sim$ 0.045 pc. Excluding the few unrealistic high points, we find that ${J_\nu}^{total,C\,I}$ $<\sim 3 \times 10^{-19}$ ergs cm^{-2} s^{-1} Hz^{-1} sr^{-1}. This limit on ${J_\nu}^{total,C\,I}$ is actually quite strong considering that the Haardt-Madau background is only $\sim$ 1 order of magnitude lower than this value. Note that the lower limit on the allowed ${J_\nu}^{total,C\,I}$ is fixed by ${J_\nu}^{Bkd}$. It is apparent from Figure 3.17 that the density is limited to the range, $7 \leq \sim$ n(H I) $\leq \sim 115$ cm^{-3} while the temperature is constrained to be 32 K $\leq\sim$ T $\leq\sim$ 2000 K, and the pressure 3.5 $\leq\sim$ log (P/k) $\leq\sim$ 4.3 cm^{-3} K. It is interesting to note that these limits are derived independent of the results of the C II* technique, using *only* the C I fine structure data and the assumption of ionization equilibrium for a range of possible radiation fields. In the case of the 2σ results, we are not able to place an upper limit on the radiation field, see Figure 3.17, however, we can place a lower limit on the density of n $\sim>$5 cm^{-3}. Although not apparent from the plot, we can also place an upper limit on the temperature of T $<\sim$2500 K.

3.4.2 FJ0812+32, z_{abs} =2.62633

DLA 0812+32 at z_{abs} =2.62633 has been studied extensively (see Prochaska et al. (2003)), and boasts one of the highest known DLA metallicities and H I column densities. Prochaska et al. (2003) used the many available transitions to show that the elemental abundance pattern is similar to that of the Milky Way. Because there are three distinct C I components in this DLA, we will analyze the C I fine structure levels in each component individually. However, we will apply the metallicity, N(C II), and N(C II*) measurements as determined by AODM over the entire (blended) profile of the low-ions, to each C I component. We measure log N(C II*) = 14.032±0.006 which along with the C II* technique determines that the radiation due to stars $J_\nu{}^{local,C\,II^*} = 7.17\times10^{-19}$ergs cm^{-2} s^{-1} Hz^{-1} sr^{-1}. Adding in the contribution from the background, $J_\nu{}^{Bkd} = 2.45 \times 10^{-20}$ergs cm^{-2} s^{-1} Hz^{-1} sr^{-1}, gives $J_\nu{}^{total,C\,II^*}$ $\sim$7.4$\times10^{-19}$ergs cm^{-2} s^{-1} Hz^{-1} sr^{-1}. We used this radiation field and the assumption of ionization equilibrium to determine solutions for the three C I components that are labeled 0812+32$_{global}$ in Table 3.6.

Relaxing the constraint of $J_\nu{}^{total,C\,II^*}$ as derived from N(C II*), we obtain the range of allowed solutions summarized in Table 3.8, again labled 0812+32$_{global}$. We can see that the density is constrained to be n $\geq$ 0.08 cm^{-3} and n $\geq$ 6 cm^{-3} for components 1 and 3 respectively. For component 2, we can place an upper limit on the temperature of $T \leq\sim$3200 K and a range of density n$\sim$0.7$-$550 cm^{-3}. In addition, the limit on the allowed $J_\nu{}^{total} \leq 3.9\times10^{-18}$ergs cm^{-2} s^{-1} Hz^{-1} sr^{-1}, approximately 100 times the background.

While this initial modeling was completed using the radiation field and metallicity as measured over the entire profile, it is clear upon careful inspection of the spectrum (see Figure 3.4), that the depletion, and hence, dust to gas ratio, is not constant over the three components. Specifically, component 3, the narrow component, contains obvious Zn II, C II* and C I, while it has no evidence

Table 3.8: 2 σ C I TECHNIQUE SOLUTIONS: FULL ${J_\nu}^{total}$ GRID

DLA	comp.	$\log(\frac{C\,II}{C\,I})$	n(H I) [cm^{-3}]	T [K]	log(P/k) [cm^{-3}K]	${J_\nu}^{total}$ /1×10^{-19} [a]
0812+32[b]	1	2.7401±0.2	18−12589	13−3981	3.74− 5.50	0.41−275
0812+32$^c{}_{global}$	1	3.1987±0.2	0.08−12587	10−10000	−0.12− 5.70	0.33−772
0812+32$^c{}_{global}$	2	3.1987±0.2	1−549	10−3162	0.98− 4.24	0.33− 39
0812+32$^c{}_{global}$	3	3.1987±0.2	6−12586	10−10000	2.94− 5.38	0.33 − 772
0812+32$^c{}_{div}$	1	3.8243±0.2	0.0007− 8316	10−10000	−2.15−5.42	0.34−819
0812+32$^c{}_{div}$	2	3.9268±0.2	0.01− 42	10−10000	−0.90−4.34	0.33− 24
0812+32$^c{}_{div}$	3	4.0763±0.2	3−479	10−10000	2.16−5.04	0.51− 149
1331+17	1	2.6498±0.2	5−12588	10− 2512	3.10−5.10	0.34−217
2231−00	2	3.0451±0.2	3−12587	10−10000	2.66−5.40	0.34−751
2340−00	1	2.42585±0.2	1−12588	10−1995	0.72−5.20	0.39−149
2340−00	2	2.42585±0.2	1−12588	10−1995	0.72− 5.20	0.39−149
2340−00	3	1.94046±0.2	40−12588	13−79	3.46− 5.20	0.39−30
2340−00	4	1.94046±0.2	33−199	32−200	3.60−3.94	0.39−1.4
2340−00	5	1.94046±0.2	39− 2630	16−158	3.66−4.62	0.39−7.7
2340−00	7	2.46959±0.2	0.4−12588	10−5012	0.64−5.60	0.39−167

[a] [ergs cm^{-2} s^{-1} Hz^{-1} sr^{-1}]

[b] z_{abs}=2.06

[c] z_{abs}=2.62

of Cr II. A natural explanation is that Cr is heavily depleted onto dust grains in component 3. By contrast, Cr II is detected in the other components.

DLA 0812+32: individual component analysis

If we analyze the metallicity and dust content in each of the three C I components individually, we find interesting results. Because Zn II and Cr II are not saturated and appear to trace the velocity structure of C I quite well, we use these ions to determine the metallicites and the dust-to-gas ratio in each component separately. To do this we first tie the redshifts and b values of each ion together and then use VPFIT to determine the column densities in each component. It is expected that Zn II and Cr II be tied together because they are both low-ion metal transitions and are likely to show the same physical/velocity structure. However, they will not necessarily exactly trace the C I, given that C I is affected by the incident ${J_\nu}^{total}$ and n_e, and if there is a gradient in ${J_\nu}^{total}$ or n, this could cause a difference between the structure of C I and the other low ions. We give the results of this fitting in Table 3.9.

Due to the nature of damped lines, we cannot use Lyman-α to determine the distribution of the neutral hydrogen among these components. Therefore, we assume that the N(H I) traces the low-ion metals, in this case Zn II, and that the neutral hydrogen is distributed proportionally to the metals. This results in each component having the same metallicity, [Zn/H] $= -0.18$. We note, that in theory, this metallicity should be the same as that determined for the global case. However, the individual component analysis revealed the presence of the narrow component 3 (with b $= 0.23\pm0.14$ km s^{-1} measured for the low ions – in agreement with the b $= 0.38\pm0.04$ km s^{-1} of the C I component, to within the error) that had been essentially missed by the AODM global measurement. Because of the narrowness of the component, the column densities are relatively large. In fact, the N(Zn II) measured in only the narrow

Table 3.9: DUST-TO-GAS RATIO COMPONENT ANALYSIS OF DLA 0812+32

	comp. 1	comp. 2	comp. 3
	z_{abs}=2.625858	z_{abs}=2.626327	z_{abs}=2.626503
	b = 12.58±2.93 [km s^{-1}]	b = 8.48±1.09 [km s^{-1}]	b = 0.23±0.14 [km s^{-1}]
N(Cr II) [cm^{-2}]	12.810 ±0.046	13.249 ±0.021	11.664 ± 0.390
N(Zn II) [cm^{-2}]	12.358 ±0.041	13.028 ±0.019	13.680 ±0.301
N(C II*) [cm^{-2}]	13.404 ± 0.043	13.771 ± 0.024	15.474 ± 0.111
N(H I)[a] [cm^{-2}]	19.924	20.594	21.246
$[Zn/H]$	−0.176±0.041	−0.176±0.019	−0.176±0.301
$[Cr/H]$	−0.744±0.046	−0.975±0.021	−3.212± 0.390
$[Cr/Zn]$	−0.568±0.062	−0.799±0.028	−3.036± 0.493
κ[b]	0.240	0.315	0.420
$\log_{10}\kappa$	−0.62	−0.50	−0.38
$\frac{CII}{CI}$	3.8243±0.2	3.9268±0.2	4.0763±0.2
l_c	−26.04	−26.34	−25.29
$J_\nu{}^{local}$ /10^{-19}[c]	32.6	8.3	235.5
f_{H_2}	7.2×10^{-5}	0.0193	0.0788
β_0 [s^{-1}]	3.53×10^{-11}	6.74×10^{-14}	1.00×10^{-14}
β_1 [s^{-1}]	5.97×10^{-11}	8.96×10^{-14}	6.24×10^{-15}
S_{self}	0.0778	0.00036	3.9×10^{-5}
S_{dust}	0.9826	0.8985	0.5218
S_{total}	0.0765	0.0003	2.04×10^{-5}
T_{ex}^{01} [K]	102	73	46
$J_\nu^{LW}/10^{-19}$[c]	0.37	0.17	0.39
n(H I)[d] [cm^{-3}]	24	10	5

[a] N(H I) scaled to trace N(Zn II)

[b] Dust to gas ratio relative to Milky Way, as defined in the text.

[c] [ergs cm^{-2} s^{-1} Hz^{-1} sr^{-1}]

[d] Density derived from the H_2 as explained in the text.

component, N(Zn II)^{component3} = 13.68 cm^{-2} , is greater than the N(Zn II)^{global} = 13.15 cm^{-2} measured over the entire profile in the global case. This is an example of hidden saturation – when narrow, unresolved components can contain large column densities of gas without being detected by AODM. However, we caution that unlike the C I component 3, for which we were able to measure distinct equivalent widths and perform the curve of growth analysis to confirm the sub-1 km s^{-1} nature of the profile, we are unable to independently measure the equivalent widths of component 3 of the metals because of blending with component 2. Despite this, it is apparent that component 3 lacks significant Cr II, indicating a high level of depletion, and consequently a higher dust-to-gas ratio than components 1 and 2. Following WPG03 (their equation 7) we define the dust to gas ratio relative to the Milky Way as follows,

$$\kappa = 10^{[Zn/H]_{int}}(10^{[Cr/Zn]_{int}} - 10^{[Cr/Zn]_{gas}}), \tag{3.6}$$

where "gas" is the abundance ratio in the gas phase and "int" is the intrinsic nucleosynthetic abundance. We calculate the dust to gas ratio in component 3 to be ∼40% of the Milky Way (log$\kappa = -0.38$). For comparison, Prochaska et al. (2003) measure $\kappa \sim 6\%$ (logκ=-1.24) over the entire profile of this DLA, and the typical dust to gas ratio in DLAs is ∼1/30 solar. We summarize information about each component in Table 3.9.

As we might expect, given that the column densities of all low ions with the exception of Cr II, but including C II*, are much higher in component 3, the $J_{\nu}{}^{local,CII^{*}}$ of component 3 deduced from the C II* technique is $1 - 1.5$ orders of magnitude larger than that determined for components 1 and 2. The $\frac{CII}{CI}$ increased as well, from $\log(\frac{CII}{CI}) = 3.2$ over the entire profile to $\log(\frac{CII}{CI}) \sim 3.8{-}4.1$ in the individual components. The results of the C I models for each component are presented in Table 3.6 where they are denoted by the subscript 'div'. Note that there are no acceptable C I solutions for the narrow component

3 because the radiation field predicted by the C II* technique is too high to be consistent with the measured C I fine structure excitation.

Relaxing the constraint of ${J_\nu}^{local}$ determined by the C II* technique, gives essentially no constraint on T or P at the 2 σ level and a constraint on the allowed radiation field in component 2 to be less than $\sim$ 24 times the galactic field and the density to be n = 0.01 − 42 cm^{-3}, see Table 3.8.

DLA 0812+32 Molecular Hydrogen

This DLA also shows evidence of relatively strong molecular hydrogen (H_2). We have used VPFIT to fit the H_2. Our method fixes the H_2 components to those of the low-ion metals, Zn II, Cr II and C II* in redshift (z) space, however, we were not able to obtain a good fit with the b values fixed as well and therefore, we allowed the b values of the H_2 components to vary independently of the b value of the metals. The H_2 is fit by three components whose redshifts roughly agree with those of the C I components, therefore, even though the b values are different from those of the C I components, we will refer to these H_2 components as components 1, 2, and 3, and assume that they are co-spatial with the C I components. While we do not understand why the b values of the H_2 would be different than that of C I, since C I and H_2 usually trace each other and the difference is not explained by the thermal effects caused by differences in masses, other observers have also found that the H_2 traces the redshift but not the b value of the C I, see for example Noterdaeme et al. (2007a) and Noterdaeme et al. (2007b). We list the parameters of the H_2 fits in Table 3.10.

Table 3.10. DLA 0812+32 COMPONENTS

comp	ion	z_{abs}	$\sigma_{z_{abs}}$	b [km s^{-1}]	σ_b	log N [cm^{-2}]	σ_{logN}
comp 1							
	ZnII	2.625812	0.000011	16.02	0.86	12.395	0.042
	CrII	2.625812	0.000000	16.02	0.00	12.831	0.049
	CII*	2.625812	0.000000	16.02	0.00	13.454	0.016
	CI	2.625808	0.000005	3.25	1.01	12.133	0.05
	CI*	...	...	...	...	11.678	0.16
	CI**	...	...	...	...	11.351	0.28
	H2J0	2.625812	0.000000	1.03	0.11	15.027	0.146
	H2J1	2.625812	0.000000	1.03	0.00	15.257	0.151
	H2J2	2.625812	0.000000	1.03	0.00	14.037	0.063
	H2J3	2.625812	0.000000	1.03	0.00	13.388	0.099
	H2J4	2.625812	0.000000	1.03	0.0	<12.64	
	H2J5	2.625812	0.000000	1.03	0.00	12.222	0.612
	total $N(H_2)$ =	3.011×10^{15}					
	log (total $N(H_2)$) =	15.48					
	f=	2.69×10^{-6}					
comp 2							
	ZnII	2.626326	0.000001	8.35	0.60	13.023	0.016
	CrII	2.626326	0.000000	8.35	0.00	13.239	0.019
	CII*	2.626326	0.000000	8.35	0.00	13.757	0.011
	CI	2.626325	0.000001	2.71	0.28	12.697	0.014
	CI*	...	...	...	...	12.328	0.035

Table 3.10—Continued

comp	ion	z_{abs}	$\sigma_{z_{abs}}$	b [km s^{-1}]	σ_b	log N [cm^{-2}]	σ_{logN}
	CI**	...	...	...	...	<11.5	
	H2J0	2.626326	0.000000	2.67	0.09	18.316	0.294
	H2J1	2.626326	0.000000	2.67	0.00	18.252	0.042
	H2J2	2.626326	0.000000	2.67	0.00	15.490	0.062
	H2J3	2.626326	0.000000	2.67	0.00	14.431	0.014
	H2J4	2.626326	0.000000	2.67	0.00	13.181	0.103
	H2J5	2.626326	0.000000	2.67	0.00	<12.60	
	total N(H_2) =	3.86×10^{19}					
	log (total N(H_2)) =	18.59					
	f=	0.003437					
comp 3							
	ZnII	2.626495	0.000001	0.28	0.14	13.621	0.464
	CrII	2.626495	0.000000	0.28	0.00	11.514	0.599
	CII*	2.626495	0.000000	0.28	0.00	15.534	0.118
	CI	2.626494	0.000001	0.38	0.04	13.092	0.093
	CI*	...	...	...	...	12.993	0.037
	CI**	...	...	...	...	12.30	0.054
	H2J0	2.626495	0.000000	2.27	0.13	19.789	0.012
	H2J1	2.626495	0.000000	2.27	0.00	19.140	0.009
	H2J2	2.626495	0.000000	2.27	0.00	14.889	0.034
	H2J3	2.626495	0.000000	2.27	0.00	14.330	0.016

Table 3.10—Continued

comp	ion	z_{abs}	$\sigma_{z_{abs}}$	b [km s^{-1}]	σ_b	log N [cm^{-2}]	σ_{logN}
	H2J4	2.626495	0.000000	2.27	0.00	13.807	0.028
	H2J5	2.626495	0.000000	2.27	0.00	12.846	0.189
	total $N(H_2)$ =	7.53×10^{19}					
	log (total $N(H_2)$) =	19.88					
	f=	0.06305					

It is interesting to note that like the low-ions, the majority of the H_2 resides in component 3, the narrow velocity C I component (however the b value of the H_2 in component 3 is not as narrow, at b = 2.27±0.13 km s^{-1}). Note that the fraction of H_2 in component 3, f = 0.08, or 8% , is among the highest found in DLAs.

We can estimate the kinetic temperature of the clouds using the column densities of H_2 in the J=0 and J=1 rotational states and assuming the states are thermalized according to the Boltzmann distribution (see equation 8 in Levshakov et al. (2002)). The excitation temperature, T_{ex}, is defined by,

$$\frac{N(J)}{N(0)} = \frac{g(J)}{g(0)} e^{-\frac{B_v J(J+1)}{T_{ex}}} \tag{3.7}$$

where B_v = 85.36 K for the vibrational ground state and g(J) is the degeneracy of level J. In Figure 3.19 we show the standard H_2 excitation diagram −− log(N/g) versus energy −− for the J=0 to J=5 levels for each component. As explained in Appendix 2 (on molecular hydrogen), the excitation temperature of the gas for the J = 0 to J = 1 state equals the kinetic temperature of the gas. For components 1, 2, and 3 we determine the following temperatures, T_{ex}^{01} = 102 K, T_{ex}^{01} = 73 K, T_{ex}^{01} = 46 K, respectively. These are just slightly higher than the temperatures derived from the C I data, which leads us to believe there is good correspondence between the C I and H_2 data and that the gas is primarily a CNM. Also, the T_{ex}^{01} = 46 K derived for the narrow component 3 is consistent with the thermal temperature of $T \leq \sim 100$ K implied by the narrow b value of the component.

We can also use the H_2 data to determine the ambient/incident radiation (UV flux) field on the cloud, $J_\nu{}^{total,H_2}$, using the J=0 and J=4 states (see Appendix 2 for details). The level populations above J = 1 are unlikely to be thermalized since their larger Einstein A coefficients implies that these

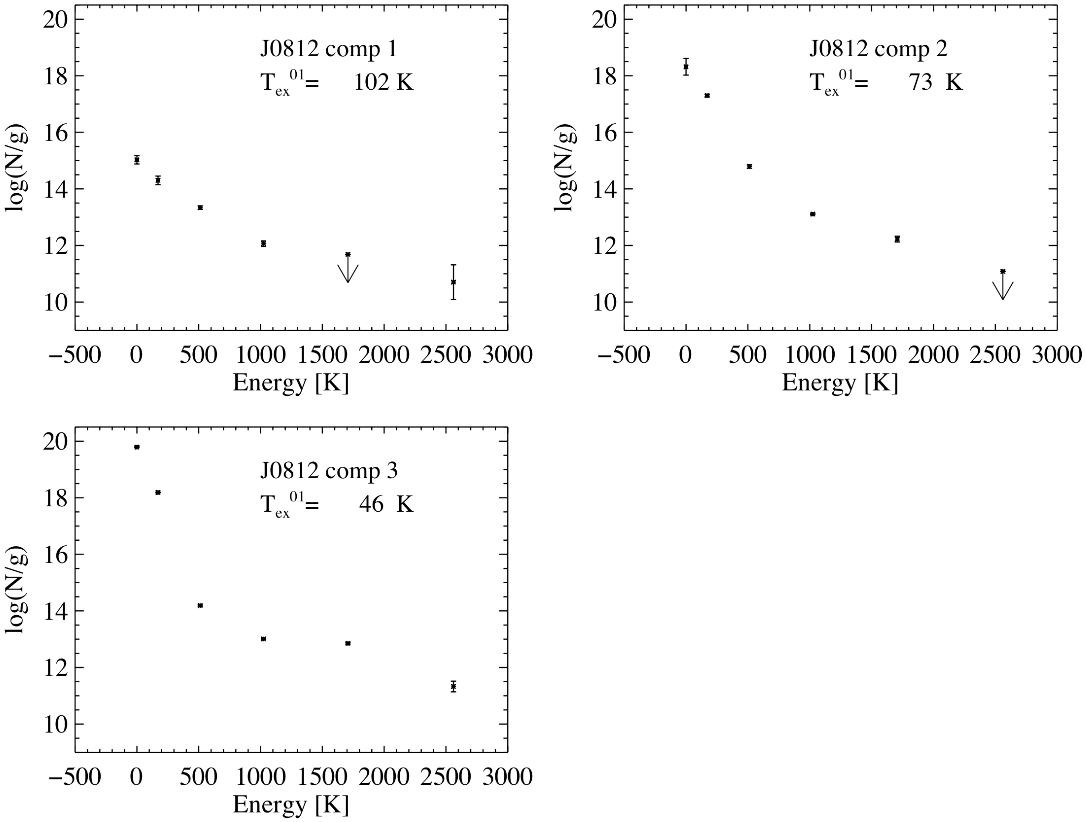

Figure 3.19: H_2 excitation diagrams for the components of DLA 0812+32.

states are depopulated by spontaneous emission more rapidly than by collisional de-excitation, which rules out the condition of detailed balance required to establish thermal equilibrium. Instead, these states are likely to be populated by UV pumping, which is what we shall assume. Following Hirashita & Ferrara (2005) we call this radiation field ${J_\nu}^{LW}$, as determined by absorption in the Lyman-Werner H_2 bands. Since the H_2 measurement should reflect the total incident radiation field, ${J_\nu}^{local}$ + ${J_\nu}^{Bkd}$= ${J_\nu}^{LW}$ = ${J_\nu}^{total,H_2}$. Results for the photoabsorption rate, β, and for the shielding terms are given in Table 3.9. Note that β_0 is derived from the J = 4 population, while β_1 is derived from the J = 5 population. Using the J = 4 population, we obtained the following radiation fields for components 1, 2, and 3 respectively: ${J_\nu}^{total,H_2}$ = $< 3.7 \times 10^{-20}$, 1.7×10^{-20}, 3.9×10^{-20} ergs cm^{-2} s^{-1} Hz^{-1} sr^{-1}. Note, that for component 1, N(H_2, 4) is an upper limit, and hence, this is technically an upper limit on the radiation field. Also notice that these radiation fields are only slightly larger, or smaller in the case of component 2, than ${J_\nu}^{Bkd}$. This places a rather strict limit on additional radiation from local star formation.

Interestingly, these results are rather independent of the choice of global versus individual component dust to gas ratios. If we use the global results, the N(H I) increases to the global value, while κ decreases in each component. These two effects essentially cancel each other in the calculation of shielding and we obtain very similar radiation fields when using the global measurements. We do not understand why the radiation field derived from the H_2 data is small compared with that derived by the C II* technique. Additionally, the radiation field predicted by the H_2 levels for component 2 is low enough that it is excluded by the C I data and the Haardt-Madau background (however, we note that the difference is not large and it could be within the errors). One solution might be the existence of narrow velocity H_2 components that are unresolved, similar to the proposed solution for DLA 1331+17.

We also derive densities from the H_2 data (see Appendix 2), assuming the excitation temperature is equal to the kinetic temperature derived from the J = 0 and J =1 states. The densities, n = 24, 10, and 5 cm^{-3} for components 1, 2, and 3 respectively, are consistent with the C I results. Additionally, we can use the J = 2 rotational state to place an upper limit on the density if the excitation temperature, T_{ex}^{02} is not equal to that of T_{ex}^{01}, indicating that the J = 2 state is not thermalized, and that the density is below n_{crit}, the critical density needed for thermalization. We plot critical density as a function of temperature for the H_2 J states in Figure 3.20. In component 1 of DLA0812+32, $T_{ex}^{02} = 132$ K is greater than $T_{01} = 102$ K, indicating that the density must be less than n_{crit}. In this case we derive a upper limit on the density of component 1 of n $<\sim 200$ cm^{-3}, consistent with the derived densities for this component (Both components 2 and 3 have T_{02} slightly less than T_{01} – so they are either thermalized, or this is within the errors. In either case, the upper limit derived from the next higher state, T_{03}, would would not be that restrictive as $n_{crit} \sim 10^3$.)

Until now, we let the b values of the H_2 components vary independently to obtain the best fit. However, because of strength of the lines, a narrow component like that of component 3 could be missed. Therefore, we ran a model in which we fixed the b value of the H_2 in component 3 to $b^{H_2} = 0.68$ km s^{-1} [8], the value it should have given $b^{CI} = 0.38$ km s^{-1} , rather than b = 2.27 km s^{-1} . We plot the excitation diagram in Figure 3.21. The decrease in b increases the column density in the J = 2, 3 and 4 states, however the J = 0 and 1 states remain the same because they are damped, i.e. a change in b value has little effect on the column density. The resultant radiation field increases by almost a factor or 2 to ${J_\nu}^{total} = 6.8\times10^{-20}$ ergs cm^{-2} s^{-1} Hz^{-1} sr^{-1}, which is compatible

---

[8] For a given line, ${b^2}_{total} = {b^2}_{thermal} + {b^2}_{turbulence}$, where ${b^2}_{thermal} = \frac{T}{60A}$ where A is the atomic weight. Given $A^{H_2} = 2$ and $A^{CI} = 12$ we get ${b^{H_2}}_{total} = (T/120 + ({b^{CI}}_{total})^2 - T/720)^{1/2}$. We take ${b^{CI}}_{total} = 0.38$ km s^{-1} and T = 46 K to get ${b^{H_2}}_{total} = 0.68$ km s^{-1} .

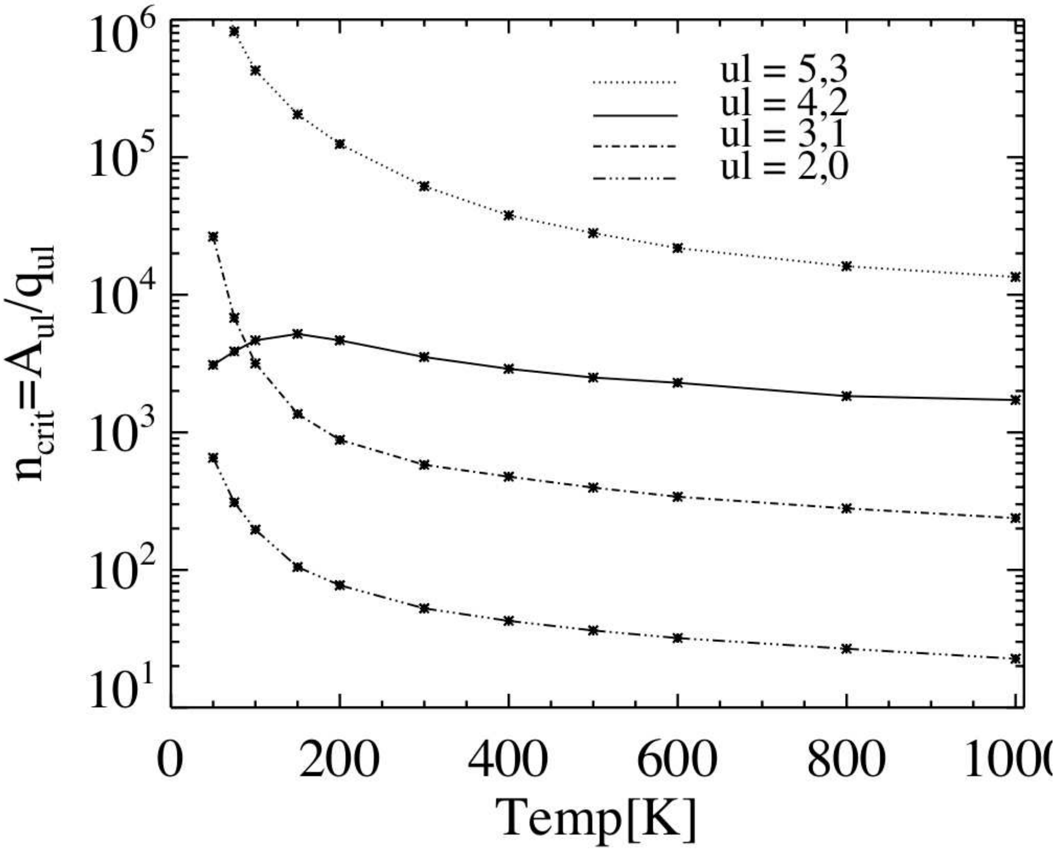

Figure 3.20: Critical densities as a function of temperature for the H_2 rotational J states. The subscripts u and l denote upper and lower respectively.

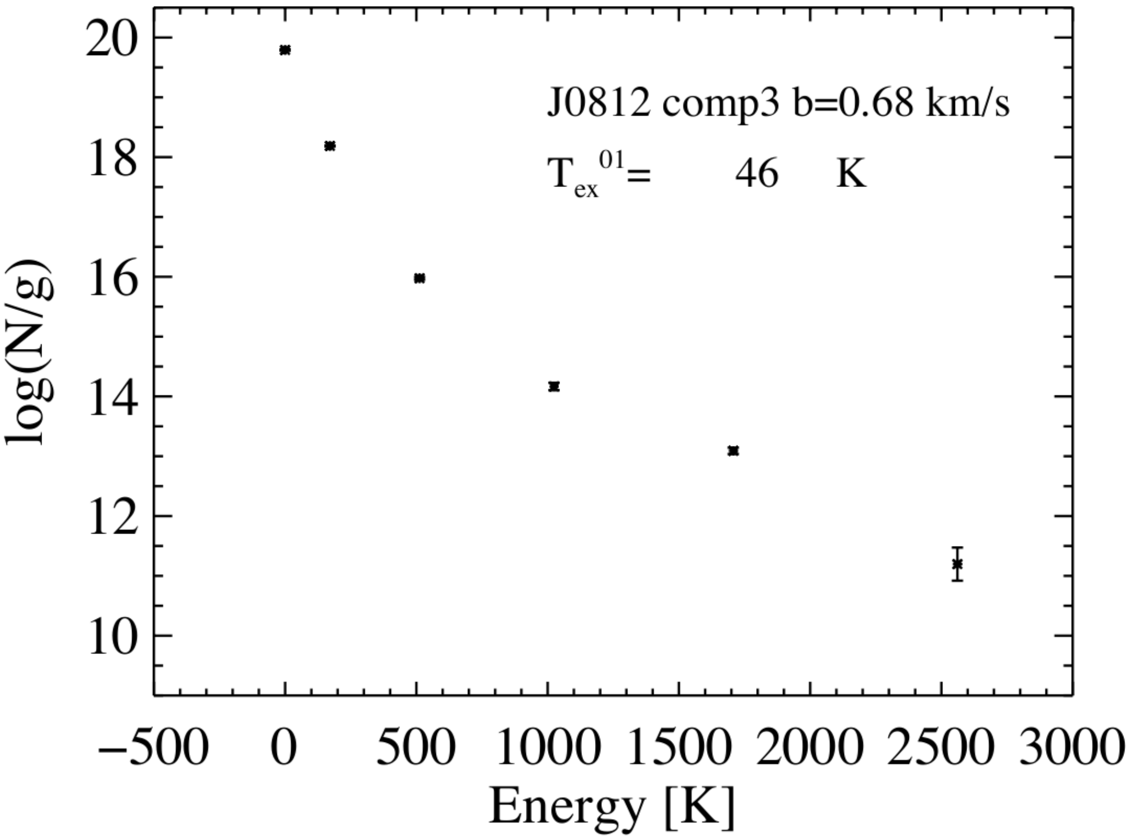

Figure 3.21: H_2 excitation diagram for component 3 of DLA 0812+32 with the H_2 b value fixed to 0.68 km s^{-1} to match that of the associated C I. It is seen that this increases the column density of H_2 in the J = 4 state (as well as other J states), but not the lowest J=0 and J=1 because they are essentially damped.

with the limits derived by the C I data.

3.4.3 FJ0812+32, z_{abs} =2.06677

The C II* transition of this DLA falls in the Lyα forest, and because the profile is quite different from that of the other low low ions (see Figure 3.22), it is impossible to make a definitive estimate of its true column density. Instead, we attempt to estimate the star formation rate by assuming three models motivated by the bimodality of DLA cooling rates (Wolfe et al. 2008). In the first case, case a, we assume this is a 'low cool' DLA and use the average low-cool ℓ_c =

$10^{-27.4}$ergs s^{-1} H^{-1}. This assumption is likely the closest to the truth given that several physical traits of this DLA match those of the low-cool population of DLAs, i.e. the small value of the low-ion velocity, $\Delta\ v = 26$ km s^{-1} is more likely to be drawn from the low-cool sample, with median $\Delta\ v = 46$ km s^{-1} , than from the high cool sample with median $\Delta\ v = 104$ km s^{-1} . The Si II 1526 rest-frame equivalent width is also small at, $W_{1526} = 0.2245 \pm 0.0024$ Å, compared with the low-cool median $W_{1526} = 0.26 \pm 0.09$Å, while the metallicity, [M/H] = -1.380 ± 0.009, is slightly higher than the median metallicity for the low-cool population [M/H] = -1.74 ± 0.19. Finally, the dust to gas ratio is $\log_{10}\kappa = -2.74$ is similar to the median low-cool dust to gas ratio, $\log_{10}\kappa = -2.57 \pm 0.17$. In the second case, case b, we will again make the low cool assumption, but instead of the standard alpha enhancement assumption of [Fe/Si] = -0.2, we will assume [Fe/Si] = 0.0. Finally, in the last model, case c, we will assume that the DLA is a 'high cool' DLA and has an ℓ_c equal to the median high cool DLA $\ell_c = 10^{-26.6}$ergs s^{-1} H^{-1}.

We present the results for the three cases in Table 3.6 and Figure 3.23. The asterisks denote the pressure-density solutions of the C II* technique. As stated earlier, the low-cool ℓ_c, minimal depletion model (case a), denoted in blue in the figure, is the most likely to be correct. In every case, pressures and densities inferred from the C II* technique are lower than deduced from the C I method.

If we now relax the constraint imposed by the C II* technique, and model a range of possible ${J_\nu}^{total,C\,I}$, we find that at the 2σ level, we can restrict the density to n $\geq$ 18 cm cm^{-3} and T $\leq$ 4000 K, see Table 3.8.

3.4.4 Q2231−00

DLA 2231−00 at $z_{abs} = 2.066$ was analyzed by Prochaska & Wolfe (1999), who reported the detection of titanium. Prochaska (1999) analyzed a

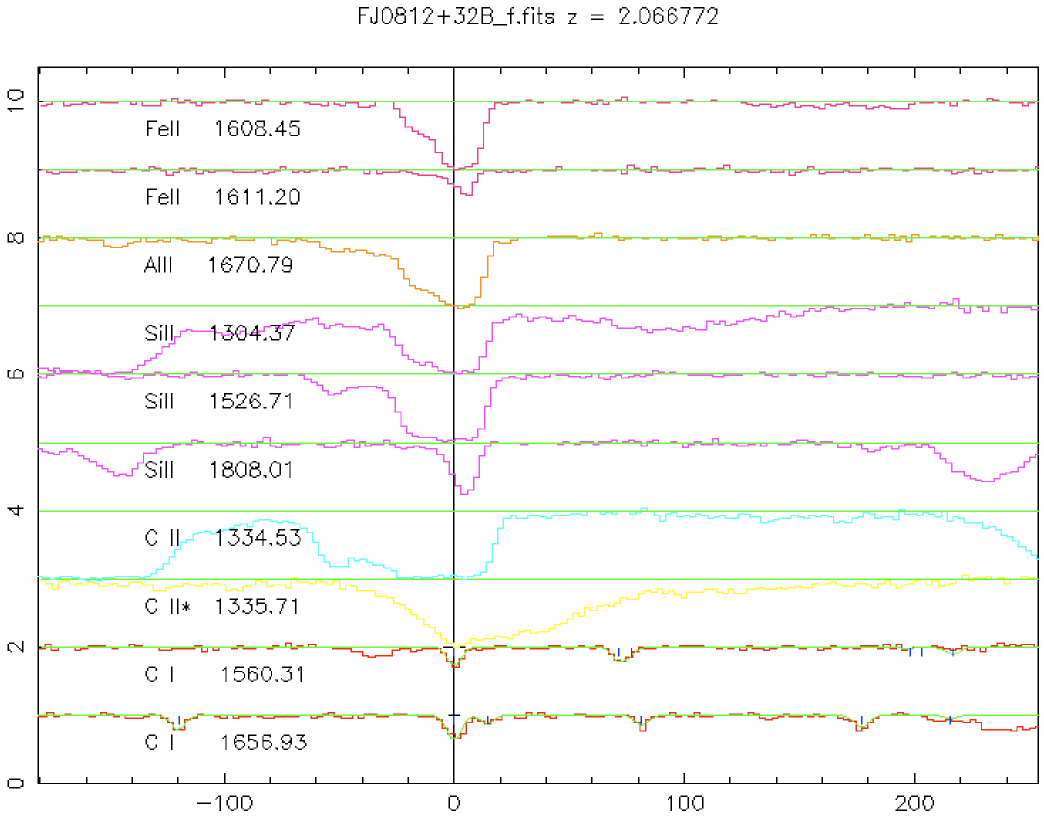

Figure 3.22: DLA 0812+32 z_{abs}=2.06 C I velocity structure along with other low ions. Note that C II* does not trace the other low ions and is therefore likely blended with a Lyman α forest line.

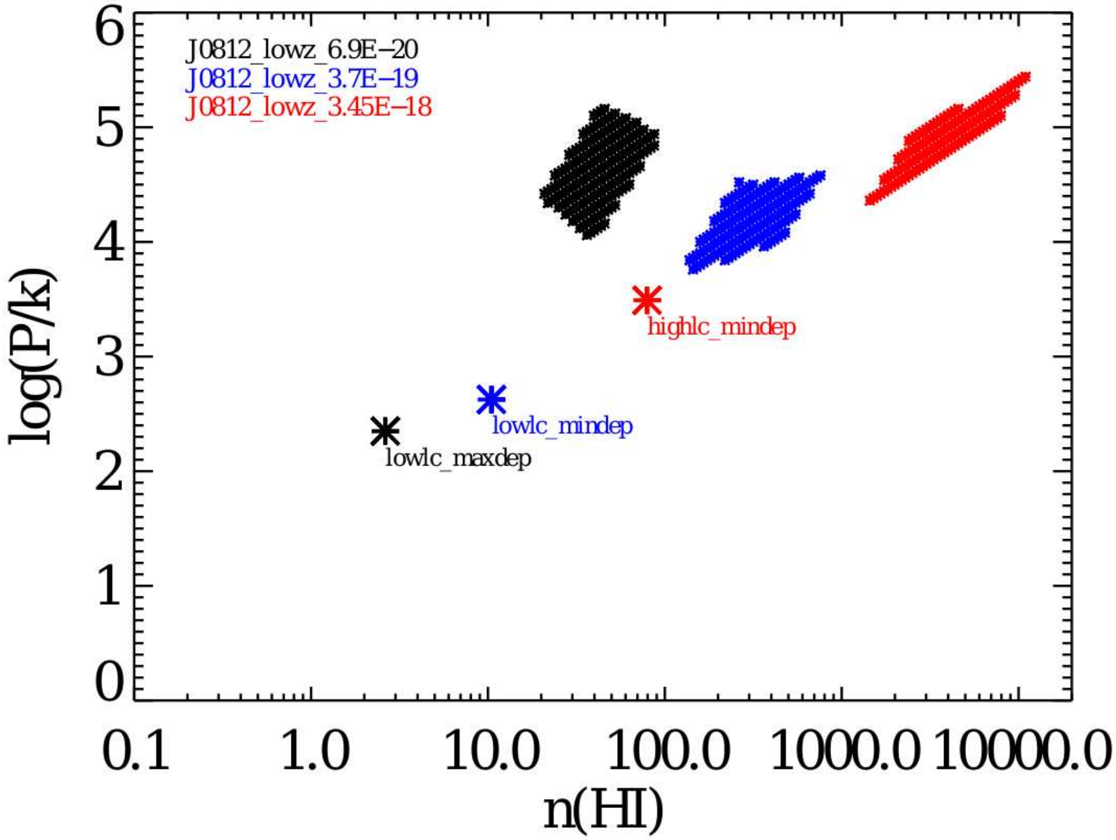

Figure 3.23: The resulting pressures (2σ) for DLA 0812+32, z_{abs}=2.06. These are the three cases a, b and c, in black, blue and red, respectively, where blue is the most likely case. Also plotted are the results from the C II* technique as asteriks.

Lyman-limit system at z_{abs}=2.652 in this sightline. Here we will focus on C I fine structure lines contained in the DLA at $z_{abs}\approx$2.066.

We estimate the ${J_\nu}^{local,C\,II^*}$ from the measured N(C II*) with some confidence, even though it falls within the Lyman-α forest, because the velocity profile of C II* closely traces that of other low ions as expected. Using this ${J_\nu}^{local,C\,II^*} \approx 24.7 \times 10^{-19}$ ergs cm^{-2} s^{-1} Hz^{-1} sr^{-1}, and the measured log($\frac{CII}{CI}$)= 3.0451±0.2, we find 2 cm^{-3} $\leq$ n $\leq$ 91 cm^{-3}, and T $\leq$ 1000 K, see Table 3.6. Relaxing the constraint of ${J_\nu}^{local,C\,II^*}$ given by the C II* technique results in a lower limit on the density of n $\geq$ 3 cm^{-3}.

3.4.5 J2340−00

DLA 2340−00 has a relatively high total column density of molecular hydrogen, logN(H_2) = 18.20 , with an H_2 fraction f = 0.014, making it and DLA 1331+17 some of the few H_2- rich DLAs. The neutral hydrogen column density, at log N(H I) = 20.35 ± 0.15 cm^{-2}, is close to the threshold defining a DLA, supporting the lack of correlation between large N(H I) and H_2 and C I content. Additionally, the low-ion velocity profile is large, with Δv = 104 km s^{-1} , and the cooling rate, as determined by C II* over the entire profile, at log $\ell_c = -26.15$, is among the highest of DLAs. Because of the complex nature of the C I, the H_2, and the low-ion profiles, all requiring multiple components, and because of heavy blending and saturation in some components of the low-ions, we were not able to obtain unique fits to all low ion components using VPFIT. Instead, we analyzed the C I data using two different model assumptions. In both cases, 1 σ upper limits to the non-detected fine structure lines were used, with the exception of component 3 in which the 2σ upper limit on logN(C I**) was used. C I component 6 was not compatible with the theoretical tracks and therefore, not analyzed.

In the first case, we assume ${J_\nu}^{total}$ is just slightly above the background,

${J_\nu}^{total} = 3.9 \times 10^{-20}$ ergs cm^{-2} s^{-1} Hz^{-1} sr^{-1}. Because this is a lower limit to the radiation field, this analysis provides an upper limit on density (i.e. for all else being constant, if we increase the radiation field, the density required to collisionally excite the C I fine structure levels is decreased). The metalicity, dust to gas ratio and $\log\frac{C\,II}{C\,I}$ are determined by AODM over the entire profile. The 2σ resultant densities and temperatures are given in Table 3.11.

Table 3.11. 2σ C I TECHNIQUE SOLUTIONS COMPARED WITH H_2 RESULTS

DLA	comp.	$J_\nu{}^{total}$ /1×10^{-19}	$\log(\frac{CII}{CI})$	2σ C I constraints n(H I) [cm^{-3}]	T [K]	log(P/k) [cm^{-3}K]	H_2 constraints n(H I) [cm^{-3}]	T [K]	log(P/k) [cm^{-3}K]
0812+32[a]	1	0.43[b1]	2.9401±0.2	21−87	316−3162	4.06−5.16	–	–	–
0812+32[a]	1	3.46[b2]	2.7401±0.2	138−758	25−126	3.76− 4.58	–	–	–
0812+32[a]	1	36.38[b3]	2.7401±0.2	1445−10964	16−32	4.36− 5.44	–	–	–
0812+32$^{c}_{global}$	1	7.4	3.1987±0.2	14−316	10− 200	2.16− 4.44			
0812+32$^{c}_{global}$	2[d]	7.4	3.1987±0.2	14−138	10− 40	2.16−3.48			
0812+32$^{c}_{global}$	3	7.4	3.1987±0.2	55− 288	32−158	3.54−4.26			
0812+32 div	1	32.8	3.8243±0.2	6−158	10−398	1.76−4.52	24	102	3.39
0812+32 div	2	15	3.9268±0.2	2−23	10−63	1.36− 2.86	10	73	2.86
0812+32 div	3	236	4.0763±0.2	–	–	–	5	46	2.36
1331+17	1	3.3	2.6498±0.2	91− 363	16− 32	3.36−3.86	–[g]		
2231−00	2	24.7	3.0451±0.2	87−1096	10−50	2.94−4.54	–	–	–
2340−00	1	0.39[e]	2.2067±0.2	1−69	10−794	1.16 −4.48	–	266	–
2340−00	2	”	2.2067±0.2	1−83	10−1000	1.16 − 4.70	–	232	–
2340−00	3	”	2.2067±0.2	–	–	–	1595	276	5.64
2340−00	4	”	2.2067±0.2	19−50	100−501	3.60 − 4.16	–	–	–
2340−00	5	”	2.2067±0.2	23−48	126−501	3.74 − 4.06	10291	587	6.78
2340−00	6	”	2.2067±0.2	–	–	–	3507	475	6.22
2340−00	7	”	2.2067±0.2	1−158	10−2511	1.16− 5.32	368	151	4.74

Table 3.11—Continued

DLA	comp.	$J_\nu{}^{total}$ $/1\times10^{-19}$	$\log(\frac{C\,II}{C\,I})$	2σ C I constraints n(H I) [cm^{-3}]	T [K]	log(P/k) [cm^{-3}K]	H_2 constraints n(H I) [cm^{-3}]	T [K]	log(P/k) [cm^{-3}K]
2340−00^f	1	–^{f}	–	–	–	–	–	266	–
2340−00^f	2	–^{f}	–	–	–	–	–	232	–
2340−00	3	52.7	1.94046±0.2	none	–	–	1595	276	5.64
2340−00	4	52.7	1.94046±0.2	none	–	–	–	–	–
2340−00	5	52.7	1.94046±0.2	none	–	–	10291	587	6.78
2340−00	6	11	2.46959±0.2	none	–	–	3507	475	6.2
2340−00	7	11	2.46959±0.2	7− 288	10− 631	1.82−5.0	368	151	4.74

[a] z_{abs}=2.06

[b1] Maximal depletion model, assuming the low cool l_c; [Fe/Si] = −0.0

[b2] The most likely model, Minimal depletion model , low l_c object with [Fe/Si] = −0.2

[b3] Minimal depletion model, assuming high cool l_c object with [Fe/Si] = −0.2

[c] z_{abs}=2.62

[d] Calculated using the 1σ upper limit on logN(C I**) < 11.39

[e] A minimum background assumption just about Haardt-Madau for this object

[f] Super solar Fe inhibited the calculation of κ and $J_\nu{}^{local,C\,II^*}$

[g] H_2 measured by Cui et al. (2005) but Carswell et al 2008 show how narrow velocity component confuses the situation.

In an attempt to refine the model, in the second case, we performed an AODM fitting over three 'super-components' of the S II, Fe II, and C II*, where super-components a, b, and c coincide with C I components (1, 2), (3, 4, 5) and (6, 7) respectively. Taking $v = 0$ km s^{-1} at z$_{abs}$ = 2.05416, the AODM super-components were defined as follows: super-component a from $v = -30$ to 15 km s^{-1} , super-component b from $v = 15$ to 70 km s^{-1} , and super-component c from $v = 70$ to 120 km s^{-1} . We then applied the metalicity, dust to gas ratio, and N(C II*) measurement derived from the AODM 'super-component' to each associated C I component. Table 3.12 contains a summary of this analysis. Looking at each super-component, we find the following:

•$Super - component\ a$: We did not perform the C II* analysis on super-component a because we measure a super-solar [Fe/S] and [Ni/S]. The absence of depletion detected for Fe and Ni implies that we cannot calculate the dust to gas ratio. If real, this super-solar (or nearly solar) value of Fe II would require a different and special star formation history. Given that we cannot calculate a dust to gas ratio or $J_\nu{}^{local,C\,II^*}$, and the fact that the C I components 1 and 2 associated with super-component a contain the smallest amount C I, we did not perform further analysis.

•$Super - component\ b$: Super-component b, which covers C I components 3, 4, and 5, contains the bulk of the gas. The C II* technique results in $J_\nu{}^{total,C\,II^*} = 5.27{\times}10^{-18}$ ergs cm^{-2} s^{-1} Hz^{-1} sr^{-1}. This $J_\nu{}^{total}$ is too high to be compatible with any of the C I components 3, 4, or 5

•$Super - component\ c$: The C II* technique applied to super-component c, which covers C I components 6 and 7, results in a $J_\nu{}^{total} = 1.1\ {\times}10^{-18}$ergs cm^{-2} s^{-1} Hz^{-1} sr^{-1}. The C I data for component 7 give the results summarized in Table 3.11.

If we relax the constraint of $J_\nu{}^{total,C\,II^*}$ as measured by the C II* technique, we can determine limits for each component for a range of possible radi-

Table 3.12: COMPONENT ANALYSIS OF DLA 2340−00 USING AODM

Super-Component	a	b	c
C I Component	(1, 2)	(3,4,5)	(6,7)
	−30−15 km s^{-1}	15−70 km s^{-1}	70−120 km s^{-1}
N(Fe II) [cm^{-2}]	14.551±0.046	14.625±0.042	14.064±0.005
N(S II) [cm^{-2}]	14.172±0.010	14.726±0.004	14.312±0.008
N(C II*) [cm^{-2}]	12.53 ± 0.09	13.60± 0.01	12.99± 0.04
N(H I)[a] [cm^{-2}]	19.575	20.129	19.715
$[Fe/H]$	−0.474±0.046	−0.954±0.042	−1.101±0.005
$[S/H]$	−0.563±0.010	−0.563±0.004	−0.563±0.008
$[Fe/Met]$	0.089±0.047	−0.391±0.042	−0.538±0.009
κ[b]	−0.062	0.061	0.093
$\log_{10}\kappa$	–	−1.211	−1.030
N(C I)^{total}	12.78	13.82	12.87
$\log\frac{CII}{CI}$	2.4259	1.9405	2.4696
l_c	−26.56	−26.05	−26.24
$J_\nu{}^{local}$ /10^{-19}[c]	–[d]	52.4	10.8
N(Fe III)[cm^{-2}]	<13.866[e]	< 13.939[e]	<13.886[e]
Fe III/Fe II[f]	<0.207	<0.206	<0.664
N(Ar I)[cm^{-2}]	13.309	13.826	13.653
$[Ar/S]$[g]	0.117	0.080	0.321
N(Ni II) [cm^{-2}]	13.214±0.018	13.499±0.011	13.144±0.024
$[Ni/H]$	−0.551±0.018	−0.820±0.011	−0.791±0.024
$[N/Met]$	0.012±0.021	−0.257±0.012	−0.228±0.025
κ	−0.008	0.021	0.011
$\log\kappa$	–	−1.673	−1.967

[a] N(H I) scaled to trace N(S II)

[b] Dust to gas ratio relative to Milky Way, defined in the text. Here we have used S II instead of Si II.

[c] [ergs cm^{-2} s^{-1} Hz^{-1} sr^{-1}]

[d] We did not determine $J_\nu{}^{local}$ for this component because the super-solar Fe II measurement.

[e] AODM measurements taken as upper limits because of possible blending with the forest.

[f] Fe III/Fe II ∼0.3 means partially ionized, HI/H = 0.5

[g] If [Ar/S] > −0.2 then x <0.1 (but low Ar/S does not require x>>0).

ation fields. 2 σ results are given in Table 3.8. In all cases we can put a lower limit on the density of n > 0.4 cm^{-3} and for components 3, 4, and 5, n > 33 cm^{-3}. The temperature for components 3, 4 and 5 is constrained to be less than ∼200 K, while $J_\nu{}^{total,C\,I} < 8\times10^{-19}$ergs cm^{-2} s^{-1} Hz^{-1} sr^{-1}, for components 4 and 5. We do not understand why the radiation field determined by the C II* technique for components 3, 4 and 5, $J_\nu{}^{local,C\,II^*} = 5.24\times10^{-18}$ergs cm^{-2} s^{-1} Hz^{-1} sr^{-1}, is not compatible with the C I data.

On the possible ionization of DLA 2340−00

Given the presence of Fe III λ1122 and the fact that the column density of DLA 2340−00, at log N(H I) = 20.35, is just above the DLA threshold of 2 × 10^{20} cm^{-2}, we considered the possibility of partial ionization of the gas. Fe III/Fe II is a measure of the fractional ionization with large values indicating high fractional ionization and low values indicating low fractional ionization (see the photoionization diagnostics summarized in Table 8 of Prochaska et al. (2002)). We used the AODM technique to measure Fe III/Fe II in the same three 'super-components' discussed above, covering C I components 1 and 2, components 3, 4, and 5, and components 6 and 7 respectively, see Figure 3.24. While our measured Fe III/ Fe II (<0.21, <0.21, and <0.66 respectively) imply partial ionization (x > 0.5) in all components, because the Fe III profile does not trace that of the low ions (see Figure 3.24), we cannot rule out the possibility of blending with the Lyman α forest and therefore, we treat our Fe III measurements as upper limits.

Instead, we can rule out a high ionization factor based on the [Ar/S] measurement. Specifically, Prochaska et al. (2002) show that photoionzation models in which [Ar I / S II] > -0.2 dex require that x < 0.1, in other words, require gas that is $> 90\%$ neutral. Using the Ar I $\lambda\lambda$ 1048, 1066 transitions, excluding blending in the super-component 3 of the λ1066 transition (see Fig-

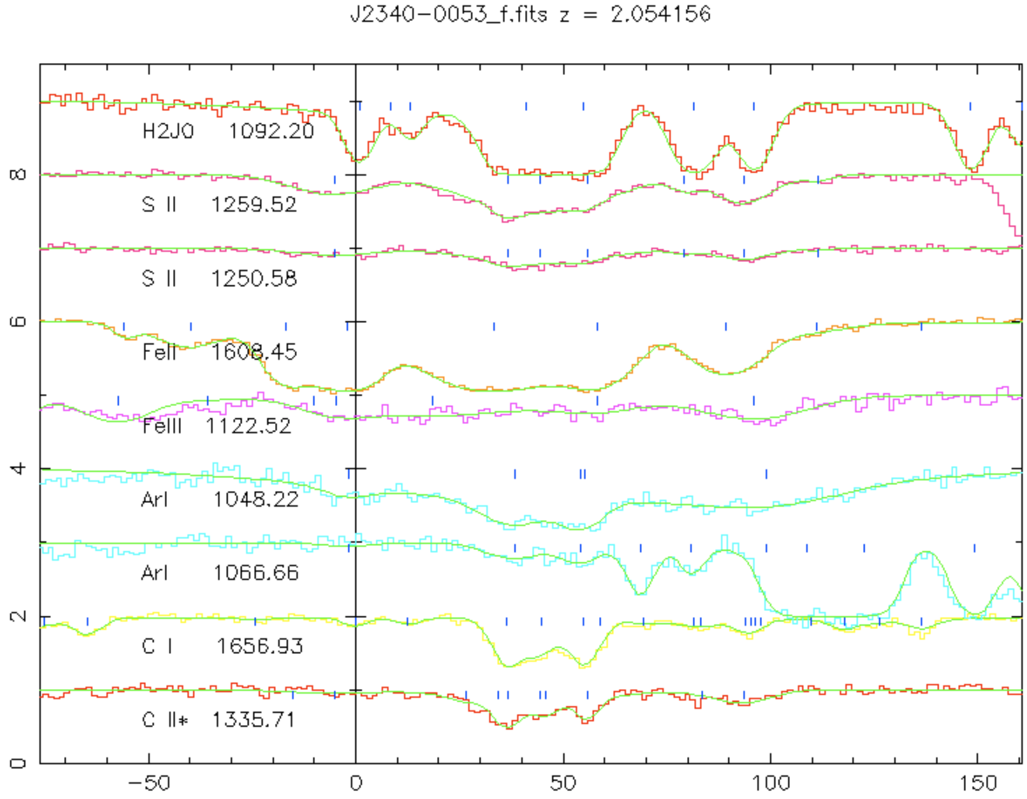

Figure 3.24: DLA 2340 plot of 7 C I components along with low ions and H_2.

ure 3.24), we find [Ar/S] > -0.2 in all components (see Table 3.12), indicating that x < 0.1 and that the gas is >90% neutral.

Molecular Hydrogen in DLA— 2340−00

The total column density of molecular hydrogen, logN(H_2) = 18.20 cm^{-2}, where f = 0.014, is large relative to most H_2 -bearing DLAs, where f is typically f $\sim 10^{-5}$. We have analyzed the H_2 using VPFIT. To allow for the best fit we have let the H_2 component redshifts and b values vary independently of the C I and low-ion components. We find that we require 6 H_2 components to achieve the best fit. In redshift space, these components lie fairly close to the C I components 1, 2, 3, 5, 6, and 7. See Table 3.13 and Figure 3.25 for details. In Figure 3.26 we plot the excitation diagrams for each H_2 component and list the excitation temperature as determined by the J=0 and J=1 states. Additionally, we use the population of the J=4 state to determine the radiation field as described in Appendix 2. Details are given in Table 3.14.

Table 3.13: DLA 2340−00 COMPONENTS

Component	**Ion**	$\mathbf{z}_{abs}$	$\sigma_{z_{abs}}$	**b** [**km s^{-1}**]	σ_b	**log N** [**cm^{-2}**]	σ_{logN}
comp1							
	C I	2.054156	0.000004	1.14	1.34	12.167	0.047
	C I*	2.054156	...	1.14	0.00	11.745	0.165
	C I**	2.054156	...	1.14	0.00	<11.36	
	H2J0	2.054165	0.000001	2.31	0.07	15.262	0.040
	H2J1	2.054165	...	2.31	0.00	15.94	0.049
	H2J2	2.054165	...	2.31	0.00	14.904	0.065
	H2J3	2.054165	...	2.31	0.00	14.251	0.049
	H2J4	2.054165	...	2.31	0.00	<13.39	
	H2J5	2.054165	...	2.31	0.00	<12.90	
	log (total N(H_2)) =	16.06					
	f^a=	1.03×10^{-4}					
comp2							
	C I	2.054284	0.000004	0.25	0.29	12.288	0.191
	C I*	2.054284	...	0.25	0.00	12.106	0.101
	C I**	2.054284	...	0.25	0.00	<11.70	
	H2J0	2.054291	0.000001	1.25	0.09	14.657	0.073
	H2J1	2.054291	...	1.25	0.00	15.292	0.079

Continued on Next Page…

Table 3.13 – Continued

Component	**Ion**	$\mathbf{z}_{abs}$	$\sigma_{z_{abs}}$	**b** [**km s**$^{-1}$]	σ_b	**log N** [**cm**$^{-2}$]	σ_{logN}
	H2J2	2.054291	...	1.25	0.00	14.478	0.079
	H2J3	2.054291	...	1.25	0.00	14.299	0.059
	H2J4	2.054291	...	1.25	0.00	<13.08	
	H2J5	2.054291	...	1.25	0.00	<13.23	
	log (total N(H_2)) =	15.47					
	f[a]=	2.63×10^{-5}					
comp3							
	C I	2.054527	0.000002	2.90	0.20	13.226	0.026
	C I*	2.054527	...	2.90	0.00	12.931	0.022
	C I**	2.054527	...	2.90	0.00	<11.64	
	H2J0	2.054573	0.000002	4.62	0.16	17.269	0.082
	H2J1	2.054573	...	4.62	0.00	17.955	0.054
	H2J2	2.054573	...	4.62	0.00	17.045	0.129
	H2J3	2.054573	...	4.62	0.00	15.326	0.028
	H2J4	2.054573	...	4.62	0.00	13.812	0.041
	H2J5	2.054573	...	4.62	0.00	13.317	0.139
	log (total N(H_2)) =	18.08					
	f[a]=	1.06×10^{-2}					
comp 4							
	C I	2.054611	0.000003	3.01	0.68	12.987	0.037
	C I*	2.054611	...	3.01	0.00	12.519	0.065
	C I**	2.054611	...	3.01	0.00	12.003	0.079
comp 5							
	C I	2.054716	0.000001	2.86	0.22	13.200	0.010
	C I*	2.054716	...	2.86	0.00	12.917	0.014
	C I**	2.054716	...	2.86	0.00	12.017	0.069
	H2J0	2.054714	0.000001	5.06	0.11	15.997	0.047
	H2J1	2.054714	...	5.06	0.00	16.825	0.065
	H2J2	2.054714	...	5.06	0.00	16.059	0.039
	H2J3	2.054714	...	5.06	0.00	15.836	0.019
	H2J4	2.054714	...	5.06	0.00	14.355	0.015
	H2J5	2.054714	...	5.06	0.00	13.932	0.040
	log (total N(H_2) =	16.98					
	f[a]=	8.51×10^{-4}					
comp 6							
	C I	2.055003	0.000015	9.90	2.13	12.496	0.077
	C I*	2.055003	...	9.90	0.00	<11.85	
	C I**	2.055003	...	9.90	0.00	11.797	0.178
	H2J0	2.054986	0.000001	3.64	0.10	15.76	0.042
	H2J1	2.054986	...	3.64	0.00	16.55	0.067
	H2J2	2.054986	...	3.64	0.00	15.63	0.047
	H2J3	2.054986	...	3.64	0.00	15.13	0.027
	H2J4	2.054986	...	3.64	0.00	13.75	0.046
	H2J5	2.054986	...	3.64	0.00	11.90	3.520
	log (total N(H_2) =	16.67					
	f[a]=	4.21×10^{-4}					
comp7							
	C I	2.055128	0.000004	1.91	1.34	12.298	0.088

Continued on Next Page. . .

Table 3.13 – Continued

Component	**Ion**	$\mathbf{z}_{abs}$	$\sigma_{z_{abs}}$	**b** [**km s^{-1}**]	σ_b	**log N** [**cm^{-2}**]	σ_{logN}
	C I*	2.055128	...	1.91	0.00	11.896	0.104
	C I**	2.055128	...	1.91	0.00	11.329	0.333
	H2J0	2.055135	0.000001	1.80	0.07	16.735	0.074
	H2J1	2.055135	...	1.80	0.00000	17.200	0.057
	H2J2	2.055135	...	1.80	0.00000	16.035	0.088
	H2J3	2.055135	...	1.80	0.00000	14.753	0.049
	H2J4	2.055135	...	1.80	0.00	<13.10	
	H2J5	2.055135	...	1.80	0.00	<13.02	
	log (total N(H_2) =	17.35					
	f[a]=	2.00×10^{-3}					

---

[a] f calculated assuming logN(HI) = 20.35

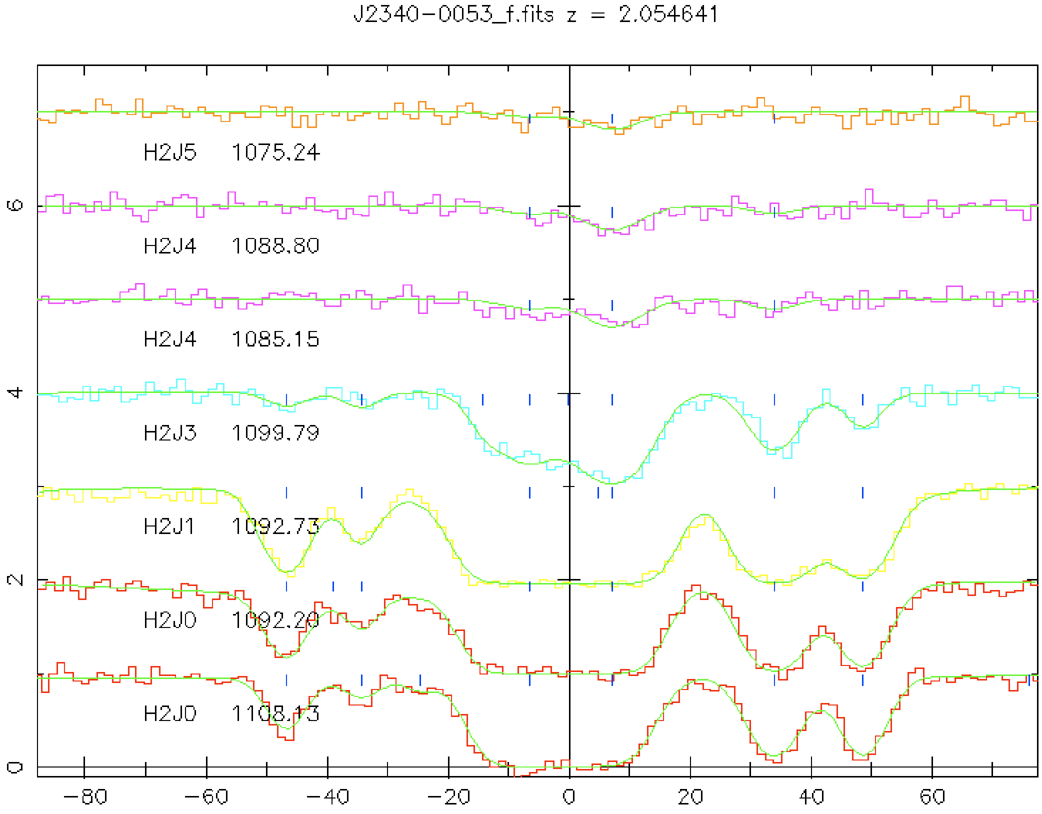

Figure 3.25: DLA 2340 plot of H_2 over several J levels.

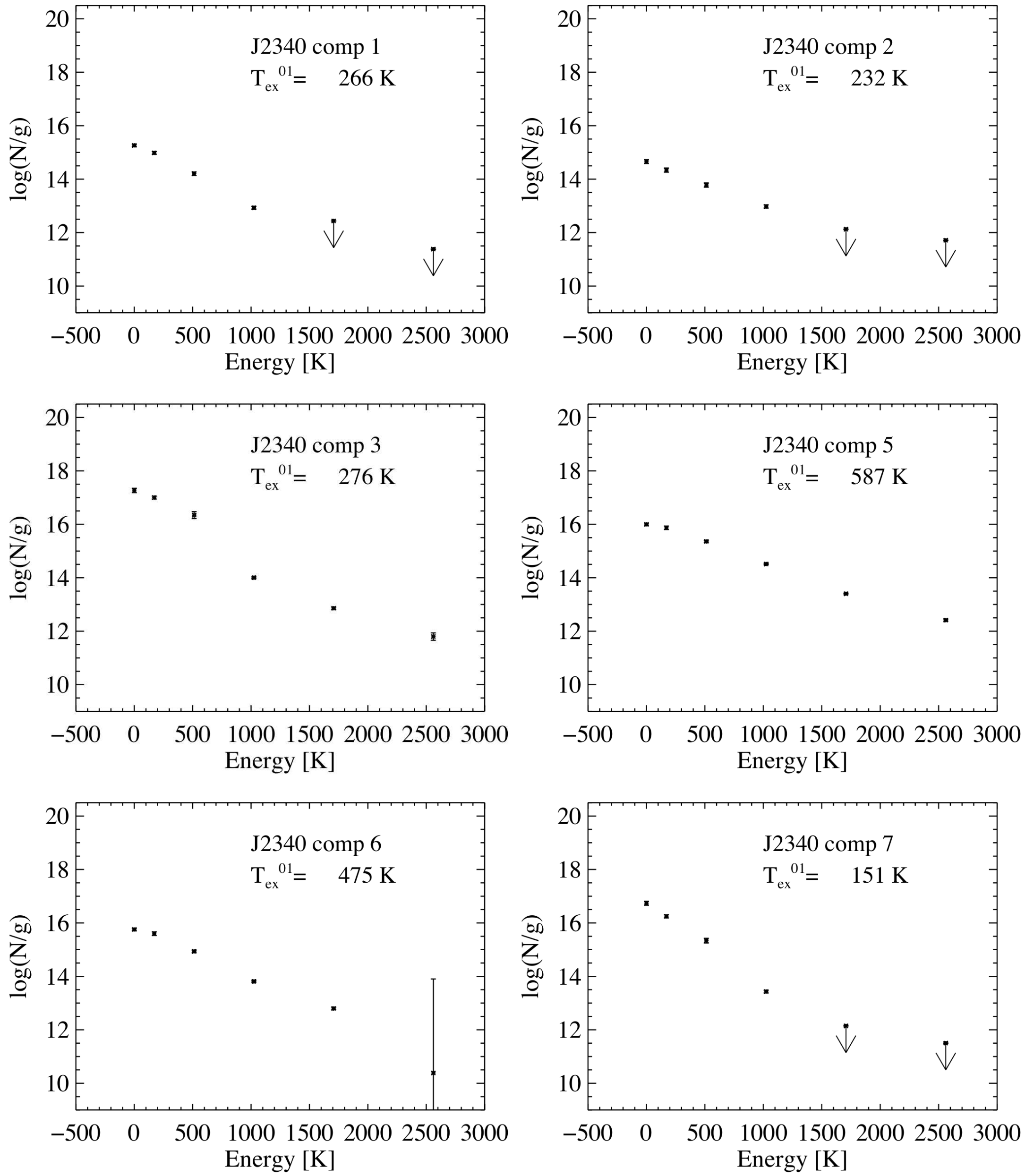

Figure 3.26: The H_2 excitation diagrams for the 6 components of DLA 2340 −00 that contain H_2.

Table 3.14. H_2 COMPONENT ANALYSIS OF DLA 2340−00 USING AODM VALUES

Super-Component component	a 1^a	a 2^a	b 3	b 4	b 5	c 6	c 7
$f_{H_2}{}^b$	6.12×10^{-4}	1.57×10^{-4}	1.75×10^{-2}	...	1.42×10^{-3}	1.82×10^{-3}	8.58×10^{-3}
T_{ex}^{01} [K]	266	232	276	...	587	475	151
β_0 [s^{-1}]	9.44×10^{-11}	1.84×10^{-10}	2.43×10^{-12}	...	1.36×10^{-10}	6.31×10^{-11}	1.84×10^{-12}
β_1 [s^{-1}]	1.00×10^{-10}	8.42×10^{-10}	2.52×10^{-12}	...	1.44×10^{-10}	2.62×10^{-12}	5.89×10^{-12}
S_{self}	2.85×10^{-2}	7.92×10^{-2}	8.72×10^{-4}	...	5.83×10^{-3}	9.88×10^{-3}	3.07×10^{-3}
S_{dust}	–[a]	–[a]	0.993	...	0.993	0.996	0.996
S_{total}	–	–	8.66×10^{-4}	...	5.78×10^{-3}	9.84×10^{-3}	3.06×10^{-3}
$J_\nu^{LW}/10^{-19c}$	–	–	2.25	...	18.84	5.13	< 0.48
n(H I)[d] [cm^{-3}]	–	–	1595	...	10291	3507	368

[a] Super-solar Fe II measurement, therefore κ was not sensible

[b] f is calculated using the N(H I) of the Super-Component, i.e. comps 1 and 2, comps 3,4,5 and then comps 6,7

[c] [ergs cm^{-2} s^{-1} Hz^{-1} sr^{-1}]

[d] Density derived from the H_2 as explained in Appendix 2.

While the radiation fields derived from the H_2 data are in general consistent with the C I constraints, it is interesting to note that the densities derived from the H_2 data alone, while generally consistent with the 2 σ C I limits, tend to be significantly higher than that required for C I. We summarize results for each component for which we could make comparisons between the different techniques:

•*Component* 3 : The H_2 derived T = 276 K is inconsistent with the 2σ C I limit of T<79 K. The density derived from H_2, n ~1600 cm^{-3} is compatible with the C I limits. Finally, the H_2 derived ${J_\nu}^{total,H_2} = 2.25 \times 10^{-19}$ ergs cm^{-2} s^{-1} Hz^{-1} sr^{-1} is within range allowed by C I and much lower than that predicted by C II* (${J_\nu}^{total,C\,II^*} = 52.7 \times 10^{-19}$ ergs cm^{-2} s^{-1} Hz^{-1} sr^{-1}).

•*Component* 5 : The H_2 derived T = 587 K is inconsistent with the 2σ C I limit T $\leq$ 158 K, and the H_2 derived n = 10, 291 cm^{-3} is also inconsistent with the C I limits of n $\leq$ 2630 cm^{-3}. The radiation field derived from the H_2, ${J_\nu}^{total,H_2} = 18.8 \times 10^{-19}$ ergs cm^{-2} s^{-1} Hz^{-1} sr^{-1}, is twice as large as the maximum allowed by the C I (${J_\nu}^{total,C\,I} \leq 7.7 \times 10^{-19}$ ergs cm^{-2} s^{-1} Hz^{-1} sr^{-1}). These are both much lower than the ${J_\nu}^{total,C\,II^*}$ predicted by the C II* technique.

•*Component* 7 : The H_2 derived T = 151 K is consistent with the 2σ C I limit, T $\leq$ 5000 K. The H_2 derived density, n = 368 cm^{-3}, is also compatible with large range allowed by C I. In addition, the H_2 derived radiation field, ${J_\nu}^{total,H_2}$ $\leq 0.48 \times 10^{-19}$ ergs cm^{-2} s^{-1} Hz^{-1} sr^{-1} is compatible with the limits set by C I. However, it is not compatible with that predicted by the C II* technique, ${J_\nu}^{total,C\,II^*} = 11 \times 10^{-19}$ ergs cm^{-2} s^{-1} Hz^{-1} sr^{-1}.

3.5 Discussion

We have used C I fine structure absorption in high resolution, high signal-to-noise data to study the physical conditions in DLAs at high redshift.

Our work differs from previous studies of C I fine structure absorption because we did not assume a gas temperature in order to derive the density. Rather, we assume ionization equilibrium, which in conjunction with the C I fine structure data, allows us to constrain both the temperature and the density of the cloud. In addition, we use the C II* technique to determine the local radiation field due to stars and include its contribution to the C I fine structure excitation, thus providing a complete and fully self-consistent model of the gas. In most cases, the C I fine structure excitation is consistent with the ${J_\nu}^{local,C\,II^*}$, derived independently by the C II* technique.

To draw meaningful comparisons between the C I results and those of the C II* technique we must first analyze our possible systematic errors. The primary source of error in the C I analysis stems from two sources – 1) measurement error of the fine structure column densities (we report results for 2σ errors), and 2) the assumption that in solar units the carbon abundance is equal to that of Si II (or S II) -0.2 dex in case of minimal depletion. The source of systematic errors in the C II* technique are slightly more difficult to assess (see WGP03 for a complete discussion). We explore the possible effects of these errors in the following section and demonstrate that, even considering these errors, the C I data appear to be probing gas of higher densities and pressures – likely small knots of gas within the larger DLA galaxies – than that probed by the 'global' C II* technique.

3.5.1 Comparison with C II* technique model

Because it is difficult to assess the systematic errors involved in the C II* technique, and because some of the potential uncertainties have been removed since the work of WGP03 (i.e. the SMC dust model is now assumed to be correct because of the non-detection of the 2175$\mathring{A}$ dust feature that would have indicated Galactic dust. Moreover, the reddening curve resembles SMC rather than Galactic or LMC), we focus on the two largest potential uncertainties: 1) the assumption of the value assumed for the equilibrium pressure, P_{eq}, and 2) the minimal versus maximal depletion model (see discussion in section 2.3 of WGP03). The standard C II* technique involves solving the equations of thermal and ionization equilibrium as described in WPG03 and Wolfire et al. (1995). A unique solution is determined by assuming that the equilibrium pressure is equal to the geometric mean between P^{max} and P^{min}, $P_{eq} = P_{geo} = (P_{min}P_{max})^{1/2}$, where P_{min} and P_{max} are the minimum and maximum pressures of the function P(n) where n is gas density. This results in two stable solutions for a given star formation rate, one WNM and one CNM, and is the basis of the two-phase model. However, a two-phase medium can achieve equilibrium with a pressure ranging from P_{min} to P_{max}, and therefore, the assumption of P_{eq} equal to the geometric mean, while reasonable (see Wolfire et al. 2003 and WPG03 discussion), is still an unproven assumption. Following WGP03 we attempt to gain a sense of the possible systematic errors by allowing P_{eq} to vary between P_{min} and P_{max}. In Figure 3.27, we show the standard two-phase diagram, plotting in (a), log(P/k) versus density for various star formation rates per unit area (which are proportional to J_ν) which are constant along each P(n) curve, and which increase from bottom to top, and in (b) $\log(\ell_c)$ versus density for ℓ_c equilibrium solutions for those same star formation rates. The green dashed line in each plot indicates the P(n) solution for heating by background radiation alone (i.e. $\log\Sigma_{SFR} = -\infty$). The black horizontal line in (b) denotes the observed cooling rate of DLA 1331+17, $\log(\ell_c) \leq -27.14$. Three vertical, black, dotted lines illustrate the location of the CNM stable points associated with, from left to right, P_{min}, $P_{geo}= (P_{min}P_{max})^{1/2}$, and P_{max} for the case of background radiation alone. The stable (ℓ_c, n) pairs for the grid of star formation rates are denoted by the three red lines in (b), where the three different pressure assumptions have been made – from left to right they are: dashed = P_{min}, dot-dashed = P_{geo}

and dotted = P_{max}. Although not relevant for our current discussion, it is seen that P_{min} requires a higher star formation rate and lower density to achieve an equilibrium solution with a cooling rate equal to that observed. On the opposite extreme, P_{max} requires a higher density and lower star formation rate.

For the purposes of this paper, we are interested in the range of densities and temperatures that result from these different model assumption inputs to the C II* technique. In Figure 3.28, we plot the resultant log(P/k) versus density for our example case of DLA 1331+17. For the minimal depletion model, the case of $\mathrm{P}_{eq} = \mathrm{P}_{geo} = (\mathrm{P}_{min}\mathrm{P}_{max})^{1/2}$ is denoted by the asterisk. Lines connect to the P_{min} and P_{max} solutions, providing a sense for the potential systematic "error" involved in the assumption of where the equilibrium pressure resides. We have also plotted the results of the maximal depletion model, denoted by the diamond, with dashed lines connecting to the associated P_{min} and P_{max} solutions. To correctly compare this range of solutions to that of the C I data we must re-model the C I theoretical curves in each case because the change in the assumed P_{eq} results in a change of star formation rate, or ${J_\nu}^{local}$, which is an input for the C I theoretical curves. We plot the 2σ results of the C I analysis for ${J_\nu}^{local}$ spanning that determined by P_{min} and P_{max}. We summarize the results of these two techniques for DLA 1331+17 in Table 3.15.

It is seen that the densities determined by the C II* technique are systematically lower than those determined by the C I data. As a result, the overall pressures are lower. The temperatures vary depending on model assumptions, but are in general agreement or higher than the C I results (see Table 3.15). In Figures 3.29, 3.30, 3.31, 3.32, we show the results for DLA 2231−00 and DLA 0812+32 components 1 and 2, done individually, and then finally the global solution of DLA 0812+32. We conclude that the C I gas is tracing a denser region of the DLA than that traced by the global C II* technique: essentially, the C I resides primarily in small, overdense knots. This implies however, that the C I

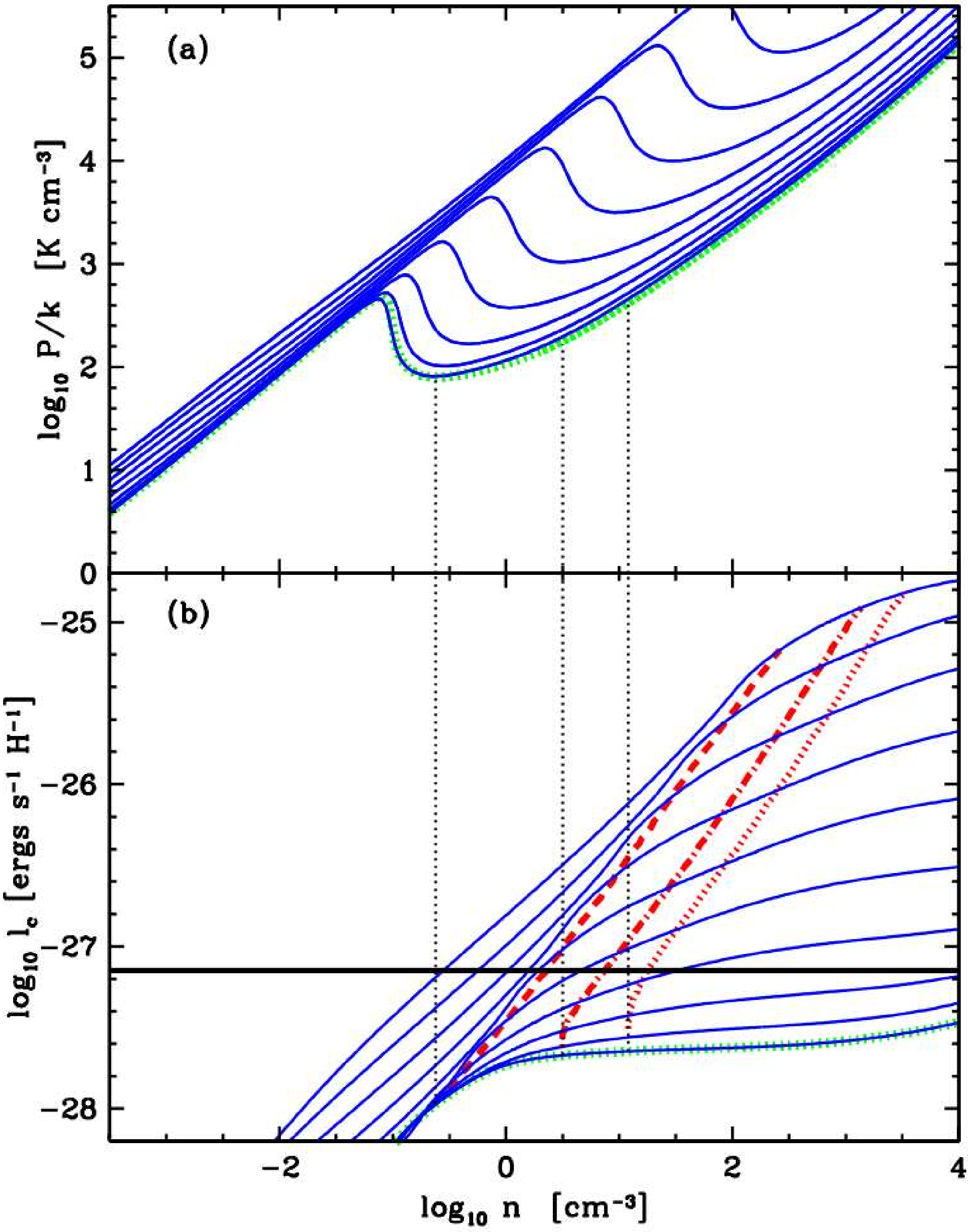

Figure 3.27: Pressure curves and star formation rate solutions for DLA 1331+17. The blue model curves for different star formation rates represent $\log\Sigma_{SFR} = -\infty, -4, -3.5, ..., 0.0$. The CNM P_{min}, P_{eq} and P_{max} solutions are indicated by the red dashed lines.

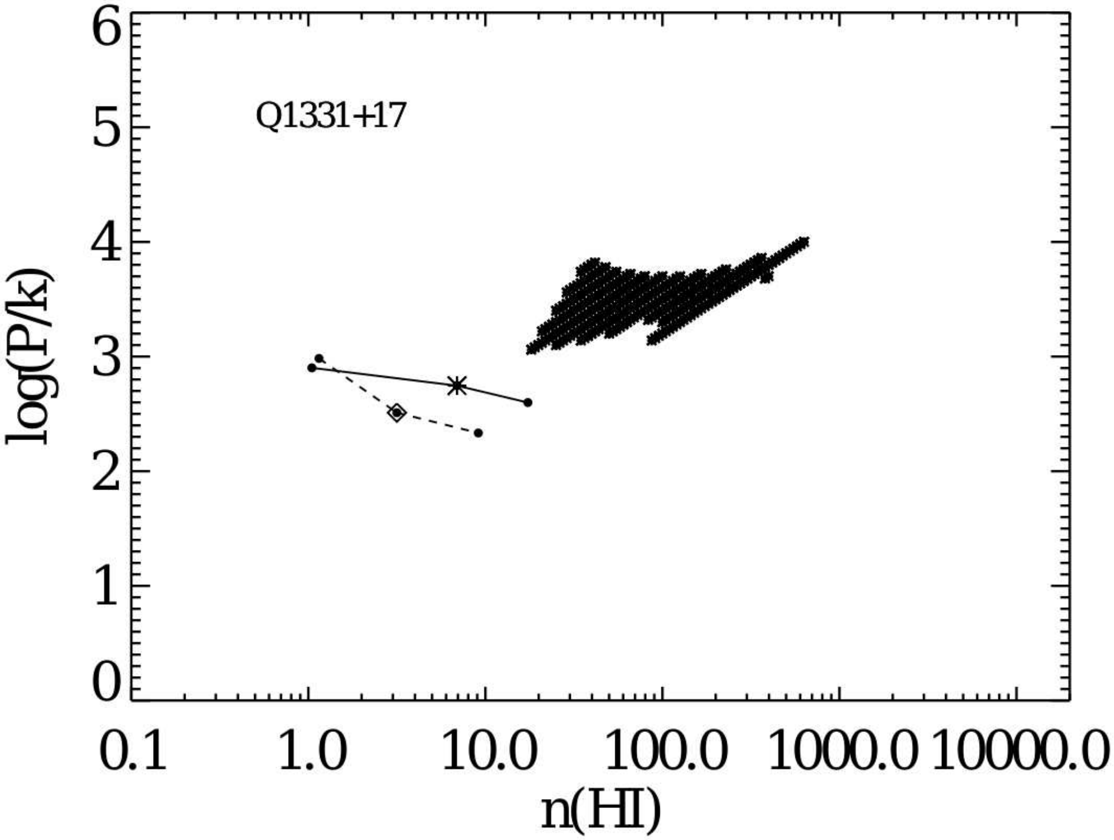

Figure 3.28: DLA 1331+17 2σ range of solutions for range of C II* technique solutiuons. The minimal depletion C II* solution is indicated by the asterik, with P_{min} and P_{max} denoted by points at the ends of attached lines, while the maximal depletion model is denoted by a diamond, and the P_{min} and P_{max} at the ends of dashed lines.

Table 3.15. COMPARISON OF C I [a] AND C II* TECHNIQUE MODELS FOR DLA 1331+17

model	J_ν^{local} /10^{-19} [b]	T [K]	n [cm^{-3}]	log(P/k) [cm^{-3} K]	$\log(\frac{CII}{CI})$
C II*, P_{eq}^{c}, min[d]	3.09	80.6	6.9	2.75	3.70
C I, P_{eq}, min	3.09	16−32	91−363	3.36−3.86	2.6498
C II*, P_{max}, min	1.74	22.9	17.4	2.6	3.23
C I, P_{max}, min	1.74	25−79	38−166	3.18−3.72	2.6498
C II*, P_{min}, min	4.90	761.5	1.0	2.88	4.51
C I, P_{min}, min	4.90	16−25	138−631	3.44−4.0	2.6498
C II*, P_{eq}, max[e]	1.64	102.4	3.2	2.52	3.69
C I, P_{eq}, max	1.64	32−158	18−87	3.06−3.82	2.8498
C II*, P_{max}, max	0.65	23.6	9.1	2.33	3.04
C I, P_{max}, max	0.65	50−398	13−52	3.12−4.06	2.8498
C II*, P_{min}, max	7.34	838.8	1.1	2.97	4.62
C I, P_{min}, max	7.34	13−25	87−457	3.14−3.86	2.8498

[a] C I results are all 2 σ

[b] ergs cm^{-2} s^{-1} Hz^{-1} sr^{-1}

[c] $P_{eq} = (P_{min} \, P_{max})^{1/2}$

[d] Minimal Depletion Model

[e] Maximal Depletion Model

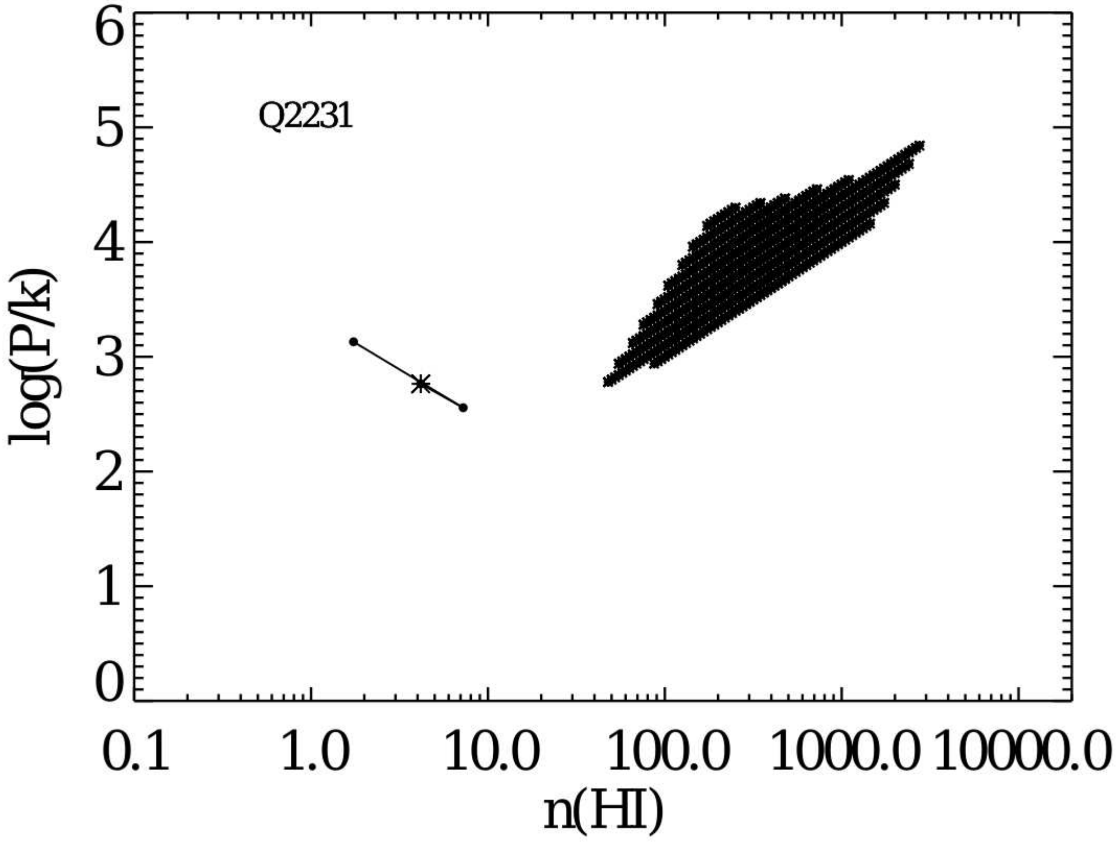

Figure 3.29: DLA 2231−00 2σ range of solutions for range of C II* technique solutiuons. The minimal depletion C II* solution is indicated by the asterik, with P$_{min}$ and P$_{max}$ denoted by points at the ends of attached lines.

region is not in pressure equilibrium with the surrounding region indicated by the C II* technique. We speculate that the higher pressures in the C I region arise in the post-shock regions located behind shock fronts propagating through the C II* region.

These comparisons also reveal a discrepancy between the $\frac{C\,II}{C\,I}$ derived by the C II* technique analysis and the observed $\frac{C\,II}{C\,I}$. In general, the observed $\frac{C\,II}{C\,I}$ ratio is approximately an order of magnitude smaller than that predicted by the C II* technique model (see Table 3.15). We avoid a detailed discussion here and refer the interested reader to WGP03, section 5.1, for a detailed discussion

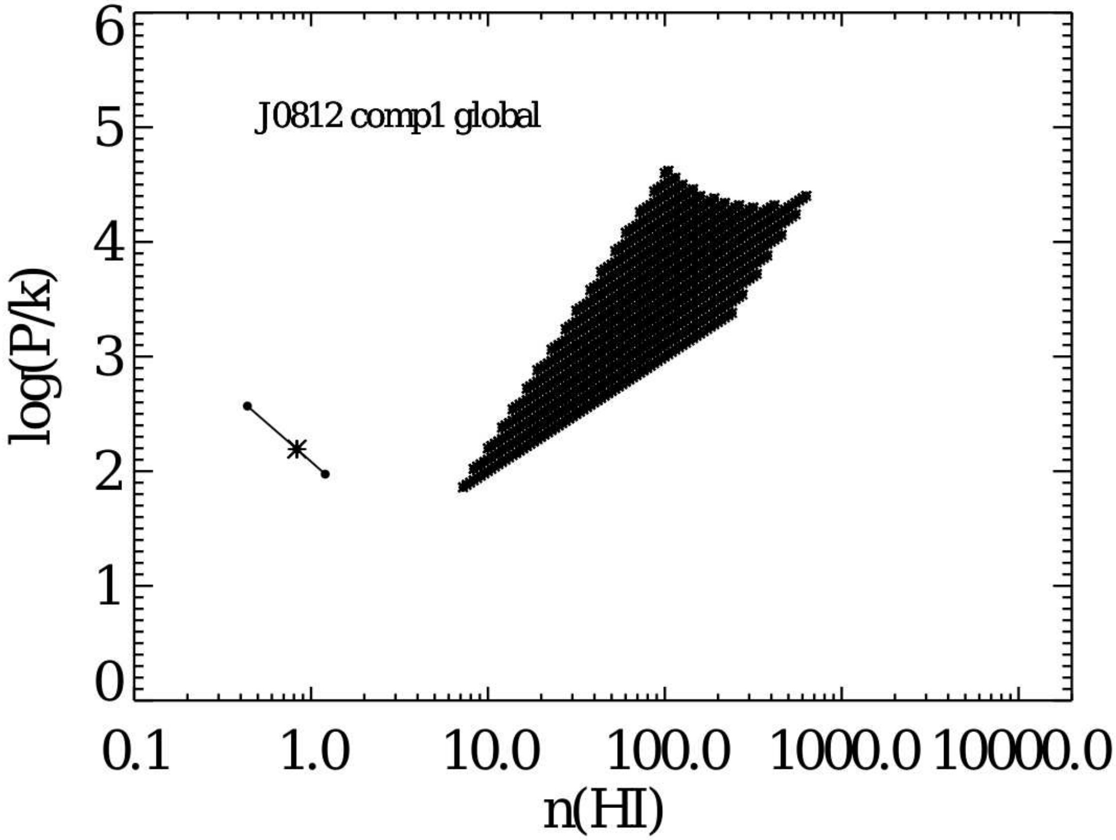

Figure 3.30: DLA 0812+32 component 1 global 2σ range of solutions for range of C II* technique solutiuons. The minimal depletion C II* solution is indicated by the asterik, with P$_{min}$ and P$_{max}$ denoted by points at the ends of attached lines.

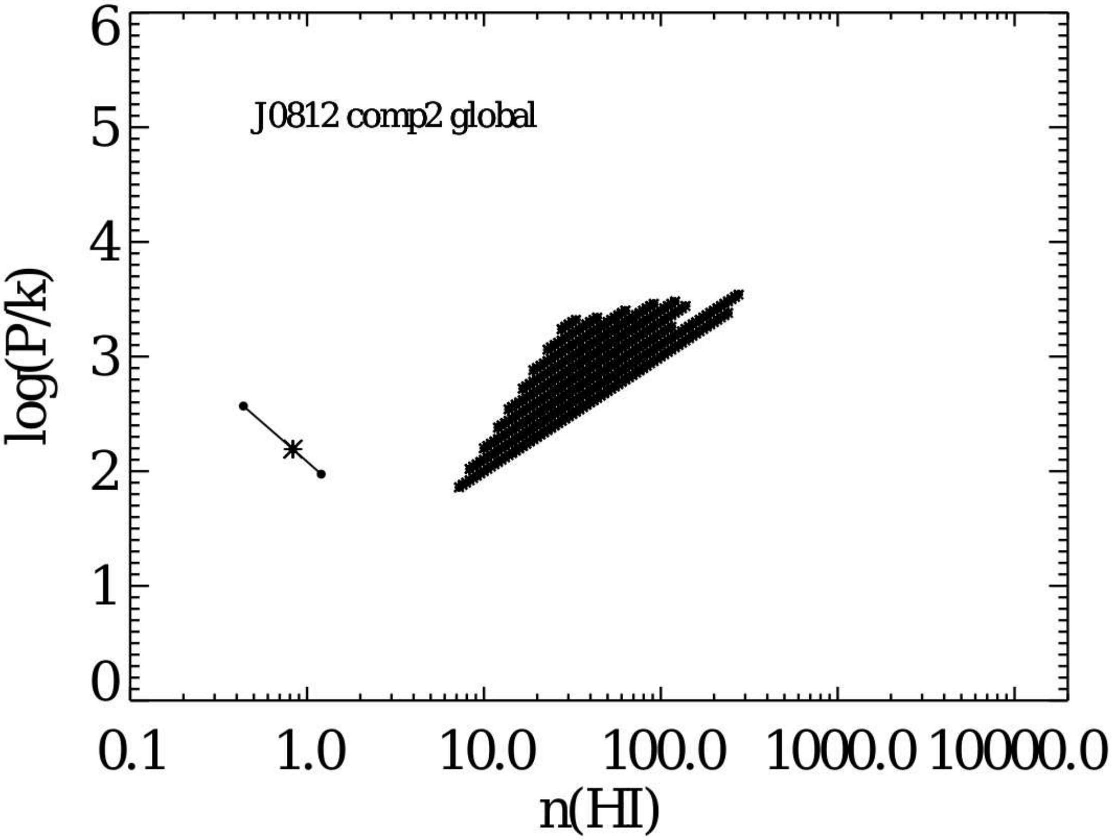

Figure 3.31: DLA 0812+32 component 2 global 2σ range of solutions for range of C II* technique solutiuons. The minimal depletion C II* solution is indicated by the asterik, with P$_{min}$ and P$_{max}$ denoted by points at the ends of attached lines.

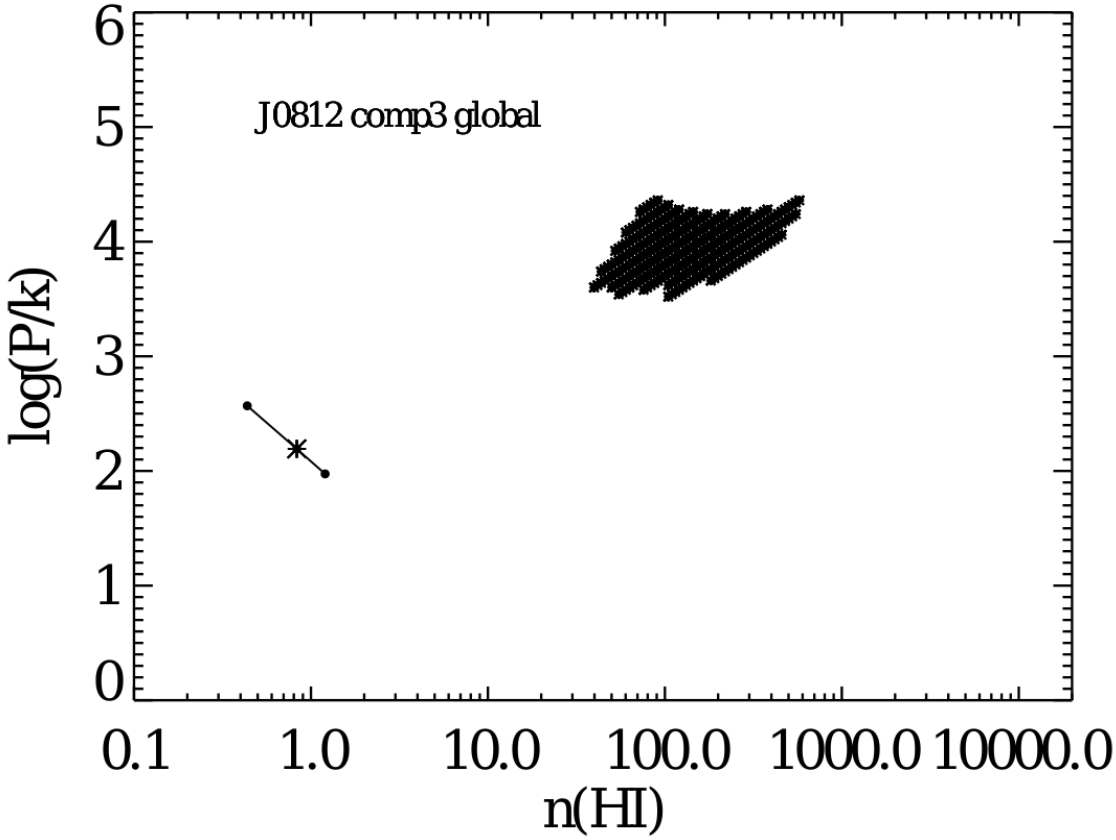

Figure 3.32: DLA 0812+32 component 3 global 2σ range of solutions for range of C II* technique solutiuons. The minimal depletion C II* solution is indicated by the asterik, with P_{min} and P_{max} denoted by points at the ends of attached lines.

of the model inputs that affect $\frac{C\,II}{C\,I}$. We only briefly mention that we have tested the results with cosmic rays turned on and off, and there is not a large effect on the results for the star formation rates we are considering. However, this is not the case for large star formation rates, $J_\nu{}^{total}$ ~10^{-18} ergs cm^{-2} s^{-1} Hz^{-1} sr^{-1}, for which the effect of cosmic rays becomes more important. Assuming that the C II* technique model is correct, we can understand this difference in terms of the new model in which the bulk of the measured C I is localized in small, dense clumps relative to the larger DLA. In this case, while the cloud is still optically thin and feels the same radiation field as the surrounding medium, the increased density, and hence, increased electron density, n_e, of the C I cloud work to lower $\frac{C\,II}{C\,I}$ because $\frac{C\,II}{C\,I}$ is inversely proportional to density for a fixed radiation field. In a sense, this conflict with the predictions of the 'global' C II* technique model, is an expected result of the overdense-C I -region model.

3.5.2 Relation to 'high-cool' DLA population

With the exception of DLA 1331+17, all of the C I -bearing objects not only contain C II* (as compared with ~50% of the general DLA population) but also have cooling rates, ℓ_c, that place them firmly in the 'high-cool' range defined by Wolfe et al. (2008) (median 'high-cool' $\log\ell_c = -26.6$). A literature search, summarized in Table 3.16, reveals that all DLAs with positive detections of C I fall into the 'high-cool' population as well. While it is not clear how the bimodality discovered by Wolfe et al. (2008) is related to C I, this correlation – that almost all C I -bearing DLAs are also high-cool DLAs, could simply be a result of the higher metallicities and dust to gas ratios that are required to form and sustain through dust shielding of UV radiation, measurable amounts of H_2 and C I. This trend, of higher metallicity DLAs being more likely to contain measurable H_2, has been observed previously by Petitjean et al. (2006). Additionally, the 'high-cool' DLAs, proven by Wolfe et al. (2008) to consist of primarily CNM, simply might be an environment more conducive to the presence of H_2 and C I.

Table 3.16. LITERATURE SEARCH FOR OBJECTS CONTAINING ALL THREE STATES C I, C I*, and C I**

DLA	z_{abs}	NHI	N(CI)	N(CI*)	N(CI**)	N(CII*)	log l_c
Q0013−004^{a,b}	1.96822	20.83±0.05	13.04±0.01	13.10±0.01	12.77±0.02	14.28^{c}	−26.07
Q0013−004^{a}	1.97296	20.83±0.05	13.44±0.01	13.20±0.01	12.53±0.04	14.28^{c}	−26.07
HE0027−1836^{d}	2.402	21.75±0.10	12.25±0.15	<12.27	...	14.32^{d}	−26.95
Q0347−383^{a}	3.02485	20.73±0.05	11.73±0.26	<11.50	<11.75	13.55±0.23	−26.70
Q0405−443^{a}	2.59474	21.05±0.10	<12.23	...	...	13.66	−26.91
Q0551−366^{a,b}	1.96214	20.70±0.10	12.66±0.12	12.69±0.11	12.11±0.34	12.58^{c}±0.09	−26.14^{e}
Q0551−366^{a,b}	1.96221	20.70±0.10	13.16±0.06	12.98±0.09	12.26±0.36	13.36^{c}±0.07	−26.14^{e}
Q1232+082^{a}	2.33771	20.90±0.10	13.86±0.22	13.43±0.07	12.63±0.22	<14.00	−26.42
Q1443+2724^{f}	4.2241	20.95±0.10	13.12±0.02	12.97±0.03	<12.5	>14.709	−25.76
Q1444+014^{a}	2.08679	20.25±0.07	12.67±0.09	12.52±0.14	...	13.12±0.08	−26.65
Q1444+014^{a}	2.08692	20.25±0.07	12.82±0.11	12.42±0.12	...	12.78±0.20	−26.99
HE2318−1107^{d}	1.989	20.68±0.05	12.63±0.02	12.30±0.04	...	...	...
Q2332−094^{a,b}	2.28749	20.25±0.07	13.33±0.03	13.14±0.03	12.34±0.11	...	...

[a] Data from Srianand et al. (2005)

[b] Contains many CI components – listed here are only the components with all three fine structure states measured

[c] C II* taken from Ge & Bechtold (1997) measurement.

[d] Data from Noterdaeme et al. (2007b); sum of the 3 C II* components

[e] ℓ_c determined from global N(C II*) = 14.0841

[f] Data from Ledoux et al. (2006)

3.5.3 Comparison with the local ISM

In this section we compare our C I-bearing clouds to the ISM of the local Universe, namely, the Milky Way and the Small and Large Magellanic Clouds (the SMC and LMC respectively). To draw these comparisons, we first determine the median values of crucial parameters describing our C I -bearing DLAs, such as n, T and P/k. Of course, this median is dependent upon which models we choose to include. Here, we include models for each DLA that we believe are the most likely to be correct. We plot the best-fit C I solutions, as determined by χ^2 minimization, in Figure 3.33. The resulting median values for this sample are: n = 110 cm^{-3}, T = 40 K, and log(P/k) = 3.54 cm^{-3} K .

In the Milky Way, Jenkins & Tripp (2001) used very high resolution (R = 200,000) STIS data to analyze C I fine structure populations and find a median log(P/k) = 3.35cm^{-3} K . This median pressure is similar to the pressures we derive in high redshift C I -bearing DLAs, where the median pressure derived from our most likely models is log(P/k) = 3.54 cm^{-3} K . However, in the case of the Milky Way, the high pressure is driven by the much higher heating rate (logℓ_c ~ -25 ergs s^{-1} H^{-1}), a result of the higher dust to gas ratio (typically 30 times that of DLAs), and similar values of ${J_\nu}^{total}$, since the heating rate is proportional to $\kappa \times J_\nu$. In contrast, the heating rates in high redshift DLAs are generally 1−2 orders of magnitude smaller. In fact, this is the reason that the global pressures derived from the C II* technique are smaller. Hence, the pressures derived in the C I -bearing clouds, while similar to those observed in the Milky Way, are not the result of the same physical conditions as those observed in the Milky Way. (Jenkins & Tripp (2001) also observe a small proportion of the gas in many sightlines to be at very high pressures, p/k > 10^5 cm^{-3} K , which they speculate are caused by converging flows in a turbulent medium or in turbulent boundary layers.)

It is perhaps more meaningful to compare DLAs with the Large and

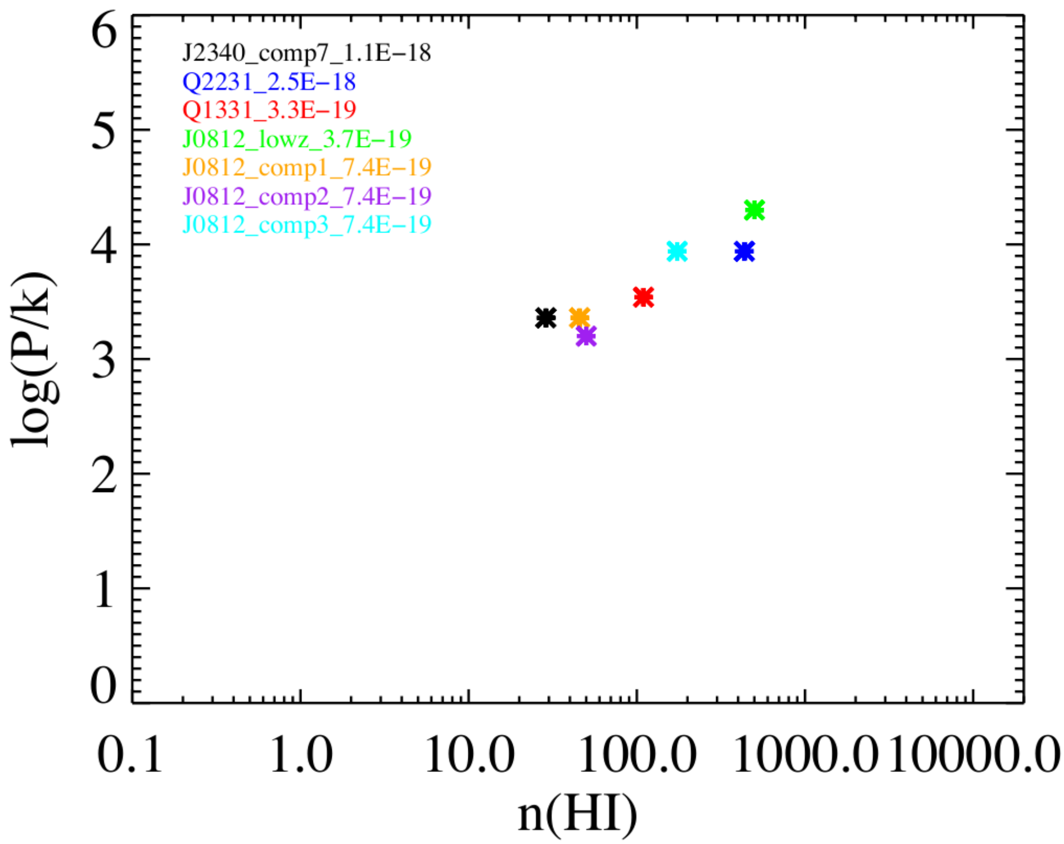

Figure 3.33: The best-fit solution for each DLA from minimum χ^2 analysis. We show here the most likely models. This sample gives a median density n = 110 cm^{-3}, median T = 40 K, and median log(P/k) = 3.54 cm^{-3}K.

Small Magellanic Clouds that, like DLAs, are known to have sub-Milky Way dust to gas ratios and metallicities. Tumlinson et al. (2002) performed a FUSE survey of H_2 along 70 sightlines to the Small and Large Magellanic Clouds. For all sightlines with $\log N(H_2) \geq 16.5$ cm^{-2} they find $< T_{01} > = 82 \pm 21$ K, whereas for all sightlines (including those at lower columns), they find $< T_{01} > = 115$ K. They compare this with the Galactic average, T = 77 ± 17 K. The temperatures found by the C I and H_2 data presented here is in broad agreement with these values. Specifically, the H_2 derived temperatures for DLA 0812+32 are in good agreement with the LMC and SMC temperatures. The H_2 derived temperatures for DLA 2340−00 are slightly higher (~200 K) and generally closer to those derived by Srianand et al. (2005) who find that in a sample of H_2 -bearing DLAs at high redshift, the mean kinetic temperature of the gas, T = 153 ± 78 K, is slightly higher than that of the local ISM.

3.6 Conclusions

The goal of this paper is to further constrain the physical conditions in high redshift DLAs through the accurate determination of densities and temperatures. In common with several other authors, we utilized C I fine structure lines to determine densities, however, instead of assuming a temperature, our work allowed for a full range of densities and temperatures and constrained the possible solutions using the C I fine structure data and the assumption of ionization equilibrium.

Our major conclusions are as follows:

1. The steady state analysis of C I fine structure populations along with the assumption of ionization equilibrium provides realistic constraints on both the volume density *and* temperature of high redshift DLAs. The C I data are in general consistent with the radiation fields, ${J_\nu}^{local,C\,II^*}$, derived from

the C II* technique and provide further evidence of the presence of CNM.

2. The densities and pressures of the C I - bearing gas are systematically higher than those of the 'global' DLA predicted by the C II* technique. We propose that the C I gas resides in overdense regions possibly created by shocks.

3. As noted by Srianand et al. (2005), all C I -bearing DLAs also contain C II* absorption. We find that, with only one exception, all C I objects for which C II* coverage is available (4 presented in this paper, 1 yet to be published, and 7 from the literature) contain strong C II* absorption, placing them in the category of 'high-cool' DLAs. This could be simply a consequence of the fact that C I -bearing DLAs generally host larger fractions of H_2 whose formation is encouraged by the higher than average metallicities and dust to gas ratios, consistent with the 'high-cool' population of DLAs.

4. High resolution studies of neutral carbon lines reveal narrow, sub-1km s^{-1} , unresolved components. These components likely contain relatively large amounts of gas and are most likely cold, dense knots, perhaps photodissociation regions on the edges of star forming regions. This would explain the presence of C I, H_2, and larger than average dust to gas ratios. We discovered a narrow component ($b = 0.38 \pm 0.04$ km s^{-1}) in DLA 0812+32, and report on the previous discovery of a narrow component in DLA 1331+17 (Carswell et. al, in preparation). It is possible that these narrow components contain significant amounts of gas that has been previously missed in lower resolution studies. However, given the evidence from AODM studies and hidden component analysis that show there is not significant amounts of gas in hidden saturated components, it is unlikely that these narrow components will solve the missing-metals problem or significantly alter the metallicities of DLAs.

3.7 Appendix 1: Empirical Determination of C I 1560.3092$\mathring{A}$ f$_{jk}$ value

We used high signal-to-noise data from five DLAs to determine the f-value of f$_{jk}$ = 0.091014 for the C I 1560.3092$\mathring{A}$ transition used in this work. We were motivated to do this because we had difficulty simultaneously fitting several multiplets for all of our objects when using either the published Morton (2003) f-value, f$_{jk}$ = 0.0774 or the f$_{jk}$= 0.131595 of Jenkins (2006).

We followed the process outlined in Jenkins & Tripp (2006) to determine the 'unknown' f-value based on the assumption that the f-value of the C I 1656.9284$\mathring{A}$ transition is correct. In principle, because the column density of C I is the same in each transition λ1656 and λ1560, the 'unknown' f-value can be determined by taking the ratio of the equivalent widths of the two transitions times their wavelengths squared and f-values as follows,

$$\frac{W_{\lambda}^{1656}}{\lambda_{1656}^{2} f_{jk}^{1656}} = \frac{W_{\lambda}^{1560}}{\lambda_{1560}^{2} f_{jk}^{1560}} \tag{3.8}$$

from which we get

$$f_{jk}^{1560} = \frac{W_{\lambda}^{1560}}{W_{\lambda}^{1656}}(0.1678) \tag{3.9}$$

We used AODM to measure the optical depth, τ, in each case for DLAs 1331+17, 0812+32 (both z$_{abs}$ = 2.06 and z$_{abs}$ = 2.626), 2340−00, and 2123−0050 (a sub-DLA not used in this paper), and plot the results in Figure 3.34. Using all 5 systems resulted in f$_{jk}{}^{1560}$ = 0.091914 ± 0.003395, the f-value that we adopt in this paper.

3.8 Appendix 2: Molecular Hydrogen

The purpose of this Appendix is to present an outline of the molecular hydrogen analysis performed in this work. While the focus of this work was

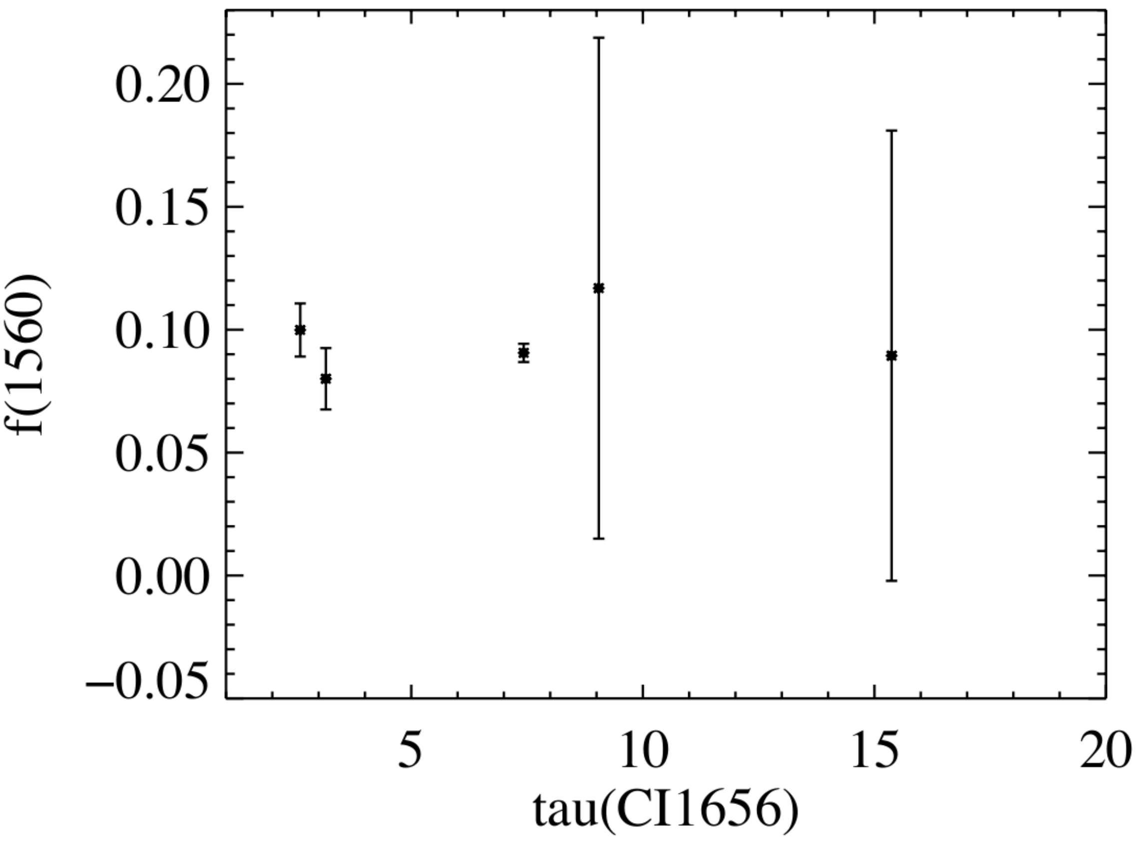

Figure 3.34: The determination of $f_{jk}{}^{1560}$. From left to right data points represent DLAs 0812+32 ($z_{abs} = 2.62$), 0812+32 ($z_{abs} = 2.06$), 1331+17, 2123−00 (not used in this paper), and 2340−00.

the analysis of neutral carbon, DLAs that contain neutral carbon are likely to also contain detectable H_2. This is because neutral carbon and molecular hydrogen are photoionized and photodissociated respectively, by photons of the same energies and therefore, they are usually found together. This is the case in several of the DLAs presented in this work, i.e. DLA 1331+17, DLA 0812+32, and DLA 2340−00. For DLA 2231−00 and the low z DLA 0812+32, we did not have coverage of the H_2 region and therefore cannot determine anything about the presence of H_2. Here we present an outline of the DLA H_2 analysis frequently performed in the literature, most recently by works such as Levshakov et al. (2002), Hirashita & Ferrara (2005), Cui et al. (2005), Noterdaeme et al. (2007a), and Noterdaeme et al. (2007b) and based upon work by Spitzer & Zweibel (1974), Jura (1975a) and Jura (1975b). Essentially, the measurement of H_2 in the different rotational J states allows for an independent estimation of the physical properties of the cloud such as density, temperature and the incident radiation field. While the H_2 analysis arguably contains several uncertainties and assumptions, it is nonetheless interesting to compare the results from these two independent methods, the H_2 analysis we present below and the C I fine structure analysis presented in this work.

First, we can estimate the kinetic temperature of the cloud using the column densities of H_2 in the J=0 and higher J rotational states. According to the Boltzmann distribution (see equation 8 in Levshakov et al. (2002)):

$$\frac{N(J)}{N(0)} = \frac{g(J)}{g(0)} e^{-} \frac{-B_v J(J+1)}{T_{ex}} \tag{3.10}$$

where B_v = 85.36 K for the vibrational ground state and g(J) is the degeneracy of level J, given by, for level J = x, $g_x = (2J_x + 1)(2I_x + 1)$ where I = 0 for even x and I = 1 for odd x (For states J = 0−5, g = [1, 9, 5, 21, 9, 33]). The excitation diagram is typically plotted as log (N_J / g_J) versus the relative energy between the level J and J = 0. The excitation temperature, defined in equation

3.10, is inversely proportional to the negative slope of the line connecting the excitation diagram points, i.e.

$$T_{ex}^{0J} = -B_v J(J+1)\frac{1}{ln\frac{g_0 N_J}{g_J N_0}} \tag{3.11}$$

The typical assumption is that the kinetic temperature of the cloud can be estimated by the excitation temperature derived from the population of H_2 in the states J = 0 and J = 1, assuming that the J = 1 level is thermalized. The higher J states (J $\geq$ 2) are typically characterized by a higher T_{ex}, or flatter slope, which is explained by population mechanisms other than collisions.

The higher T_{ex} derived from the population of H_2 in the higher rotational J states was originally unexpected (Spitzer & Zweibel 1974). After observations by Spitzer and Chochran in the 1970s in which they observed the high excitation temperatures derived from the high J states, Spitzer & Zweibel (1974) proposed methods other than collisions that could populate the higher J states. They proposed two methods other than collisions: 1) the cascade down from upper vibrational levels following the absorption and reemission of Lyman and Werner band photons – i.e. the J = 0 molecule is excited to a higher vibrational state and then de-excites to a higher J state in the ground vibrational state (rather than staying in the original J=0 or J=1 state), or 2) the direct formation of H_2 in a higher state (i.e. the H_2 pops off the dust particle in an excited state and cascades to say J = 4). Since these processes are believed to dominate collisions, the typical practice is to neglect collisions and to consider only these two processes, as we show in the following analysis.

Assuming steady state and neglecting collisions, we use the two afore mentioned populating mechanisms and assume depopulation by spontaneous emission (true until the density is above 10^4), to write the following steady state equations for state J = 4 and J = 5 respectively (these are equations 2a and 2b from Jura (1975b)),

$$p_{4,0}\beta_0 n(H_2, J=0) + 0.19Rn(HI)n(H) = A_{4,2}n(H_2, J=4) \qquad (3.12)$$

and

$$p_{5,0}\beta_1 n(H_2, J=1) + 0.44Rn(HI)n(H) = A_{5,3}n(H_2, J=5) \qquad (3.13)$$

where p is the pumping coefficient or pumping efficiency (Jura calls this the redistribution probability) into the J=4 and J=5 levels from the J=0 and J=1 levels respectively, β is the photoabsorption rate, R is the H_2 molecule formation rate (on dust grains, also known as R_{dust}), n(H I) is the neutral hydrogen number density, n(H) $\approx$n(H I) + 2n(H_2), and $A_{i,j}$ are the spontaneous transition probabilities. In other words, the first term is the UV excitation and decay to higher J state, while the second term represents the direct formation in the higher J states. The values of the constants are as follows: $A_{4,2} = 2.75 \times 10^{-9}s^{-1}$, $A_{5,3} = 9.9 \times 10^{-9}s^{-1}$ (Spitzer 1978), $p_{4,0} = 0.26$, and $p_{5,1} = 0.12$ (Jura 1975b). Solving for β will allow us to estimate the UV field incident on the cloud, while β together with R will allow us to estimate the neutral hydrogen density.

In order to solve for β and to get rid of the N(H I) dependence in equation 3.12, we take advantage of the assumption of equilibrium between the formation and the destruction of H_2 (which is reasonable because the time scales of H_2 formation and destruction are well below a dynamical time), as follows,

$$Rn(HI)n(H) = R_{diss}n(H_2) \qquad (3.14)$$

If we substitute equation 3.14 into equation 3.12, and make the common assumption that 11% of photoabsorption leads to photodissociation (Jura 1974)
,

$$R_{diss} = 0.11\beta \qquad (3.15)$$

we obtain equilibrium equations that are independent of the neutral hydrogen column density $N_{\rm HI}$,

$$p_{4,0}\beta_0\frac{N(H_2, J=0)}{N(H_2)} + 0.021\beta_0 = A_{42}\frac{N(H_2, J=4)}{N(H_2)} \tag{3.16}$$

and

$$p_{5,0}\beta_1\frac{N(H_2, J=1)}{N(H_2)} + 0.049\beta_1 = A_{53}\frac{N(H_2, J=5)}{N(H_2)} \quad . \tag{3.17}$$

Using the measured H_2 column densities we can then solve for β, the photoabsorption rate of H_2 in each component. Note, that β_0 should equal β_1.

Once we have solved for β we can determine the incident radiation field by using the relation between the radiation field and the photodissociation rate that it induces on the molecular hydrogen. Following Abel et al. (1997) and Hirashita & Ferrara (2005),

$$R_{diss} = (4\pi)1.1\times10^8 J_\nu^{LW} S_{shield} s^{-1} \tag{3.18}$$

where R_{diss} is the photodissociation rate (= 0.11β as above), ${J_\nu}^{LW}$ (LW stands for Lyman-Werner) is the UV intensity at hν = 12.87 eV averaged over the solid angle (12.87 eV is the dominant energy at which the photodissociation happens. This can be compared with the J_ν of the C II* technique that is calculated at λ = 1500Å, or 8.27 eV). S_{shield} accounts for shielding due to two effects: 1) dust shielding and 2) self-sheilding. In order to solve for ${J_\nu}^{LW}$ we must determine the effects of shielding in equation 3.18. We estimate the shielding, following Hirashita & Ferrara (2005), as

$$S_{shield} = (\frac{N(H_2)}{10^{14}cm^{-2}})^{-0.75}e^{-\sigma_d N_d} \tag{3.19}$$

where the first term expresses the self-shielding and the exponential term is the shielding due to dust. N_d, the column density of dust, is related to the HI column density by: $(4/3)\pi\ a^3\delta N_d = 1.4\ m_H N_H D$, where 1.4 is the correction for the helium content, and σ_d is the cross-section of a grain, $\sigma_d = \pi\ a^2$. $\sigma_d\ N_d = \tau_{UV}$ is the optical depth in dust and is expressed by Hirashita & Ferrara (2005) as,

$$\tau_{UV} = \frac{4.2 N_H m_H D}{4a\delta} = 0.879(\frac{a}{0.1\mu m})^{-1}(\frac{\delta}{2g\ cm^{-3}})^{-1}(\frac{D}{10^{-2}})(\frac{N_H}{10^{21}cm^{-2}}) \quad (3.20)$$

where a is the radius of a grain, δ is the grain material density, and D is the dust-to-gas mass ratio. Hirashita & Ferrara (2005) assume the Galactic (Milky Way) dust-to-gas mass ratio to be $D_\odot = 0.01$. They define the normalized dust-to-gas ratio $\kappa = D/D_\odot$. Assuming a=0.1 and δ=2, equation 3.20 can be written,

$$\tau_{UV} = 0.879\kappa(\frac{N_H}{10^{21}cm^{-2}}) \quad (3.21)$$

also see Cui et al. (2005) equation 7.

The first part of equation 3.19, the self-sheidling of H_2, is taken from an analytic approximation from Draine & Bertoldi (1996) and is valid for $N(H_2) > 10^{14}\ cm^{-2}$. We can therefore rewrite equation 3.19 as,

$$S_{shield} = (\frac{N(H_2)}{10^{14}cm^{-2}})^{-0.75} exp[-0.879\kappa(\frac{N_H}{10^{21}cm^{-2}})] \quad (3.22)$$

Therefore, given β and S_{shield} we can use equation 3.18 to solve for the ambient radiation field, ${J_\nu}^{LW}$. Note that this is the total radiation field, or ${J_\nu}^{LW} = {J_\nu}^{total}$.

We can also use the measurements of $N(H_2)$ to estimate the volume density of H I. We define the molecular fraction, f_{H_2} as follows,

$$f_{H_2} = \frac{2n(H_2)}{n(HI) + 2n(H_2)} = \frac{2N(H_2)}{N(HI) + 2N(H_2)} \quad (3.23)$$

where we measure N(H I) and $N(H_2)$ directly. If we substitute 3.23 into 3.14 and remember that $n(H) \approx n(H\ I) + 2n(H_2)$, we can solve for the number density of hydrogen,

$$Rn(HI) = R_{diss}\frac{n(H_2)}{n(HI) + 2n(H_2)} = R_{diss}\frac{f_{H_2}}{2} \tag{3.24}$$

or

$$n(HI) = \frac{R_{diss}}{R}\frac{f_{H_2}}{2} \tag{3.25}$$

This expressions is dependent on temperature however, and we will use the detailed expression for R given by Hirashita & Ferrara (2005) (note, they use the term R$_{dust}$ to refer to R),

$$R = 4.1 \times 10^{-17} S_d(T)(\frac{a}{0.1\mu m})^{-1}(\frac{D}{10^{-2}})(\frac{T}{100K})^{1/2}(\frac{\delta}{2gcm^{-3}})^{-1} \tag{3.26}$$

where S$_d$(T) is the sticking coefficient of hydrogen atoms onto dust and everything else was defined previously. The sticking coefficient is given by,

$$\begin{aligned} S_d(T) = [1 + 0.04(T + T_d)^{0.5} + 2 \times 10^{-3}T + 8 \times 10^{-6}T^2]^{-1} \times \\ (1 + exp[7.5 \times 10^2(1/75 - 1/T_d)])^{-1} \end{aligned} \tag{3.27}$$

see Hollenbach & McKee (1979) and Omukai (2000), where T$_d$ is the dust temperature and is given by

$$T_d = 12(\chi Q_{UV})^{1/6}(\frac{A}{3.2 \times 10^{-3}cm})^{-1/6}(\frac{a}{0.1\mu m})^{-1/6}K \tag{3.28}$$

where A is a constant that depends on the optical properties of the dust grains. For silicate grains, A = 1.34 × 10^{-3} cm and for carbonaceous grains, A = 3.20 × 10^{-3} cm. Following Hirashita & Ferrara (2005) we assume Q$_{UV}$ = 1 (Q$_{UV}$ is the dimensionless absorption cross-section normalized by the geometrical cross-section) , A = 3.20 × 10^{-3} cm and a = 0.1 μm, while χ, the normalized radiation field, was calculated previously from the H$_2$ levels ($\chi = {J_\nu}^{LW} / {J_\nu}^{LW}{}_\odot$ where ${J_\nu}^{LW}{}_\odot$ = 3.2 × 10^{-20} ergs cm^{-2} s^{-1} Hz^{-1} sr^{-1}. Therefore, we can determine

R as a function of T. In the present work, we assume that T is equal to the excitation temperature as derived from the J=0 and J=1 H_2 states. Finally, we use equation 3.25 to estimate the neutral hydrogen density. Note, this method of determining temperature, density and radiation field, is independent of the C I fine structure data.

3.9 Acknowledgments

The authors wish to extend special thanks to those of Hawaiian ancestry on whose sacred mountain we are privileged to be guests. Without their generous hospitality, none of the observations presented here would have been possible. R. A. J. wishes to thank Bob Carswell for many useful conversations and help with using the VPFIT software.

4

Bimodality in Damped Lyman α Systems

This chapter is a reprint of “Bimodality in Damped Lyman-α Systems”, by Arthur M. Wolfe, Jason X. Prochaska, Regina A. Jorgenson, & Marc Rafelski, published in the The Astrophysical Journal, 2008, Vol. 681, p. 881.

4.1 Abstract

We report evidence for a bimodality in damped Lyα systems (DLAs). Using [C II] 158 μm cooling rates, ℓ_c, we find a distribution with peaks at ℓ_c=$10^{-27.4}$ and $10^{-26.6}$ ergs s^{-1} H^{-1} separated by a trough at $\ell_c^{\rm crit} \approx 10^{-27.0}$ ergs s^{-1} H^{-1}. We divide the sample into ‘low cool’ DLAs with $\ell_c \leq \ell_c^{\rm crit}$ and ‘high cool’ DLAs with $\ell_c > \ell_c^{\rm crit}$ and find the Kolmogorv-Smirnov probabilities that velocity width, metallicity, dust-to-gas ratio, and Si II equivalent width in the two subsamples are drawn from the same parent population are small. All these quantities are significantly larger in the ‘high cool’ population, while the H I column densities are indistinguishable in the two populations. We find that heating by X-ray and FUV background radiation is insufficient to balance the cooling rates of either population. Rather, the DLA gas is heated by local radiation

fields. The rare appearance of faint, extended objects in the Hubble Ultra Deep Field rules out *in situ* star formation as the dominant star-formation mode for the 'high cool' population, but is compatible with *in situ* star formation as the dominant mode for the 'low cool' population. Star formation in the 'high cool' DLAs likely arises in Lyman Break galaxies. We investigate whether these properties of DLAs are analogous to the bimodal properties of nearby galaxies. Using Si II equivalent width as a mass indicator, we construct bivariate distributions of metallicity, ℓ_c, and areal SFR versus the mass indicators. Tentative evidence is found for correlations and parallel sequences, which suggest similarities between DLAs and nearby galaxies. We suggest that the transition-mass model provides a plausible scenario for the bimodality we have found. As a result, the bimodality in current galaxies may have originated in DLAs.

4.2 Introduction

Recent studies of $\sim 10^5$ low-redshift galaxies reveal a striking bimodality in their properties. The galaxy population is divided into two mass sequences; a 'blue' sequence with stellar masses $M_* < 10^{10.5}$ $\mathrm{M}_\odot$ and a red sequence in which $M_* > 10^{10.5}$ $\mathrm{M}_\odot$ (Kauffmann et al. 2003; Baldry et al. 2004). The 'blue' sequence is comprised of late-type galaxies undergoing active star formation, while the 'red' sequence consists of early-type galaxies with little, if any, star formation. Dekel & Birnboim (2006) suggest that the mass sequences reflect the different paths for the build up of stellar populations in galaxies. The critical parameter in their scenario is the dark-matter halo 'shock mass' , M_{shock}=$10^{11.5}$ $\mathrm{M}_\odot$, which corresponds to $M_* = 10^{10.5}$ $\mathrm{M}_\odot$. Gas accreted onto halos with masses $M_{\mathrm{DM}} < M_{\mathrm{shock}}$, i.e., halos encompassing the 'blue' population, is not heated to the virial temperature of the halo, but rather produces star-forming disks through the infall of cold streams. By contrast gas accreted onto halos with masses $M_{\mathrm{DM}} > M_{\mathrm{shock}}$, i.e., halos encompassing the 'red' population, is shock heated to the virial temperature, and accretes onto the halos in a hot cooling flow. Cold filaments penetrate the hot gas and their inflow results in star-forming bulges in massive galaxies (Dekel & Birnboim 2006; see also Bell et al. 2004; Faber et al. 2007). In this case the low density of the hot gas and feedback processes suppress star formation at $z \leq 2$.

Our purpose here is to present evidence for an analogous bimodality in the properties of damped Lyα systems (DLAs). Because these neutral-gas layers are the likely progenitors of modern galaxies (see Wolfe, Gawiser, & Prochaska 2005 [hereafter referred to as WGP05] for a review), the DLA bimodality may be related to the galaxy phenomenon discussed above. In fact we shall argue that the bimodality in modern galaxies originates in DLAs. We use a technique which, for the first time, measures bimodality in absorption-line gas [1]. Rather than obtain signatures based on starlight emitted by galaxies (e.g. Kauffmann et al. 2003), we rely on an absorption-line diagnostic, which we argue is a signature of star formation. Specifically, we measure the C II* λ1335.7 absorption line, which, if thermal balance is assumed, is an indicator of the rate at which neutral gas is heated. The crucial parameter is the [C II] 158 μm cooling rate per H atom, ℓ_c, which divides the DLA sample in such a way that objects with $\ell_c > \ell_c^{\rm crit}$ differ fundamentally from those with $\ell_c \leq \ell_c^{\rm crit}$, where $\ell_c^{\rm crit} \sim 10^{-27}$ ergs s^{-1} H^{-1}. We shall argue that ℓ_c is a tracer of star formation rates (see Wolfe, Prochaska, & Gawiser 2003 [hereafter referred to as WPG03]) and that the bimodality in ℓ_c is physically related to a transition in star-formation modes, from *in situ* star formation in DLAs with $\ell_c \leq \ell_c^{\rm crit}$ to star formation in compact 'bulge' regions sequestered away from the DLA gas in objects in which $\ell_c > \ell_c^{\rm crit}$: the higher star formation rates (SFRs) predicted for the 'bulge' models account for the higher heating rates of the surrounding DLA gas (see § 4.8). We shall argue that the bimodality in star formation modes is caused by a transition in galaxy-formation

---

[1] Prochaska et al. (2002) report evidence for bimodality in the ratio of the nitrogen to alpha element abundance, but its statistical significance is tentative owing to the small size of the sample.

modes, which ultimately is due to a transition in mass (Dekel & Birnboim (2006).

The paper is organized as follows. In § 4.3 we examine the ℓ_c distribution and discuss the results of tests to assess whether the distribution is bimodal. In § 4.4 we divide our DLA sample into two sub-samples: 'low cool' DLAs with $\ell_c \le \ell_c^{\rm crit}$ and 'high cool' DLAs with $\ell_c > \ell_c^{\rm crit}$. For each sub-sample we compile distributions of physical parameters such as absorption-line velocity width, metallicity, dust-to-gas ratio, Si II λ 1526 equivalent width, and H I column density $N_{\rm HI}$. We then determine the probability that the pair of distributions corresponding to a given parameter is drawn from the same parent population, and describe the results of these tests. In § 4.5 we discuss the physical significance of $\ell_c^{\rm crit}$ and conclude that it signifies a dividing line between two modes of star formation. In § 4.6 we give a brief summary of the results and conclude that the crucial parameter distinguishing the two populations is dark-matter mass. In § 4.7 we draw analogies between bimodality in DLAs and in modern galaxies and show how the two are related. We also place these results in the context of modern theories of galaxy formation. Conclusions are given in § 4.8.

Throughout this paper we adopt a cosmology with
$(\Omega_{\rm M}, \Omega_\Lambda, h)$=(0.3,0.7.0.7).

4.3 Bimodality of the ℓ_c Distribution

In this section we describe evidence for bimodality in the distribution of 158 μm cooling rates, ℓ_c. The values of ℓ_c for the 76 DLAs in our sample are listed in Table 4.1 (column 7). As in previous papers (e.g. WPG03) we define ℓ_c as follows:

$$\ell_c \equiv \frac{N({\rm CII}^*)}{N_{\rm HI}} A_{ul} h\nu_{ul} \quad , \tag{4.1}$$

where N(C II*) is the column density of the excited $^2P_{3/2}$ state in the 2s^{2}2p term of C^+, A_{ul} is the Einstein coefficient for spontaneous photon decay to the ground $^2P_{1/2}$ state (A_{ul}=2.4×10^{-6} s^{-1}), and $h\nu_{ul}$ is the energy of this transition ($h\nu_{ul}/k$=92 K). All of the N(C II*) values in Table 4.1 (column 6) were deduced from velocity profiles of the C II* λ 1335.7 transition arising from the $^2P_{3/2}$ state. We obtained 47 profiles with the High Resolution Echelle Spectrometer (HIRES; Vogt et al. 1994) on the Keck I 10 m telescope. The HIRES spectra were acquired using either a 0.8 $''$ or 1.1 $''$ wide decker, resulting in velocity resolution with FWHM = 6 and 8 km s^{-1} respectively. Sixteen of the profiles were obtained with the Echellette Spectrograph Imager (ESI; Sheinis et al. 2002) on Keck II. The ESI spectra were obtained with a 0.5 $''$ or 0.75 $''$ slit (FWHM $\approx$ 33 and 44 km s^{-1} respectively). The remaining 13 profiles were obtained by other observers with the UVES spectrograph on the VLT 8 m telescope. The $N_{\rm HI}$ values were derived by fitting Voigt profiles to damped Lyα lines detected in the SDSS survey (Prochaska et al. 2005) and with the Keck telescopes, the VLT, and several 4 m class telescopes (Peroux et al. 2003; Storrie-Lombardi & Wolfe 2000; Wolfe et al. 1995). The sample in Table 4.1 comprises 32 upper limits (95 % confidence level), 37 positive detections, and 7 lower limits on ℓ_c.

Table 4.1: DLA Sample

Quasar	**RA (2000)**	**DEC (2000)**	z_{abs}[a]	**log**$_{10}$/ $N_{\rm HI}$[b]	$\log_{10} N(\rm CII^*)$[c]	$\log_{10} \ell_c$[d]	Δv_{90}[e]	**[M/H]**[f]	**[Fe/H]**[g]	W_{1526}[h]	**Ref**
Q0405-443	00:00:00.00	00:00:00.00	2.5950	$20.90^{+0.10}_{-0.10}$	13.66 ± 0.21	-26.76 ± 0.23	79	-0.96 ± 0.10	-1.33 ± 0.10	—	24
Q2359-02	00:01:50.00	-01:59:40.34	2.1539	$20.30^{+0.10}_{-0.10}$	< 14.48	< -25.34	78	-1.58 ± 0.01	-1.88 ± 0.03	0.28	6,13
Q2359-02	00:01:50.00	-01:59:40.34	2.0951	$20.70^{+0.10}_{-0.10}$	13.70 ± 0.06	-26.51 ± 0.12	142	-0.77 ± 0.02	-1.65 ± 0.03	0.83	6,13
J001328.21+135827	00:13:28.21	+13:58:27.9	3.2811	$21.55^{+0.15}_{-0.15}$	13.67 ± 0.04	-27.40 ± 0.16	10	-2.10 ± 0.16	-2.72 ± 0.02	0.28	32
BR0019-15	00:22:08.01	-15:05:38.78	3.4389	$20.92^{+0.10}_{-0.10}$	13.84 ± 0.02	-26.60 ± 0.10	118	-1.06 ± 0.05	-1.58 ± 0.04	0.76	6,13
PH957	01:03:11.38	+13:16:16.7	2.3090	$21.37^{+0.08}_{-0.08}$	13.59 ± 0.05	-27.30 ± 0.09	56	-1.46 ± 0.01	-1.90 ± 0.04	0.38	1,6,13
SDSS0127-00	01:27:00.69	-00:45:59	3.7274	$21.15^{+0.10}_{-0.10}$	13.20 ± 0.06	-27.46 ± 0.12	40	-2.40 ± 0.10	-2.90 ± 0.02	0.28	22
PSS0133+0400	01:33:40.4	+04:00:59	3.7736	$20.55^{+0.10}_{-0.15}$	14.02 ± 0.01	-26.05 ± 0.10	123	-0.75 ± 0.10	-1.07 ± 0.08	0.92	22
PSS0133+0400	01:33:40.4	+04:00:59	3.6919	$20.70^{+0.10}_{-0.15}$	12.95 ± 0.03	-27.27 ± 0.11	39	-2.34 ± 0.15	-2.74 ± 0.05	0.31	22
J013901.40-082443	01:39:01.40	-08:24:43.9	2.6773	$20.70^{+0.15}_{-0.15}$	13.81 ± 0.03	-26.40 ± 0.15	110	-1.27 ± 0.19	-1.62 ± 0.02	0.67	32
Q0149+33	01:52:34.472	+33:50:33.23	2.1408	$20.50^{+0.10}_{-0.10}$	< 12.78	< -27.24	40	-1.49 ± 0.05	-1.77 ± 0.02	0.22	6,13
Q0201+11	02:03:46.53	11:34:40.4	3.3869	$21.26^{+0.10}_{-0.10}$	14.12 ± 0.10	-26.66 ± 0.14	67	-1.25 ± 0.11	-1.41 ± 0.05	0.64	15
PSS0209+0517	02:09:44.52	+05:17:17.3	3.8636	$20.55^{+0.10}_{-0.10}$	< 12.51	< -27.55	47	-2.60 ± 0.10	-2.96 ± 0.09	0.06	22
SDSS0225+0054	02:25:54.85	+00:54:51	2.7137	$21.00^{+0.15}_{-0.15}$	> 13.37	> -27.15	60	-0.91 ± 0.14	-1.31 ± 0.04	1.08	29
J023408.97-075107	02:34:08.97	-07:51:07.6	2.3180	$20.95^{+0.15}_{-0.15}$	< 13.41	< -27.05	10	-2.74 ± 0.14	-3.14 ± 0.04	0.09	32
J0255+00	02:55:18.62	+00:48:47.94	3.9146	$21.30^{+0.05}_{-0.05}$	13.44 ± 0.04	-27.37 ± 0.06	38	-1.78 ± 0.01	-2.05 ± 0.09	—	13
J0307-4945	03:07:22.85	-49:45:47.6	4.4679	$20.67^{+0.09}_{-0.09}$	< 13.59	< -26.60	192	-1.55 ± 0.08	-1.96 ± 0.21	—	11
Q0336-01	03:39:00.99	-01:33:18.07	3.0621	$21.20^{+0.10}_{-0.10}$	14.01 ± 0.01	-26.71 ± 0.10	102	-1.54 ± 0.01	-1.81 ± 0.02	—	13
Q0347-38	03:49:43.54	-38:10:04.91	3.0247	$20.63^{+0.00}_{-0.00}$	13.47 ± 0.03	-26.68 ± 0.03	84	-1.16 ± 0.03	-1.62 ± 0.01	0.45	6,13,20
Q0458-02	05:01:12.81	-01:59:14.25	2.0396	$21.65^{+0.09}_{-0.09}$	> 14.80	> -26.37	82	-1.19 ± 0.02	-1.76 ± 0.05	0.67	6,13
HS0741+4741	07:45:21.75	+47:34:35.56	3.0174	$20.48^{+0.10}_{-0.10}$	< 12.55	< -27.44	42	-1.68 ± 0.00	-1.93 ± 0.00	0.21	13
FJ0747+2739	07:47:11.19	+27:39:03.6	3.9000	$20.50^{+0.10}_{-0.10}$	13.35 ± 0.07	-26.66 ± 0.12	150	-2.01 ± 0.01	-2.45 ± 0.03	0.22	22
FJ0812+32	08:12:40.8	+32:08:08	2.6263	$21.35^{+0.10}_{-0.10}$	14.30 ± 0.01	-26.56 ± 0.10	70	-0.93 ± 0.05	-1.76 ± 0.01	0.60	22,31,
J081435.18+502946	08:14:35.18	+50:29:46.5	3.7082	$21.35^{+0.15}_{-0.15}$	< 13.18	< -27.69	30	-3.00 ± 0.15	-2.91 ± 0.03	0.25	32
J082619.70+314848	08:26:19.70	+31:48:48.0	2.9122	$20.30^{+0.15}_{-0.15}$	< 12.60	< -27.21	35	-1.88 ± 0.15	-2.01 ± 0.01	—	32
Q0836+11	08:39:33.015	+11:12:03.82	2.4653	$20.58^{+0.10}_{-0.10}$	< 13.12	< -26.97	88	-1.15 ± 0.05	-1.40 ± 0.01	0.59	13
J0929+2825	09:29:14.49	+28:25:29.1	3.2627	$21.10^{+0.00}_{-0.00}$	13.15 ± 0.02	-27.47 ± 0.02	43	-1.62 ± 0.01	-1.78 ± 0.01	—	32
BR0951-04	09:53:55.69	-05:04:18.5	4.2029	$20.40^{+0.10}_{-0.10}$	13.37 ± 0.08	-26.54 ± 0.13	36	-2.62 ± 0.03	< -2.57	0.04	6,13
BRI0952-01	09:55:00.10	-01:30:06.94	4.0244	$20.55^{+0.10}_{-0.10}$	13.55 ± 0.02	-26.52 ± 0.10	302	-1.46 ± 0.18	-1.86 ± 0.08	—	8,13
PC0953+47	09:56:25.2	+47:34:44	4.2442	$20.90^{+0.15}_{-0.15}$	13.60 ± 0.10	-26.82 ± 0.18	70	-2.19 ± 0.03	-2.52 ± 0.08	0.24	22
J1014+4300	10:14:47.18	+43:00:30.1	2.9588	$20.50^{+0.00}_{-0.00}$	12.76 ± 0.04	-27.25 ± 0.04	108	-0.71 ± 0.14	-1.11 ± 0.04	—	32
Q1021+30	10:21:56.84	+30:01:31.3	2.9489	$20.70^{+0.10}_{-0.10}$	< 12.91	< -27.31	100	-1.94 ± 0.02	-2.16 ± 0.01	0.25	13,22

Continued on Next Page...

Table 4.1 – Continued

Quasar	**RA (2000)**	**DEC (2000)**	z_{abs}[a]	**log**$_{10}$/ $N_{\rm HI}$[b]	$\log_{10} N({\rm CII}^*)$[c]	$\log_{10} \ell_c$[d]	Δv_{90}[e]	**[M/H]**[f]	**[Fe/H]**[g]	W_{1526}[h]	**Ref**
J103514.22+544040	10:35:14.22	+54:40:40.1	2.6840	$20.50^{+0.20}_{-0.20}$	> 13.59	> -26.42	160	-0.62 ± 0.21	-0.45 ± 0.12	1.43	32
Q1036-230	10:39:09.4	-23:13:26	2.7775	$21.00^{+0.10}_{-0.10}$	12.97 ± 0.05	-27.55 ± 0.11	80	-1.41 ± 0.10	-1.82 ± 0.10	—	13
Q1104-18	11:06:32.96	-18:21:09.82	1.6614	$20.80^{+0.10}_{-0.10}$	13.44 ± 0.05	-26.88 ± 0.11	56	-1.04 ± 0.01	-1.48 ± 0.02	—	7
BRI1108-07	11:11:13.64	-08:04:02.47	3.6076	$20.50^{+0.10}_{-0.10}$	< 12.34	< -27.67	32	-1.80 ± 0.00	-2.12 ± 0.01	0.19	8,13
J113130.41+604420	11:31:30.41	+60:44:20.7	2.8760	$20.50^{+0.15}_{-0.15}$	< 12.66	< -27.36	53	-2.13 ± 0.15	-2.31 ± 0.03	—	32
HS1132+2243	11:35:08.03	+22:27:06.8	2.7835	$21.00^{+0.07}_{-0.07}$	< 12.69	< -27.82	56	-1.99 ± 0.07	-2.22 ± 0.02	0.27	22
J115538.60+053050	11:55:38.60	+05:30:50.6	3.3268	$21.05^{+0.10}_{-0.10}$	13.73 ± 0.03	-26.84 ± 0.10	120	-0.81 ± 0.10	-1.44 ± 0.05	1.21	32
Q1157+014	11:59:44.81	+01:12:07.1	1.9440	$21.80^{+0.10}_{-0.10}$	> 14.80	> -26.51	84	-1.36 ± 0.06	-1.81 ± 0.04	0.73	9
BR1202-07	12:05:23.63	-07:42:29.91	4.3829	$20.60^{+0.14}_{-0.14}$	< 13.06	< -27.06	170	-1.81 ± 0.02	-2.19 ± 0.12	—	2
J120802.65+630328	12:08:02.65	+63:03:28.7	2.4439	$20.70^{+0.15}_{-0.15}$	13.55 ± 0.03	-26.67 ± 0.15	60	-2.32 ± 0.15	-2.55 ± 0.01	0.18	32
Q1215+33	12:17:32.54	+33:05:38.39	1.9991	$20.95^{+0.07}_{-0.07}$	< 13.17	< -27.29	42	-1.48 ± 0.03	-1.70 ± 0.05	0.35	6,13
Q1223+17	12:26:07.22	+17:36:48.98	2.4661	$21.50^{+0.10}_{-0.10}$	< 14.01	< -27.01	94	-1.59 ± 0.01	-1.84 ± 0.02	0.62	8,13
Q1232+08	12:34:37.55	+07:58:40.5	2.3371	$20.90^{+0.10}_{-0.10}$	14.00 ± 0.10	-26.42 ± 0.14	85	-1.28 ± 0.09	-1.72 ± 0.09	—	9
J1240+1455	12:40:20.91	+14:55:35.6	3.1078	$21.30^{+0.00}_{-0.00}$	> 14.34	> -26.47	335	-0.85 ± 0.03	-2.11 ± 0.02	—	32
J1240+1455	12:40:20.91	+14:55:35.6	3.0241	$20.45^{+0.00}_{-0.00}$	< 13.32	< -26.65	134	-0.74 ± 0.07	-0.81 ± 0.12	—	32
Q1331+17	13:33:35.78	+16:49:04.03	1.7764	$21.14^{+0.08}_{-0.08}$	< 13.54	< -27.12	72	-1.42 ± 0.00	-2.02 ± 0.00	0.50	6,13
Q1337+11	13:40:02.44	+11:06:29.6	2.7959	$20.95^{+0.10}_{-0.10}$	13.11 ± 0.10	-27.36 ± 0.14	60	-1.72 ± 0.12	-2.03 ± 0.08	0.25	22,31
BRI1346-03	13:49:16.82	-03:37:15.06	3.7358	$20.72^{+0.10}_{-0.10}$	12.55 ± 0.11	-27.69 ± 0.15	38	-2.33 ± 0.01	-2.63 ± 0.02	0.12	6,13
PKS1354-17	13:57:06.07	-17:44:01.9	2.7800	$20.30^{+0.15}_{-0.15}$	12.76 ± 0.06	-27.06 ± 0.16	30	-1.37 ± 0.19	-1.79 ± 0.05	0.21	22
J141030+511113	14:10:30.60	+51:11:13.5	2.9642	$20.85^{+0.20}_{-0.20}$	< 13.01	< -27.35	46	-1.96 ± 0.15	-2.27 ± 0.02	—	
J141030+511113	14:10:30.60	+51:11:13.5	2.9344	$20.80^{+0.15}_{-0.15}$	> 13.39	> -26.92	247	-0.95 ± 0.15	-1.16 ± 0.10	—	32
J141906.32+592312	14:19:06.32	+59:23:12.3	2.2476	$20.95^{+0.20}_{-0.20}$	< 13.08	< -27.39	20	-2.85 ± 0.20	-2.76 ± 0.04	0.09	32
Q1425+6039	14:26:56.44	60:25:42.74	2.8268	$20.30^{+0.04}_{-0.04}$	< 13.33	< -26.49	136	-0.79 ± 0.04	-1.32 ± 0.00	0.70	2,13,31
PSS1443+27	14:43:31.22	+27:24:37.23	4.2241	$20.80^{+0.10}_{-0.10}$	> 14.71	> -25.61	90	-0.70 ± 0.16	-1.10 ± 0.06	—	8,13
PSS1506+5220	15:06:54.6	+52:20:05	3.2244	$20.67^{+0.07}_{-0.07}$	< 12.91	< -27.28	44	-2.98 ± 0.08	-2.60 ± 0.04	0.16	22
Q1759+75	17:57:46.39	+75:39:16.01	2.6253	$20.76^{+0.01}_{-0.01}$	12.80 ± 0.05	-27.48 ± 0.05	74	-0.79 ± 0.01	-1.18 ± 0.00	0.63	6,13
J203642.29-055300	20:36:42.29	-05:53:00.2	2.2805	$21.20^{+0.15}_{-0.15}$	13.36 ± 0.08	-27.36 ± 0.17	71	-1.71 ± 0.17	-2.24 ± 0.02	0.31	32
SDSS2100-0641	21:00:25.03	-06:41:46	3.0924	$21.05^{+0.15}_{-0.15}$	14.06 ± 0.01	-26.51 ± 0.15	187	-0.73 ± 0.15	-1.20 ± 0.02	—	29
J214129.38+111958	21:41:29.38	+11:19:58.3	2.4264	$20.30^{+0.20}_{-0.20}$	< 13.28	< -26.54	30	-1.97 ± 0.20	-2.00 ± 0.03	0.15	32
J215117.00-070753	21:51:17.00	-07:07:53.3	2.3274	$20.45^{+0.15}_{-0.15}$	< 13.09	< -26.87	20	-1.65 ± 0.15	-1.94 ± 0.02	0.31	32
Q2206-19	22:08:52.05	-19:43:57.61	1.9200	$20.65^{+0.07}_{-0.07}$	13.97 ± 0.25	-26.20 ± 0.26	132	-0.42 ± 0.00	-0.86 ± 0.02	0.99	4,6,13
Q2206-19	22:08:52.05	-19:43:57.61	2.0762	$20.43^{+0.06}_{-0.06}$	< 13.16	< -26.79	26	-2.31 ± 0.04	-2.61 ± 0.02	—	4,6,13
Q2231-002	22:34:08.80	+00:00:02.00	2.0661	$20.56^{+0.10}_{-0.10}$	13.71 ± 0.04	-26.37 ± 0.11	122	-0.88 ± 0.02	-1.40 ± 0.07	0.79	2,6,13,25

Continued on Next Page. . .

Table 4.1 – Continued

Quasar	**RA (2000)**	**DEC (2000)**	z_{abs}[a]	**log**$_{10}$/ $N_{\rm HI}$[b]	$\log_{10} N({\rm CII}^*)$[c]	$\log_{10} \ell_c$[d]	Δv_{90}[e]	**[M/H]**[f]	**[Fe/H]**[g]	W_{1526}[h]	**Ref**
J223438.52+005730	22:34:38.52	+00:57:30.0	2.8175	$20.80^{+0.20}_{-0.20}$	< 13.50	< -26.81	80	-0.99 ± 0.21	-1.52 ± 0.02	0.66	32
J223843.56+001647	22:38:43.56	+00:16:47.9	3.3654	$20.40^{+0.15}_{-0.15}$	< 13.12	< -26.80	30	-2.34 ± 0.15	-2.57 ± 0.14	0.09	32
BR2237-0607	22:39:53.39	-05:52:20.78	4.0803	$20.52^{+0.11}_{-0.11}$	< 12.53	< -27.51	144	-1.87 ± 0.02	-2.14 ± 0.12	—	2
J231543.56+145606	23:15:43.56	+14:56:06.4	3.2729	$20.30^{+0.15}_{-0.15}$	13.55 ± 0.08	-26.27 ± 0.17	110	-1.78 ± 0.15	-2.03 ± 0.03	0.37	32
FJ2334-09	23:34:46.44	-09:08:11.8	3.0569	$20.45^{+0.10}_{-0.10}$	< 12.82	< -27.15	134	-1.04 ± 0.11	-1.49 ± 0.01	—	22
J2340-00	23:40:23.7	-00:53:27.0	2.0545	$20.35^{+0.15}_{-0.15}$	13.84 ± 0.04	-26.03 ± 0.15	104	-0.74 ± 0.16	-0.92 ± 0.03	0.75	29,
J234352.62+141014	23:43:52.62	+14:10:14.6	2.6768	$20.50^{+0.15}_{-0.15}$	< 12.96	< -27.06	35	-1.50 ± 0.28	-1.09 ± 0.13	—	32
Q2342+34	23:44:51.10	+34:33:46.8	2.9082	$21.10^{+0.10}_{-0.10}$	13.70 ± 0.06	-26.92 ± 0.12	100	-1.04 ± 0.02	-1.58 ± 0.06	0.76	22,31
Q2343+125	23:46:28.22	+12:48:59.9	2.4313	$20.34^{+0.10}_{-0.10}$	12.77 ± 0.05	-27.09 ± 0.11	290	-0.54 ± 0.01	-1.20 ± 0.00	—	5
Q2344+12	23:46:45.79	+12:45:29.98	2.5379	$20.36^{+0.10}_{-0.10}$	< 12.95	< -26.93	66	-1.74 ± 0.01	-1.82 ± 0.03	—	2,13
Q2348-14	23:51:29.91	-14:27:47.55	2.2794	$20.56^{+0.08}_{-0.08}$	< 13.21	< -26.87	30	-1.92 ± 0.02	-2.24 ± 0.02	0.19	6,13

---

[a] DLA redshift

[b] H I column density [cm^{-2}]

[c] C II* column density [cm^{-2}]

[d] 158 μm cooling rate per atom [ergs s^{-1} H^{-1}].

[e] Low-ion velocity width (km/s) as defined in (**?**).

[f] Logarithmic α-metal abundance with respect to solar.

[g] Logarithmic Fe abundance with respect to solar.

[h] Rest frame Si II λ 1526 equivalent width [Å].

1: Wolfe et al. (1994); 2: Lu *et al.* (1996); 3: Prochaska & Wolfe (1996); 4: Prochaska & Wolfe (1997); 5: Lu et al. (1999); 6: Prochaska & Wolfe (1999); 7: Lopez et al. (1999); 8: Prochaska & Wolfe (2000); 9: Petitjean et al. (2000); 10: Molaro et al. (2000); 11: Dessauges-Zavadsky et al. (2001); 12: Molaro et al. (2001); 13: Prochaska et al. (2001); 14: Prochaska, Gawiser & Wolfe (2001); 15: Ellison et al. (2001); 16: Prochaska *et al.* (2002); 17: Ledoux et al. (2002); 18: Lopez et al. (2002); 19: Levshakov et al. (2002); 20: Lopez & Ellison (2003); 21: Songaila & Cowie (2002); 22: Prochaska *et al.* (2003); 23: Prochaska et al. (2003); 24: Ledoux et al. (2003); 25: Dessauges-Zavadsky et al. (2004); 26: Ledoux et al. (2006); 27: Akerman *et al.* (2005); 28: O'Meara et al. (2006); 29: Herbert-Fort et al. (2006); 30: Dessauges-Zavadsky et al. (2006); 31: Prochaska et al. (2007); 32: This paper

We first noticed evidence for bimodality in previous plots of ℓ_c versus $N_{\rm HI}$ (e.g. WGP05). An updated version of these plots is shown in Fig. 4.1. The red data points are positive detections, green are upper limits, and blue are lower limits. The positive detections are distributed into two distinct regions centered near ℓ_c=$10^{-27.4}$ ergs s^{-1} H^{-1} and ℓ_c=$10^{-26.6}$ ergs s^{-1} H^{-1}. A histogram of the positive detections is plotted in Fig. 4.2, which shows the two peaks separated by a trough at $\ell_c = \ell_c^{\rm crit} \approx 10^{-27.0}$ ergs s^{-1} H^{-1}. Note, the trough is not an artifact caused by selection effects, since the signal-to-noise ratios of the C II* absorption profiles for the 5 DLAs with $\ell_c \approx \ell_c^{\rm crit}$ are not exceptional for DLAs with positive detections. Standard statistical tests applied to these data support the bimodal hypothesis. We first used the KMM algorithm (Ashman et al. 1994; McLachlan & Basford 1987), which fits Gaussians to the data, computes the maximum likelihood estimates of their means and variances, and evaluates the improvement of that fit over the null hypothesis of a single Gaussian. We found the probability of the null hypothesis to be $P_{\rm KMM}(\ell_c)$=0.016; i.e., a single Gaussian fit can be excluded with 98.4 % confidence. This result is robust, as the value of $P_{\rm KMM}(\ell_c)$ is insensitive to a wide range of initial guesses for the means and variances of the input Gaussians. We then used the Bayesian mixture algorithm NMIX (Richardson & Green 1997), which models the number of Gaussian components and mixture component parameters jointly and evaluates the statistical significance of these quantities based on their posterior probabilities. J. Strader (priv. comm.; 2007) kindly analyzed the data with NMIX and found that the probability of the null hypothesis, $P_{\rm NMIX}$=0.08. The latter test yielded peak locations of ℓ_c=$10^{-27.34\pm0.06}$ and ℓ_c=$10^{-26.58\pm0.06}$ ergs s^{-1} H^{-1} and values of 0.38 and 0.62 for the sample fractions associated with the respective peaks.

These results were obtained by excluding both the lower limits and upper limits on ℓ_c. This does not affect our conclusions provided the true values of ℓ_c, i.e., $\ell_c^{\rm true}$, are drawn from the same parent population as the positive

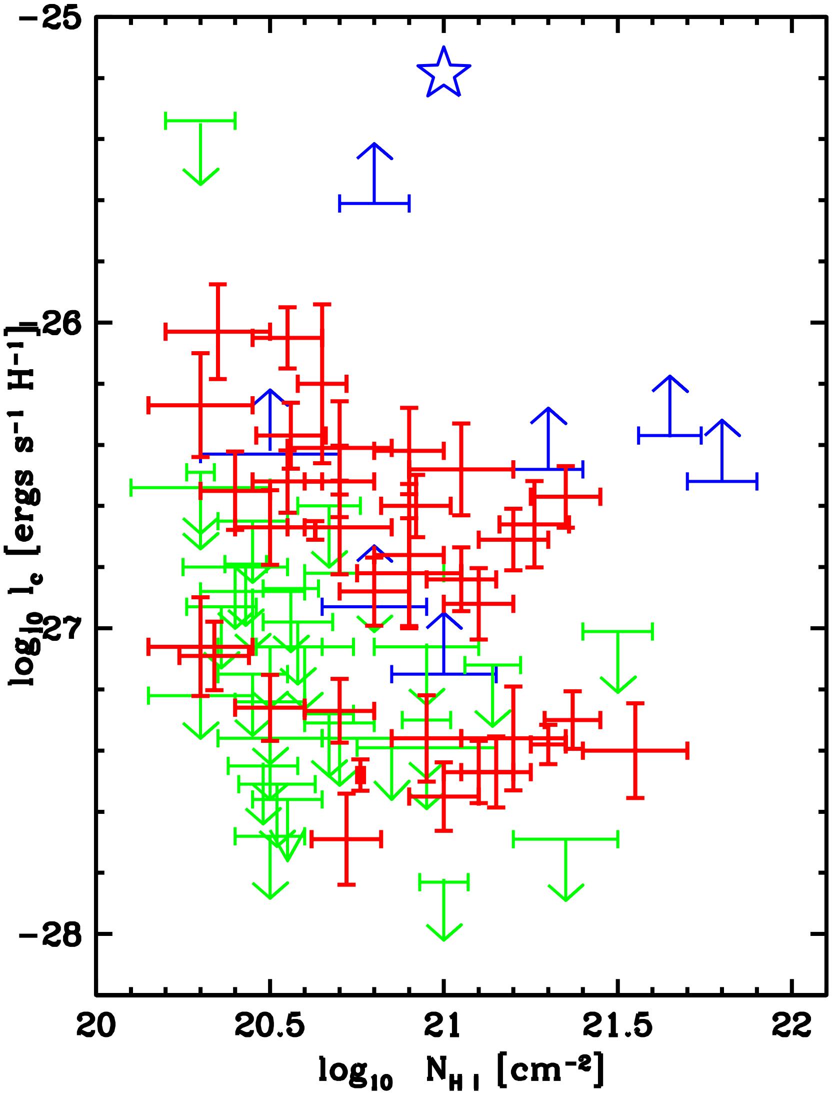

Figure 4.1: ℓ_c versus $N_{\rm HI}$ for the 76 DLAs in our sample. Red data points are positive detections, green are upper limits, and blue are lower limits. The blue star is the average value for the Galaxy disk.

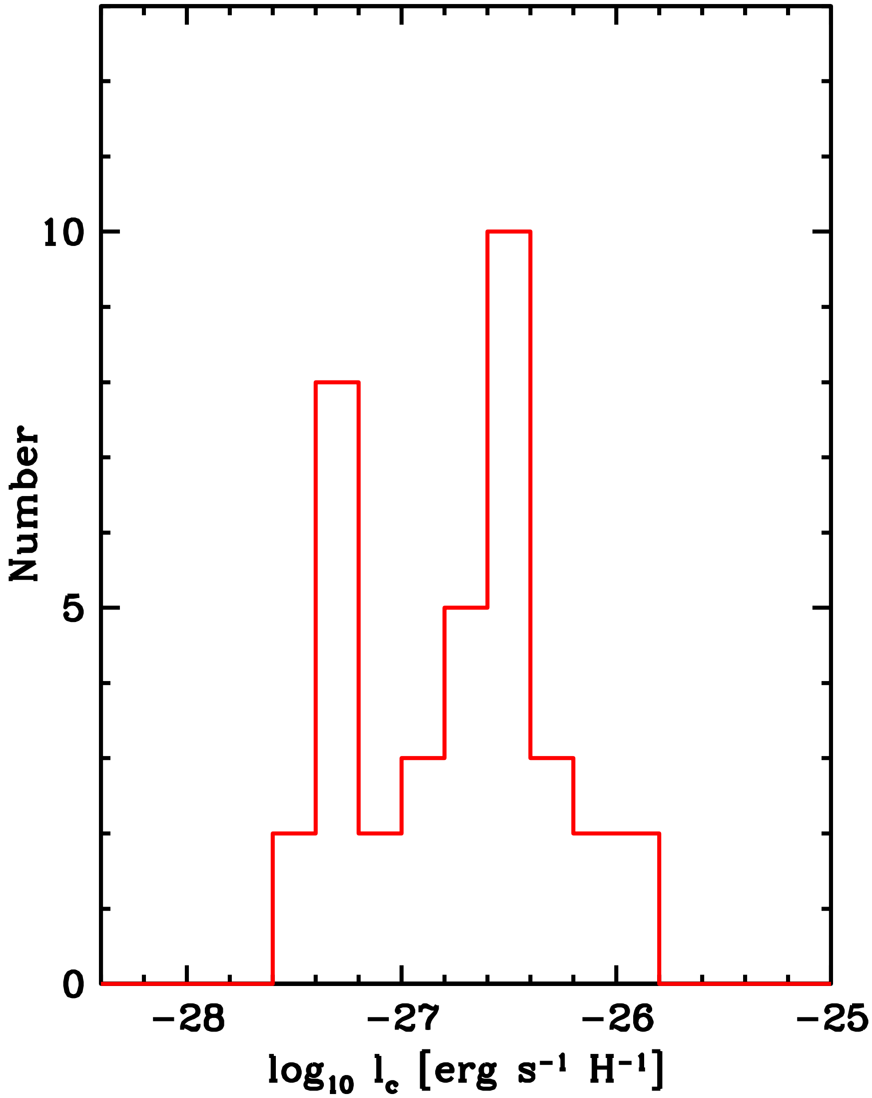

Figure 4.2: Histogram depicting distribution of the 37 positive detections of ℓ_c reported in Table 4.1.

detections, which we assume is a bimodal distribution. Note by definition the values of $\ell_c^{\rm true}$ equal the measured values of ℓ_c in the case of positive detections, are less than the measured ℓ_c for the upper limits, and are greater than the measured ℓ_c for the lower limits. The distributions of lower limits and positive detections shown in Fig. 4.3a are clearly compatible. However, because the values of $\ell_c^{\rm true}$ must exceed the corresponding lower limits, it is possible that the $\ell_c^{\rm true}$ are drawn from a separate population concentrated above the peak at $\ell_c \approx 10^{-26.6}$ ergs $\rm s^{-1}$ $\rm H^{-1}$ characterizing the positive detections. But there is no sign in any of the other properties of DLAs with lower limits that distinguishes them from the DLAs with positive detections. This suggests that both sets of DLAs are drawn from a common population. In any case the small number of lower limits implies they have negligible impact on the case for bimodality or on the location of either peak inferred from the positive detections.

By contrast, Fig. 4.3b shows that the ℓ_c distribution of the upper limits peaks at $\approx 10^{-27.0}$ ergs $\rm s^{-1}$ $\rm H^{-1}$, the same value of ℓ_c where the positive detections exhibit a trough. The difference between the distributions is potentially important owing to the comparable sizes of the two samples. However, the distribution of upper limits shown in Fig. 4.3b does not accurately represent the corresponding distribution of $\ell_c^{\rm true}$. Because the values of $\ell_c^{\rm true}$ should be lower than the associated upper limits, the resulting distribution of $\ell_c^{\rm true}$ should peak at values lower than shown in the figure. While we do not know how much lower, our recent (2006 Dec., 2007 April, and 2007 Sept.) HIRES observations provide a clue. We observed 13 DLAs with upper limits set previously by data acquired with ESI. Using the higher spectral resolution of HIRES (R=43,000 compared to R=9000 for ESI), we detected four of these while the other nine remained undetected. The HIRES observations moved five of eight ESI upper limits out of the trough to upper limits below the trough, while two of the four new detections were also moved below the trough and one remained within the

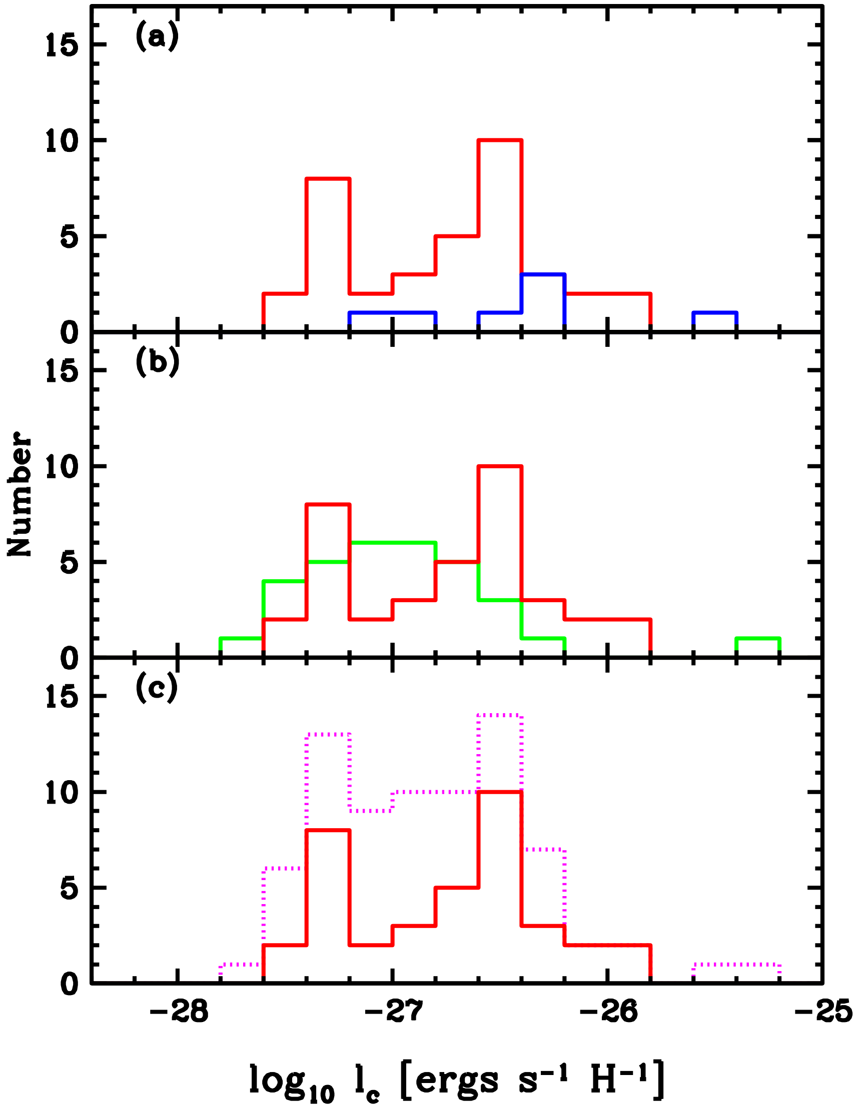

Figure 4.3: Histograms comparing positive detections (red) and (a) lower limits (blue), (b) upper limits (green), and (c) all the ℓ_c values in Table 4.1 (magenta).

trough. Therefore, it is plausible to assume that $\ell_c^{\rm true}$ could typically be more than 0.4 dex lower than the upper limits; i.e., the evidence is consistent with a distribution resembling the positive detections by exhibiting a peak at $\ell_c{\approx}10^{-27.4}$ ergs s^{-1} H^{-1}.

Fig. 4.3c plots the empirical ℓ_c distribution for all 76 DLAs in Table 4.1: the plot includes the positive detections, lower limits, and upper limits. While the corresponding $\ell_c^{\rm true}$ distribution for the entire sample has not fully been determined, the above arguments provide good evidence for a 'high cool' peak at $\ell_c{\approx}10^{-26.6}$ ergs s^{-1} H^{-1} and growing evidence for a 'low cool' peak at $\ell_c{\approx}10^{-27.4}$ ergs s^{-1} H^{-1}; i.e., a distribution resembling that of the positive detections. Although we do not know which values of $\ell_c^{\rm true}$ to assign to the upper limits, we suggest that in most cases the range of values is given by $\ell_c^{\rm true}{=}[10^{-28.5}, 10^{-27.0}]$ ergs s^{-1} H^{-1}. Lower bounds on $\ell_c^{\rm true}$ are set by the heating rates due to FUV and X-ray background radiation and excitation rates due to CMB radiation. The CMB sets a floor of $\ell_c^{\rm true}{>}{\sim}10^{-28}$ ergs s^{-1} H^{-1} for DLAs with $z >{\sim}3.5$ (Wolfe et al. 2004; hereafter referred to as WHGPL), whereas X-ray heating provides the lower bound for DLAs with lower redshifts. We reject values of ℓ_c lower than $10^{-28.5}$ ergs s^{-1} H^{-1} since the densities implied in the case of thermal balance $n < 10^{-1.5}$ cm^{-3} (WHGPL). In that case the length scale d of gas clouds for DLAs with median column density $N_{\rm HI}{=}8{\times}10^{20}$ cm^{-2} (WGP05), would exceed 8 kpc. While the line-of-sight might traverse such distances through DLAs, the multi-component structure of the absorption-line profiles indicates the gas is confined to several smaller "clouds" characterized by a low volume filling factor (Nagamine et al. 2007). This scenario is supported by multi-phase models in which the DLA gas density $n > 10$ cm^{-3} and $d < 30$ pc (Wolfe, Gawiser, Prochaska 2003; hereafter referred to as WPG03). At the same time it is likely that $\ell_c^{\rm true}$ corresponding to most of the upper limits in Fig. 4.3c is less than 10^{-27} ergs s^{-1} H^{-1}: since only four out of 32 upper limits exceeds $10^{-26.6}$ ergs s^{-1} H^{-1}

and we expect $\ell_c^{\rm true}$ to be more than 0.4 dex lower than the corresponding upper limit, then $\ell_c^{\rm true}$ for over $\approx 90\%$ of the upper limits should be lower than 10^{-27} ergs $\rm s^{-1}$ $\rm H^{-1}$.

To summarize, standard statistical tests applied to the ℓ_c distribution of positive detections support the bimodal hypothesis. The above arguments concerning the lower and upper limits are consistent with the hypothesis of two peaks in the $\ell_c^{\rm true}$ distribution. Because the presence of two peaks is supported by physical arguments concerning the range of $\ell_c^{\rm true}$, the case for bimodality is sufficiently compelling to consider independent tests to which we now turn.

4.4 Independent Tests for Bimodality

If the ℓ_c distribution is bimodal, the critical cooling rate $\ell_c^{\rm crit}$ should divide the DLA sample into independent populations with physically distinct properties. In this section we investigate whether this is the case.

4.4.1 Velocity Interval

We first determine whether $\ell_c^{\rm crit}$ divides DLAs into populations with distinct velocity structures. We choose the absorption-line velocity interval Δv_{90} as a measure of velocity structure, where Δv_{90} is defined as the velocity interval containing the central 90% of the optical depth of unsaturated low-ion absorption lines (Prochaska & Wolfe 1997): this definition guarantees that Δv_{90} corresponds to the bulk of the neutral gas producing the absorption. The measured values of Δv_{90} are listed in column 8 of Table 4.1. To generate suitable subsamples we adopted the following criteria. For the positive detections we assigned DLAs with $\ell_c \le \ell_c^{\rm crit}$ to a 'low cool' subsample and DLAs with $\ell_c > \ell_c^{\rm crit}$ to a 'high cool' subsample. The division is not as clear for DLAs with upper limits because $\ell_c^{\rm true}$ may be lower than $\ell_c^{\rm crit}$ for objects with upper limits on ℓ_c exceeding $\ell_c^{\rm crit}$. To account for this possibility we assigned DLAs with upper limits given by $\log_{10}\ell_c$

$\leq \log_{10}\ell_c^{\rm crit} + \Delta\log_{10}\ell_c^{\rm crit}$ to the 'low cool' subsample and those with higher upper limits to the 'high cool' subsample. Similarly we assigned DLAs with lower limits given by $\log_{10}\ell_c \leq \log_{10}\ell_c^{\rm crit} - \Delta\log_{10}\ell_c^{\rm crit}$ to the 'low cool' sample and those with higher lower limits to the 'high cool' subsample. The value of $\Delta\log_{10}\ell_c^{\rm crit}$ is determined by the ratio of the ℓ_c limit to our estimate of $\ell_c^{\rm true}$.

Histograms with $\Delta\log_{10}\ell_c^{\rm crit}$= 0.2 and $\ell_c^{\rm crit}$=$10^{-27.0}$ ergs $\rm s^{-1}$ $\rm H^{-1}$ are shown in Fig. 4.4. In this case the 'low cool' and 'high cool' histograms are clearly different. Whereas the bulk of the 'low cool' subsample clusters around $\Delta v_{90} \approx$ 50 km $\rm s^{-1}$, the bulk of the 'high cool' subsample DLAs exhibits a wider distribution centered near 100 km $\rm s^{-1}$. The difference between the two subsamples is also evident in the cumulative distribution shown in the inset in Fig. 4.4. The cumulative distributions are obviously different with medians Δv_{90} = 46 km $\rm s^{-1}$ for the 'low cool' subsample and 104 km $\rm s^{-1}$ for the 'high cool' subsample. Applying the standard Kolmogorov-Smirnov (KS) test we find the probability that the two distributions are drawn from the same parent population, $P_{\rm KS}(\Delta v_{90})$ =2.7×10^{-5}; i.e., the null hypothesis can be rejected at a high confidence level.

To test the sensitivity of this conclusion to uncertainties in $\ell_c^{\rm crit}$ and $\Delta\log_{10}\ell_c^{\rm crit}$ we recomputed $P_{\rm KS}(\Delta v_{90})$ for a range of values compatible with the ℓ_c distribution in Fig. 4.2; i.e., $10^{-27.1} \leq \ell_c^{\rm crit} \leq 10^{-26.7}$ ergs $\rm s^{-1}$ $\rm H^{-1}$ and $0 \leq \Delta\log_{10}\ell_c^{\rm crit} \leq 0.4$. The results shown in Table 4.2 indicate that $8.5\times10^{-6} \leq P_{\rm KS}(\Delta v_{90}) \leq 1.5\times10^{-3}$, with the largest value corresponding to the case $\Delta\log_{10}\ell_c^{\rm crit}$=0, which is unlikely. Next we checked whether the Δv_{90} distribution was bimodal with respect to other parameters measured in DLAs. The only parameter suitable for this purpose is redshift. Accordingly we divided our sample into low-z and high-z subsamples around the median redshift z_{med}=2.85. When we compared the resulting Δv_{90} distributions, we found that $P_{\rm KS}(\Delta v_{90})$ = 0.69. In other words velocity width is unlikely to be bimodal with respect to redshift.

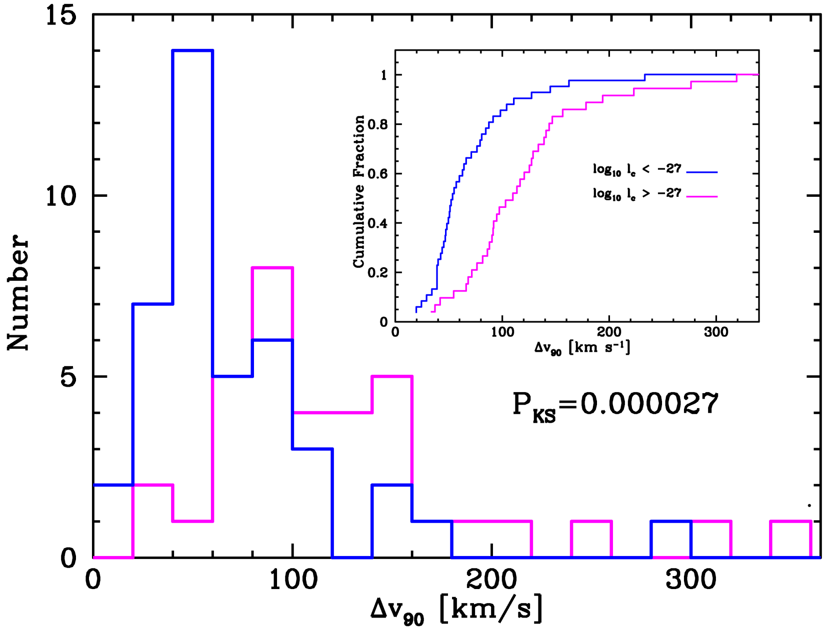

Figure 4.4: Histograms of velocity intervals Δv_{90} divided such that the magenta histogram depicts DLAs with $\ell_c > \ell_c^{\rm crit}$ and the blue histogram depicts DLAs with $\ell_c \leq \ell_c^{\rm crit}$. The inset shows the cumulative distributions for both subsamples.

Table 4.2: KS PROBABILITIES

				$\log_{10}(P_{\rm KS})$[a]				
$\log_{10}\ell_c^{\rm crit}$ [b]	$\Delta\log_{10}\ell_c^{\rm crit}$ [c]	n_{lo}[d]	n_{hi}[e]	Δv_{90}	[M/H]	κ	W_{1526}	$N_{\rm HI}$
−27.1	0.0	28	48	−4.01	−3.19	−1.85	−2.36	−0.73
−27.1	0.2	34	42	−3.71	−4.36	−3.40	−2.59	−0.69
−27.1	0.4	39	37	−5.07	−5.45	−4.43	−2.81	−0.22
−27.0	0.0	34	42	−3.92	−3.93	−1.91	−2.59	−0.69
−27.0	0.2	40	36	−4.57	−4.34	−2.99	−3.14	−0.06
−27.0	0.4	43	33	−4.35	−4.66	−3.30	−3.14	−0.02
−26.9	0.0	39	37	−2.82	−2.75	−2.31	−2.23	−0.55
−26.9	0.2	44	32	−4.35	−3.71	−3.30	−2.51	−0.07
−26.9	0.4	47	29	−4.33	−4.05	−3.69	−2.84	−0.03
−26.8	0.0	46	30	−4.24	−2.78	−2.42	−2.25	−0.75
−26.8	0.2	49	27	−4.11	−3.11	−2.78	−2.25	−0.91
−26.8	0.4	51	25	−4.39	−3.08	−2.80	−2.19	−0.02
−26.7	0.0	49	27	−4.30	−3.11	−2.97	−2.25	−0.47
−26.7	0.2	52	24	−4.04	−3.53	−3.31	−2.61	−0.07
−26.7	0.4	53	23	−3.70	−3.07	−2.91	−2.19	−0.02

[a] KS probabilities that parameters in ‘low cool’ and ‘high cool’ sub-sample are drawn from same parent population

[b] Critical cooling rate separating positive detections in ‘low cool’ and ‘high cool’ subsamples

[c] Correction to critical cooling rate for upper limits (see text)

[d] Number of DLAs in ‘low cool’ sub-sample

[e] Number of DLAs in ‘high cool’ sub-sample

4.4.2 Metallicity

Fig. 4.5 shows the metallicity distributions of the ‘low cool’ and ‘high cool’ subsamples. The logarithmic metal abundances with respect to solar, [M/H], are listed in column 9 of Table 4.1, where M stands for an element found to be undepleted in DLAs such as S, Si, or Zn (Prochaska et al. 2003). As in Fig. 4.4 we divide the sample with $\ell_c^{\rm crit}$=10^{-27} ergs s^{-1} H^{-1} and $\Delta\log_{10}\ell_c^{\rm crit}$ =0.2. Similar to the case of the Δv_{90} distributions we find the ‘low cool’ and ‘high cool’ distributions of metallicity are different. For these values of $\ell_c^{\rm crit}$ and $\Delta\log_{10}\ell_c^{\rm crit}$ the median metallicity of the ‘low cool’ subsample is given by $[{\rm M/H}]_{low} = -1.74$, and $[{\rm M/H}]_{hi} = -1.06$ for the ‘high cool’ subsample. Applying the KS test, we find the probability that the two subsamples are drawn from the same parent population is given by $P_{\rm KS}$([M/H])=4.5×10^{-5}. When we recomputed $P_{\rm KS}$([M/H]) for the range of $\ell_c^{\rm crit}$ and $\Delta\log_{10}\ell_c^{\rm crit}$ shown in Table 4.2,

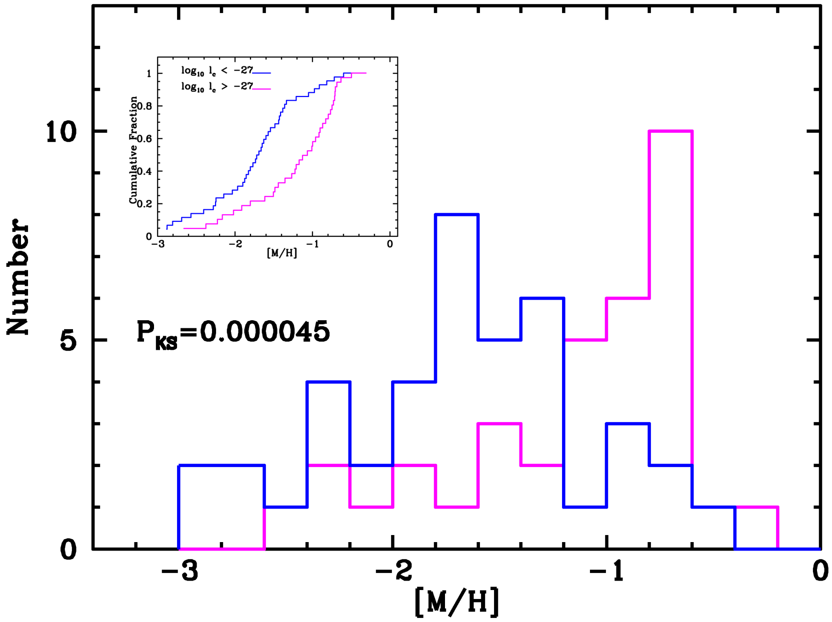

Figure 4.5: Histograms of DLA metallicity divided such that the magenta histogram depicts DLAs with $\ell_c > \ell_c^{\rm crit}$ and the blue histogram depicts DLAs with $\ell_c \leq \ell_c^{\rm crit}$. The inset shows the cumulative distributions for both subsamples.

we found that $3.5{\times}10^{-6} \leq P_{\rm KS}([{\rm M/H}]) \leq 1.8{\times}10^{-3}$, where the largest value again corresponds to the unlikely case of $\Delta{\rm log}_{10}\ell_c^{\rm crit}$=0. By contrast, when we split the sample according to redshift we found that $P_{\rm KS}$([M/H])=0.50, indicating that DLA metallicities in the two redshift bins are not drawn from the same parent population. This may conflict with our detection of metallicity evolution with redshift (Prochaska et al. 2003) in which we found weak but statistically significant redshift evolution; i.e., $d[{\rm M/H}]/dz = -0.26{\pm}0.07$. Part of the difference between the results could be due to sample size, since for the Prochaska et al. (2003) sample, which is about twice the size of the current sample, we find $P_{\rm KS}$([M/H])=0.001. While it is possible that some of the more recent measurements may dilute the original result, the vastly different values of $P_{\rm KS}$([M/H]) is puzzling.

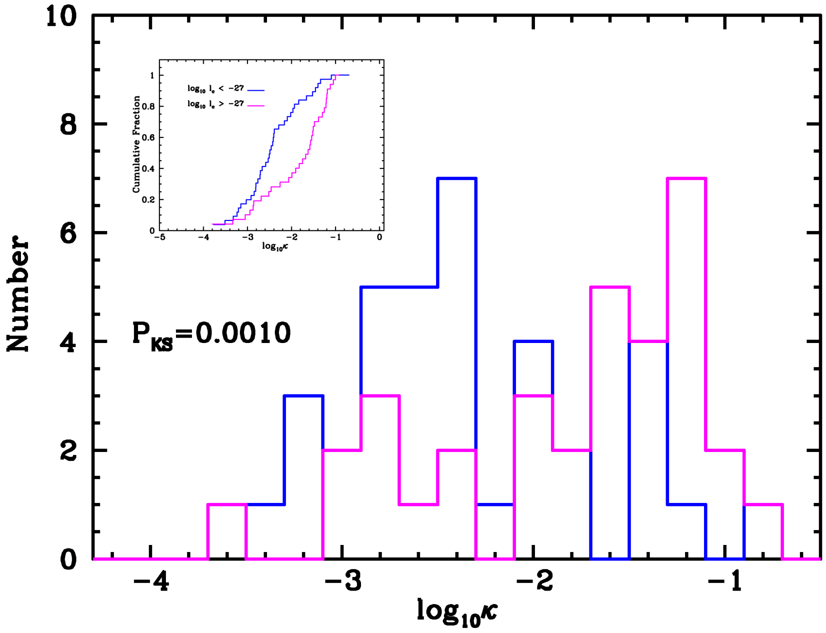

Figure 4.6: Histograms of DLA dust-to-gas ratio divided such that the magenta histogram depicts DLAs with $\ell_c > \ell_c^{\rm crit}$ and the blue histogram depicts DLAs with $\ell_c \leq \ell_c^{\rm crit}$. The inset shows the cumulative distributions for both subsamples.

4.4.3 Dust-to-Gas Ratio

Not surprisingly the results for dust-to-gas ratio, κ, resemble the results for metallicity. This is shown in Fig. 4.6, which compares the κ distributions for the 'high cool' and 'low cool' subsamples where κ= $10^{\rm [M/H]}(10^{\rm [Fe/M]_{int}}$-$10^{\rm [Fe/M]})$ (see WPG03) and [Fe/M] and $\rm [Fe/M]_{int}$ are the measured and intrinsic logarithmic abundances of Fe with respect to an undepleted α element, M: all abundances are with respect to solar ([Fe/H] is given in column 10 in Table 4.1). We computed the numerical values for κ in Table 4.2 by assuming $\rm [Fe/M]_{int}$ $=-0.2$ when $\rm [Fe/M] \leq -0.2$ and $\rm [Fe/M]_{int}$ $=0$ when $-0.2 \leq \rm [Fe/M] \leq 0.0$ (see WGP05).

Fig. 4.6 shows that the dust-to-gas ratios of the 'high cool' subsample are significantly higher than for the 'low cool' subsample. We find $P_{\rm KS}(\kappa)$= 1.0×10^{-3} for the distributions shown in Fig. 4.6, where $\ell_c^{\rm crit}$=$10^{-27.0}$ ergs s^{-1} H^{-1} and $\Delta\log_{10}\ell_c^{\rm crit}$ $= 0.2$. We also find that $3.7\times10^{-5} < P_{\rm KS}(\kappa) < 1.4\times10^{-2}$

for the range in $\ell_c^{\rm crit}$ and $\Delta{\rm log}_{10}\ell_c^{\rm crit}$ in Table 4.2, with the largest values again given by the unlikely case $\Delta{\rm log}_{10}\ell_c^{\rm crit}$=0. When we divided the sample according to redshift we found that $P_{\rm KS}(\kappa)$=0.17. Although a unimodal distribution of κ with respect to redshift is less likely, it still cannot be ruled out with high significance. As a result bimodality is unlikely to arise with respect to redshift.

4.4.4 Si II λ 1526 Equivalent Width

Prochaska et al. (2007) recently showed that DLAs exhibit a tight correlation between Si II λ 1526 rest-frame equivalent width, W_{1526}, and metallicity, [M/H]. Interestingly the correlation exhibits less scatter than the Δv_{90} versus [M/H] correlation. This is a striking result because whereas Δv_{90} and [M/H] are determined from the same neutral gas, W_{1526} is dominated by the kinematics of low optical-depth clouds that make an insignificant contribution to [M/H]. Prochaska et al. (2007) argue that W_{1526} is determined by the virialized random motions of clouds in the outer halo of the DLA galaxy, while Δv_{90} is set by the motions (e.g. rotation) of the neutral ISM. As a result, the wide range of values expected for impact parameter and galaxy inclination will cause sizable scatter in Δv_{90} among galaxies with the same virial velocity. By contrast, the scatter in W_{1526} will be lower for sightlines encountering large numbers of randomly moving clouds in the halos of the same galaxies. Because of the tight correlation between W_{1526} and [M/H], one might expect that W_{1526} determined for the 'low cool' and 'high cool' DLAs are not drawn from the same parent population.

Fig. 4.7 compares the W_{1526} distributions of the 'high cool' and 'low cool' subsamples for the standard values $\ell_c^{\rm crit} = 10^{-27}$ ergs s^{-1} H^{-1} and $\Delta{\rm log}_{10}\ell_c^{\rm crit}$ = 0.2. In this case the 51 measured values of W_{1526} are listed in column 11 of Table 4.1. The figure shows that the 'low cool' subsample exhibits systematically lower values of W_{1526} than the 'high cool' subsample: we find $P_{\rm KS}(W_{1526}) = 7.2\times10^{-4}$. When we recomputed $P_{\rm KS}(W_{1526})$ for the range of $\ell_c^{\rm crit}$ and $\Delta{\rm log}_{10}\ell_c^{\rm crit}$

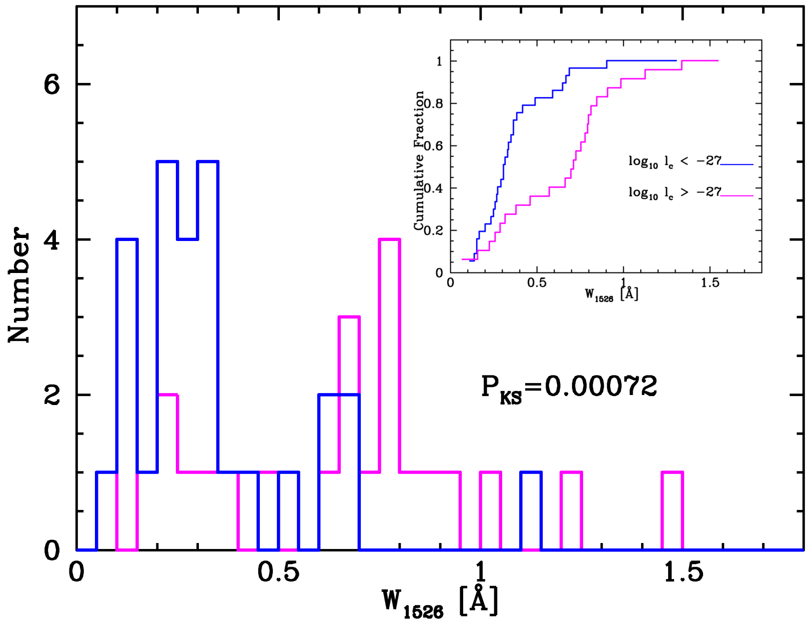

Figure 4.7: Histograms of Si II λ1526 equivalent width divided such that the magenta histogram depicts DLAs with $\ell_c > \ell_c^{\rm crit}$ and the blue histogram depicts DLAs with $\ell_c \leq \ell_c^{\rm crit}$. The inset shows the cumulative distributions for both subsamples.

shown in Table 4.2, we found that $7.2{\times}10^{-4} < P_{\rm KS}(W_{1526}) < 6.5{\times}10^{-3}$. When we split the sample according to redshift we found $P_{\rm KS}(W_{1526})$ =0.87, which further supports the hypothesis that the DLA sample is not bimodal with respect to redshift.

4.4.5 H I Column Density

Fig. 4.8 compares the $N_{\rm HI}$ distributions of the 'high cool' and 'low cool' subsamples for the standard case ℓ_c=10^{-27} ergs s^{-1} H^{-1} and $\Delta\log_{10}\ell_c^{\rm crit}$=0.2, where the values of $N_{\rm HI}$ are listed in column 5 of Table 4.1. By contrast with the previous results, the null hypothesis cannot be excluded at high confidence levels. Specifically, in this case $P_{\rm KS}(N_{\rm HI})$=0.87. More generally, $0.19 < P_{\rm KS}(N_{\rm HI})$ < 0.96 for the range of values spanned by $\ell_c^{\rm crit}$ and $\Delta\log_{10}\ell_c^{\rm crit}$ in Table 4.2. This

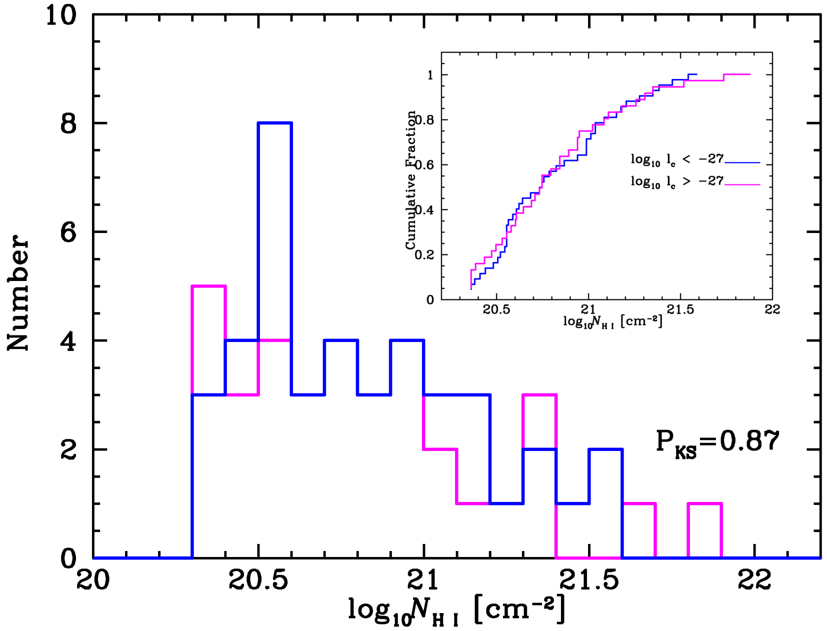

Figure 4.8: Histograms of H I column density divided such that the magenta histogram depicts DLAs with $\ell_c > \ell_c^{\rm crit}$ and the blue histogram depicts DLAs with $\ell_c \leq \ell_c^{\rm crit}$. The inset shows the cumulative distributions for both subsamples.

has important implications to be discussed in § 4.6. When we split the data according to redshift we found that $P_{\rm KS}(N_{\rm HI})$=0.21, indicating that we cannot confidently rule out that $N_{\rm HI}$ values in the two redshift bins are drawn from the same parent population. As a result, the DLA sample is unlikely to be bimodal with respect to redshift.

4.5 Modes of Heating

In this section we describe the heating processes that balance cooling in DLAs. We interpret the physical significance of the critical cooling rate $\ell_c^{\rm crit}$ and discuss differences between the heat input into the 'low cool' and 'high cool' DLAs. We consider two possibilities.

4.5.1 Background Heating of 'Low Cool' DLAs

The first possible explanation for the presence of a trough at $\ell_c^{\rm crit} \approx 10^{-27}$ ergs s^{-1} H^{-1} is that $\ell_c^{\rm crit}$ is the maximum [C II] 158 μm emission rate of low-metallicity gas heated by background radiation at $z \sim 3$. According to this scenario, DLAs with $\ell_c \leq \ell_c^{\rm crit}$, i.e., the 'low cool' DLAs, are neutral gas layers heated by background radiation alone, while DLAs with $\ell_c > \ell_c^{\rm crit}$, the 'high cool' DLAs, are in addition heated by internal sources (see WHGPL and Wolfe & Chen 2006; hereafter referred to as WC06).

This interpretation of $\ell_c^{\rm crit}$ is illustrated in Fig. 4.9, which shows ℓ_c and the total heating rate, $\Gamma_{\rm tot}$, as functions of gas volume density n. We assume that $\Gamma_{\rm tot}$=$\Gamma_{\rm XR}$+ $\Gamma_{\rm pe}$+$\Gamma_{\rm C^0}$, where $\Gamma_{\rm XR}$, $\Gamma_{\rm pe}$, and $\Gamma_{\rm C^0}$ are heating rates due to X-ray photoionization, grain photoelectric emission, and photoionization of C^0 (Wolfire et al. 1995). The curves in Fig. 4.9 are solutions to the thermal balance and ionization equilibrium equations for neutral gas layers with $N_{\rm HI}$=$10^{20.6}$ cm^{-2} that are heated and ionized by background radiation fields computed for z=2.3 (Haardt & Madau 1996: and more recently using CUBA[2]). The panels in this figure show the resulting $\Gamma_{\rm tot}(n)$ and $\ell_c(n)$ for metallicities spanning the range of values found in DLAs.

Fig. 4.9 illustrates why background heating is an attractive explanation for DLAs with $\ell_c \leq \ell_c^{\rm crit}$. In particular ℓ_c remains below 10^{-27} ergs s^{-1} H^{-1} for the entire range of densities and metallicities in the figure. At densities below $n_{\rm max}$, the lowest density where ℓ_c is a local maximum (=$\ell_c^{\rm max}$), the gas is a warm neutral medium (WNM) in which $T \approx 8000$ K and $\ell_c << \Gamma_{\rm tot}$, since cooling is dominated by Lyα and electron recombination onto grains. At densities above $n_{\rm max}$ the gas is a cold neutral medium (CNM) in which $T \approx 100$ K and ℓ_c= $\Gamma_{\rm tot}$, because cooling is dominated by 158 μm emission. While a detailed discussion about the behavior of $\ell_c(n)$ is beyond the scope of this paper (see WHGPL and

---

[2] CUBA(Haardt & Madau 2003) is available at: http://pitto.mib.infn.it/~haardt/cosmology.html

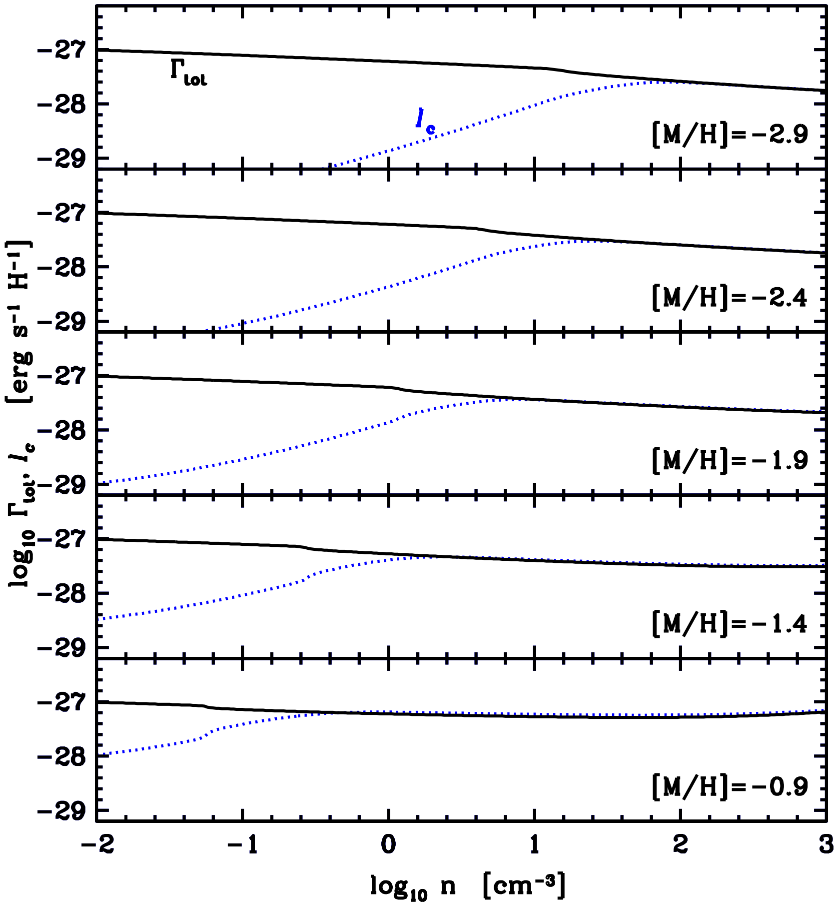

Figure 4.9: Thermal equilibria computed for neutral gas at $z \sim 3$ heated by background radiation. Dominant heating mechanism is production of primary electrons by photoionization of H and He by soft X-rays ($h\nu \geq 0.4$ kev). Primary electron energy degraded by photoionization and collisional excitation processes, leading to the production of secondary electrons that heat ambient electrons by Coulomb interactions. Grain photoelectric heating by FUV radiation is also included. Background radiation fields computed by Haardt & Madau (2003; using CUBA). Panels show the background heating rates per H atom (solid black) and the [158] μm cooling rates, ℓ_c, per H atom (dotted blue) as functions of gas density. Panels show results for several values of gas metallicity, [M/H]. Notice, ℓ_c does not exceed 10^{-27} ergs s^{-1} H^{-1}. See text for physical interpration of these curves.

Wolfire et al. [1995] for more extensive discussions), we wish to emphasize two points. First, although $\ell_c^{\rm max}$ increases with increasing [M/H], Fig. 4.9 shows that it never exceeds 10^{-27} ergs s^{-1} H^{-1}. Second, because ℓ_c undergoes a sharp decline with *decreasing* density at $n < n_{\rm max}$, the range of 158 μm cooling rates available in the WNM for low values of ℓ_c is much larger than the limited range of CNM cooling rates available at $n > n_{\rm max}$. Combined with the upper limits on density required in the case of background heating to explain the large observed ratios of C II/C I (WHGPL), this suggests that DLAs with $\ell_c \le \ell_c^{\rm crit}$ are low-density WNM gas layers without local heat input.

Because these conclusions are based on specific values of $N_{\rm HI}$ and z, we tested their generality by computing $\ell_c^{\rm max}$ for the 40 DLAs in the standard 'low cool' population (see § 4.3). We adopted the metallicity, dust-to-gas ratio, and $N_{\rm HI}$ appropriate for each DLA, exposed the gas to the background radiation intensity inferred for the DLA redshift (Haardt & Madau 2003; using CUBA), and then computed $\ell_c^{\rm max}$ for the $\ell_c(n)$ equilibrium curves. We found that $\ell_c^{\rm max}$ exceeded 10^{-27} ergs s^{-1} H^{-1} for only 5 of the 40 DLAs. This is consistent with our expectation, owing to the low metallicity of the 'low cool' population.

However, despite the attractive features of this model it has serious problems. While it predicts ℓ_c to be less than $\ell_c^{\rm max}$, the *measured* values of ℓ_c exceed $\ell_c^{\rm max}$ for 9 out of the 14 positive detections in the 'low cool' population. This indicates the presence of local heat sources for these DLAs, which contradicts the assumption of background heating alone. Of course this conclusion is based on our determinations of $\ell_c^{\rm max}$ which for low-metallicity gas is a sensitive function of the X-ray background intensity at $z{\approx}3$ and photon energies $h\nu \ge 0.5$ keV. Because the background intensity depends on volume emissivity, the critical quantity is the normalization of the X-ray luminosity function for high-z AGNs at the characteristic luminosity, L_*. Results from the recent study of Silverman et al. (2006; 2007) suggest that the Haardt-Madau (2003; using CUBA) determination, which was based on earlier work by Ueda et al. (2003), is a factor of 3 higher than the Silverman et al. (2006; 2007) determination for $3.0 < z < 4.0$, the relevant redshift interval for background radiation at $z \approx 3$. In addition the Haardt-Madau (2003; using CUBA) background must be increased by at least a factor of three for background heating to explain the measured values of ℓ_c for the 'low cool' population. As a result, the X-ray luminosity function must be a factor of 9 higher than the Silverman et al. (2006; 2007) value to explain the ℓ_c values. While there are other uncertainties in determining the heating rates such as the carbon abundance and the grain-photoelectric heating efficiencies, we conclude that while it cannot be ruled out altogether, the background heating hypothesis is not likely to be correct.

4.5.2 Local Heating

We next consider the alternative hypothesis that the 'low cool' DLAs are heated primarily by local sources. Suppose the background intensity, $J_{\nu}^{\rm bkd}$, at $z \approx 3$ is half the Haardt & Madau (2003; using CUBA) intensity, in agreement with observational uncertainties. In that case the measured values of ℓ_c exceed $\ell_c^{\rm max}$ for 11 of the 14 positive detections, indicating that local energy input is required for most of this population. To determine the level of input we adopted the model of WPG03 in which the star formation rate per unit area projected perpendicular to a uniform gaseous disk, $\Sigma_{\rm SFR}$ [3], generates FUV radiation that heats the gas by the grain photoelectric mechanism. Heat inputs by cosmic rays and locally generated X-rays are also included and are assumed to be proportional to $\Sigma_{\rm SFR}$. The gas is a two phase medium in which the CNM and WNM are in pressure equilibrium at the pressure given by the geometric mean of the minimum and maximum pressures characterizing the equilibrium $P(n)$ curve

---

[3] In WC06 we denoted this quantity by $(\dot{\psi}_*)_\perp$ to distinguish it from $\dot{\psi}_*$, the SFR per unit area determined from the observed H I column density by assuming the Kennicutt-Schmidt relation. Since such distinctions are not relevant here and to be consistent with the more general usage (cf Kennicutt 1998) we adopt the $\Sigma_{\rm SFR}$ notation.

(Wolfire et al. 2003). Because the detected C II* absorption likely arises in the CNM, WPG03 were able to deduce unique values for the local FUV radiation intensity $J_\nu^{\rm local}$ from measured values of ℓ_c. Specifically, in the case of thermal balance WPG03 found that

$$\ell_c = 10^{-5}\kappa\epsilon J_\nu \tag{4.2}$$

where J_ν=$J_\nu^{\rm bkd}$+$J_\nu^{\rm local}$ and ϵ is the photoelectric heating efficiency (e.g. Bakes & Tielens 1994; Weingartner & Draine 2001). To obtain $\Sigma_{\rm SFR}$, WPG03 solved the transfer equation in a uniform disk and found that in the optically thin limit

$$J_\nu^{\rm local} = \frac{C\Sigma_{\rm SFR}}{8\pi}[1+\ln(r_{\rm DLA}/h)] \tag{4.3}$$

where C ($\equiv$8.4$\times$10^{-16} ergs cm^{-2}s^{-1}Hz^{-1}[M$_\odot$yr^{-1}kpc^{-2}]$^{-1}$) is a conversion constant (see WC06), and $r_{\rm DLA}$ and h are the radius and scale-height of the DLA disk.

Applying the same technique to the DLA sample in Table 4.1 and assuming $r_{\rm DLA}/h$=50, we determined values of $\Sigma_{\rm SFR}$ for 38 of the 44 DLAs with positive detections and lower limits. [4] The resulting distribution of $\Sigma_{\rm SFR}$ is shown in Fig. 4.10, where we have plotted the results for the 'low cool' and 'high cool' populations separately. We include results for the 'high cool' DLAs, since background heating is insufficient to balance the 158 μm cooling rates from this population, indicating that local heating is also required in this case. The $\Sigma_{\rm SFR}$ distribution is of interest for several reasons. First, application of the KS test provides strong evidence for two distinct modes of star formation, since the probability that the two populations are drawn from the same parent distribution is given by $P_{\rm KS}(\Sigma_{\rm SFR})$=3.4$\times$10^{-7}. Furthermore, comparison of Fig. 4.10 with Figs. 4.3 to 4.6 shows evidence for less overlap between the 'low cool' and

---

[4] We could not determine $\Sigma_{\rm SFR}$ for the remaining 6 DLAs either because background heating was sufficient to balance the observed cooling, or we could not deduce a dust-to-gas ratio from our depletion model since [Fe/H] > [M/H].

'high cool' distributions of $\Sigma_{\rm SFR}$ than for Δv_{90}, [M/H], κ, and W_{1526}. Indeed, comparison with Figure 4.2 suggests that the $\Sigma_{\rm SFR}$ and ℓ_c distributions are both bimodal.

Second, although the WPG03 model assumes *in situ* star formation throughout the neutral-gas disk, the survey of the Hubble Ultra Deep Field (UDF) by WC06 places upper limits on such star formation, which rule out some of the scenarios discussed above. Specifically, WC06 searched the UDF F606W image for low surface-brightness emission from DLAs in the redshift interval z=[2.5,3.5] with angular (linear) diameters between $\theta_{\rm DLA}$=0.25 $''$ ($d_{\rm DLA}$=2 kpc) and $\theta_{\rm DLA}$=4.0 $''$ ($d_{\rm DLA}$=31 kpc). They optimized the survey sensitivity by convolving the F606W image with Gaussian smoothing kernels with FWHM diameters $\theta_{\rm kern}= \theta_{\rm DLA}$: the resulting $\approx 5\sigma$ surface brightness thresholds varied between $\mu_V^{\rm thresh}$=28.0 mag arcsec^{-2} for $\theta_{\rm kern}$=0.25$''$ to $\mu_V^{\rm thresh}$=29.7 mag arcsec^{-2} for $\theta_{\rm kern}$=4.0$''$. They found the number of detected objects to decrease steeply with increasing $\theta_{\rm kern}$ and to be at least two orders of magnitude lower than predicted, which is determined by dividing the large DLA area covering factor, $C_{\rm A}$=0.33 (for z=[2.5,3.5]), by the area per DLA, $\pi {\theta_{\rm DLA}}^2/4$. Stated differently, *in situ* star formation is unlikely to occur in DLAs at values of $\Sigma_{\rm SFR}$ above the SFR thresholds, $\Sigma_{\rm SFR}^{\rm thresh}$, set by the UDF threshold surface brightnesses. To compute $\Sigma_{\rm SFR}^{\rm thresh}$ we note that I_{ν_0}=$C\Sigma_{\rm SFR}[4\pi(1+z)^3 {\rm cos}(i)]^{-1}$ where I_{ν_0} is the intensity observed from a disk at redshift z, and i is the disk inclination angle. Therefore, a disk with a given $\Sigma_{\rm SFR}^{\rm thresh}$ generates a range of intensities that depend on i. To assure the detection of a significant fraction of disks with threshold SFRs we set i=60^o. This guarantees that $I_{\nu_0} \geq I_{\nu_0}^{\rm thresh}$ (or $\mu_V \leq \mu_V^{\rm thresh}$) for half the disks for which $\Sigma_{\rm SFR}$ =$\Sigma_{\rm SFR}^{\rm thresh}$ and $i \geq 60^o$.

The resulting $\Sigma_{\rm SFR}^{\rm thresh}$ are plotted as functions of $\theta_{\rm kern}$ in Fig. 4.11 for three redshifts spanning the redshift interval of the WC06 survey.[5] The fig-

---

[5] For a given surface brightness the above definition results in values of $\Sigma_{\rm SFR}^{\rm thresh}$ that are a factor of 2.8 smaller than the effective SFR per unit area, $\dot{\psi_*}$, discussed in WC06 (see their eq. 3).

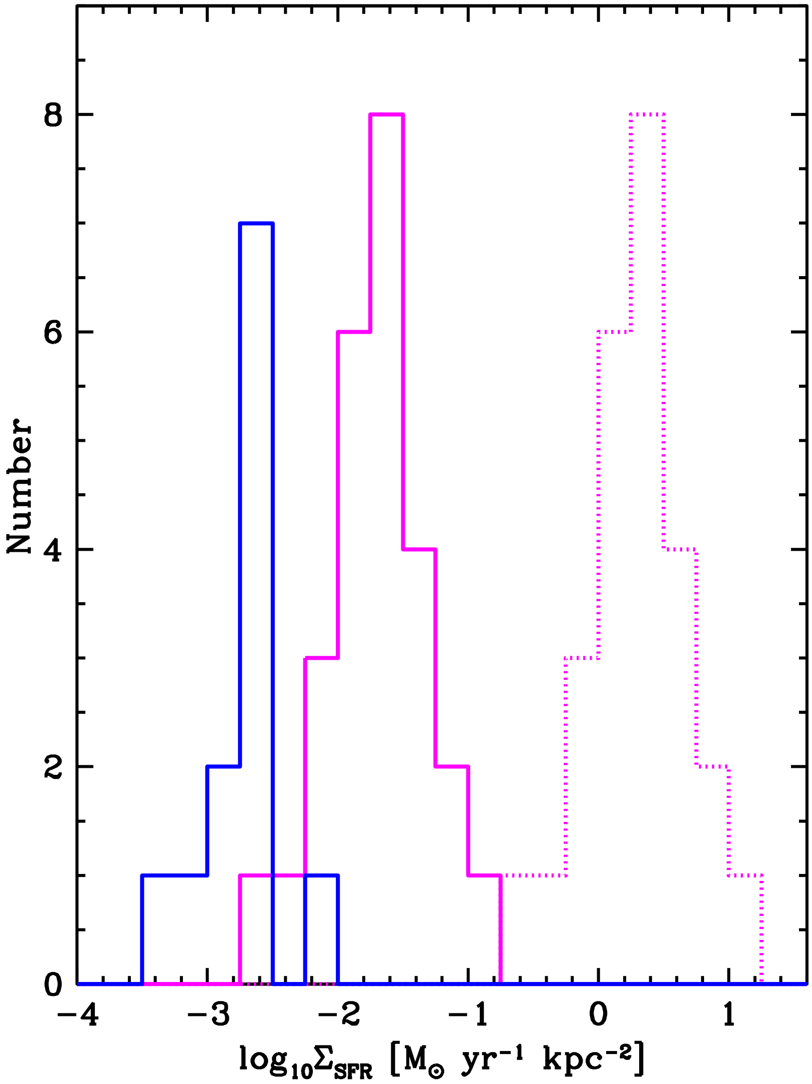

Figure 4.10: Histograms of $\Sigma_{\rm SFR}$ obtained using the C II* model of WP03 and WGP03. Blue histogram refers to 'low cool' DLAs. Magenta histograms refer to 'high cool' DLAs, where solid and dotted histograms respectively depict lower limits and true values of of $\Sigma_{\rm SFR}$.

ure shows that $\Sigma_{\rm SFR}^{\rm thresh}$ decreases in the interval $\theta_{\rm kern}$=[0.25$''$,2.0$''$]. The decrease is caused by the Poisson error in surface brightness, which decreases with increasing aperture size. The decline of $\Sigma_{\rm SFR}^{\rm thresh}$ ceases at $\theta_{\rm kern} > 2.0''$ due to the appearance of the systematic error, which WC06 attribute to confusion noise arising from the low surface-brightness outer regions of bright galaxies. Comparison with Fig. 4.10 shows that the SFR per unit area for the bulk of the 'high cool' population, exceeds $10^{-2.2}$ M$_{\odot}$ yr^{-1} kpc^{-2}. Since this exceeds $\Sigma_{\rm SFR}^{\rm thresh}$ for all values of the redshifts and $\theta_{\rm kern}$ depicted in Fig. 4.11, such star formation would have been detected by WC06. Because WC06 detected less than 1% of the DLAs predicted for this population, we conclude that the heat input from *in situ* star formation in 'high cool' DLAs cannot balance the rate at which they cool. This is in agreement with the results of WC06 who worked with the Kennicutt-Schmidt relation rather than the C II* technique. As a result, the FUV intensity that heats the gas is likely emitted by compact (i.e., $\theta_{\rm FWHM} <$ 0.25 $''$), centrally located, regions that WC06 identified as Lyman Break Galaxies (hereafter referred to as LBGs; Steidel et al. 2003). Note, in that case the $\Sigma_{\rm SFR}$ obtained for this population (see Fig. 4.10) are lower limits on the true values of $\Sigma_{\rm SFR}$, which we estimate from the following argument. Assuming the 'high cool' DLAs account for half the DLA population and contain LBGs, the ratio of areas occupied by DLAs to LBGs, $\pi r_{\rm DLA}^{2}/\pi r_{\rm LBG}^{2}$, is given by the ratio of area covering factors, $C_{\rm DLA}^{\rm highcool}/C_{\rm LBG}$. Since WC06 found that $C_{\rm DLA}/C_{\rm LBG}$=330 in the redshift interval z=[2.5,3.5], we find that $\pi r_{\rm DLA}^{2}/\pi r_{\rm LBG}^{2}$=165, where $C_{\rm DLA}^{\rm highcool}= 0.5C_{\rm DLA}$. As a result, the true values of $\Sigma_{\rm SFR}$ are a factor of 165 higher than the lower limits for the 'high cool' population. The distributions of both the lower limits and true values of $\Sigma_{\rm SFR}$ are depicted in Fig. 4.10.

Fig. 4.10 also shows that $\Sigma_{\rm SFR} \geq 10^{-3}$ M$_{\odot}$ yr^{-1} kpc^{-2} for the bulk of the 'low cool' population. From Fig. 4.11 we see that this exceeds $\Sigma_{\rm SFR}^{\rm thresh}$ for $\theta_{\rm kern}$ $\geq 0.7''$ at z=2.5, $\theta_{\rm kern} \geq 1.3''$ at z=3.0, and $\theta_{\rm kern} \geq 2.0''$ at z=3.5. Therefore, *in*

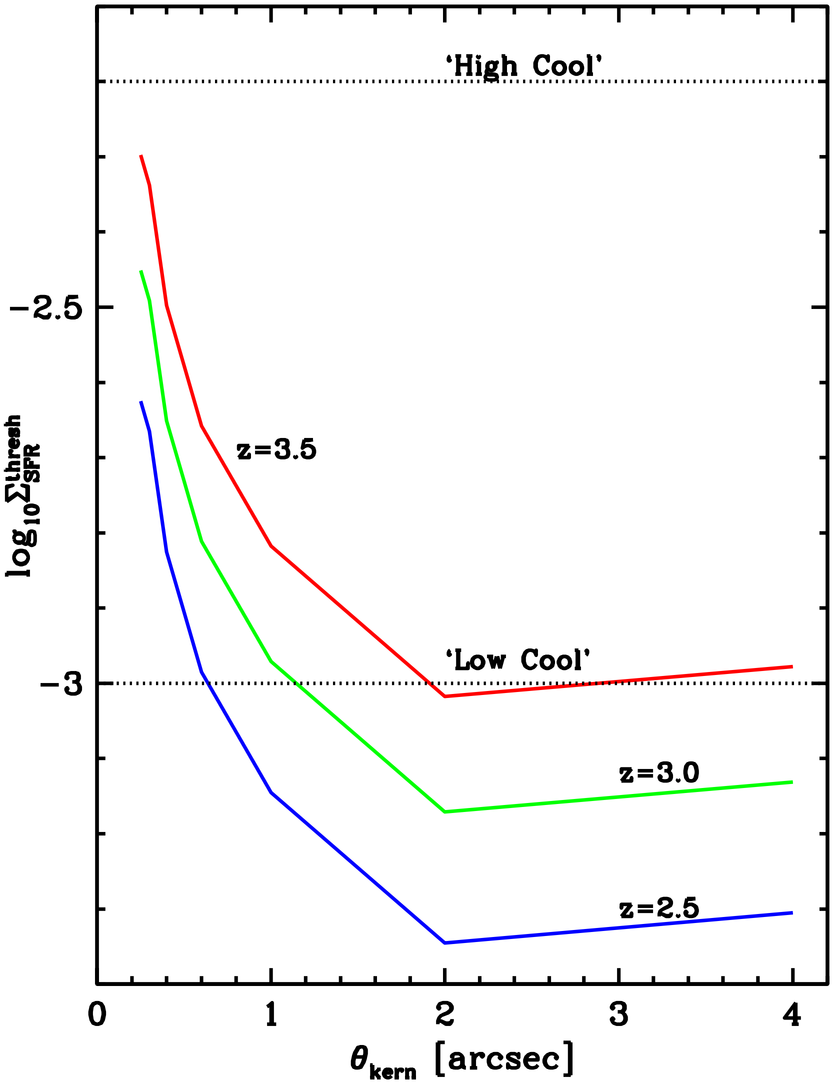

Figure 4.11: Solid curves are *threshold* values of $\Sigma_{\rm SFR}$ versus diameter of smoothing kernel used by the search of WC06. Results shown for $z = 2.5$ (blue), 3.0 (green), and 3.5 (red). Horizontal dotted lines depict cooling rates per H atom characterizing 'low cool' and 'high cool' populations.

situ star formation is detectable from ‘low cool’ DLAs with angular diameters $\theta_{\rm DLA}$ above these limits. Since less than 1 % of the predicted number of DLAs were detected by WC06 and since the ‘low cool’ population comprises about half of all high z DLAs, we conclude that *in situ* star formation for this population is compatible with the observations only if the values of $\theta_{\rm DLA}$ are smaller than these limits. Note, we cannot rule out the possibility that similar to the ‘high cool’ population, star formation in ‘low cool’ DLAs is sequestered away from the DLA gas in compact LBG cores. However, owing to the different properties of the two populations, it is more likely that within the context of the local heating hypothesis the ‘low cool’ DLAs undergo *in situ* star formation.

4.6 Summary of DLA Properties

At this point we pause to give an overview of the DLA properties discussed above. A summary is given in Table 4.3 which lists the median values of the directly measurable properties ℓ_c, Δv_{90}, [M/H], W_{1526}, and $N_{\rm HI}$, and the model-dependent quantities κ, $J_\nu^{\rm local}$, and $\Sigma_{\rm SFR}$. With the exception of $N_{\rm HI}$, all the properties of the ‘high cool’ DLAs have systematically larger values than their ‘low cool’ counterparts. Because Δv_{90} and W_{1526} measure spatial variations in velocity, it is plausible to assume they measure mass. In that case the median halo mass of the ‘high cool’ DLAs would be 30 times larger than that of the ‘low cool’ DLAs. This follows from the assumptions that (1) Δv_{90} and W_{1526} are each proportional to the halo circular velocity $v_{\rm circ}$ and (2) $M_{\rm DM} \propto v_{\rm circ}^3$ (see Mo et al. 1998) where $M_{\rm DM}$ is the halo dark-matter mass. A higher mass for the ‘high cool’ population is also consistent with its higher metallicity, since metallicity is an increasing function of mass in modern galaxies (Tremonti et al. 2004), and chemical evolution in ΛCDM models predict a similar trend at high redshifts (e.g. Nagamine 2002). Because the dust-to-gas ratio κ traces metallicity, the higher median value of κ for the ‘high cool’ DLAs is expected. On the other hand higher values of ℓ_c and $\Sigma_{\rm SFR}$ in the ‘high cool’ DLAs goes against the trend in current galaxies where star-formation activity is more common in low-mass late type galaxies than in massive early-type galaxies (Kauffmann et al. 2003).

Table 4.3: POPULATION PROPERTIES

	Population	
Property(median)	‘Low Cool’	‘High Cool’
$\log_{10}\ell_c$ [ergs s^{-1} H^{-1}]	-27.29 ± 0.07	-26.54 ± 0.13
Δv_{90} [km s^{-1}]	46 ± 10	104 ± 15
[M/H]	-1.74 ± 0.19	-1.06 ± 0.13
W_{1526} [Å]	0.26 ± 0.09	0.67 ± 0.19
$\log_{10}N_{\rm HI}$ [cm^{-2}]	20.7 ± 0.17	20.7 ± 0.19
$\log_{10}\kappa$	-2.57 ± 0.17	-1.60 ± 0.26
$\log_{10}[J_\nu^{\rm local}/10^{-19}$ ergs cm^{-2} s^{-1} Hz^{-1} sr^{-1}]	-18.58 ± 0.17	-17.71 ± 0.12
$\log_{10}\Sigma_{\rm SFR}$[a] [M$_\odot$ yr^{-1} kpc^{-2}]	-2.78 ± 0.34	>-1.85

[a] SFRs per unit area inferred assuming *in situ* star formation. Since *in situ* star formation ruled out for ‘high cool’ DLAs, entry for ‘high cool’ DLAs is a lower limit.

While we have interpreted the two types of DLAs as physically distinct populations, let us consider the alternative hypothesis that they are distinguished by the difference in impact parameters of sightlines passing through a unique population of DLAs. Suppose ‘low cool’ DLAs are metal-poor outer regions connected to metal-rich inner regions of the ‘high cool’ DLAs by a negative metallicity gradient. In this case the lower values of Δv_{90} in the ‘low cool’ DLAs would arise from passage of QSO sightlines through neutral gas at larger impact parameters where smaller changes in velocity generated by the systematic motions of the neutral gas are expected (Prochaska & Wolfe 1997). There are, however, at least two difficulties with this idea. First, since the values of W_{1526} are plausibly determined by the virialized random motions of clouds in the outer halo, W_{1526} would not be affected by a change in impact parameter, since $r_{\rm DLA}$ is small compared to the radius of the halo. Yet the median value of W_{1526} for the ‘low cool’ DLAs is is significantly lower than for the ‘high cool’ DLAs (see Table 4.3). Secondly, one would also expect a decrease in $N_{\rm HI}$ to accompany the decrease in [M/H] with increasing impact parameter, which is contradicted by the good agreement between the median values of $N_{\rm HI}$ in Table 4.3 (but see Johansson & Efstathiou 2003). Third, it is difficult to understand how a difference in impact parameter could produce bimodality in ℓ_c.

Therefore, while we cannot rule out the alternative possibility that the velocity fields in DLAs could be due to non-gravitational motions (e.g. galactic-scale winds, see discussion in § 4.8), we shall adopt the working hypothesis that the crucial quantity distinguishing the two populations is mass.

4.7 Connections to Bimodality in Galaxies

In this section we discuss analogies with bimodality in modern galaxies, and then place the results within the context of galaxy formation.

4.7.1 Bivariate Distributions

The bimodality of the ℓ_c distribution in Fig. 4.2 brings to mind bimodal distributions in contemporary galaxies. From their analysis of $\sim 10^5$ galaxies drawn from the SDSS survey, Baldry et al. (2004; see also Blanton et al. 2003) find the $u - r$ color distribution to be bimodal. The distribution exhibits a blue peak at $u - r \approx 1.4$ and a red peak at $u - r \approx 2.4$. In a similar analysis, Kauffmann et al. (2003) find bimodality in the distribution of the age parameter $D_n(4000)$ and the indicator of recent star-formation activity, Hδ_A. The galaxies centered at the blue peak are roughly the same objects exhibiting peaks at young stellar ages and recent star-formation, while the the galaxies centered at the red peak exhibit peaks at older stellar ages and low levels of recent star-formation activity.

A possible link to bimodality in DLAs follows from the bivariate galaxy distributions in the $(u-r,M_*)$ [6], $(D_n(4000),M_*)$, and (Hδ_A, M_*) planes. Specifically, galaxies in the $(u-r,M_*)$ plane divide into separate blue and red sequences.

---

[6] Baldry et al. actually use the $u - r,M_r$ plane where M_r is the Petrosian absolute red magnitude. But the tight correlation between M_* and M_r implies that M_r is an accurate indicator of stellar mass.

Within each sequence, $u-r$ is correlated with M_*. Bimodality in the $u-r$ distribution arises from extracting the colors of galaxies within bins of constant M_*. As M_* increases from low values, where the color distribution is dominated by the blue peak, a red peak grows while the blue peak declines in strength until at the highest masses the distribution is dominated by the red peak. Similar behavior is seen in the ($D_n(4000)$,M_*) and (Hδ_A, M_*) planes, except that Hδ_A is anti-correlated with M_*.

In Fig. 4.12 we plot DLA analogues to these bivariate galaxy distributions. Following the discussion in § 4.4.4 we substitute W_{1526} for M_* because of evidence that W_{1526} is an indicator of dark-matter mass, $M_{\rm DM}$ (Prochaska et al. 2007), and since M_* should be proportional to $M_{\rm DM}$. Fig. 4.12a shows an analogous and unambiguous correlation between [M/H] and log$_{10}W_{1526}$. By analogy with the galaxy result the W_{1526} bin corresponding to low values of W_{1526} (log$_{10}W_{1526}$(Å) < -0.8) produces an [M/H] distribution which peaks at [M/H] ~ -2.3, while the bin corresponding to higher values, i.e., log$_{10}W_{1526}$(Å) > -0.2, gives rise to an [M/H] distribution, which peaks at [M/H] ~ -0.7. Although bins at intermediate values of W_{1526} do not result in clear evidence for two peaks in the [M/H] distribution, this may be a consequence of small numbers statistics. Furthermore, small numbers statistics may be responsible for the absence of a clear discontinuity between the 'blue' and 'magenta' distributions in the ([M/H], log$_{10}W_{1526}$) plane.

On the other hand such a discontinuity is present in Fig. 4.12b, which plots log$_{10}\ell_c$ versus log$_{10}W_{1526}$. In this case we only plot positive detections, since the upper and lower limits would obscure possible trends in the (ℓ_c,W_{1526}) plane. While neither population shows evidence for correlations between these variables, the bin with log$_{10}W_{1526}$(Å) > -0.2 produces an ℓ_c disribution dominated by large cooling rates. Interestingly, the absence of a clear anti-correlation between log$_{10}\ell_c$ and log$_{10}W_{1526}$ runs counter to the trend in the (Hδ_A, M_*) plane, which

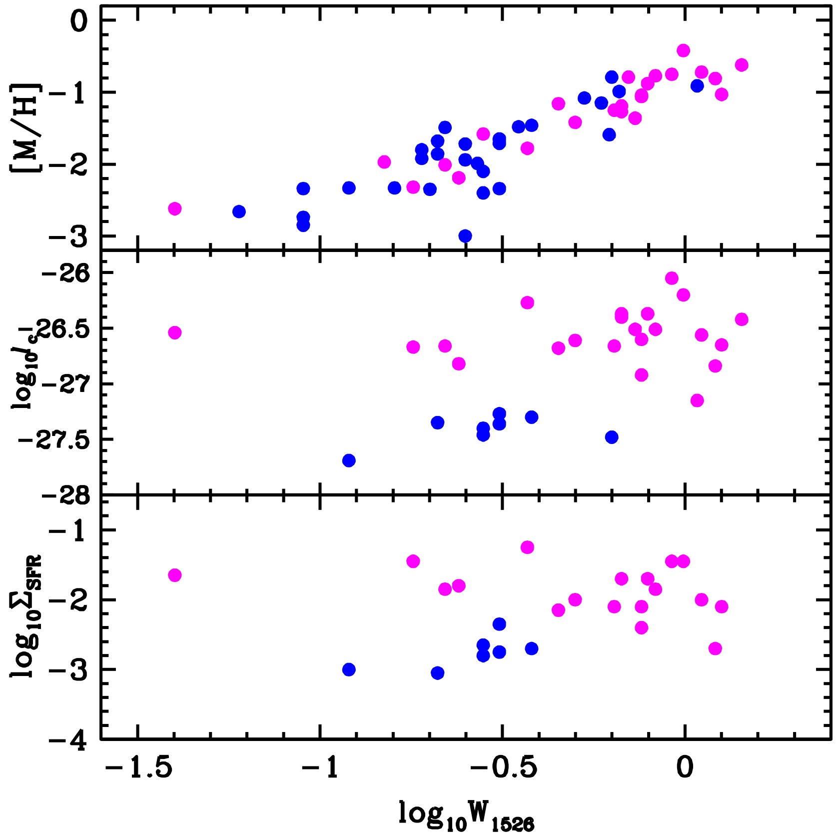

Figure 4.12: Bivariate distributions of various parameters versus W_{1526}. Plots are DLA analogues of bivariate distributions of various galaxy parameters versus stellar mass. (a) Metallicity versus W_{1526}. Blue and magenta points are 'low cool' and 'high cool' populations with measured values of W_{1526}. Note the strong positive correlation between [M/H] and W_{1526}, and the dominance of 'low cool' points for low values of W_{1526} and 'high cool' points for high values of W_{1526}. (b) $[\ell_c/\mathrm{ergs\ s^{-1}\ H^{-1}}]$ versus W_{1526}. In this case only DLAs with positive detections of C II* are shown. The discontinuity between the two populations is obvious but no evidence for correlations is present. (c) $[\Sigma_{\rm SFR}/\mathrm{M_\odot\ yr^{-1}\ kpc^{-2}}]$ versus W_{1526}. Systems with high $\Sigma_{\rm SFR}$ dominate at large values of W_{1526}. *Note, values of* $\Sigma_{\rm SFR}$ *for 'high cool' DLAs are lower limits.*

is the closest galaxy analogue, as we have interpreted ℓ_c as an indicator of star formation. Fig. 4.12c plots $\log_{10}\Sigma_{\rm SFR}$ versus $\log_{10} W_{1526}$, which is also analogous to the bivariate distribution in the (Hδ_A, M_*) plane since $\Sigma_{\rm SFR}$ is, of course, a star-formation indicator. In this case, evidence for discontinuities between the two populations is strengthened by arguments in § 4.2, which imply that the values of $\Sigma_{\rm SFR}$ for the 'high cool' DLAs in Fig. 4.12 are conservative lower limits. We find similar results, with somewhat larger scatter, when Δv_{90} is used as a mass proxy, as shown in Fig. 4.13.

However, we wish to point out an important difference between the C II* and traditional star-formation signatures. While the Hδ_A index is sensitive to star bursts ending $\sim 10^8$ to 10^9 years before the detection of Hδ absorption in galaxies, the ℓ_c cooling rate is sensitive only to star formation contemporaneous with the epoch at which C II* absorption is detected. The reason for this stems from the short cooling times in DLAs, where

$$t_{\rm cool} = \frac{5}{2}\frac{kT}{\ell_c} \tag{4.4}$$

in the case of CNM gas. Here we have assumed the gas to be in pressure equilibrium (Wolfire et al. 1995) and we have ignored the contribution of CMB excitations to the 158 μm emission rate defined in Eq. 1 (WGP03). Assuming $T = 100$K, we find cooling times of $\approx 3\times10^6$ yr and 2×10^5 yr for the median 'low cool' and 'high cool' DLAs in Table 4.3. Therefore, our observations are unlikely to detect 158 μm cooling rates from starbursts with duration Δt short compared to the $\sim 2\times10^9$ yr time interval corresponding to the redshift search window used to find the DLAs in Table 4.1. The implication is that while the star formation history of DLAs may be punctuated with isolated, short-lived starbursts, the C II* technique is sensitive only to a continuous mode of star formation, or multiple bursts with a high duty cycle. Consequently, we may have detected the latter modes of star formation.

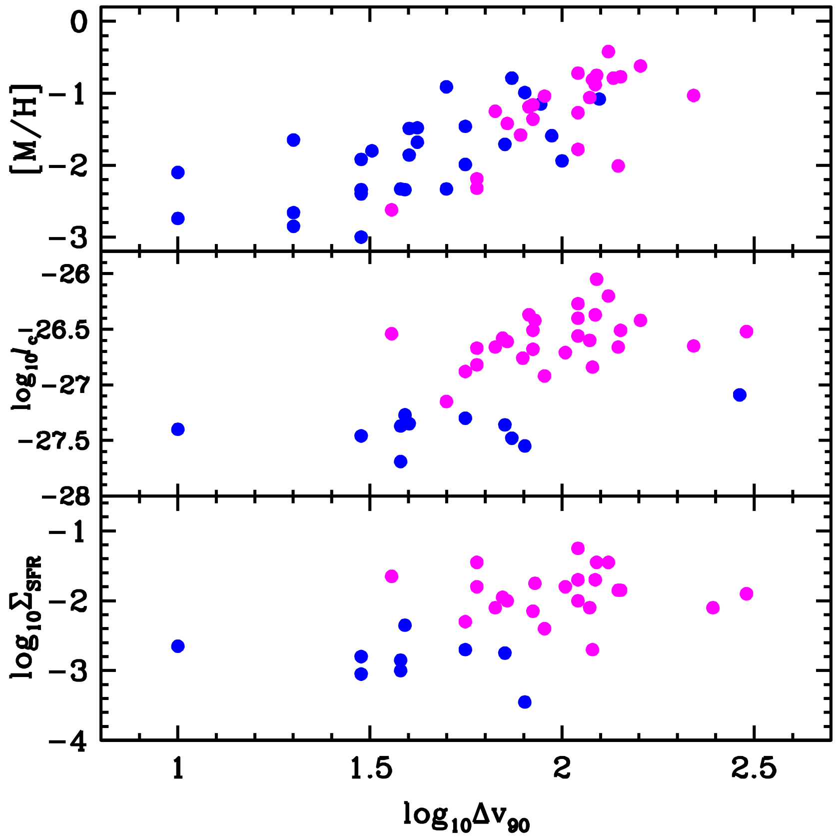

Figure 4.13: Same as Fig. 4.12 except that Δv_{90} is substituted for W_{1526} as the independent variable.

The short cooling times raise the possibility that the ‘low cool’ and ‘high cool’ DLAs represent different levels of star formation activity in the same object. In this scenario an underlying base level of activity gives rise to the ‘low cool’ DLAs, while bursts in star-formation rates produce the ‘high cool’ DLAs. The ℓ_c values would track the star formation rates because of the short cooling times. However, the metallicity distributions of the two populations would be indistinguishable since metallicity is a byproduct of star formation history rather than instantaneous star formation rate. While the star bursts in the ‘high cool’ mode could affect the velocity structure of the gas through stellar winds, the high duty cycle of the bursts implies that the velocity structure of the gas is also a function of star-formation history rather than instantaneous rate. For these reasons it is difficult to understand how varying star formation rates in a single class of DLAs could explain why the metallicity and velocity structure of the two populations are so different.

Therefore, in common with modern galaxies the bimodality in DLAs may arise from the presence of two distinct sequences in mass and star-formation activity. The obvious question is whether the DLA phenomenon is the precursor to the bimodality detected in galaxies? Stated differently, have we detected the early stages of galaxy bimodality in DLAs?

4.7.2 Galaxy Formation Models

To answer this question we turn to models for the origin of galaxy bimodality and then suggest an empirical test.

Transition Mass Models

Dekel & Birnboim (2005) interpret galaxy bimodality in terms of a transition occurring at the ‘shock’ dark-matter mass, $M_{\rm shock}{\approx}10^{11.5}$ $M_{\odot}$ (Keres et al. 2005; Dekel & Birnboim 2005), corresponding to $M_* \approx 10^{10.5}$ $M_{\odot}$, which is the stellar mass separating the two sequences in the ($D_n(4000)$,M_*) and ($H\delta_A$, M_*) planes (Kauffmann et al. 2003). At high redshifts, halos with $M_{\rm DM} < M_{\rm shock}$ accrete gas in a cold flow in which the temperature never climbs to the virial temperature of the halo: such processes result in the formation of disks observed along the lower-mass blue sequence. By contrast, gas accreting onto high-redshift halos with $M_{\rm DM} > M_{\rm shock}$ is first heated to the virial temperature ($\sim 10^6$ K) by stable shocks. The gas later contracts in a quasi-static spherically symmetric cooling flow to form the bulges found in the more massive galaxies populating the red sequence. In this case outlying cold gas accretes along filaments connecting the massive halos to the IGM.

This scenario provides plausible explanations for several phenomena related to bimodality in DLAs. First, the cold gas accreting onto halos with $M_{\rm DM}$ $< M_{\rm shock}$ naturally evolves into disk-like structures, which act as neutral-gas reservoirs for *in situ* star formation. This is in accord with our finding that *in situ* star formation in DLAs is the dominant mode in the 'low cool' population, which we identify with halos having $M_{\rm DM} < M_{\rm shock}$. The low level of star formation predicted for these objects is probably related to the low molecular content of the DLA gas or to the increase with redshift of the Toomre critical surface density (see WC06). Second, the transition-mass scenario predicts little, if any, *in situ* star formation in the hot gas accreting onto halos with $M_{\rm DM} > M_{\rm shock}$. Rather, star formation in these objects is predicted to occur in dense, centrally located bulges that are fueled by filamentary cold flows penetrating the hot gas (Dekel & Birnboim 2005; Keres et al. 2005). This fits in naturally with our finding that star formation in the 'high cool' population, which we identify with halos having $M_{\rm DM} > M_{\rm shock}$, mainly occurs in compact star-forming bulges sequestered away from the DLA gas detected in absorption, which we associate with the dense filamentary gas predicted in the simulations. This crucial result suggests that the red-blue bimodality in galaxies and the 'high cool'/'low cool' bimodality in

DLAs have a common physical origin. As a result bimodality in galaxies may originate in DLAs since it predicts that at large redshifts the most active star-forming objects are bulges located in the most massive halos. This is in contrast to bimodality in modern galaxies, in which the bulges and spheroids of massive galaxies exhibit little evidence of star formation. Presumably feedback by AGNs and supernovae that form in the bulges inhibits star formation subsequent to the epochs during which the outlying neutral gas is detected as high-redshift DLAs (e.g. Governato et al. 2004).

If bimodality in DLAs stems from a transition in star-formation modes at $M_{\rm DM} \approx M_{\rm shock}$, then about half of all DLAs would need to arise in halos with $M_{\rm DM} > M_{\rm shock}$: this conclusion follows from our finding that about half of our DLA sample is in the 'high cool' population. Because of the large value of $M_{\rm shock}$, the high median mass $M_{\rm med}$ predicted for DLA halos would seem to contradict the standard hierarchical paradigm in which $M_{\rm med} \approx 10^{10}$ $\rm M_\odot$ (Haehnelt et al. 1998; Johansson & Efstathiou 2006). However, the results of recent numerical simulations reveal a more complex picture. Nagamine et al. (2004) find that $M_{\rm med}$ is a sensitive function of feedback. The model in best accord with observations is their Q5 run in which high-velocity (~ 400 km s^{-1}) winds effectively eject most of the neutral gas from low-mass halos. In this case $M_{\rm med} \approx 10^{11.5}$ $\rm M_\odot$ (Nagamine et al. 2007), which agrees with the values predicted for $M_{\rm shock}$ and is consistent with the range of masses deduced from the cross-correlation between DLAs and LBGs (Cooke et al. 2006). While this model does not explain all the DLA data, in particular the predicted area covering factor for $z = [2.5,3.5]$ is about a factor of 2 lower than observed, the overall agreement is sufficient to imply that such large values of $M_{\rm med}$ are plausible.

O VI Absorption Tests

An important feature of the transition-mass model is the presence of hot gas behind the accretion shock in halos with $M_{\rm DM} > M_{\rm shock}$. Hot gas is predicted only in this mass range, as halos with $M_{\rm DM} < M_{\rm shock}$ accrete gas in cold flows even when heating due to supernova feedback is included (Keres et al. 2005). Consequently, hot gas may be a signature of the 'high cool' population. The recent detection of O VI absorption in a large fraction of DLAs by Fox et al. (2007) and their interpretation that O VI is collisionally ionized suggests that hot gas is present in many DLAs. Although Fox et al. (2007) suggest this gas is shock heated by supernova remnants, the upper limits on star formation in DLAs set by WC06 restrict this form of energy input, provided the WC06 limits apply to gas surrounding compact LBGs. While such limits do not yet exist, let us assume that O VI absorption in DLAs arises in gas heated by accretion shocks. In that case the DLAs with O VI absorption would belong to the 'high-cool' population. Searches for C II* absorption have been carried out for three of the six DLAs in which O VI absorption was unambiguously detected in intervening systems. In DLA0112$-$306 at z=2.702 (Srianand et al. 2005), ℓ_c exceeds $\ell_c^{\rm crit}$, while in DLA2138$-$444 at $z = 2.852$ (Srianand et al. 2005) and DLA2206$-$199 at $z = 2.076$ (see Table 4.1) ℓ_c is less than $\ell_c^{\rm crit}$. Thus, the C II* data do not provide a statistically meaningful test.

We have considered an alternative test in which we compared the [M/H] distributions of DLAs in the 'high cool' population with those exhibiting O VI absorption. The results are shown in Fig. 4.14. When all nine intervening systems are included in the O VI sample, the KS tests yields $P_{\rm KS}$([M/H])=0.009 for the probability that the two distributions are drawn from the same parent population. This suggests that O VI absorption need not occur in 'high cool' DLAs. On the other hand, three of the O VI identifications are problematic: in each case only one member of the O IV$\lambda\lambda$ 1031, 1033 doublet was identified,

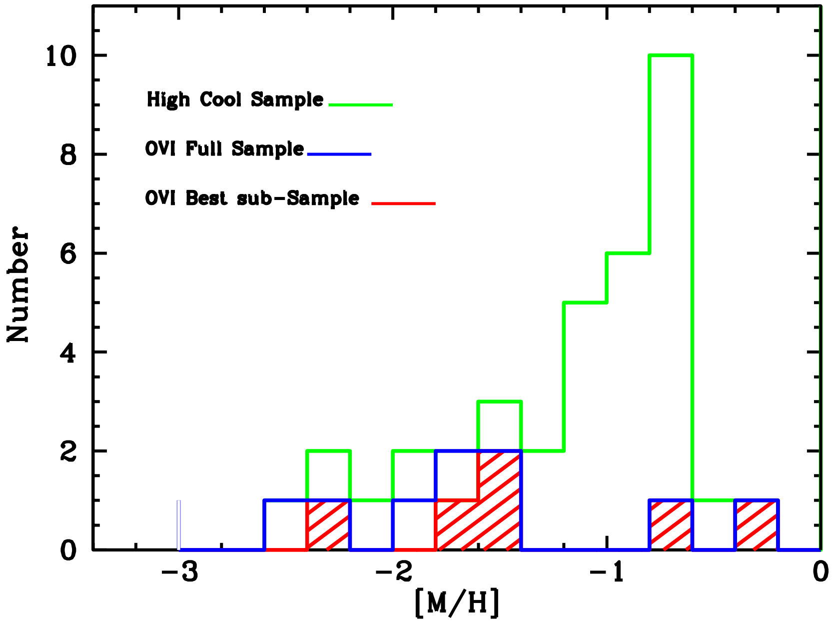

Figure 4.14: Comparison between [M/H] histograms for DLAs in ‘high cool’ sample (green) with blue histogram depicting 9 DLAs reported to exhibit intervening O VI absorption and red striped subsample showing the 6 of these with robust detections of O VI absorption.

possibly due to blending of the missing O VI line with Lyα forest absorption lines. But, it is equally plausible that all three features were misidentified as O VI. In that case only six DLAs would exhibit O VI absorption (see Fig. 4.14), and a revised KS tests yields $P_{\rm KS}$([M/H])=0.15. As a result, the data are not inconsistent with the hypothesis that the ‘high cool’ DLAs are in massive halos.

4.8 Conclusions

In this paper we searched for evidence of bimodality in DLAs. Our principal diagnostic tool was the [C II] 158 μm cooling rate per H atom, ℓ_c, which we obtained from measurements of the C II* λ 1335.7 and damped Lyα absorption lines. In addition to the C II* transition we used accurate velocity profiles of resonance transitions to measure velocity widths, equivalent widths, abundances, and dust-to-gas ratios for 76 DLAs. Our results are summarized as follows.

(1) Our studies of the C II* λ 1335.7 absorption line resulted in 37 positive detections, 7 lower limits, and 32 upper limits of ℓ_c. The positive detections show strong evidence for a bimodal distribution with two peaks at ℓ_c=$10^{-27.4}$ and $10^{-26.6}$ ergs s^{-1} H^{-1} separated by a trough at $\ell_c^{\rm crit}$$\approx$$10^{-27.0}$ ergs s^{-1} H^{-1}. In § 4.3 we argued that the distribution of the true values of ℓ_c corresponding to the lower and upper limits is consistent with the distribution of positive detections. Stated differently, there is compelling evidence that the ℓ_c distribution in Fig. 4.2 is a faithful representation of the parent population from which all the true values of ℓ_c are selected.

(2) In § 4.4 we tested the bimodality hypothesis by the following method. We first divided the full DLA sample into a 'low cool' subsample with $\ell_c \le \ell_c^{\rm crit}$ and a 'high cool' subsample with $\ell_c > \ell_c^{\rm crit}$. We then compared distributions of various physical parameters in the two subsamples. The probability that the parameters Δv_{90}, [M/H], κ, and W_{1526} in the two subsamples are drawn from the same parent populations is small, ranging between 10^{-5} to $\approx$$5\times10^{-3}$. On the other hand the distributions of $N_{\rm HI}$ are consistent with being drawn from the same parent population. Therefore, the two subsamples are likely to be separate populations with distinct distributions of velocity width, metal abundances, and gas-to-dust ratio, but similar H I column-density distributions.

(3) In § 4.5 we considered different physical processes responsible for heating the 'low cool' and 'high cool' DLAs. We studied the possibility that the 'low cool' DLAs were comprised of warm neutral-medium gas heated by background radiation alone, but considered it to be unlikely because background heating does not provide sufficient energy input to account for the cooling rates in the majority of these DLAs.

(4) We then investigated whether local heating could account for the

cooling rates in both DLA populations. Applying the two-phase model of WPG03, in which FUV radiation emitted by massive stars heats the gas by the grain photoelectric mechanism and assuming that C II* absorption arises in CNM gas, we found the resulting SFRs per unit area, $\Sigma_{\rm SFR}$, to be bimodal. We further found that the infrequent occurrence of extended low surface-brightness galaxies in the UDF (WC06) rules out *in situ* star formation as the heat source for the 'high cool' DLAs. Rather, these DLAs are likely heated by FUV radiation emitted by compact bulge sources, identified as Lyman Break Galaxies, embedded in the neutral gas. On the other hand *in situ* star formation in the 'low cool' DLAs is compatible with the UDF results, provided the DLA diameters are less than $\sim$ 10 kpc. The short cooling times of the gas further imply that the star formation we detect occurs continuously rather than in a few isolated bursts. We conclude that star formation occurs in all DLAs and proceeds in one of two modes, *in situ* or bulge dominated.

(5) In § 4.6 we compared the median values of properties in the two populations. The results suggest that the crucial parameter distinguishing the two populations is mass. That is, 'high cool' DLAs are embedded in halos that are significantly more massive than the halos encompassing the 'low cool' DLAs.

(6) The idea of mass sequences brings up analogies with bivariate distributions in modern galaxies. Recent surveys reveal separate parallel 'blue' and 'red' galaxy sequences in which galaxy color and age are correlated with stellar mass, while star-formation activity is anti-correlated with stellar mass. When the galaxy sample is divided into bins of stellar mass, the color distribution in each mass bin is bimodal, with an increase in the ratio of 'red' to 'blue' galaxies with stellar mass. In § 4.7 we constructed bivariate distributions for analogous properties of DLAs. Using W_{1526} (or Δv_{90}) as a proxy for mass and [M/H], as a proxy for $u - r$ color, we found strong evidence for a correlation between [M/H] and W_{1526}. We also found tentative evidence for two parallel sequences in

the (ℓ_c,W_{1526}) and ($\Sigma_{\rm SFR}$,W_{1526}) planes, where ℓ_c and $\Sigma_{\rm SFR}$ are possible proxies for H$\delta_{\rm A}$, an indicator of recent star formation in galaxies. We found tentative evidence for (1) bimodal distributions of ℓ_c and $\Sigma_{\rm SFR}$ in bins of fixed W_{1526}, and (2) a larger fraction of 'high cool' DLAs with high values of ℓ_c and $\Sigma_{\rm SFR}$ in bins with the largest values of W_{1526}. Therefore, star-formation activity in DLAs may increase with mass, which is consistent with periods of high-z star formation in early-type galaxies.

(7) In § 4.7 we placed these results in the context of current galaxy formation theory. We found that the transition-mass scenario, introduced to explain bimodality in modern galaxies, provides a plausible scenario for the onset of bimodality in high-z DLAs. In this picture the 'high cool' DLAs comprise outlying neutral gas filaments penetrating hot, virialized gas that fills halos with mass, $M_{\rm DM} > M_{\rm shock}(\equiv 10^{11.5}$ M$_{\odot}$). The inflow of these cold streams through the hot gas results in active star formation in compact bulges, which we presume are the embedded LBGs that heat the surrounding neutral gas. On the other hand accretion of gas onto halos with $M_{\rm DM} \leq M_{\rm shock}$ only produces cold inflows that result in the formation of neutral disks. We associate these objects with the 'low cool' DLAs in which the gas is heated by *in situ* star formation. Since independent simulations demonstrate that half of the DLA population could have $M_{\rm DM} > M_{\rm shock}$, this scenario is in accord with the ℓ_c statistics.

To summarize, the most significant result of this paper is that the bimodality observed in modern galaxies may originate in high-z DLAs. According to Dekel & Birnboim (2006) at high redshift the modes of star formation bifurcate around halos with $M_{\rm DM} \approx M_{\rm shock}$: halos with $M_{\rm DM} > M_{\rm shock}$ accrete gas in hot spherical inflows that are penetrated by cold streams generating starbursts in the inner disks or bulges, while the inflow of cold gas onto halos with $M_{\rm DM}$ $< M_{\rm shock}$ leads to disk growth and *in situ* star formation throughout the disks. This results in a bifurcation in cooling rates, ℓ_c, for the following reasons. First, the bifurcation of star formation modes around $M_{\rm shock}$ creates a bifurcation in $<J_{\nu}^{\rm local}>$, the locally generated mean intensity averaged over all impact parameters, which is given by the same expression for bulge dominated and *in situ* star formation modes (WGP03). In both cases $<J_{\nu}^{\rm local}> \propto \dot{M}_{*}/\pi r_{\rm DLA}^{2}$ (Eq. 3), where $\dot{M}_{*}$ is the total SFR and $r_{\rm DLA}$ is the radius of the neutral-gas disk. While both $\dot{M}_{*}$ and $r_{\rm DLA}$ presumably depend on $M_{\rm DM}$ (Springel & Hernquist 2003; Mo et al. 1998), they also depend on environmental factors, such as gas density, which clearly differ for the two populations. As a result, $<J_{\nu}^{\rm local}>$ will not be a continuous function of $M_{\rm DM}$ near $M_{\rm shock}$, but rather will bifurcate. Because $\ell_{c} \propto \kappa\epsilon J_{\nu}^{\rm local}$ for photoelectrically heated gas in thermal balance (eq. 2) and the product $\kappa\epsilon$ is about the same in the 'high cool' and 'low cool' DLAs, the ℓ_{c} distribution should exhibit an analogous bifurcation or bimodality. The transition to bimodality in modern galaxies occurs at lower redshifts, say $z < 2$, where feedback processes quench star formation at $M_{\rm DM} > M_{\rm shock}$ (Dekel & Birnboim 2006) and the 'high cool' DLAs shut down their cooling rates and evolve onto the red sequence.

Of course, there are caveats to these conclusions. First, the analogies with mass correlations in modern galaxies are tentative due to the limited number of DLAs with positive detections of C II* absorption. We need to increase the size of the sample to establish the reality of this result.

The second caveat is related to our assumption that Δv_{90} and W_{1526} are measures of virial velocities, hence of dark-matter mass. Razoumov et al. (2007) describe the difficulties in constructing self-consistent numerical ΛCDM models in which the DLA velocity fields are caused by virial motions alone: the challenge is to restrict DLA gas to halos sufficiently massive to generate significant virial velocities and sufficiently numerous to reproduce the observed DLA covering factors. An alternative explanation is that gas motions in DLAs are due to outflows; i.e. winds (see Nulsen et al. 1998; Schaye 2001). The presence of winds is plausible in the case of 'high cool' DLAs, since we have associated these DLAs with LBGs, which exhibit P Cygni profiles (Pettini et al. 2002). It is reasonable to assume that DLAs with higher SFRs would produce higher outflow velocities, which would be consistent with the larger values of Δv_{90} and W_{1526} in 'high cool' DLAs. This possibility is also consistent with observations of nearby starburst galaxies, which exhibit correlations between outflow velocities of neutral gas and SFRs (Martin 2005). As a result, the parameters Δv_{90} and W_{1526} could be direct signatures of outflows rather than virial velocities. However, since starburst galaxies also exhibit a correlation between outflow velocity and circular velocity (Martin 2005), the DLA parameters could be indirect signatures of dark-matter mass even in this scenario. Therefore, while the physical origin of the velocities within DLAs remains controversial, a bimodal distribution of dark-matter mass is the most plausible explanation for the bimodal properties of DLAs.

We finish with the following question: where are the DLAs in which C II* absorption arises in WNM gas? In § 4.2 we argued that C II* absorption in 'high cool' and 'low cool' DLAs arises in CNM gas exposed, respectively, to high and low values of $J_\nu^{\rm local}$. But if DLAs are multi-phase media in which the CNM and WNM are in pressure equilibrium, we would expect a similar fraction of DLA sightlines to intersect each phase if, by analogy with the Galaxy ISM, they have comparable area covering factors (McKee & Ostriker 1977). Because the grain photoelectric heating efficiency, ϵ (Eq. 2), is considerably lower in the WNM than in the CNM (Weingartner & Draine 2001), it is also possible for C II* absorption resulting in $\ell_c \le \ell_c^{\rm crit}$ to form in sightlines intersecting *only* WNM gas in 'high cool' DLAs. The problem with this scenario is that it would also predict velocity widths, metallicities, and dust-to-gas ratios significantly larger than observed for the 'low cool' DLAs. Thus, while some DLAs with $\ell_c \le \ell_c^{\rm crit}$ may arise in the 'high cool' population, most of them plausibly form in a separate population of CNM gas. Therefore, if the area covering factors of the WNM gas in both populations are significant, the heating efficiencies must be sufficiently low for the resulting values of ℓ_c to be less than the $10^{-27.4}$ ergs s^{-1} H^{-1} peak of the 'low cool' population. Consequently, the answer to our question may be that the sightlines encountering only WNM gas may be responsible for many of the upper limits in Fig. 4.1.

4.9 Acknowledgments

We wish to thank Eric Gawiser, Kim Griest, and Crystal Martin for valuable discussions and Jay Strader for performing the NMIX statistical tests. AMW, JXP, and MR were partially supported by NSF grant AST 07-09235.

4.10 Copyright

This chapter, in full (with minor exceptions to conform to this thesis), is a reprint of "Bimodality in Damped Lyman-α Systems", Wolfe, A. M., Prochaska, J. X., Jorgenson, R. A., & Rafelski, M. 2008, The Astrophysical Journal, Vol. 681, p. 881.

5

An 84-μG Magnetic Field in a Galaxy at $z = 0.692$

Content from this chapter has been accepted as a Letter to *Nature* with the following author list: Arthur M. Wolfe, Regina A. Jorgenson, Timothy Robishaw, Carl Heiles & Jason X. Prochaska.

5.1 Introduction

The magnetic field pervading our Galaxy is a crucial constituent of the interstellar medium: it mediates the dynamics of interstellar clouds, the energy density of cosmic rays, and the formation of stars (Beck 2005). The field associated with *ionized* interstellar gas has been determined through observations of pulsars in our Galaxy. Radio-frequency measurements of pulse dispersion and the rotation of the plane of linear polarization, i.e., Faraday rotation, yield an average value $B \approx 3$ μG (Han et al. 2001). The possible detection of Faraday rotation of linearly polarized photons emitted by high-redshift quasars (Kronberg et al. 2008) suggests similar magnetic fields are present in foreground galaxies with redshifts $z > 1$. As Faraday rotation alone, however, determines neither the magnitude nor the redshift of the magnetic field, the strength of galactic magnetic fields at redshifts $z > 0$ remains uncertain. Here we report of a magnetic field of $B \approx 84$ μG in a galaxy at z =0.692, using the same Zeeman-splitting technique that revealed an average value of $B = 6$ μG in the *neutral* interstellar gas of our Galaxy (Heiles & Troland 2004). This is unexpected, as the leading theory of magnetic field generation, the mean-field dynamo model, predicts large-scale magnetic fields to be weaker in the past rather than stronger (Parker 1970).

5.2 The Detection

We detected Zeeman splitting of the z=0.692 21 cm absorption line in the direction of the quasar 3C 286 (Brown & Roberts 1973)(Davis & May 1978) using the 100-m Robert C. Byrd Green Bank Telescope (GBT) of the National Radio Astronomy Observatory. The absorption arises in a damped Lyα system (henceforth denoted DLA-3C286) that is drawn from a population of neutral gas layers widely thought to be the progenitors of modern galaxies (Wolfe, Gawiser, & Prochaska 2005). The radio data for DLA-3C286 are summarized in Fig. 5.1, which shows the line-depth spectra constructed from the measurable quantities used to describe polarized radiation, that is, the Stokes parameters. We show the line-depth spectra constructed from the $I(\nu)$ and $V(\nu)$ Stokes parameters (where ν denotes frequency) near the 839.4 MHz frequency centroid of the redshifted 21 cm absorption line. Fig. 5.1a shows the line-depth spectrum constructed from $I(\nu)$. A Gaussian fit to the absorption line in Fig. 5.1a yields a redshift z=0.6921526±0.0000008, central optical depth of τ_0=0.095±0.006, and a velocity dispersion σ_v=3.75±0.20 km s^{-1} , which are in good agreement with previous results (Brown & Roberts 1973)(Davis & May 1978).

Fig. 5.1b plots the line-depth spectrum constructed from $V(\nu)$, which shows the classic 'S curve' pattern expected for Zeeman splitting. From our least squares fit to the data, we find $B_{\rm los}$=83.9±8.8 μG, where $B_{\rm los}$ is the magnetic field component projected along the line of sight (we note that the direction of $B_{\rm los}$ is unknown since the instrumental sense of circular polarization was not calibrated). This magnetic field differs in two respects from the magnetic fields obtained from Zeeman splitting arising in interstellar clouds in the Galaxy. First, the field strength corresponds to the line-of-sight component of the mean field $< B_{\rm los} >$ averaged over transverse dimensions exceeding 200 pc, as very-long-baseline interferometry observations of the 21-cm absorption line show that the gas layer must must extend across more than 0.03 $''$ to explain the difference between the velocity centroids of the fringe amplitude and phase-shift spectra (Wolfe et al. 1976) (although the data are consistent with a B-field coherence length less than 200 pc, the resulting gradient in magnetic pressure would produce velocity differences exceeding the shift of $\approx$ 3 km s^{-1} shift across 200 pc detected by very-long-baseline interferometry). By contrast, the transverse dimensions of radio beams subtended at neutral interstellar clouds in the Galaxy are typically less than 1 pc. Second, this field is at least an order of magnitude stronger than the 6-μG average of B fields inferred from Zeeman splitting for such clouds (Heiles & Troland 2004).

5.2.1 Detection Details

The data were acquired in 12.6 hrs. of on-source integration with the GBT radio antenna. Because the GBT feeds detect only orthogonal linearly polarized signals, while Zeeman splitting requires measuring circular polarization to construct Stokes $V(\nu)$, we generated $V(\nu)$ by cross-correlation techniques (Heiles 2001). In Figure 5.1a, the velocity v=0 km s^{-1} corresponds to z=0.6921526. Line-depth function $D_I(\nu) \equiv [I(\nu) - I_c(\nu)]/I_c(\nu)$, where $I(\nu) \equiv s_0 + s_{90}$, with s_θ the power measured in linear polarization position angle θ, corresponds to the total intensity spectrum, and $I_c(\nu)$ is a model fit to the $I(\nu)$ continuum. $D_I(\nu)$ $=\exp[-\tau(\nu)]-1$ where $\tau(\nu) \equiv [\tau(\nu)_0 + \tau(\nu)_{90}]/2$ is the average optical depth in

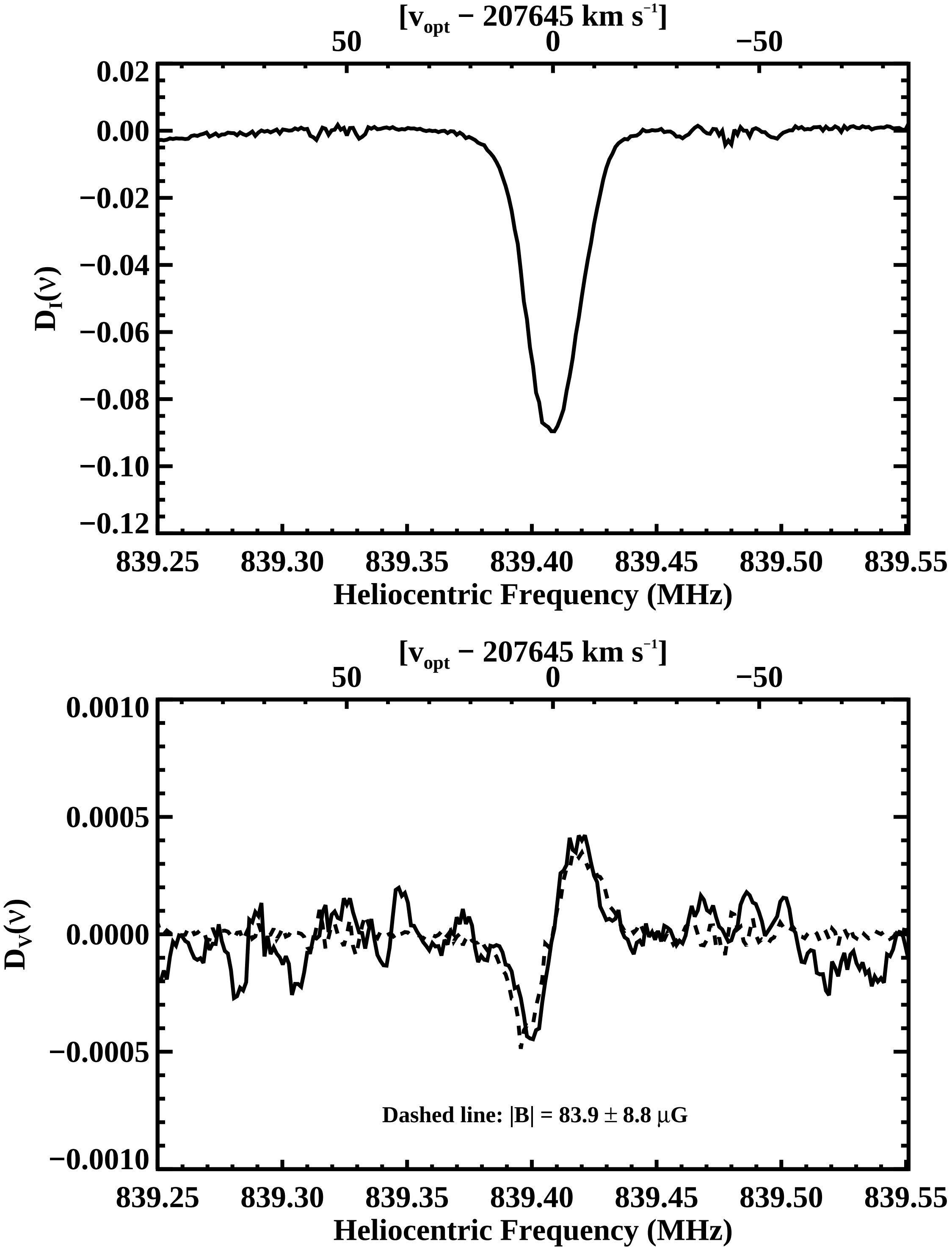

Figure 5.1: Line-depth spectra of Stokes-parameters, explained in detail in the text.

the two orthogonal states of linear polarization (Heiles & Troland 2004). Figure 5.1b is the line-depth function $D_V(\nu) \equiv V(\nu)/I_c(\nu)$, where $V(\nu) \equiv s_{\rm RCP} - s_{\rm LCP}$ is difference in power between the right-hand and left-hand circularly polarized (respectively RCP and LCP) signals. Here $D_V(\nu) = -[\tau_V(\nu)/2]\exp[-\tau(\nu)]$, where $\tau_V(\nu) \equiv \tau_{\rm RCP}(\nu) - \tau_{\rm LCP}(\nu) << 1$ (Heiles & Troland 2004) is the difference between the optical depths of RCP and LCP photons. For Zeeman splitting of the 21 cm line, the degeneracy of the $F = 0$ to $F = 1$ hyperfine transition is removed since the $m_F = -1, 0, +1$ states differ in energy. This results in a small frequency difference between absorbed LCP photons ($m_F = -1$) and RCP photons ($m_F = +1$). $V(\nu)$ is crucial for detecting Zeeman splitting because the orthogonal, circularly polarized states of the photon are eigenstates of the spin angular momentum operator with eigenvalues $\pm\ \hbar$, that is, angular momenta directed along or opposite to the direction of photon propagation (Baym 1981). When $B_{\rm los} = B$, transitions between the hyperfine $F = 0$ and $F = 1$ states occur exclusively through absorption of LCP or RCP photons through excitation of the $m_{\rm F} = -1$ and $m_{\rm F} = +1$ hyperfine states respectively. Because $V(\nu)$ is the difference in the RCP and LCP intensities, the resulting $V(\nu)$ line profile is the difference between two Gaussian absorption profiles with frequency centroids shifted by $\Delta\nu_B = 2.8(B_{\rm los}/\mu{\rm G})(1 + z)^{-1}$ Hz (where $B_{\rm los}$ is measured in microgauss). The 'S curve' is due to the sign flip in RCP-minus-LCP intensity difference as ν passes through line center.

5.3 Optical Data

We obtained further information about conditions in the absorbing gas in DLA-3C286 from accurate optical spectra acquired with the HIRES Echelle spectrograph on the Keck I 10 m telescope. Fig. 5.2 shows velocity profiles for several resonance absorption lines arising from dominant low-ionization states of abundant elements. The results of our least squares fit of Voigt profiles to

Table 5.1: PHYSICAL PARAMETERS OF DLA-3C286[a,b] INFERRED FROM OPTICAL ABSORPTION

Ion X	$\log_{10} N(X)$ cm^{-2}	[X/H]
H I	21.25±0.02	—
Fe II	15.09±0.01	−1.66±0.02
Cr II	13.44±0.01	−1.48±0.02
Zn II	12.53±0.03	−1.39±0.03
Si II	>15.48	>-1.31

[a] Redshift $z = 0.69217485 \pm 0.00000058$

[b] Velocity Dispersion $\sigma_v = 3.08 \pm 0.13$ km s^{-1}

the data are shown in Table 1, where the optical redshift is displaced +3.8 ±0.2km s^{-1} from the 21 cm redshift. This solution also yields ionic column densities from which we derived the logarithmic metal abundances with respect to solar abundances, [M/H], and dust-to-gas ratios with respect to the Galactic interstellar medium, [D/G]. These are among the lowest values of [M/H] and [D/G] deduced for damped Lyα systems at z=0.7 (refs. 10, 11). The low metallicity indicates a history of low star formation rates (SFR). Because the intensity of far ultra-violet radiation emitted by young massive stars is proportional to the concurrent SFR per unit area $\Sigma_{\rm SFR}$, low values of $\Sigma_{\rm SFR}$ should result in low grain photoelectric heating rates per H atom, $\Gamma_{\rm pe}$ (Wolfe, Prochaska & Gawiser 2003). This is consistent with the low upper limit, $\Gamma_{\rm pe} < 10^{-27.4}$ ergs s^{-1} H^{-1}, obtained by combining the assumption of thermal balance with the absence of C II* absorption (that is, absorption from C II in the excited $^2P_{3/2}$ fine structure state) at a wavelength of 1335.7 Å in the previous low-resolution Hubble Space Telescope (HST) spectra of 3C 286 (Boisse et al. 1998), and indicates $\Sigma_{\rm SFR} < 10^{-2.9}$ M$_\odot$ yr^{-1} kpc^{-2} (95 % confidence level), which is less than the solar-neighborhood value of $10^{-2.4}$ M$_\odot$ yr^{-1} kpc^{-2} (Kennicutt 1998).

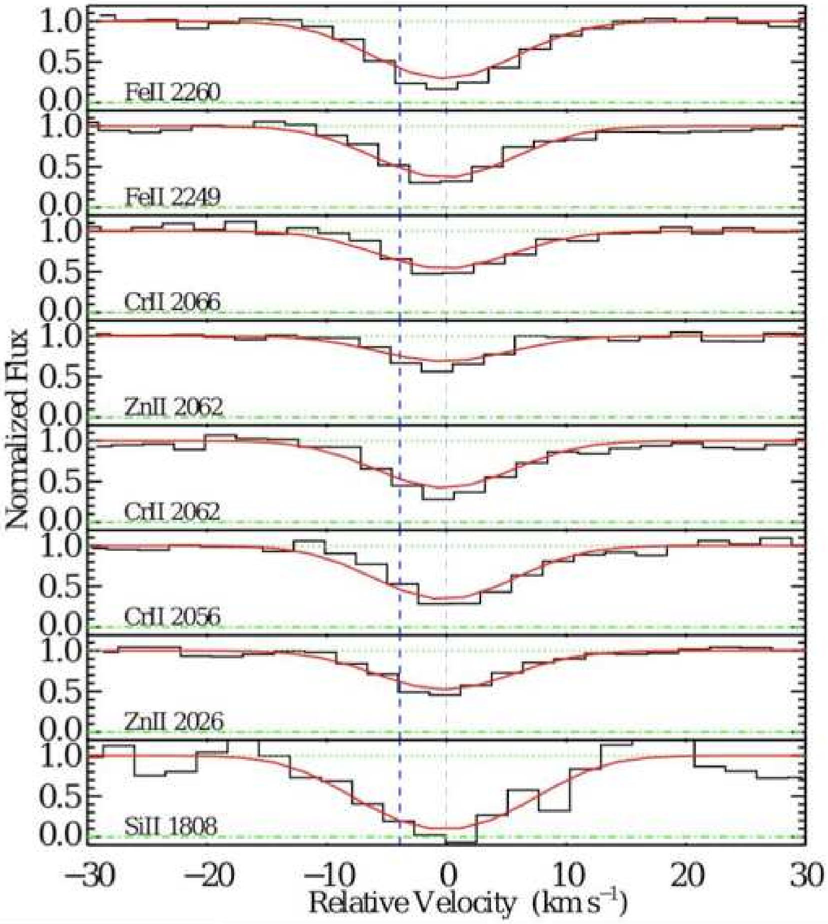

Figure 5.2: HIRES velocity profiles for dominant low-ionization states of abundant elements in the 21 cm absorber towards 3C 286. Spectral resolution Δv=7.0 km s^{-1} and the average signal-to-noise ratio per 2.1 km s^{-1} pixel is about 30:1. The bold dashed vertical line denotes the velocity centroid of single-dish 21 cm absorption feature and the faint dashed vertical line denotes the velocity centroid of the resonance lines shown in the figure. Our least squares fit of Voigt profiles (red) to the data (black) yields ionic column densities as well as the redshift centroid and velocity dispersion shown in Table 1 (lower and upper green horizontal lines refer to zero and unit normalized fluxes). Because refractory elements such as Fe and Cr can be depleted onto dust grains (Savage & Sembach 1996), we used the volatile elements Si and Zn to derive a logarithmic metal abundance with respect to solar abundances of [M/H]=−1.30. The depletion ratios [Fe/Si] and [Cr/Zn] were then used to derive a conservative upper limit on the logarithmic dust-to-gas ratio relative to Galactic values of [D/G] <−1.8.

5.4 Discussion

As a result, we have detected an unusually strong magnetic field at $z = 0.692$ with a coherence length that probably exceeds 200 pc in neutral gas that is quiescent, metal-poor, nearly dust-free, and presents little evidence for star formation. To model this configuration, we first consider the magnetostatic equilibrium of a plane-parallel sheet with in-plane magnetic field $B_{\rm plane}$ orthogonal to the vertical gravitational field exerted by gas with perpendicular mass surface density, Σ. In magnetostatic equilibrium the total midplane pressure, $(B^2_{\rm plane}/8\pi) + \rho\sigma^2_v$, equals the 'weight' of the gas, $\pi G\Sigma^2/2$, where ρ is the mass volume density of the gas and G is the gravitational constant. However, because the pressure-to-weight ratio exceeds 715 in DLA-3C286, the magnetized gas cannot be confined by its self-gravity. Therefore, self-consistent magnetostatic configurations are ruled out unless the contribution of stars to Σ exceeds ≈ 350 M$_\odot$pc^{-2}. Although this is larger than the 50 M$_\odot$pc^{-2} surface density perpendicular to the solar neighborhood, such surface densities are common in the central regions of galaxies. In fact high surface densities of stars probably confine the highly magnetized gas in the nuclear rings of barred spirals. These exhibit *total* field strengths of ~ 100 μG, inferred by assuming equipartition of magnetic and cosmic-ray energy densities[1]. However, because the rings are associated with regions of active star formation, high molecular content, and high dust content, they are unlikely sites of the magnetic field detected in DLA-3C286.

On the other hand the absorption site might consist of highly magnetized gas confined by the gravity exerted by a disk of old stars. The H I disks found at the centers of early-type S0 and elliptical galaxies (Morganti et al. 2006) are possible prototypes. Support for this idea stems from a high-resolution image obtained with the Hubble Space Telescope: a Wide Field and Planetary Camera 2 (WFPC2) I-band image, from which the quasar has been subtracted, reveals residual emission spread over angular scales of $\sim 1''$ (Le

Brun et al. 1997). The asymmetry of the light distribution with respect to the point-source quasar suggests that some of the light is emitted by a foreground galaxy with a brightness centroid displaced less than 0.5 $''$ from the quasar. The location of diffuse emission in the direction of an amorphous object detected 2.5 $''$ from the quasar in ground-based imaging (Steidel et al. 1994) further suggests that the diffuse emission comes from central regions of the amorphous object. A recent reanalysis of the WFPC2 image shows the amorphous object to be a filament resembling a spiral arm or tidal tail (H.-W. Chen, personal communication), that is, the outer appendage of a galaxy centered within a few kpc of the quasar sightline.

However, the magnetic field detected in DLA-3C286 may not be confined by gravity in an equilibrium configuration. Rather, the detected field may be enhanced by a shock (F.H.Shu 2008, personal communication). Assuming a typical value of $B_{\rm plane}\approx$ 5 μG for the equilibrium field of the preshock gas, we find that a shock-front velocity of $\approx$ 250 km s^{-1} will result in a post-shock field strength of $\approx$ 100 μG in the limit of flux freezing in a radiative shock with post-shock density of $\approx$ 10 cm^{-3}. This scenario seems plausible because 250 km s^{-1} is reasonable for the impact velocity generated by the merger between the gaseous disks of two late-type galaxies, and the WFPC2 image is consistent with the presence of two foreground galaxies. But the second disk would create another set of absorption lines displaced $\geq$ 250 km s^{-1} from the redshift of DLA-3C286, which is the only redshift observed. By contrast, the merger between a gaseous disk and an elliptical galaxy could result in only one damped Lyα system redshift, as a significant fraction of ellipticals do not contain H I disks (Morganti et al. 2006). In this case a shock front moving in the plane of the disk galaxy would be generated by the gravitational impulse induced by the elliptical moving normal to the plane. Preliminary estimates indicate that an elliptical with a modest mass, M=2$\times$10^{11} M$_{\odot}$, and impact velocity of $\approx$ 300 km s^{-1} would produce a cylindrical shock of sufficient strength to boost an initial field with $B_{\mathrm{plane}} \approx 10\ \mu$G to $\approx 100\ \mu$G.

Let us examine these scenarios more closely. The quiescent velocity field of the gas fits in naturally with the 'magnetostatic equilibrium' scenario, because the low value of Σ_{SFR} suggests a low rate of energy injection into the gas by supernovae (McKee & Ostriker 1977), which could result in a velocity dispersion of $\sigma_v \approx 4$ km s^{-1} . Moreover, the weak radio jets associated with early-type galaxies containing central H I disks are natural sources of B fields for these disks. However, 21 cm absorption measurements of such disks in nearby galaxies reveal the presence of absorption-line widths far broader than the narrow-line width of DLA-3C286 (Morganti et al. 2004). Also, it is unclear whether or not the high surface density of old stars required to confine the B fields are present in these disks, and whether or not the build-up of B_{plane} to 100 μG is possible in the 4 to 5 Gyr age of the disk. In the case of the 'merger scenario' the dynamo need only build up to $\approx 10\ \mu$G in the same time interval, but it is then necessary to explain why the post-shock velocity field averaged over length scales of 200 pc is so quiescent. Furthermore, the probability p for detecting $\sim$ 100-μG magnetic fields in a random sample of 21 cm absorbers is small. Our estimates, based on the merger fraction of galaxies with $z \sim 1$ (Lotz 2008) and on the duration time for magnetic field enhancement, suggest that $p \approx 0.005$ to 0.03: either we were lucky, or some characteristic of DLA-3C286, such as narrow line width, is a signature of strong magnetic fields.

Therefore, it is premature to decide among these and other possible models to explain the presence of the 84 μG magnetic field in DLA-3C286. However, our data support the inference from recent tenetative evidence for Faraday rotation in high-z quasars (Bernet et al. 2008) that magnetic fields are generic features of galaxies at high redshifts, which potentially have a more important role in galaxy formation and evolution (Rees 2006) than hitherto realized. Specifically, the highly magnetized gas that we have detected could suppress gravitational collapse and hence may be a reason for the low in situ star formation rates of high-z DLAs (Wolfe & Chen 2006). We plan to test this hypothesis by using the GBT to search for Zeeman splitting in high-redshift DLAs exhibiting 21 cm absorption.

5.5 Acknowledgements

We wish to thank Frank H. Shu for suggesting the merger model and H.-W. Chen for providing us with her reanalyzed images of 3C 286.. We also thank Frank H. Shu, Eric Gawiser, and Alex Lazarian for valuable comments and the US National Science Foundation for financial support. The GBT is one of the facilities of the National Radio Astronomy Observatory, which is a center of the National Science Foundation operated under cooperative agreement by Associated Observatories, Inc. A. M. W., R. A. J., and J. X. P. are Visiting Astronomers at the W. M. Keck Telescope. The Keck Oservatory is a joint facility of the University of California, the California Institute of Technology and the National Aeronautics and Space Administration.

5.6 Copyright

This chapter, in full (with minor exceptions to conform to this thesis), is a reprint of "An 84 μG Magnetic Field in a Galaxy at Redshift $z = 0.692$", Wolfe, A. M., Jorgenson, R. A., Robishaw, T., Heiles, C., & Prochaska, J. X., 2008, Nature, Accepted August 2008.

Bibliography

Abel, N. P., Brogan, C. L., Ferland, G. J., O'Dell, C. R., Shaw, G., Troland, T. H., 2004 ApJ, 609, 247

Abrahamsson, E., Krems, R.V. & Dalgarno, A. 2007, ApJ, 654,1171

Akerman, C. J. *et al.* 2005, A&A, 440, 499.

Anders, E. & Grevesse, N., 1989, GeCoA, 53, 197

Ashman, K. M., Bird, C. M., & Zepf, S. E., 1994, AJ, 108, 2348

Bakes, E. L. O., & Tielens, A. G. G. M., 1994, ApJ 427, 822

Baldry, I. K., Glazebrook, K., Brinkmann, J., Zelljko, I., Lupton, R., Nichol, R. C., & Szaly, A. S., 2004, ApJ, 600, 681

Baym, G. *Lectures on quantum mechanics* Ch. 1 (W. A. Benjamin Inc. Reading, Mass. 1981).

Beck, R. 2005, Cosmic Magnetic Fields, Lecture Notes in Physics, 664, 41

Bell, E. F., Wolf, C., Meisenheimer, K., Rix, H.-W., Borch, A., Dye, S., Kleinheinrich, M., Wisotzki, L, & McIntosh, D. H., ApJ, 608, 752

Bennett, C.L., et al. 2003, ApJS, 148, 1

Bernet, M. L., Miniati, F., Lilly, S. J., Kronberg, P. P. & Dessauges-Zavadsky, M. 2008, Nature, 454, 302

Blanton, M. R., Hogg, D. W., Bahcall, N. A. et al., 2003, ApJ, 594, 186

Boisse, P., Le Brun, V., Bergeron, J., Deharveng, J.-M. 1998, A&A, 333, 841

Brown, R. L. & Roberts, M. S., 1973, ApJ, 184, L7

Carswell, R. F., Hilliard, R. L., Strittmatter, P. A., Taylor, D. J., & Weymann, R. J. 1975, ApJ, 196, 351

Cooke, J., Wolfe, A. M., Gawiser, E., & Prochaska, J. X., 2006, ApJ, 652, 994

Crutcher, R., Heiles, C., & Troland, T. 2003, Turbulence and Magnetic Fields in Astrophysics, 614, 155

Cui, J., Bechtold, J., Ge, J., Meyer, D. M. 2005, ApJ, 633, 649

Curran, S. J., & Webb, J. K. 2006, MNRAS, 371, 356

Davis, M. M. & May, L. S. , 1978, ApJ, 219, 1

Dekel, A., & Birnboim, Y., 2006, MNRAS, 368, 2

Dessauges-Zavadsky, M. *et al.* 2001, A&A, 370, 426.

Dessauges-Zavadsky, M., Calura, F., Prochaska, J. X., D'Oorico, S., & Matteucci, F., 2004, A&A, 416, 79

Dessauges-Zavadsky, M. *et al.* 2006, A&A, 445, 93.

Draine, B. T., Bertoldi, F. 1996, ApJ, 468, 269

Eggen, O. J., Lynden-Bell, D., & Sandage, A. R. 1962, ApJ, 136, 748

Ellison, S.L., Yan, L., Hook, I.M., Pettini, M., Wall, J.V., & Shaver, P. 2001, A&A, 379, 393

Ellison, S. L. *et al.* 2001, ApJ, 549, 770. bibitem[Faber (2007)]faber07 Faber, S. M., Wilmer, C. N.A., Wolfe, C. et al., 2007, ApJ, 665, 265

Fall, S.M. & Pei, Y.C. 1993, ApJ, 402, 479

Fox, A. J., Petitjean, P., Ledoux, C., & Srianand, R., 2007, A&A, 473, 791

Ge, J., Bechtold, J., & Black, J. 1997, ApJ, 474, 67

Ge, J., & Bechtold, J. 1997, ApJL, 477, L73

Gehrels, N. 1986, ApJ, 303, 336

Genzel, R., et al. 2006, Nature, 442, 786

Governato, G. L., DeZotti, G., Silva, L, Bressan, A., & Danese, L., 2004, ApJ, 600, 580

Haehnelt, M. G., Steinmetz, M., & Rauch, M., 1998, ApJ, 495, 647

Han, J. L., Manchester, R. N., Lyne, A. G., Qiao, G. J. & van Straten, W., 2006, ApJ, 642, 868

Haardt, F. & Madau, P. 1996, ApJ, 461, 20

Heiles, C., 2001, Pub. Astron. Soc. Pac., 113, 1243

Heiles, C. & Troland, T. H., 2004, ApJS, 151, 271

Henstock, D.R., Browne, I.W.A., Wilkinson, P.N., Taylor, G.B., Vermeulen, R.C., Pearson, T.J., Readhead, A.C.S. 1995, ApJS, 100, 1

Henstock, D.R., Browne, I.W.A., Wilkinson, P.N., McMahon, R.G. 1997, MNRAS, 290, 380

Herbert-Fort, S. *et al.* 2006, PASP, 118, 1077.

Hirashita, H. & Ferrara, A. 2005, MNRAS, 356, 1529

Hollenbach D. J., McKee C. F., 1979, ApJS, 41, 555

Howk, J. C., Wolfe, A. M., Prochaska, J. X., 2005, ApJ, 622, L81

Jackson, C.A., Wall, J.V., Shaver, P.A., Kellerman, K.I., Hook, I.M., & Hawkins, M.R.S. 2002, A&A, 386, 97

Jenkins, E. B., & Shaya, E. J., 1979, ApJ, 231 55

Jenkins, E. B., $ Tripp, T. M. 2001, ApJ, 137, 297

Jenkins, E. B., & Tripp, T. M. 2006, ApJ, 637, 548

Jenkins, E. B., private communication

Jenkins, E. B., & Tripp, T. M. 2007, ASPC, 365, 51

Jura, M. 1974, ApJ, 191, 375

Jura, M. 1975, ApJ, 197, 575

Jura, M. 1975, ApJ, 197, 581

Johansson, P. H., & Efstathiou, G. 2006, MNRAS, 371, 1519

Johnson, C.T., Burke, P.G., & Kingston, A.E. 1987, J. Phys. B. 20, 2553

Kanekar, N. & Chengalur, N. J. 2003, A&A, 399, 857

Kanekar, N. & Chengalur, N. J. & Lane, W. M. 2007, MNRAS, 375, 1528

Kauffmann, G., Heckman, T. M., White, S. D. M., Charlot, S., Tremonti, C., Peng, E. W., Seibert, M., Brinkmann, J., Nichol, R. C., SubbaRao, M., & York, D., 2003, MNRAS, 341, 54

Kennicutt, R. C.,Jr. 1998, ARA&A, 36, 189

Keres, D., Katz, N., Weinberg, D. H., & Dave, R., 2004, MNRAS, 363, 2

Kronberg, P. P., Bernet, M. L., Miniati, F., Lilly, S. J., Short, M. B. & Higdon, D. M. , 2008, ApJ, 676, 70

Kuhlbrodt, B., Orndahl, E., Wisotzki, L., & Jahnke, K. 2005, A&A, 439, 497

Lanzetta, K. M., Wolfe, A. M., Turnshek, D. A., Lu, L., McMahon, R. G., & Hazard, C. 1991, ApJS, 77, 1

Le Brun, V., Bergeron, J., & Deharveng, J. M., 1997, A&A, 321, 733

Ledoux, C., Srianand, R., and Petitjean, P. 2002, A&A, 392, 781.

Ledoux, C., Petitjean, P., and Srianand, R. 2003, MNRAS, 346, 209.

Ledoux, C., Petitjean, P., Fynbo, J. P. U., Møller, P., & Srianand, R. 2006, A&A, 457, 71

Lehner, N., Howk, J. C., Prochaska, J. X., & Wolfe, A. M. 2008, ArXiv e-prints, 807, arXiv:0807.0930

Levshakov, S. A., Dessauges-Zavadsky, M., D'Ordorico, S., & Molaro, P., 2002, ApJ, 565, 696

Lopez, S. and Ellison, S. L. 2003, A&A, 403, 573.

Lopez, S. *et al.* 2002, A&A, 385, 778.

Lopez, S. *et al.* 1999, ApJ, 513, 598.

Lotz, J. M., et al. 2008, ApJ, 672, 177

Lu, L., Wolfe, A. M., Turnshek, D. A., & Lanzetta, K. M. 1993, ApJ, 84, 1

Lu, L. *et al.* 1996, ApJS, 107, 475.

Lu, L., Sargent, W. L. W., and Barlow, T. A. 1999, in ASP Conf. Ser. 156: Highly Redshifted Radio Lines, ed. C. L. Carilli, S. J. E. Radford, K. M. Menten, and G. I. Langston, 132.

Mather, J. C., Fixsen, D. J., Shafer, R. A., Mosier, C., & Wilkinson, D. T., 1999, ApJ, 512, 511

McKee, C. F. & Ostriker, J. P. 1977, ApJ, 218, 148

McLachlan, G. J., & Basford, K. E., 1988, in Mixture Models: Interference and Applications to Clustering (Marcel Dekker, New York)

Meiring, J. D., Kulkarni, V. P., Khare, P., Bechtold, J., York, D. G., Cui, J., Lauroesch, J. T., Crotts, A. P. S., & Nakamura, O. , 2006, MNRAS, 370, 43

Meyer, D.M., York D.G., Black, J.H.,Chaffee, Jr., F.H., & Foltz, C.B.,1986, ApJ, 308L, 37M

Mo, H. J., Mao, S., & White, S. D. M. 1998, MNRAS, 295, 319

Molaro, P. *et al.* 2000, ApJ, 541, 54.

Molaro, P. *et al.* 2001, ApJ, 549, 90.

Morganti, R., Greenhill, L. J., Peck, A. B., Jones, D. L. & Henkel, C. 2004, New Astron. Rev., 48, 1195

Morganti, R. et al. 2006, MNRAS, 371, 157

Morton, D. C. 2003, ApJS, 149, 205

Murphy, M.T., & Liske, J. 2004, MNRAS, 354, L31

Murphy, et al. 2005, private communication

Nagamine, K., 2002, ApJ, 564, 73

Nagamine, K., Springel, V., & Hernquist, L. 2004, MNRAS, 350, 421

Nagamine, K., Wolfe, A. M., Hernquist, L., &Springel, V., & Springel, F. 2007, ApJ, 660, 945

Noterdaeme, P., Petitjean, P., Srianand, R., Ledoux, C. & Le Petit, F. 2007, A&A, 469, 425

Noterdaeme, P., Ledoux, C., Petitjean, P., Le Petit, F., Srianand, R., & Smette, A. 2007, A&A, 474, 393

Noterdaeme, P., Ledoux, C., Petitjean, P., & Srianand, R. 2008, A&A, 481, 327

Nulsen, P. E. J., Barcons, X., & Fabian, A. C. 2000, MNRAS, 301, 346

Oke, J. B., Cohen, J. G., Carr, M., Cromer, J., Dingizian, A., Harris, F. H., Labrecque, S., Lucinio, R., Schaal, W., Epps, H., Miller, J. 1995, PASP, 107, 375

O'Meara, J. M. *et al.* 2006, ApJL, 649, L61.

Omukai K. 2000, ApJ, 534, 809

Parker, E. 1970, ApJ, 160, 383

Pearson, T. J. & Readhead, A. C. S. 1988, ApJ, 328, 114

Péroux, C., Storrie-Lombardi, L.J., McMahon, R.G., Irwin, M., & Hook, I.M. 2001, AJ, 121, 1799

Péroux, C., McMahon, R., Storrie-Lombardi, L., & Irwin, M.J. 2003, MNRAS, 346, 1103

Pei, Y.C., & Fall, S.M. 1995, ApJ, 454, 69

Perlmutter, S., et al. 1999, ApJ, 517, 565

Petitjean, P., Ledoux, C., Noterdaeme, P., & Srianand, R. 2006, A&A, 456, L9

Pettini, M., Ellison, S.L., Steidel, C.C., Bowen, D.V. 1999, ApJ, 510, 576

Polatidis A.G., Wilkinson P.N., Xu W., Readhead A.C.S., Pearson T.J., Taylor G.B., & Vermeulen R.C. 1995, ApJS, 98, 1

Press, W. H., & Schechter, P. 1974, ApJ, 187, 425

Peroux, C., McMahon, R. G., Storrie-Lombardi, L. J., & Irwin, M. J., 2003, MNRAS, 346, 1103

Petitjean, P., Srianand, R., and Ledoux, C. 2000, A&A, 364, L26.

Pettini, M., Rix, S. A., Steidel, C. C., Adelberger, K. L., Hunt, M. P., & Shapley, A. E., 2002, ApJ, 569, 742

Prochaska, J. X. and Wolfe, A. M. 1996, ApJ, 470, 403.

Prochaska, J. X. and Wolfe, A. M. 1997a, ApJ, 474, 140.

Prochaska, J. X., & Wolfe, A. M. 1997, ApJ, 487, 73

Prochaska, J. X., Wolfe, A. M., 1999, ApJ, 121, 369.

Prochaska, J. X. 1999, ApJ, 511, L71.

Prochaska, J. X. and Wolfe, A. M. 2000, ApJL, 533, L5.

Prochaska, J. X., Gawiser, E., and Wolfe, A. M. 2001, ApJ, 552, 99.

Prochaska, J. X., et al. 2001, ApJS, 137, 21

Prochaska, J. X., Howk, J. C., O'Meara, J. M., Tytler, D., Wolfe, A. M., Kirkman, D., Lubin, D., & Suzuki, N. 2002, ApJ, 571, 693

Prochaska, J. X. *et al.* 2002, PASP, 114, 933.

Prochaska, J. X., & Wolfe, A. M. 2002, ApJ, 566, 68

Prochaska, J.X. 2003, IAU,

Prochaska, J.X., Gawiser, E., Wolfe, A.M., Cooke, J., & Gelino, D. 2003, ApJS, 147, 227

Prochaska, J. X., Gawiser, E., Wolfe, A. M., Castro, S., & Djorgovski, S. G. 2003, ApJL, 595, L9

Prochaska, J. X. *et al.* 2003, ApJS, 147, 227.

Prochaska, J. X., Howk, J. C., Wolfe, A. M. 2003, Nature, 423, Issue 6935, pp. 57-59

Prochaska, J. X., Herbert-Fort, S., & Wolfe, A. M. 2005, ApJ, 635, 123

Prochaska, J. X., Chen, H.-W., & Bloom, J. S. 2006, ApJ, 648, 95

Prochaska, J. X., Chen, H.-W., Wolfe, A. M., Dessauges-Zavadsky, M., & Bloom, J. S., 2007, astro-ph/0703701

Prochaska, J. X. *et al.* 2007, ApJS, 171, 29.

Quast, R., Baade, R., & Reimers, D. 2002, A&A, 386, 796

Rao, S.M. & Turnshek, D.A. 2000, ApJS, 130, 1

Razoumov, A. O., Norman, M. L., Prochaska, J. X., Sommer-Larsen, J., Wolfe, A. M., & Yang, Y.-L., 2007, astrophy/07104137

Rees, M. J. , 2006, Aston. Nachr., 327, 495

Richardson, S., & Green, P. J., J.R.Statist. Soc. B, 59, 731

Riess, A. G., et al. 1998, AJ, 116, 1009

Roueff, E., & Le Bourlot, J., 1990, A&A, 236,515

Sargent, W. L. W., Steidel, C. C., & Boksenberg, A. 1989, ApJS, 69,703

Savage, B. D., & Sembach, K. R. 1991, ApJ, 379, 245

Savage, B. D., & Sembach, K. R., 1996, ARA&A, 34, 279

Schaye, J., 2001, ApJ, 559, L1

Schroder, K., Staemmler, V., Smith, M. D., Flower, D. R., & Jaquet, R. , 1991, JPhB, 24, 2487S

Searle, L., & Zinn, R. 1978, ApJ, 225, 357

Sheinis, A. I., Bolte, M., Epps, H. W., Kibrick, R. I., Miller, J. S., Radovan, M. V., Bigelow, B. C., Sutin, B. M. 2002, PASP, 114, 851

Silva, A. I., & Viegas, S. M., 2001, CoPhC, 136, 319S

Silverman, J. D., Green, P. J., et al., 2006, ESASP, 604, 795

Silverman, J. D., Green, P. J., et al., 2007, astrophy/07102641

Songalia, A., Cowie, L. L., Vogt, S., Keane, M., Wolfe, A. M., Hu, E. M., Oren, A. L., Tytler, D. R. & Lanzetta, K. M. 1994, Nature, 371, 43

Songaila, A. and Cowie, L. L. 2002, AJ, 123, 2183.

Spitzer, L. J., & Zweibel, E. G. 1974, ApJL, 191, L127

Spitzer, L. J., Physical Processes in the Interstellar Medium, 1978

Springel, V., & Hernquist, L., 2003, MNRAS, 339, 312

Srianand, R., Petitjean, P., Ledoux, C., Ferland, G., & Shaw, G. 2005, MNRAS, 362, 549

Steidel, C. C., Adelberger, K. L., Shapley, A. E., Pettini, M., Dickinson, M., & Giavalisco, M., 2003, ApJ, 592, 728

Spergel, D. N., et al. 2007, ApJS, 170, 377

Steidel, C. C., Pettini, M., Dickinson, M., & Persson, S. E. 1994, AJ, 108, 2046

Storrie-Lombardi, L.J. & Wolfe, A.M. 2000, ApJ, 543, 552

Taylor, G.B., et al. 1994, ApJS, 95, 345

Taylor, G. B., Vermeulen, R. C., Readhead, A. C. S., Pearson, T. J., Henstock, D. R., Wilkinson, P. N. 1996, ApJS, 107, 37

Thakkar D.D., Xu W., Readhead A.C.S., Pearson T.J., Taylor G.B., Vermeulen R.C., Polatidis A.G., Wilkinson P.N. 1995, ApJS, 98, 33

Tremonti, C. A., Heckman, T. M., Kauffmann, G., et al., 2003, ApJ, 613, 898

Tumlinson, J., et al. 2002, ApJ, 566, 857

Ueda, Y., Akiyama, M., Ohta, K., & Takamitsu, M., 2003 ApJ, 598, 886

Veron-Cetty, M.-P. & Veron, P. 1993, ESO Scientific Report No. 13

Vogt, S. S., 1994, Proc. SPIE, 2198, 362

Weingartner, J. C., & Draine, B. T., 2001, ApJ, 553, 581

White, S. D. M., & Rees, M. J. 1978, MNRAS, 183, 341

Wild, V. & Hewett, P. 2005, MNRAS, 361, L30

Wolfe, A. M., Broderick, J. J., Condon, J. J., & Johnston, K. J. 1976, ApJ, 208, L47

Wolfe, A. M., & Davis, M. M., AJ, 1979, 84, 699

Wolfe, A. M., Turnshek, D. A., Smith, H. E., & Cohen, R. D. 1986, ApJS, 61, 249

Wolfe, A.M. 1985, Phil. Trans. Roy. Soc. Lon., 321, 503

Wolfe, A. M. *et al.* 1994, ApJL, 435, L101

Wolfe, A. M., Lanzetta, K. M., Foltz, C. B., and Chaffee, F. H. 1995, ApJ, 454, 698

Wolfe, A. M., Prochaska, J.X. & Gawiser, E. 2003, ApJ, 593, 215

Wolfe, A. M., Gawiser, E., & Prochaska, J.X. 2003, ApJ, 593, 235

Wolfe, A. M., Howk, J. C., Gawiser, E., Prochaska, J.X. & Lopez, S. 2004, ApJ, 615, 625

Wolfe, A. M., Gawiser, E., & Prochaska, J.X. 2005, ARA&A, 43, 861

Wolfe, A. M., & Chen, H.-W. 2006, ApJ, 652, 981

Wolfe, A. M., Prochaska, J. X., Jorgenson, R. A., & Rafelski, M. 2008, ApJ, 681, 881

Wolfire, M. G., Hollenbach, D., McKee, C. F., Tielens, A. G. G. M., & Bakes, E. L. O. 1995, ApJ, 443, 152

Wolfire, M., G., Hollenbach, D., McKee, C. F., &Tielens, A. G. G. M., 2003, ApJ, 587, 278

Wright, A. & Ostrupcek, R. 1990, Parkes Catalog, Australia Telescope National Facility

Xu W., Readhead A.C.S., Pearson T.J., Polatidis A.G., Wilkinson P.N. 1995, ApJS, 99, 297

York, B. A., Kanekar, N., Ellison, S. L., & Pettini, M. 2007, MNRAS, 382, L53

Zweibel, E. G., & Heiles, C. 1997, Nature, 385, 131